UNIVERSITAT POLITÈCNICA DE CATALUNYA BARCELONATECH

Synergistic optical and microwave remote sensing approaches for soil moisture mapping at high resolution

Gerard Portal González

ADVERTIMENT La consulta d'aquesta tesi queda condicionada a l'acceptació de les següents condicions d'ús: La difusió d'aquesta tesi per mitjà del repositori institucional UPCommons (http://upcommons.upc.edu/tesis) i el repositori cooperatiu TDX (http://www.tdx.cat/) ha estat autoritzada pels titulars dels drets de propietat intel·lectual **únicament per a usos privats** emmarcats en activitats d'investigació i docència. No s'autoritza la seva reproducció amb finalitats de lucre ni la seva difusió i posada a disposició des d'un lloc aliè al servei UPCommons o TDX. No s'autoritza la presentació del seu contingut en una finestra o marc aliè a UPCommons (*framing*). Aquesta reserva de drets afecta tant al resum de presentació de la tesi com als seus continguts. En la utilització o cita de parts de la tesi és obligat indicar el nom de la persona autora.

ADVERTENCIA La consulta de esta tesis queda condicionada a la aceptación de las siguientes condiciones de uso: La difusión de esta tesis por medio del repositorio institucional UPCommons (http://upcommons.upc.edu/tesis) y el repositorio cooperativo TDR (http://www.tdx.cat/?locale-attribute=es) ha sido autorizada por los titulares de los derechos de propiedad intelectual **únicamente para usos privados enmarcados** en actividades de investigación y docencia. No se autoriza su reproducción con finalidades de lucro ni su difusión y puesta a disposición desde un sitio ajeno al servicio UPCommons No se autoriza la presentación de su contenido en una ventana o marco ajeno a UPCommons (*framing*). Esta reserva de derechos afecta tanto al resumen de presentación de la tesis como a sus contenidos. En la utilización o cita de partes de la tesis es obligado indicar el nombre de la persona autora.

WARNING On having consulted this thesis you're accepting the following use conditions: Spreading this thesis by the institutional repository UPCommons (http://upcommons.upc.edu/tesis) and the cooperative repository TDX (http://www.tdx.cat/?locale- attribute=en) has been authorized by the titular of the intellectual property rights **only for private uses** placed in investigation and teaching activities. Reproduction with lucrative aims is not authorized neither its spreading nor availability from a site foreign to the UPCommons service. Introducing its content in a window or frame foreign to the UPCommons service is not authorized (framing). These rights affect to the presentation summary of the thesis as well as to its contents. In the using or citation of parts of the thesis it's obliged to indicate the name of the author.

PhD Thesis

Synergistic optical and microwave remote sensing approaches for soil moisture mapping at high resolution

Gerard Portal González

Departament de Teoria del Senyal i Comunicacions

Universitat Politècnica de Catalunya

Thesis Advisors:

Dr. Mercè Vall-llossera and Dr. Maria Piles

Barcelona, March 2022

Synergistic optical and microwave remote sensing approaches for soil moisture mapping at high resolution. Gerard Portal González, PhD Thesis. Universitat Politècnica de Catalunya.

This work has been founded by the Spanish government through grants ESP2017-89463-C3-2-R and PID2020-114623RB-C32, and the award MDM-2016-0600.

A mi madre, a mi hermana y a mis sobrinos.

Abstract

Soil moisture is an essential climate variable that plays a crucial role linking the Earth's water, energy, and carbon cycles. It is responsible for the water exchange between the Earth's surface and the atmosphere, and provides key information about soil evaporation, plant transpiration, and the allocation of precipitation into runoff, surface flow and infiltration. Therefore, an accurate estimation of soil moisture is needed to enhance our current climate and meteorological forecasting skills, and to improve our current understanding of the hydrological cycle and its extremes (e.g., droughts and floods). L-band Microwave passive and active sensors have been used during the last decades to estimate soil moisture, since there is a strong relationship between this variable and the soil dielectric properties.

Currently, there are two operational L-band missions specifically devoted to globally measure soil moisture: the ESA's Soil Moisture and the Ocean Salinity (SMOS), launched in November 2009; and the NASA's Soil Moisture Active Passive (SMAP), launched in January 2015. The spatial resolution of the SMOS and SMAP radiometers, in the order of tens of kilometers (~40 km), is adequate for global applications. However, to fulfill the needs of a growing number of applications at local or regional scale, higher spatial detail (< 1 km) is required. To bridge this gap and improve the spatial resolution of the soil moisture maps, a variety of spatial enhancement or spatial (sub-pixel) disaggregation approaches have been proposed.

This Ph.D. Thesis focuses on the study of the Earth's surface soil moisture from remotely sensed observations. This work includes the implementation of several soil moisture retrieval techniques and the development, implementation, validation and comparison of different spatial enhancement or downscaling techniques, applied at local, regional, and continental scale. To meet these objectives, synergies between several active/passive microwave sensors (SMOS, SMAP and Sentinel-1) and optical/thermal sensors (MODIS) have been explored. The results are presented as follows:

- *Spatially consistent downscaling approach for SMOS using an adaptive moving window*

A passive microwave/optical downscaling algorithm for SMOS is proposed to obtain fine-scale soil moisture maps (1 km) from the native resolution (~40 km) of the instrument. This algorithm introduces the concept of a shape-adaptive window as a central improvement of the disaggregation technique presented by Piles et al. (2014), allowing its application at continental scales.

- *Assessment of multi-scale SMOS and SMAP soil moisture products across the Iberian Peninsula*

The temporal and spatial characteristics of SMOS and SMAP soil moisture products at coarse- and fine-scales are assessed in order to learn about their distinct features and the rationale behind them, tracing back to the physical assumptions they are based upon.

- *Impact of incidence angle diversity on soil moisture retrievals at coarse and fine scales*

An incidence angle (32.5°, 42.5° and 52.5°)-adaptive calibration of radiative transfer effective parameters single scattering albedo and soil roughness has been carried out, highlighting the importance of such parameterization to accurately estimate soil moisture at coarse-resolution. Then, these parameterizations are used to examine the potential application of a physically-based active-passive downscaling approach to upcoming microwave missions, namely CIMR, ROSE-L and Sentinel-1 Next Generation. Soil moisture maps obtained for the Iberian Peninsula at the three different angles, and at coarse and fine scales are inter-compared using *in situ* measurements and model data as benchmarks.

Contents

List of Figures

List of Tables

List of Symbols

Latin symbols

$\boldsymbol{a_k}$ Model fitting coefficients

$\boldsymbol{A_r}$ Antenna effective aperture [m^2]

$\boldsymbol{B}$ Brightness of a gray body [$W \cdot m^{-2} \cdot sr^{-1}$]

$\boldsymbol{B_{av}}$ Average Earth's magnetic field along the propagation path [$Wb \cdot m^{-2}$]

$\boldsymbol{B_{bb}}$ Brightness of a blackbody [$W \cdot m^{-2} \cdot sr^{-1}$]

$\boldsymbol{B_f}$ Spectral brightness [$W \cdot m^{-2} \cdot Hz^{-1} \cdot sr^{-1}$]

$\boldsymbol{B_i}$ Incident brightness on the antenna [$W \cdot m^{-2} \cdot sr^{-1}$]

$\boldsymbol{c}$ Speed of light in vacuum ($3 \cdot 10^8$ $m \cdot s^{-1}$)

$\boldsymbol{e}$ Emissivity

$\boldsymbol{E_h}$ Electric field of a polarized wave at horizontal polarization [$V \cdot m^{-1}$]

$\boldsymbol{E_v}$ Electric field of a polarized wave at vertical polarization [$V \cdot m^{-1}$]

$\boldsymbol{f}$ Frequency [Hz]

$\boldsymbol{F_n}$ Normalized radiation antenna pattern

$\boldsymbol{h}$ Plank's constant ($6.63 \cdot 10^{-34}$ [J·s])

$\boldsymbol{h_s}$ Effective soil roughness parameter

H Horizontal polarization

$\boldsymbol{I}$ First Stokes parameter

$\boldsymbol{k}$ Electromagnetic wavenumber

$\boldsymbol{k_B}$ Boltzmann's constant ($1.38 \cdot 10^{-23}$ [$J \cdot K^{-1}$])

$\boldsymbol{m_g}$ Gravimetric soil moisture

$\boldsymbol{m_t}$ Transition moisture

$\boldsymbol{m_v}$ Volumetric soil moisture

$\boldsymbol{m_{vt}}$ Maximum bound water fraction of the soil

$\boldsymbol{n}$ Refractive index

$\boldsymbol{n_p}$ Angular dependence of soil roughness

$\boldsymbol{N}$ Number of samples

$\boldsymbol{N_T}$ Ionospheric total electron content [$el \cdot m^{-2}$]

$\boldsymbol{P}$ Power collected by an antenna [W]

$\boldsymbol{P_{bb}}$ Power of a blackbody [W]

$\boldsymbol{P_o}$ Porosity

$\boldsymbol{Q}$ Second Stokes parameter

Q_s Polarization mixing factor

R Pearson's correlation

t Time [s]

t_R Revisit time

T_A Antenna temperature [K]

T_{AP} Apparent brightness temperature [K]

$T_{B_{+45°}}$ Brightness temperature skewed +45°with respect to normal [K]

$T_{B_{-45°}}$ Brightness temperature skewed -45°with respect to normal [K]

T_{B_H} Brightness temperature at horizontal polarization [K]

$T_{B_{lc}}$ Brightness temperature at left-hand circular polarization [K]

$T_{B_{rc}}$ Brightness temperature at right-hand circular polarization [K]

T_{B_V} Brightness temperature at vertical polarization [K]

T_B Brightness temperature [K]

T_I First Stokes parameter in brightness temperature [K]

T_{ph} Physical temperature [K]

T_Q Second Stokes parameter in brightness temperature [K]

T_s Soil effective temperature [K]

T_{SS} Downward-emitted atmospheric brightness temperature [K]

T_U Third Stokes parameter in brightness temperature [K]

T_{UP} Self-emitted atmospheric upward brightness temperature [K]

T_V Fourth Stokes parameter in brightness temperature [K]

U Third Stokes parameter

V Vertical polarization

V Fourth Stokes parameter

V_T Total volume of a soil sample [m^3]

V_w Volume of water in a soil sample [m^3]

W_d Dry weight of a soil sample [g]

W_w Wet weight of a soil sample [g]

Greek symbols

β' Active/passive microwave covariation parameter [-]

γ Transmissivity of the vegetation layer

γ_a Attenuation of the atmosphere

$\Gamma_{s,p}{}^*$ Fresnel's soil reflectivity at p-polarization

$\boldsymbol{\Delta f}$ Bandwidth [Hz]

$\boldsymbol{\varepsilon}$ Complex dielectric constant of a material ($\varepsilon = \varepsilon' - j\varepsilon''$)

$\boldsymbol{\varepsilon'}$ Permittivity of a material (real part of ε)

$\boldsymbol{\varepsilon''}$ Loss factor of a material (imaginary part of ε)

$\boldsymbol{\varepsilon_0}$ Is the permittivity of free space ($8.854 \cdot 10^{-12}$[F· m^{-1}])

$\boldsymbol{\eta}$ Intrinsic impedance of free space (120π Ω)

$\boldsymbol{\theta}$ Incidence angle referred to nadir [°]

$\boldsymbol{\kappa}$ Normalized attenuation coefficient

$\boldsymbol{\lambda}$ Wavelength [m]

$\boldsymbol{\rho_b}$ Soil bulk density [g·cm^{-3}]

$\boldsymbol{\rho_s}$ Specific density [g·cm^{-3}]

$\boldsymbol{\sigma_{eff}}$ Effective conductivity [S·m^{-1}]

$\boldsymbol{\sigma_0}$ Backscatter [-]

$\boldsymbol{\sigma_s}$ Standard deviation of the surface height

$\boldsymbol{\tau}$ Vegetation optical depth [Np]

$\boldsymbol{\phi}$ Azimuth angle referred to nadir [°]

$\boldsymbol{\phi'}$ Faraday rotation angle [rad]

$\boldsymbol{\omega}$ Single scattering albedo

$\boldsymbol{\Omega_p}$ Antenna solid angle [sr]

List of Acronyms

AACES	**A**ustralian **A**irborne **C**alibration/validation **E**xperiments for **S**MOS
AIRSAR	**Air**borne **S**ynthetic **A**perture **R**adar
AMSR-E	**A**dvanced **M**icrowave **S**canning **R**adiometer **E**arth observing system
ANN	**A**rtificial **N**eural **N**etwork
ARIEL-2	**A**irborne **R**ad**I**om**E**ter at **L**-band
ASCAT	**A**dvanced **SCAT**terometer
ASTER	**A**dvanced **S**paceborne **T**hermal **E**mission and **R**eflection radiometer
AVHRR	**A**dvanced **V**ery **H**igh-**R**esolution **R**adiometer
BEC	**B**arcelona **E**xpert **C**enter
BRT	**B**oosted **R**egression **T**rees
CASI	**C**ompact **A**irborne **S**pectrographic **I**mager
CCI	**C**limate **C**hange **I**nitiative
CDTI	**C**entro para el **D**esarrollo **T**ecnológico **I**ndustrial
CESBIO	**C**entre d'**E**tudes **S**patiales de la **BIO**sphère
CF	**C**lay **F**raction
CIMR	**C**opernicus **M**icrowave **I**maging **R**adiometer
CNES	**C**entre **N**ational d'**E**studes **S**patiales
CR	**C**oarse **R**esolution
CRP	**Cr**o**p**lands
CSIC	**C**onsejo **S**uperior de **I**nvestigaciones **C**ientíficas
CUB	**CUB**ist
DCA	**D**ual **C**hannel **A**lgorithm
DisPATCh	**Dis**aggregation based on **P**hysical **A**nd **T**heoretical scale **Ch**ange
DQX	**D**ata **Q**uality **I**ndex
EASE	**E**qual-**A**rea **S**calable **E**arth
ECMWF	**E**uropean **C**entre for **M**edium-**R**ange **W**eather **F**orecasts
ECV	**E**ssential **C**limate **V**ariables
EEF	**E**arth **E**xplorer **F**ile
EO	**E**arth **O**bservation
ERA5	**E**CMWF **A**tmospheric **R**eanalysis **5**th Generation
ESA	**E**uropean **S**pace **A**gency
EVI	**E**nhanced **V**egetation **I**ndex
FAL	**FAL**low

FOP	**Fo**rest-**P**asture
GCOM	**G**lobal **C**hange **O**bservation **M**ission
GCOS	**G**lobal **C**limate **O**bserving **S**ystem
GMI	**G**PM **M**icrowave **I**mager
GPM	**G**lobal **P**recipitation **M**easurement
GRS	**Gr**a**ss**lands
GSFC	**G**oddard **S**pace **F**light **C**enter
GSFC	**G**oddard **S**pace **F**light **C**enter
HR	**H**igh **R**esolution
IC	**I**NRA **C**ESBIO
IW	**I**nterferometric **W**ide
IGBP	**I**nternational **G**eosphere-**B**iosphere **P**rogramme
INRA	**I**nstitut **N**ational de la **R**echerche **A**gronomique
IR	**I**nfra**R**ed
IRR	**IRR**igated
ISEA	**I**cosahedral **S**nyder **E**qual **A**rea
ISMN	**I**nternational **S**oil **M**oisture **N**etwork
JPL	**J**et **P**ropulsion **L**aboratory
L1B	**L**evel **1B**
L1C	**L**evel **1C**
L2	**L**evel **2**
L3	**L**evel **3**
L4	**L**evel **4**
LAI	**L**eaf **A**rea **I**ndex
LC	**L**and **C**over
L-MEB	**L**-band **M**icrowave **E**mission of the **B**iosphere
LPDAAC	**L**and **P**rocessed **D**istributed **A**ctive **A**rchive **C**enter
LPRM	**L**and **P**arameter **R**etrieval **M**odel
LSMEM	**L**and **S**urface **M**icrowave **E**mission **M**odel
MIRAS	**M**icrowave **I**maging **R**adiometer using **A**perture **S**ynthesis
ML	**M**achine **L**earning
MODIS	**Mod**erate resolution **I**maging **S**pectroradiometer
MPDI	**M**icrowave **P**olarization **D**ifference **I**ndex
MR	**M**edium **R**esolution

MSG	**M**eteosat **S**econd **G**eneration
MT-DCA	**M**ulti-**T**emporal Dual **C**hannel **A**lgorithm
MWRI	**M**icro**w**ave **R**adiation **I**mager
NASA	**N**ational **A**eronautics and **S**pace **A**dministration
NDVI	**N**ormalized **D**ifference **V**egetation **I**ndex
NDWI	**N**ormalized **D**ifference **W**ater **I**ndex
NetCDF	**Net**work **C**ommon **D**ata **F**orm
NIR	**N**oise **I**njection **R**adiometers
NSIDC	**N**ational **S**now and **I**ce **D**ata **C**enter
OSSE	**O**bservation **S**ystem **S**imulation **E**xperiment
PALS	**P**assive and **A**ctive **L**- and **S**-bands sensor
PLMR2	**P**olarimetric **L**-band **M**ulti-beam **R**adiometer **2**
RAI	**RAI**nfed cereal
REMEDHUS	Soil Moisture Measurements Station Network of the University of Salamanca **RE**d de **MED**ición de **HU**medad del **S**uelo
RF	**R**andom **F**orest
RFI	**R**adio **F**requency **I**nterference
RMSE	**R**oot **M**ean **S**quare **E**rror
ROSE-L	**R**adar **O**bserving **S**ystem for **E**urope in **L**-band
RVM	**R**elevance **V**ector **M**achine
SAOCOM	**S**atélite **A**rgentino de **O**bservación **CO**n **M**icroondas
SAR	**S**ynthetic **A**perture **R**adars
SAV	**SAV**annas
SCA	**S**ingle **C**hannel **A**lgorithm
SEE	**S**oil **E**vaporative **E**fficiency
SEVIRI	**S**pinning **E**nhanced **V**isible and **I**nfra-**R**ed **I**mager
SF	**S**and **F**raction
SGP99	**S**outhern **G**reat **P**lains experiment in 19**99**
SHR	**SHR**ublands
SM	**S**oil **M**oisture
SMAP	**S**oil **M**oisture **A**ctive **P**assive
SMAPEx	**S**oil **M**oisture **A**ctive **P**assive **Ex**periment
SMEX02	**S**oil **M**oisture **Ex**periments 20**02**
SMOS	**S**oil **M**oisture and **O**cean **S**alinity

SMOSMANIA	**S**oil **M**oisture **O**bserving **S**ystem - **M**eteorological **A**utomatic **N**etwork **I**ntegrated **A**pplication
SSM/I	**S**pecial **S**ensor **M**icrowave **I**mager
SSS	**S**ea **S**urface **S**alinity
STD	**ST**andard **D**eviation
SVM	**S**upport **V**ector **M**achine
SW	**S**oil **W**etness
SWIR	**S**hort**W**ave **I**nfra**R**ed
TASI	**T**hermal **A**irborne **S**pectrographic **I**mager
TEC	**T**otal **E**lectron **C**ontent
TMI	**T**RMM **M**icrowave **I**mager
TRMM	**T**ropical **R**ainfall **M**easuring **M**ission
UPC	**U**niversidad **P**olitécnica de **C**ataluña
uRMSE	**u**nbiased **RMSE**
VAS	**V**alencia **A**nchor **S**tation
VIN	**Vin**eyard
VIS	**Vis**ible
VTCI	**V**egetation **T**emperature **C**ondition **I**ndex
VWC	**V**egetation **W**ater **C**ontent
WP	**W**ilting **P**oint

Chapter 1

Introduction

1.1 Motivation

In 2010, the Global Climate Observing System (GCOS) defined 21 key indicators, known as Essential Climate Variables (ECV), that characterize the Earth's changing climate. Among these ECV, soil moisture (SM) is considered one of the most important [1] due to the crucial role it plays linking the Earth's water (Figure 1.1), energy and carbon cycles. It is involved in the energy flux partition into latent and sensible heat from the land to the atmosphere, and is closely linked to hydro-ecological processes such as soil evaporation, plant transpiration, and the allocation of precipitation into runoff, subsurface flow and infiltration. Therefore, knowledge of SM will allow advancing our physical understanding of land-atmosphere processes interactions, which is key for several applications in climatology [2], hydrology [3], meteorology [4], and water resource management [5].

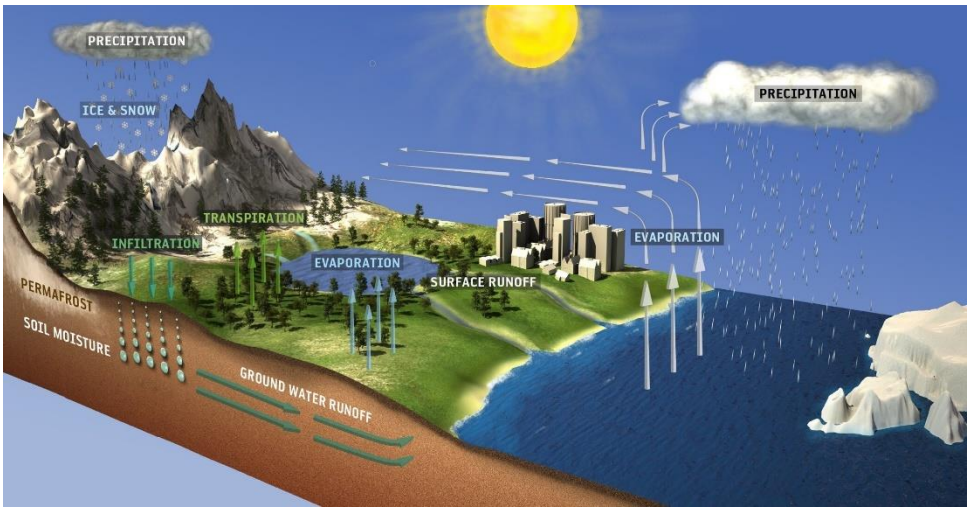

Figure 1.1 Hydrological cycle of the Earth as the sum of the evaporation, transpiration, precipitation, infiltration and runoff processes. Adapted from www.esa.int.

A wide range of techniques have been developed to measure SM using ground instruments including time-domain reflectometry, gravimetric measurements, tensiometers, capacitance sensors, heat pulse sensors, neutron probes, electrical resistance blocks and fiber optic sensors. The main advantages of these ground-based techniques are: (i) the easy installation and deployment of instrumentation, (ii) the relative maturity of the measuring techniques, and (iii) the ability to accurately measure SM at specific soil depth levels. Due to these advantages, SM measurements carried out through the methods proposed above are usually considered as "ground truth" data, and are used as a benchmark to validate and improve global satellite products, as well as hydrological, climate and land surface models. A set of several ground-based instruments deployed within an area is known as a SM network. Main available SM ground-based measurements covering a wide range of spatial locations and spanning different time periods, have been harmonized in a dataset by Dorigo et al. in [6] and are freely accessible at https://ismn.geo.tuwien.ac.at/en/. Data go back as far as 1952 but the longest available time series is ~40 years. This is a very valuable resource yet it comes with the limitation that *in situ* SM observations provide local information that is spatially restricted to the region where they are placed, and may not be representative for the neighboring areas, being therefore very challenging to extrapolate these results at continental or even global scale. This effect is aggravated over heterogeneous regions, since SM depends to a great extent on the interactions between different environmental variables (e.g., soil texture and structure, land cover pattern, topographic features, among others) [7,8].

Figure 1.2 Location of all *in situ* SM networks that make up the ISMN database [6]. Obtained from https: https://ismn.geo.tuwien.ac.at/en/.

In the last few decades, remote sensing measurements have allowed estimating SM from regional to global scales, in some cases with a revisit time of a few days. Among the different technologies, low-frequency microwave (from 1 to 10 GHz) is considered the most suitable technique, due to the strong relationship between water content and soil dielectric properties (Section 2.2.2) at these range of frequencies [9]. Within low-frequency microwaves, L-band (see Table 1.1) is generally preferred to globally estimate SM [10–12], since at these frequencies the atmosphere is considered nearly transparent, and measurements are less affected by soil roughness and vegetation attenuation than at higher frequencies (e.g., X- or C-bands).

Microwave remote sensing includes both passive and active forms. While active sensors (radars) consist of a transmitter and receiver that measures its own signal after being reflected, scattered or refracted, passive sensors (radiometers) consist of a receiver that measures the radiation naturally emitted from the Earth. Microwave radiometers have high radiometric sensitivity (leading to SM accuracies on the order of 0.04 m^3/m^3) but coarse spatial resolution. Past and current passive microwave missions were placed in low-Earth orbits that allow for a high revisit (about 1-3 days) but due to technical limitations (i.e., antenna size), their spatial resolution is limited to tens of kilometers. Therefore, microwave radars, especially Synthetic Aperture Radars (SARs) step in, as their spatial resolution is significantly higher, in the range of some meters. However, radar sensors commonly have lower temporal resolution (around one week vs 1-3 days of passive sensors) and may be significantly affected by soil roughness and the soil-covering vegetation canopy, which complicates the active-only SM retrieval. Moreover, low-frequency microwaves are only sensitive to the soil top 5 cm.

Table 1.1 Satellite frequency bands

Band	Frequency range	Wavelength range
L	1-2 GHz	30-15 cm
S	2-4 GHz	15-7.5 cm
C	4-8 GHz	7.5-3.75 cm
X	8-12 GHz	3.75-2.5 cm
Ku	12-18GHz	2.5-1.67 cm
K	18-26 GHz	1.67-1.15 cm
Ka	26-40 GHz	1.15-0.75 cm

Several techniques have been proposed over time to accurately retrieve SM from measurements of different active and passive microwave sensors. Soil moisture from active sensors can be obtained by inverting physical [13], semi-empirical [14], or empirical [15,16] algorithms which are based on single time-period backscatter information, although multi-temporal passes can also be used to measure relative changes in SM [17,18]. Moreover, almost all SM retrieval algorithms that use passive information are based on the tau-omega ($\tau - \omega$) radiative transfer model i.e., the Single Channel Algorithm (SCA) [19], the Dual Channel Algorithm (DCA) [20], the Multi-Temporal DCA (MT-DCA) [21], the Land Parameter Retrieval Model (LPRM) [22] or the SMOS-INRA-CESBIO (SMOS-IC) [23] (Section 2.2.5). Currently, there are two operational L-band missions specifically devoted to globally measuring SM, the Soil Moisture and Ocean Salinity (SMOS) [11] and the Soil Moisture Active Passive (SMAP) [12] missions, launched by the European Space Agency (ESA) in 2009 and the National Aeronautics and Space Administration (NASA) in 2015, respectively (Section 2.3). In the near future, the Copernicus Imaging Microwave Radiometer (CIMR) mission will provide multi-frequency observations at unprecedented spatial resolutions by using a very large deployable antenna (http://cimr.eu).

The spatial resolution of radiometer-based SM maps is in the order of tens of kilometers. However, to fulfill the needs of a growing number of applications higher spatial detail (< 1 km) is required [24]. To bridge this gap and improve the spatial resolution of the SM maps, a variety

of spatial enhancement or spatial (sub-pixel) disaggregation approaches have been proposed [8,25]. These techniques can be classified according to the nature of the linking model (e.g., Machine Learning (ML)-based [26], semi-empirical [27], physical [28]) and depending on the input of ancillary data (e.g. microwave/optical [27,29,30], microwave active/passive [31,32], topography [33], etc.). Currently, the explosive growth of multi-sensor and multi-resolution Earth Observation (EO) data, along with the great advances in statistical learning, have led to the development of a myriad of ML downscaling approaches, which are able to exploit heterogeneous information and find complex nonlinear relations learned directly from data [34–39]. ML approaches typically excel in accuracy but their interpretability is challenging, yet important to allow for process understanding [40]. In geosciences and remote sensing, physics-aware ML approaches are particularly promising, as they can potentially allow to reconcile data-driven and process-based approaches [41].

1.2 Objectives

This Ph.D. Thesis focuses on the study of the Earth's surface SM using remotely sensed observations, including the implementation of different retrieval algorithms, and the development, validation and comparison of optical/passive and active/passive downscaling techniques, applied at local, peninsular and continental scale. It also analyzes how these retrieval and downscaling techniques could be adapted to work under the specific conditions of upcoming microwave missions i.e., the Copernicus Microwave Imaging Radiometer (CIMR), the Radar Observing System for Europe in L-band (ROSE-L) and Sentinel-1 Next Generation. The activities are presented as follows:

Spatially consistent downscaling approach for SMOS using an adaptive moving window

- The spatial resolution of the SMOS SM maps is about 40 km, which meets the needs of global applications, particularly for climate research and applications [42]. Still, higher resolution (≤ 1 km) is required for local or regional studies [43–45]. The combination of data from different sensors is a common practice to overcome the limitations (e.g., low spatial and temporal resolution, or information masked by clouds) of current technology for SM sensing [32,46,47]. Among the existing multi-sensor/multi-resolution disaggregation techniques, this Thesis focuses on a well-known microwave/optical-based method first introduced by Piles et al. [30,46], that has been operational at BEC-SMOS facilities from 2012 to 2019. It stands out for its simplicity of implementation, the low number of inputs it requires and its good performance when validated against SM *in situ* networks. Its main limitation is that its applicability is restricted to areas with similar climate conditions. The first objective of this Thesis is:

  Develop an enhanced version of the microwave/optical-based downscaling technique initially introduced by Piles et al., [46]*. The focus is to maintain the simplicity and the performance of the original technique, but using an adaptive regional window to allow for seamless downscaling at continental scales. Validate the new proposed downscaling technique using in situ SM measurements (e.g., from REMEDHUS and OzNet networks) as reference, and testing consistency, energy conservation and resulting dynamic range with respect to the native (not disaggregated) SMOS data.*

Assessment of multi-scale SMOS and SMAP soil moisture products across the Iberian Peninsula

- Measuring SM accurately through remote sensing represents a significant challenge due to its high variability in time and space. Two current operational missions, SMOS and SMAP, were specifically designed to measure this variable with a target accuracy of 0.04 m^3/m^3, a revisit time of about 3 days and a spatial resolution between ~30 and 40 km. Although both missions have the same objective, the final retrieved SM at coarse (native) or fine resolution (disaggregated) may show certain discrepancies, for example due to the intrinsic differences of: (i) the technology used by both sensors; (ii) the retrieval or downscaling techniques applied; and (iii) the input parameters used. The second objective of this Thesis is:

  Analyze temporal and spatial characteristics of coarse- and fine-resolution SM products provided by the SMAP and the SMOS missions, with special emphasis on the most recently developed fine resolution ones. Are there relevant differences between the SMAP and the SMOS products? Can be seen clear spatial or temporal patterns of these differences, or are they randomly distributed?

Impact of incidence angle diversity on soil moisture retrievals at coarse and fine scales

- Incidence angle diversity of space-borne radiometer and radar systems operating at low microwave frequencies needs to be taken into consideration to accurately estimate SM. The required input parameters (e.g., the effective single scattering albedo or the effective soil roughness) used in retrieval techniques and downscaling algorithms need to be specifically optimized for the incidence angle of the satellite [48–50] so that the vegetation attenuation and the soil roughness effects can be precisely corrected. This is especially relevant in the light of upcoming missions, such as CIMR that is planned to operate at a constant incidence angle of 55°, ROSE-L planned to work at 25°-46° or Sentinel-1 Next Generation, which are not designed to exclusively estimate SM as are the SMOS (also devoted to estimate the sea surface salinity) and the SMAP missions. Does the quality of the resulting SM maps (at coarse or fine resolution) depend on the incidence angle? Would it be necessary to optimize the input parameters (for retrieval and downscaling algorithms) for the upcoming missions? The third objective of this Thesis is:

  Develop an incidence angle (32.5°, 42.5° and 52.5°)-adaptive calibration of the single scattering albedo and soil roughness effective parameters. Use the above information to retrieve and downscale SM at coarse and fine resolution for each SMOS incidence angle (32.5°, 42.5° and 52.5°) and compare the results obtained at these angles.

1.3 Thesis outline

This Ph.D. Thesis is organized as follows:

Chapter 1 describes the motivation, the objectives and the organization of the document.

Chapter 2 reviews the fundamental concepts on microwave radiometry, including the theoretical background of passive remote sensing over land for estimating SM. This chapter also provides an overview of the most relevant SM retrieval techniques, and introduces in detail the two first space missions devoted to SM monitoring: the ESA's SMOS and the NASA's SMAP.

Chapter 3 provides a comprehensive review of the state of the art of the SM downscaling approaches with emphasis on: optical/microwave, active/passive, and model/data-based downscaling methods. This chapter also contains a brief description of all the datasets used in this Thesis.

Chapter 4 presents a passive microwave/optical downscaling algorithm which introduces the concept of a shape-adaptive window to accurately disaggregate the SMOS SM from its native resolution (~40 km) to 1 km. This methodology is used to generated two SM products: (i) the "MODIS" version which uses SMOS and Moderate-Resolution Imaging Spectroradiometer (MODIS) data exclusively, and (ii) the "cloud-free" version which combines SMOS, MODIS and European Centre for Medium-Range Weather Forecasts (ECMWF) Atmospheric Reanalysis 5th generation (ERA5) data to provide full coverage SM maps under all weather conditions. A comprehensive validation of the products under different climates and biomes is provided.

Chapter 5 analyzes the spatial and temporal characteristics of six SM products derived from SMOS (including the "cloud free" version from Chapter 4) and SMAP missions in order to characterize their distinct features, their advantages and limitations, as well as the rationale behind them.

Chapter 6 includes the implementation of a model-based retrieval approach applied to SMOS brightness temperatures to estimate SM at coarse resolution (25 km) and develop a land use-specific and incidence angle (32.5°, 42.5° and 52.5°)-adaptive calibration of the single scattering albedo and soil roughness parameters. These effective parameters are used together with fine-scale multi-angular Sentinel-1 backscatter in a single-pass active/passive downscaling approach, to estimate brightness temperature at vertical polarization at high resolution (1 km) for each SMOS incidence angle. These brightness temperatures are finally inverted to obtain the corresponding high-resolution SM maps. The impact of incidence angle diversity on SM retrievals at coarse and high resolution is then analyzed.

Chapter 7 summarizes the main conclusions of this Ph.D. Thesis, highlights the original contributions and provides suggestions for future work.

Chapter 2

Review of passive microwave remote sensing

The emissivity of the Earth in the microwave region depends to a great extent on the variations of SM, although it can also be affected by other variables such as soil temperature, soil surface roughness and vegetation canopy. This chapter presents the fundamental concepts on microwave radiometry, including the theoretical background of passive remote sensing over land for estimating SM. Additionally, the two operational L-band missions specifically devoted to measure SM, the ESA's SMOS and the NASA's SMAP, are introduced, including the main characteristics of their sensors and the data products they provide.

2.1 Basic concepts on microwave radiometry

The Earth continuously receives electromagnetic radiation, with most of this energy being emitted mainly by the Sun. While a fraction of this energy is scattered by the Earth's atmosphere, the remainder is transmitted to the Earth's surface. Similarly, part of this transmitted energy is scattered outward or absorbed by the surface. The absorption of electromagnetic energy by a material implies an increase in its temperature. This process, known as thermal emission, balances the absorbed solar radiation and the radiation emitted by the Earth's surface to achieve a thermodynamic balance [9].

2.1.1 Blackbody radiation

All bodies at an absolute physical temperature above zero Kelvin emit electromagnetic radiation. Kirchhoff's law states that a material at thermodynamic equilibrium radiates the same amount of energy it absorbs from the environment. A black body is an ideal, perfectly opaque physical body that absorbs all the incident radiation at all frequencies, directions and polarizations, reflecting none. A black body in thermal equilibrium is also a perfect emitter, radiating all the absorbed energy isotropically, with a frequency dependence according to the Plank's law:

$$B_f = \frac{2hf^3}{c^2}\left(\frac{1}{e^{\frac{hf}{k_B T_{ph}}} - 1}\right) \tag{2.1}$$

where B_f $[W \cdot m^{-2} \cdot Hz^{-1} \cdot sr^{-1}]$ is the spectral brightness density, which represents the amount of power radiated per unit of area, per unit of spectral width and per unit of solid angle; $h = 6.63 \cdot 10^{-34}$ $[J \cdot s]$ is the Plank's constant; $c = 3 \cdot 10^8$ $[m \cdot s^{-1}]$ is the speed of light; f $[Hz]$ is the frequency; $k_B = 1.38 \cdot 10^{-23}$ $[J \cdot K^{-1}]$ is the Boltzmann's constant; and T_{ph} $[K]$ is the absolute temperature.

Figure 2.1a shows the spectral brightness plotted against frequency, where each curve corresponds to a different temperature. This figure demonstrates that an increment in the physical temperature causes: (i) an increase in the brightness; and (ii) an increase of the frequency at which the brightness is maximum.

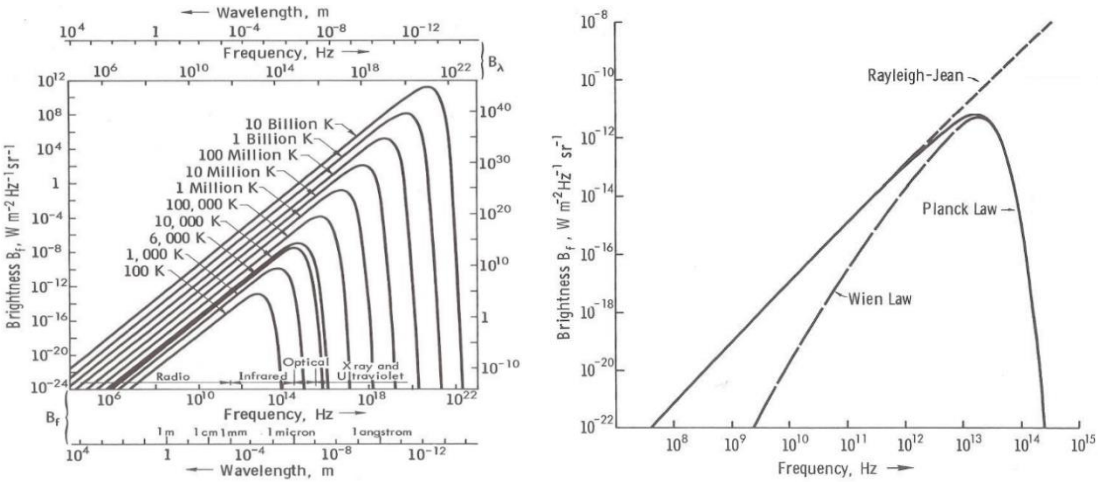

(**a**) (**b**)

Figure 2.1 (a) Plank's radiation law at different temperatures, and (b) Rayleigh-Jeans and Wien laws approximations to the Plank's radiation law, for low and high frequencies, respectively. From [51].

Since $hf/k_B\,T_{ph} \ll 1$ at microwave frequencies, the Taylor approximation of Equation (*2.2*) can be applied to Equation (*2.1*), to approximate the Plank's radiation by the Rayleigh-Jeans law (Equation (*2.3*)).

$$e^x - 1 = \left(1 + x + \frac{x^2}{2!} + \cdots\right) - 1 \approx x \;(for\; x \ll 1) \tag{2.2}$$

$$B_f \approx \frac{2k_B f^2 T_{ph}}{c^2} = \frac{2k_B T_{ph}}{\lambda^2} \tag{2.3}$$

where $\lambda = \frac{c}{f}\;[m]$ is the wavelength. The value of the Rayleigh-Jeans approximation lies in its simplicity with respect to Plank's law. In fact, Equation (2.3) shows a simple linear relation between spectral brightness and physical temperature of the body. The Rayleigh-Jeans deviation from the Plank's exact expression (see Figure 2.1b) is less than 1%, for most of the usable part of the microwave spectrum ($f < 117\;GHz$ and $T_{ph} = 300\;K$).

Therefore, at microwave frequencies, the brightness of a black body at a physical temperature T_{ph} and a bandwidth $\Delta f\;[Hz]$, can be defined as follows:

$$B_{bb} = B_f \cdot \Delta f = \frac{2k_B T_{ph}}{\lambda^2} \cdot \Delta f \tag{2.4}$$

A. Power collected by an antenna surrounded by a black body

Considering the scenario presented in Figure 2.2, at the microwave frequencies and under the Rayleigh-Jeans approximation, the total power received by a lossless antenna with effective aperture A_r $[m^2]$, being characterized by a normalized radiation pattern $F_n(\theta, \phi)$ is given by the Equation (*2.5*):

$$P_{bb} = \frac{A_r}{2} \int_f^{f+\Delta f} \iint_{4\pi} \frac{2k_B T_{ph}}{\lambda^2} F_n(\theta, \phi) d\Omega df \tag{2.5}$$

where the subscript bb refers to a black body. In general, the thermal power emitted by a natural source is randomly polarized. The term $1/2$ appears because the antennas are polarized and detect only half of the randomly polarized incident power noise.

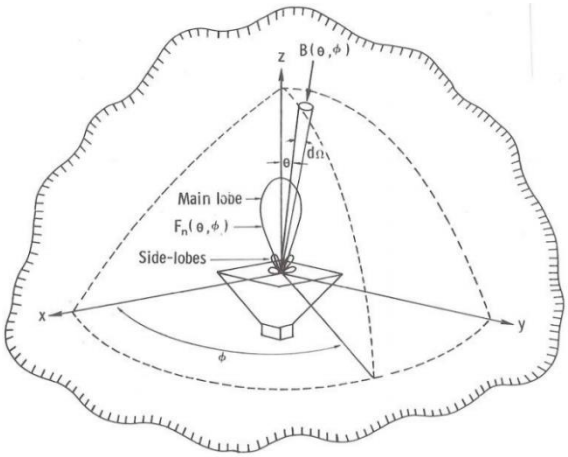

Figure 2.2 Geometry of incident radiation on a lossless antenna: the antenna normalized radiation pattern is $F_n(\theta, \phi)$. From [51].

Assuming a narrow bandwidth signal ($\Delta f \ll f$) to consider B_f constant, Equation (*2.5*) can be simplified to:

$$P_{bb} = k_B T_{ph} \Delta f \frac{A_r}{\lambda^2} \iint_{4\pi} F_n(\theta, \phi) d\Omega \tag{2.6}$$

The solid angle Ω_p of the antenna is related to the effective aperture A_r and is defined as:

$$\Omega_p = \iint_{4\pi} F_n(\theta, \phi) d\Omega = \frac{\lambda^2}{A_r} \tag{2.7}$$

Hence, Equation (2.6) becomes:

$$P_{bb} = k_B T_{ph} \Delta f \tag{2.8}$$

2.1.2 Gray body radiation

A black body is an ideal model, absorbing all the incident energy (perfect absorber) and re-radiating it (perfect radiator), in thermal equilibrium. Real materials, usually called gray bodies, do not have the same behavior as a black body. Gray bodies do not absorb all the energy incident upon them, instead, a fraction is reflected and the other part is transmitted to the body. Then, the absorbed energy is emitted, although it does not have to be isotropically, as a black body would. Instead, the brightness of a gray body $B(\theta, \phi)$ $[W \cdot m^{-2} \cdot sr^{-1}]$ depends on the incidence (θ) and azimuth (ϕ) angles. Therefore, to express the brightness of a gray body in a similar way to Equation (2.4), it is convenient to define a microwave brightness temperature $T_B(\theta, \phi)$ $[K]$ so that the resulting brightness of a gray body is:

$$B(\theta, \phi) = \frac{2k_B T_B(\theta, \phi)}{\lambda^2} \cdot \Delta f \tag{2.9}$$

$T_B(\theta, \phi)$ is the temperature that a black body would have in order to radiate the brightness $B(\theta, \phi)$. The parameter that relates the brightness $B(\theta, \phi)$ of a real material to that of a black body at the same temperature is the emissivity $e(\theta, \phi)$:

$$e(\theta, \phi) = \frac{B(\theta, \phi)}{B_{bb}} = \frac{T_B(\theta, \phi)}{T_{ph}} \tag{2.10}$$

Since gray bodies do not necessarily absorb all the incident energy, the emission from real materials is always less than or equal to that emitted by a black body $B(\theta, \phi) \leq B_{bb}$ and therefore, the emissivity is restricted to the range $0 \leq e(\theta, \phi) \leq 1$. Hence, the brightness temperature of a material is always lower than or equal to its physical temperature $T_B(\theta, \phi) \leq T_{ph}$.

A. Power collected by an antenna surrounded by a gray body

The brightness temperature $T_B(\theta, \phi)$ is used to characterize the radiation $B(\theta, \phi)$ from a gray body (see Equation (2.9)). Equivalently, the apparent temperature $T_{AP}(\theta, \phi)$ is defined to characterize the total incident brightness on the antenna $B_i(\theta, \phi)$:

$$B_i(\theta, \phi) = \frac{2k_B T_{AP}(\theta, \phi)}{\lambda^2} \cdot \Delta f \tag{2.11}$$

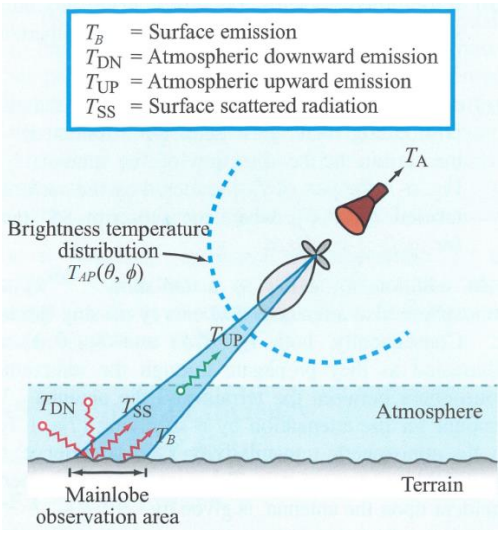

Figure 2.3 Emission from Earth's surface and atmosphere, that contribute to the apparent temperature $T_{AP}(\theta, \phi)$. Adapted from [9].

Considering the scenario of Figure 2.3, the total power received by a lossless antenna, with a normalized radiation pattern $F_n(\theta, \phi)$ surrounded by a gray body is:

$$P = \frac{A_r}{2} \int_f^{f+\Delta f} \iint_{4\pi} \frac{2k_B T_{AP}(\theta, \phi)}{\lambda^2} F_n(\theta, \phi) d\Omega df \tag{2.12}$$

Similar to Equation (*2.8*), the total power received by the antenna can be expressed with respect to an equivalent temperature called the antenna temperature T_A (see Equation (2.14)), and can be expressed as:

$$P = k_B T_A \Delta f \tag{2.13}$$

Therefore, given Equations (2.12) and (2.13), the antenna temperature can be defined as:

$$T_A = \frac{A_r}{\lambda^2} \iint_{4\pi} T_{AP}(\theta, \phi) F_n(\theta, \phi) d\Omega \tag{2.14}$$

It is important to clarify that the antenna temperature includes the contribution of: (i) the radiation emitted by the surface (T_B) attenuated by the atmosphere (γ_a); (ii) the atmospheric downward emission reflected by the Earth's surface towards the antenna (T_{SS}); and (iii) the atmospheric upward emission (T_{UP}). These contributions are expressed as follows:

$$T_{AP}(\theta, \phi) = T_{UP} + \gamma_a (T_B + T_{SS}) \tag{2.15}$$

At low microwave frequencies, from 1 GHz to 10 GHz, the atmospheric effects are practically negligible ($\gamma_a = 1$ and $T_{SS} = T_{UP} = 0$). Thus, the apparent antenna temperature (T_{AP}) can be approximated by that of the brightness temperature T_B.

2.1.3 Faraday rotation

The ionosphere is part of the Earth's upper atmosphere, on average it extends approximately between 80 km and 400 km in altitude and is composed of ionized gases. The Faraday rotation is an effect that occurs at the ionosphere layer, causing a change in the direction of the polarization plane [52]. At L-band, it can be expressed as [53]:

$$\phi' = 2.36 \cdot 10^{-14} B_{av} N_T f^{-2} \tag{2.16}$$

where ϕ' $[rad]$ is the angle of rotation, B_{av} $[Wb \cdot m^{-2}]$ is the average Earth magnetic field, and N_T $[el \cdot m^{-2}]$ is the Total Electron Content (TEC).

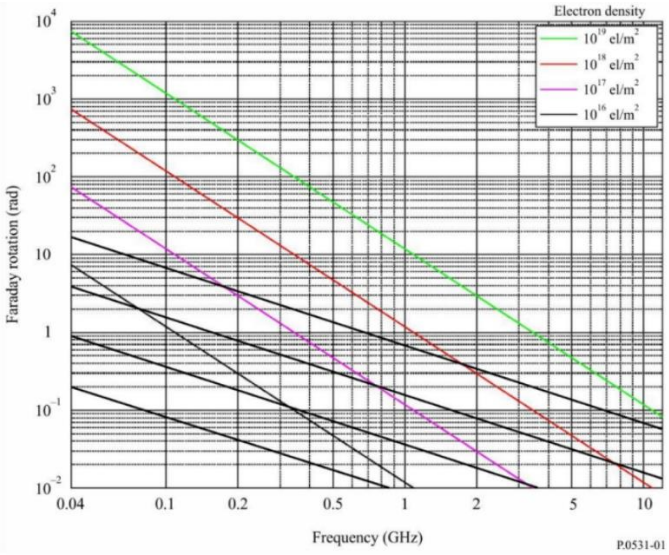

Figure 2.4 Faraday rotation as a function of TEC and frequency. From [53].

Figure 2.4 shows that the Faraday rotation is inversely proportional to the square of the frequency and directly proportional to the TEC. Since the TEC is highly affected by solar radiation, it shows diurnal, seasonal and latitudinal variations. At L-band, the faraday rotation can range from 4°, at night, to 30°, at noon. This effect may result in brightness temperature estimation errors of up to 10 K, which can ultimately result in the minimum requirements for some space missions not being met.

2.1.4 Stokes parameters

Stokes parameters are a set of values (I, Q, U, V) that fully describe the polarization of an electromagnetic wave at a certain frequency:

$$\begin{aligned} \boldsymbol{I} &= \frac{\langle |\boldsymbol{E_v}|^2 \rangle + \langle |\boldsymbol{E_h}|^2 \rangle}{\eta} \\ \boldsymbol{Q} &= \frac{\langle |E_v|^2 \rangle - \langle |E_h|^2 \rangle}{\eta} \\ \boldsymbol{U} &= \frac{2 \cdot Re\langle E_v E_h^* \rangle}{\eta} \\ \boldsymbol{V} &= \frac{2 \cdot Im\langle E_v E_h^* \rangle}{\eta} \end{aligned} \tag{2.17}$$

where η is the electromagnetic wave impedance of the medium, I is the first Stokes parameter and denotes the total intensity of electromagnetic emission, Q is the second Stokes parameter, computed as the difference between the intensity in two orthogonal directions in a given polarization frame. U and V are the third and fourth Stokes parameters, respectively, and represent twice the real (Re) and imaginary (Im) parts of the cross-correlation between these two orthogonal polarizations (Equation (2.17)). The third Stokes parameter can also be expressed as the difference between orthogonal measurements skewed +45° and -45° with respect to normal, and the fourth Stokes parameter represents the difference between left- and right-handed circular polarized quantities [54].

In polarimetric radiometry these parameters are generally expressed in terms of brightness temperature:

$$\begin{aligned} T_I &= T_{B_V} + T_{B_H} = \frac{\lambda^2}{k_B \Delta f} \cdot I \\ T_Q &= T_{B_V} - T_{B_H} = \frac{\lambda^2}{k_B \Delta f} \cdot Q \\ T_U &= T_{B_{+45^\circ}} - T_{B_{-45^\circ}} = \frac{\lambda^2}{k_B \Delta f} \cdot U \\ T_V &= T_{B_{lc}} - T_{B_{rc}} = \frac{\lambda^2}{k_B \Delta f} \cdot V \end{aligned} \tag{2.18}$$

where T_{B_V} and T_{B_H} are the brightness temperatures at vertical (V) and horizontal (H) polarization, $T_{B_{+45^\circ}}$ and $T_{B_{-45^\circ}}$ are the brightness temperatures at $\pm 45°$, and $T_{B_{lc}}$ and $T_{B_{rc}}$ are the brightness temperatures at left- and right-hand circular polarizations.

2.2 L-band microwave emission from Earth's surface

The emissivity of the Earth's continental surface is directly related with its dielectric constant, which is mainly affected by: (i) the soil moisture, (ii) the soil temperature, (iii) the soil surface roughness, and (iv) the vegetation canopy, among others. The relationship between some of these parameters and their effect on emissivity are described below.

2.2.1 Wet soil

A wet soil is commonly a heterogeneous medium, made up of a mixture of soil particles, liquid water, and air pockets. Water contained in soils is commonly divided into: (i) bound water, the water molecules generally contained in the first molecular layers and held by soil particles; and (ii) free water, which refers to the water molecules located several layers away from soil particles and that can move through the soil medium more easily than bound water molecules. The total amount of water contained in a unit volume is determined by the porosity of the soil particles. Soils can be classified according to their particle size distribution as: sand, silt or clay (Figure 2.5a). The relative percentages of the three categories determine the soil texture (Figure 2.5b) [9]. Soils with larger pores (sand) are mostly filled with air, so they hold less water than soils with small pores (clay), where water fills the pore spaces.

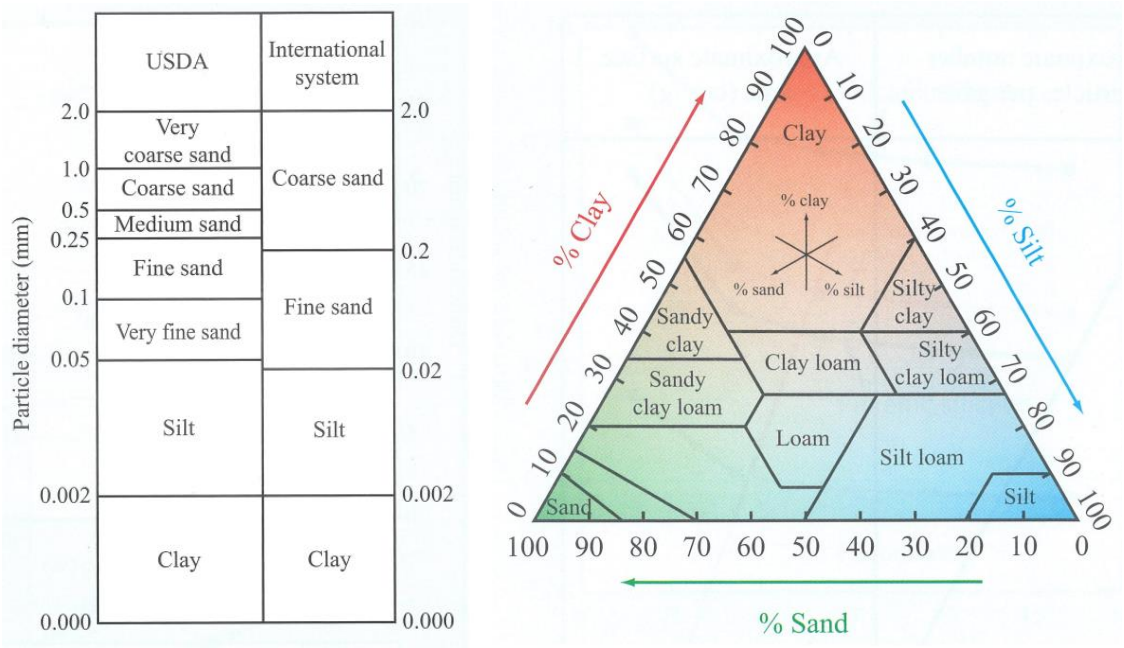

(**a**) (**b**)

Figure 2.5 (a) Particle-size and (b) soil texture classification triangle. From [9].

The water that is held in the spaces between soil particles is called soil moisture (SM) and is expressed as a ratio (Equations (2.19) and (2.20)). Soil moisture ranges from 0 m^3/m^3, when the soil is completely dry, to approximately 0.6 m^3/m^3, when the pores of the material are saturated.

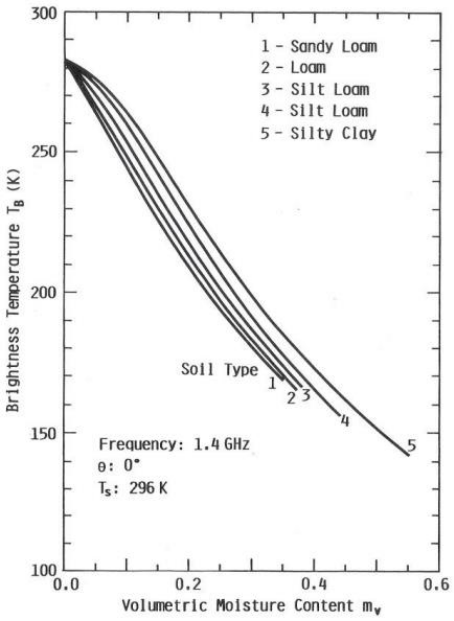

Figure 2.6 Effect of soil type and SM on brightness temperature at 1.4 GHz. From [51].

The gravimetric soil moisture $m_g[m^3/m^3]$ is defined as the mass of water per unit of dry soil:

$$m_g = \frac{W_w - W_d}{W_d} \tag{2.19}$$

where W_w and W_d are the wet and dry weights of a soil sample, respectively.

The volumetric soil moisture m_v $[m^3/m^3]$ is defined as the volume of water per unit volume of soil:

$$m_v = \frac{V_w}{V_T} = m_g \rho_b = \frac{W_d}{V_T} m_g \tag{2.20}$$

where V_w is the volume of water; V_T is the total volume, including the soil and water volumes, and the void space; and ρ_b is the bulk density of the dry soil.

Figure 2.6 shows the impact of different bare soils (sandy loam, loam, silt loam and silty clay) on the T_B at 1.4 GHz at nadir as a function of SM. As it can be seen, the higher the SM value, the lower the T_B. For the same value of SM, this effect is slightly more noticeable for sandy soils than for silty clay soils, which can be explained by the higher fraction of free water molecules within the pores of sandy soils.

2.2.2 Soil dielectric properties

The dielectric constant (ε) determines the response of a soil to an incident electromagnetic wave. It is complex and consist of a real part, ε', and an imaginary part, ε'':

$$\varepsilon = \varepsilon' + j\varepsilon'' \tag{2.21}$$

where ε' is the relative permittivity, which determines the wave velocity, and ε'' is the dielectric loss factor. The soil is a heterogeneous medium (Section 2.2.1) and its complex dielectric constant is the result of the contribution of the different parts that compose it (e.g., water, air, rocks, etc.).

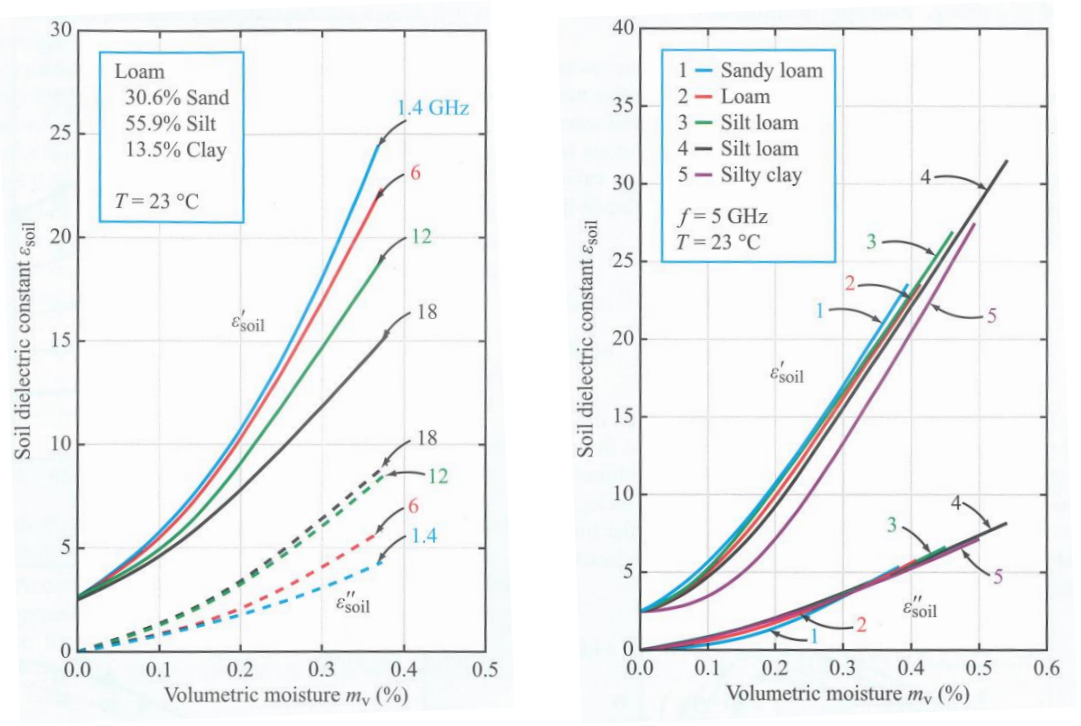

(**a**) (**b**)

Figure 2.7 (a) Dielectric constant as function of SM for: (a) a loamy soil at four microwave frequencies (1.4 GHz, 6 GHz, 12 GHz and 18 GHz); and (b) five soil types at a frequency of 5 GHz. From [9].

Figure 2.7a shows the impact of volumetric soil moisture on the soil dielectric constant at different frequencies (1.4 GHz, 6 GHz, 12 GHz y 18 GHz) for a loamy soil. It can be seen that ε' increases with decreasing frequency, and the opposite happens for ε''. Hence, lower frequencies are less attenuated. The high dynamic range of the soil dielectric constant at 1.4 GHz explains why the L-band is ideally selected as the frequency range for remotely estimating SM. Figure 2.7b shows the dependence of the soil dielectric constant for different soil types (sandy loam, loam, silt loam and silty clay) on SM at a frequency of 5 GHz. As it can be seen, the higher the SM content, the greater the value of the dielectric constant, both for the real ε' and for the imaginary ε'' part. This relationship between SM and measured dielectric constant is almost lineal, except at low moisture content. The region of non-linearity in Figure 2.7b appears

because, in areas with low moisture content, the fraction of free water molecules is low, and bound water molecules predominate, making it difficult for water molecules to rotate freely. Furthermore, it has been proven that the dielectric constant corresponding to dry soils is practically independent of frequency and temperature [55], while the dielectric constant of wet soils is strongly dependent on the soil, water and air particles. In the last decades, different semi-empirical models have been proposed to derive this parameter (i.e., Dobson [56], Wang & Schmugge [15] and Mironov [57] models are some of the most commonly used in the literature). Although they may differ in the analytical forms, they generally depend on SM, soil texture and frequency. The Dobson, Wang & Schmugge and Mironov dielectric mixing models are described below.

A. Dobson model

The Dobson model is based on the dielectric mixing approach proposed by Birchak [58] and requires as input variables, the SM, the weight percent of the sand (SF [%]) and clay fractions (CF [%]), the soil temperature, the frequency and the soil bulk density. For a given soil bulk density ρ_b and specific density ρ_s the Dobson modelled dielectric constant $\varepsilon_m^{\alpha 1}$ is expressed as:

$$\varepsilon_m^{\alpha 1} = 1 + \frac{\rho_b}{\rho_s}(\varepsilon_s^{\alpha 1} - 1) + m_v^b \varepsilon_{fw}^{\alpha 1} - m_v \tag{2.22}$$

where subscripts s and fw refer to solid soil and free water, respectively. The empirical constants $\alpha 1$ and b depend on the soil texture. The value of ε_s is calculated for a given ρ_s by:

$$\varepsilon_s = (1.01 + 0.44\rho_s)^2 - 0.062 \tag{2.23}$$

The dielectric constant of the free water is calculated as:

$$\varepsilon_{fw} = \varepsilon_{w\infty} + \frac{\varepsilon_{w0} - \varepsilon_{w\infty}}{1 + j2\pi f \varepsilon_0} - j\frac{\sigma_{eff}}{2\pi f \varepsilon_0}\frac{\rho_s - \rho_b}{\rho_s m_v} \tag{2.24}$$

where ε_{w0} is the static dielectric constant of pure water, $\varepsilon_{w\infty}$ is the high-frequency limit of pure water, $\varepsilon_0 = 8.854 \cdot 10^{-12}\ [F \cdot m^{-1}]$ is the permittivity of free space, and $\sigma_{eff}\ [S \cdot m^{-1}]$ is the effective conductivity. For $\alpha 1 = 0.65$, b and σ_{eff} depend on the soil texture and can be calculated as:

$$\begin{aligned} b_{\varepsilon'} &= (127.48 - 0.519\ SF - 0.152\ CF)/100 \\ b_{\varepsilon''} &= (1.33797 - 0.603\ SF - 0.166\ CF)/100 \\ \sigma_{eff} &= -1.645 + 1.939\rho_b - 0.02013\ SF + 0.01594\ CF \end{aligned} \tag{2.25}$$

B. Wang & Schmugge model

The Wang & Schmugge dielectric model was proposed for 1.4 GHz and 5 GHz. This model has two expressions for the dielectric constant, depending on whether the volumetric moisture content m_v is less than or greater than the transition moisture m_t:

$$\varepsilon = m_v\varepsilon_x + (Po - m_v)\varepsilon_a + (1-P)\varepsilon_r \qquad if\ m_v \le m_t$$
$$\varepsilon_x = \varepsilon_i + (\varepsilon_{fw} - \varepsilon_i)\frac{m_v}{m_t}\Upsilon \tag{2.26}$$

and:

$$\varepsilon = m_t\varepsilon_x + (m_v - m_t)\varepsilon_{fw} + (P - m_v)\varepsilon_a + (1-P)\varepsilon_r \qquad if\ m_v > m_t$$
$$\varepsilon_x = \varepsilon_i + (\varepsilon_{fw} - \varepsilon_i)\Upsilon \tag{2.27}$$

with:

$$m_t = 0.49 \cdot \mathrm{WP} + 0.165$$
$$\Upsilon = -0.57 \cdot \mathrm{WP} + 0.481 \tag{2.28}$$
$$P_o = 1 - \frac{\rho_d}{\rho_s}$$

where ε_x, ε_{fw}, ε_a, ε_r and ε_i are the dielectric constants of the initial absorbed water, free water, air, rock and ice, respectively, P_o is the porosity, and Υ is a fitting parameter. The wilting point (WP) is a function of static soil properties and marks the SM level below which plants cannot extract water from soil [59].

C. Mironov model

The Mironov model is a generalized refractive mixing dielectric model [57], which is considered one of the best models to provide SM estimates [60] from passive microwaves, and it is the one adopted by the SMOS and SMAP missions. Its main advantages are [61]: (i) it requires fewer input parameters than the Dobson model, being less sensitive to the impact of inaccuracies of these auxiliary inputs; (ii) it is based on a physical approach; and (iii) it has been validated on a wide range of soil textures. The Mironov dielectric constant is expressed as:

$$\varepsilon' = n^2 - \kappa^2$$
$$\varepsilon'' = 2n\kappa \tag{2.29}$$

with:

$$n = \begin{cases} n_d + (n_{bw} - 1)m_v & if\ m_v \le m_t \\ n_d + (n_{bw} - 1)m_v + \left(n_{fw} - 1\right)(m_v - m_{vt}) & if\ m_v > m_{vt} \end{cases} \tag{2.30}$$

and:

$$\kappa = \begin{cases} \kappa_d + \kappa_{bw}\, m_v & if\ m_v \le m_{vt} \\ \kappa_d + \kappa_{bw} m_v + \kappa_{fw}(m_v - m_{vt}) & if\ m_v > m_{vt} \end{cases} \tag{2.31}$$

where the subscripts d, bw, fw refers to dry soil, bound water and free water. n is the refractive index, κ is the normalized attenuation coefficient, and m_{vt} is the value of the maximum bound water fraction of the soil, which can be expressed as:

$$m_{vt} = 0.02863 + 0.30673 \cdot 10^{-2}\ CF \tag{2.32}$$

The refractive index n_d and normalized attenuation coefficient κ_d of dry soil can be written as a function of the percentage of clay CF:

$$\begin{aligned} n_d &= 1.634 - 0.539 \cdot 10^{-2}\ CF + 0.2748 \cdot 10^{-4} CF^2 \\ \kappa_d &= 0.03952 - 0.04038 \cdot 10^{-2}\ CF \end{aligned} \tag{2.33}$$

The refractive index and the normalized attenuation coefficient for free (n_{fw}, k_{fw}) and bound water (n_{bw}, k_{bw}) can be written, through their respective permittivity and loss factor, as:

$$\begin{aligned} n_{bw,fw}\sqrt{2} &= \sqrt{\sqrt{(\varepsilon'_{bw,fw})^2 + (\varepsilon''_{bw,fw})^2} + (\varepsilon'_{bw,fw})^2} \\ \kappa_{bw,fw}\sqrt{2} &= \sqrt{\sqrt{(\varepsilon'_{bw,fw})^2 + (\varepsilon''_{bw,fw})^2} - (\varepsilon'_{bw,fw})^2} \end{aligned} \tag{2.34}$$

where the real and imaginary part of the dielectric constant of free and bound water can be expressed as:

$$\begin{aligned} \varepsilon'_{bw,fw} &= \varepsilon_{w\infty} + \frac{\varepsilon_{bw0,fw0} - \varepsilon_{w\infty}}{1 + \left(2\pi f \tau_{bw,fw}\right)^2} \\ \varepsilon''_{bw,fw} &= \frac{2\pi f \tau_{bw,fw}(\varepsilon_{bw0,fw0} - \varepsilon_{w\infty})}{1 + \left(2\pi f \tau_{bw,fw}\right)^2} + \frac{\sigma_{bw,fw}}{2\pi\varepsilon_0 f} \end{aligned} \tag{2.35}$$

Static dielectric constant, relaxation time and effective conductivity can be written as a function of percent clay CF. For free water, these variables can be expressed as:

$$\begin{aligned} \varepsilon_{fw0} &= 100 \\ \tau_{fw} &= 8.5 \cdot 10^{-12} \\ \sigma_{fw} &= 0.3631 + 1.217 \cdot 10^{-2}\ CF \end{aligned} \tag{2.36}$$

and for bound water:

$$\begin{aligned} \varepsilon_{bw0} &= 79.8 - 85.4 \cdot 10^{-2}\ CF + 32.7 \cdot 10^{-4}\ CF^2 \\ \tau_{bw} &= 1.062 \cdot 10^{-11} + 3.45 \cdot 10^{-14}\ CF \\ \sigma_{bw} &= 0.312 + 0.467 \cdot 10^{-2}\ CF \end{aligned} \tag{2.37}$$

2.2.3 Bare soil emission

The Earth's surface brightness temperature is defined by its emissivity e_p and the soil effective temperature T_s (see Section 2.1.2):

$$T_{Bp} = e_p \cdot T_s \tag{2.38}$$

where the subscript p refers to the vertical or horizontal polarization. Different approaches have been proposed to estimate T_s from soil properties, and soil moisture and temperature profiles. Wigneron et al. [62] developed a parametrization of T_s based on an earlier work by Choudhury et al. [63]. This method weighs the deep soil temperature $T_{deep}\ [K]$ and the skin temperature $T_{skin}[K]$ through a fitting parameter C', that depends on the volumetric water content m_v, and two constants a and b:

$$T_s = T_{deep} + C' \cdot (\, T_{skin} - T_{deep}) \tag{2.39}$$

with

$$C' = \left(\frac{m_v}{a}\right)^b \tag{2.40}$$

a and b are semi-empirical parameters that depend on the specific characteristics of the soil [62].

The emissivity of a perfectly flat surface ${e_p}^*$, with a polarization p in a chosen observation direction θ, can be expressed as a function of the specular Fresnel reflectivity at p polarization ${\Gamma_{s,p}}^*$:

$${e_p}^*(\theta) = 1 - {\Gamma_{s,p}}^*(\theta) \tag{2.41}$$

Figure 2.8a shows the behavior of the emissivity (reflectivity) of a specular surface for vertical and horizontal polarizations at 10 GHz. From this figure it can be concluded that: (i) at nadir the emissivity (reflectivity) of both polarizations is the same; (ii) at horizontal polarization the emissivity (reflectivity) gradually decreases (increases) to zero (one) at an incidence angle of 90°; and (iii) at vertical polarization, the emissivity (reflectivity) increases (decreases) to a maximum (minimum) at a particular angle (Brewster angle). From this maximum, the emissivity (reflectivity) gradually decreases (increases) to zero (one) at an incidence angle of 90°. The Brewster angle increases for higher dielectric constant values, but it may not reach a maximum (minimum) of one (zero) if there are losses.

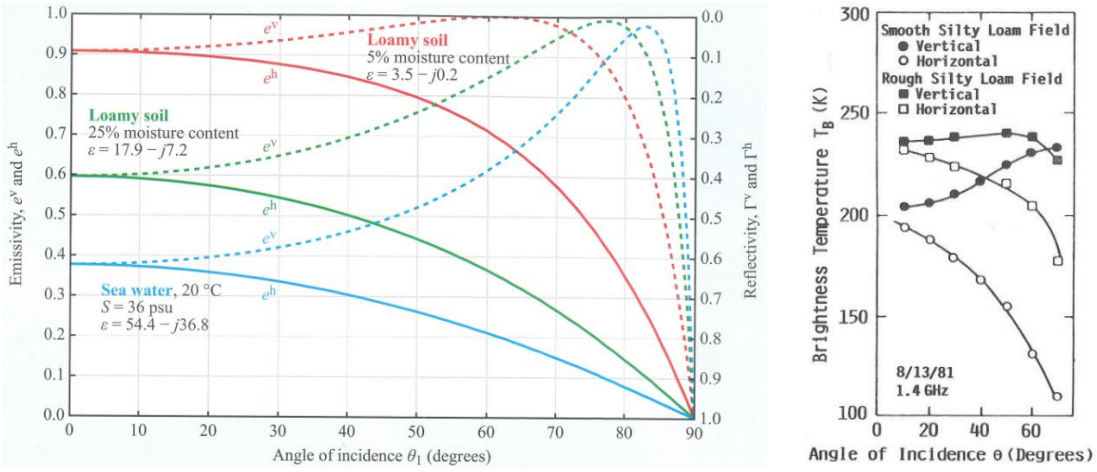

(**a**) (**b**)

Figure 2.8 (a) Horizontal (continuous line) and vertical (dotted line) emissivity and reflectivity of a specular surface at 10 GHz [9], and (b) horizontal and vertical brightness temperature measured for a rough and smooth surface at 1.4 GHz [51].

The specular reflectivity of the soil $\Gamma_{s,p}{}^{*}$ can be described by the Fresnel reflection coefficients as a function of the incidence angle θ and the soil dielectric constant ε:

$$\Gamma_{s,V}{}^{*} = \left|\frac{\varepsilon\cos\theta - \sqrt{\varepsilon - \sin^2\theta}}{\varepsilon\cos\theta + \sqrt{\varepsilon - \sin^2\theta}}\right|^2$$
$$\Gamma_{s,H}{}^{*} = \left|\frac{\cos\theta - \sqrt{\varepsilon - \sin^2\theta}}{\cos\theta + \sqrt{\varepsilon - \sin^2\theta}}\right|^2 \quad (2.42)$$

Beyond the ideal specular conditions, the Earth's surface is typically rough since it naturally presents irregularities. Figure 2.8b shows the behavior of the brightness temperature of a rough and smooth surface for vertical and horizontal polarizations at 1.4 GHz. It illustrates that roughness: (i) increases the emissivity due to the increased soil area interacting with the atmosphere; (ii) reduces the differences between vertical and horizontal polarizations; and (iii) reduces the sensitivity of the emissivity to changes in soil moisture, since the range of emissivity has also been reduced from dry to wet soil conditions.

In [64] Choudhury et al. proposed a simple semi-empirical model to mimic rough surface reflectivity $\Gamma_{s,v}$:

$$\Gamma_{s,p} = \Gamma_{s,p}{}^{*} e^{-h_s\cos^2\theta} \quad (2.43)$$

where $\Gamma_{s,p}{}^{*}$ is the specular Fresnel reflectivity at p (vertical/horizontal) and q (horizontal/vertical) polarization, respectively; θ is the incidence angle; and h_s is the effective soil roughness. Wang and Choudhury [65] reviewed this model and proposed a more elaborated equation (see Equation (2.44)).

$$\Gamma_{s,p} = [(1 - Q_s)\Gamma_{s,p}{}^{*} + Q_s\Gamma_{s,q}{}^{*}]e^{-h_s \cos^{n_p}\theta} \quad (2.44)$$

where Q_s is the polarization mixing factor, and n_p expresses the angular dependence of roughness and may depend on the polarization.

Many studies have explored the link between these three geophysical and roughness parameters (Q, h_s and n_p) [61,62,64–77]. A brief summary of these studies is presented in Section 2.2.5 and main adopted approximations are summarized hereafter.

There is a general agreement on the value of Q which has been found to be very small, increasing slightly as frequency increases, from 0 at L-band [49,78], ~0.1 at C-band, and to 0.2-0.3 at X-band [66].

The formulation for the roughness parameter $h_s = 4k^2\sigma_s^2$, where k is the electromagnetic wavenumber and σ_s is the standard deviation of the surface height, was proposed by Choudhury et al. in [64] and has been widely used in literature [67–69]. Although, other studies [62] found that this formulation could be overestimating the roughness effect h_s in areas with rough soil conditions ranging from medium to very high. Some authors introduced a h_s parametrization dependent on soil moisture [62,70,71]. It was found that at lower-frequency bands, such as L-band, h_s depends more on the distribution of the water in the soil than at higher frequencies [71]. This sensitivity of h_s with the soil moisture was called “dielectric roughness” or “apparent soil roughness”. The accuracy of the approach, linking soil moisture and h_s, has been tested in several studies with satisfactory results [50,79].

A typical value of $n_p = 2$ was used in some initial studies [64,65], while in [62,69] it is found that this dependence was too strong at L-band, and it was proposed to set $n_p = 0$. Since then, n_p values equal to 0, 1 or even -1 have been used in the literature [62,72–74,80]. In [70], Escorihuela et al. showed that the value of n_p does not necessarily have to be the same for vertical and horizontal polarizations.

2.2.4 Vegetated soil emission

In remote sensing, when a sensor is located over a canopy pointing towards the Earth’s surface, the total brightness measured will contain the soil emission, but also the vegetation effect. A canopy layer radiates its own energy and also scatters and attenuates the radiation emitted from the soil. Several models of the land emission have been proposed, which take into account the contribution of vegetation to the observed microwave signal [81–85]. Radiation from a vegetated soil is usually expressed using a zero-order radiative model, the so-called $\tau - \omega$ model [81]:

$$T_{B_{p,\theta}} = e_p T_s \gamma + (1 - \omega)T_v(1 - \gamma) + \left(1 - e_p\right)(1 - \omega)T_v(1 - \gamma)\gamma \quad (2.45)$$

where T_v and T_s are the effective temperature of the vegetation and the soil, respectively, γ is the transmissivity of the vegetation layer, and ω is the single scattering albedo. Equation (2.45) includes the contribution of three terms (see Figure 2.9a): (i) the soil radiation that is attenuated

by the overlaying vegetation; (ii) the upward radiation emitted directly by the vegetation; and (iii) the downward radiation of the vegetation, reflected upward by the soil and again attenuated by the vegetation.

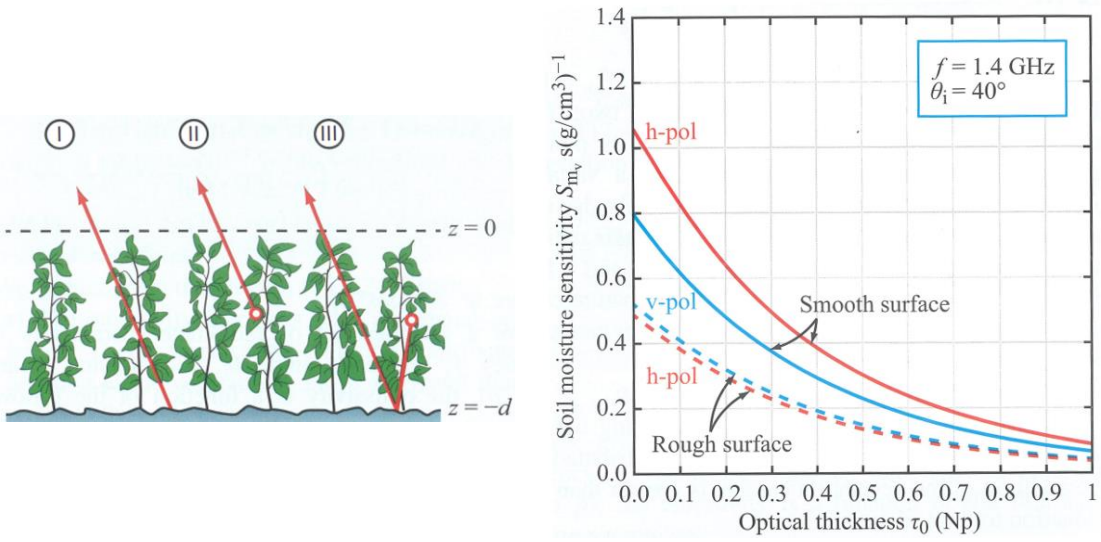

(**a**) (**b**)

Figure 2.9 (a) Emissivity contributions of a soil covered by vegetation: (i) radiation from the soil attenuated by the overlaying vegetation; (ii) direct upward emission from vegetation; and (iii) downward emission from the vegetation, reflected upward by the soil and again attenuated by the vegetation. (b) Sensitivity to soil moisture in relation to the vegetation optical depth. From [9].

The single scattering albedo describes the scattering of the vegetation, and depends on the plant characteristics. At L-band, it is usually assumed that scattering effects due to vegetation are minimal, and parameter ω is set to a very low value [21,86]. Although, several sensitivity analysis [49,50,79,87] of the $\tau - \omega$ model revealed that ω is a crucial parameter to correctly estimate SM in vegetated regions. The transmissivity is the attenuation due to the vegetation cover and can be defined in terms of vegetation optical depth τ and the incidence angle θ:

$$\gamma = e^{-\tau/\cos\theta} \tag{2.46}$$

The optical depth is related to the vegetation density and frequency. At L-band, this parameter is linearly related to the vegetation water content VWC $[kg \cdot m^{-2}]$ through an empirical parameter b that depends on the vegetation type and frequency:

$$\tau = b \cdot VWC \tag{2.47}$$

The estimation of VWC using visible near-infrared data through vegetation indices has been widely studied in the literature. The most commonly used vegetation indices are: the normalized difference vegetation index (NDVI) [88–90], the leaf area index (LAI) [91,92], the enhanced vegetation index (EVI) [93] or the normalized difference water index (NDWI) [94]. As discussed

in [95], very few algorithms have included the effects of rain and litter together with the VWC, to accurately model τ [96], or combine the effects of vegetation and roughness [72,97–99].

Figure 2.9b shows the reduction in SM sensitivity due to vegetation effects for a smooth and a rough surface. It can be seen that the SM sensitivity gradually decreases as the optical depth increases. This effect occurs for both rough and smooth surfaces, although the sensitivity is always lower for a rough surface (Section 2.2.3).

Figure 2.10 shows the variations in emissivity at horizontal polarization for a dry (Figure 2.10a) and a wet (Figure 2.10b) soil surface covered with vegetation at five different values of nadir vegetation optical depth τ. From this figure it can be deduced that: (i) emissivity increases with increasing optical depth. This occurs because the contribution to emissivity due to the increase in vegetation density is greater than the reduction to soil emissivity; and (ii) since the emissivity of wet soils is lower than that of dry soils, the dynamic range of emissivity between the maximum and the minimum value of τ is much higher for wet soils than for dry soils.

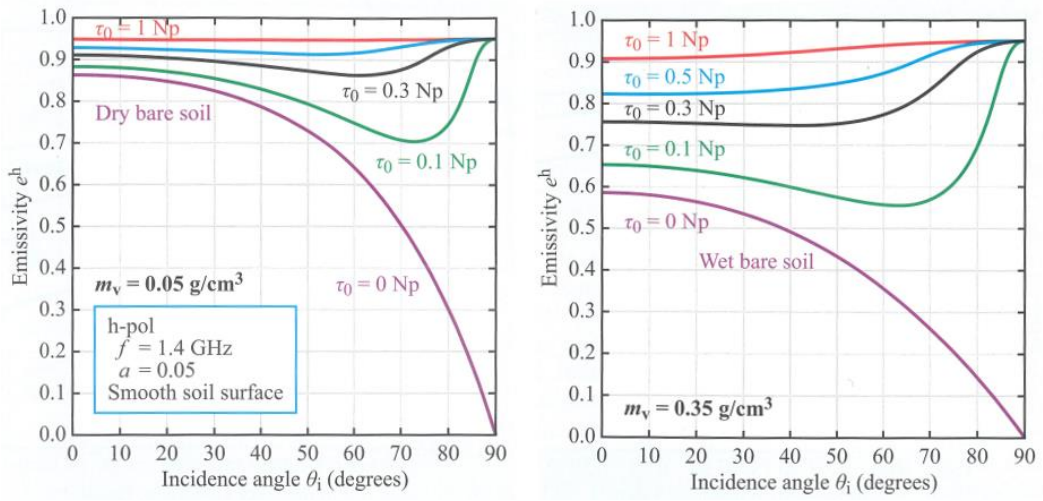

(**a**) (**b**)

Figure 2.10 Emissivity at horizontal polarization respect to the incidence angle for (a) dry and (b) wet soils. It is considered a smooth surface, covered with vegetation, represented by five values of vegetation optical depth (τ_0 in this figure) at nadir. From [9].

Figure 2.11 shows the emissivity response, in horizontal polarization to SM, for a smooth (see Figure 2.11a) and a rough soil surface (see Figure 2.11b), where τ is a parameter. A similar behavior can be appreciated for smooth and rough surfaces, emissivity decreases with increasing SM. They differ in that the emissivity slope is steeper for smooth soils than for rough soils.

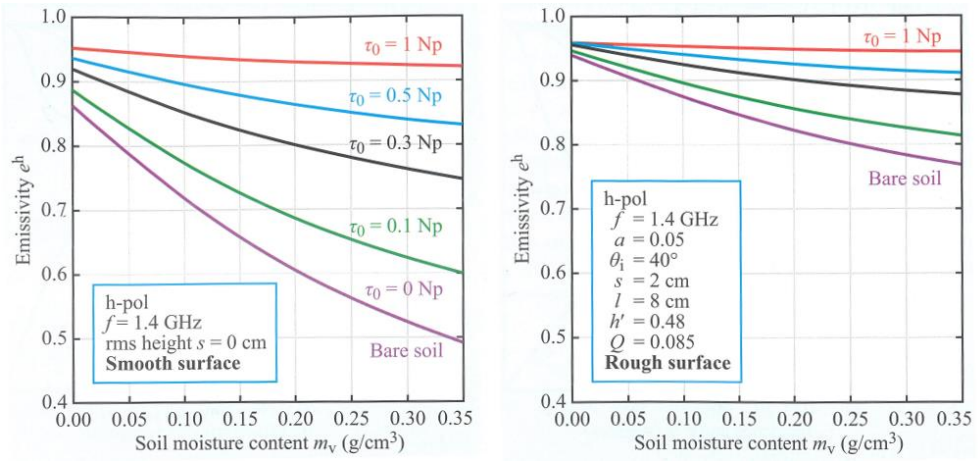

(**a**) (**b**)

Figure 2.11 Variation of emissivity at horizontal polarization with soil moisture content, for a (a) smooth and (b) a rough soil surface. Several values of nadir vegetation optical depth are considered. From [9].

2.2.5 Soil moisture retrieval models

Previous sections have demonstrated that the emissivity of the Earth's surface is influenced by many variables (see Equations (2.44) and (2.45)), the most relevant, directly related to the soil surface, are: SM, T_s, and h_s; and other variables related to the vegetation characteristics i.e., ω and τ. The brightness temperature measurement, related to the Earth's surface emissivity can be used to obtain some of these geophysical parameters. SMOS and SMAP are the first missions (see Section 2.3) dedicated to obtain SM using L-band microwave measurements.

The retrieval or inversion techniques developed for deriving SM from L-band radiometric measurements assume that some of the above variables are known (e.g., T_s, h_s, ω) and this information is used to estimate other unknown variables (e.g., SM and τ) minimizing the mismatch between the observed ($T_{B_p}^{obs}$) and the modelled brightness temperature ($T_{B_p}^{mod}$):

$$\min_{\bar{X}} J(\bar{X}) = \sum_{t_{op}=1}^{N} \sum_{p=V,H} \left(T_{B_p}^{obs} - T_{B_p}^{mod}(\bar{X}) \right)^2 \tag{2.48}$$

where $\overline{X}$ is the vector of unknown parameters (e.g., SM or τ); t_{op} are the number of overpasses for which τ can be considered time independent, and p is the polarization (vertical or horizontal).

The potential of the $\tau - \omega$ geophysical model to retrieve SM over bare and vegetated soils has been widely studied in the literature [23,30,46,79]. Although to a lesser extent, there are also some studies that have used higher-order solutions for the radiative transfer equation [100–102] to retrieve SM [103,104], such as the two-streams emission model.

Retrieval techniques have evolved to meet the needs of progressive advances in sensor configurations [95]. The first version of the retrieval algorithms was developed according to the mono-configuration of the sensors (single polarization, viewing angle and frequency channel).

These algorithms estimate the SM by minimizing the mismatch between the observed and the modelled brightness temperature at vertical or horizontal polarization. This category includes the Single Channel Algorithm (SCA) [19] and the Land Surface Microwave Emission Model (LSMEM) [105]. In addition to the measured T_B, these algorithms require ancillary data such as T_s, τ, h_s and ω. The SCA was the original postlaunch baseline algorithm for the SMAP mission from 2015 to 2021.

Since most of today's passive microwave satellite sensors– SMOS Microwave Imaging Radiometer using Aperture Synthesis (MIRAS), SMAP, Global Precipitation Measurement (GPM) Microwave Imager (GMI), Tropical Rainfall Measuring Mission's (TRMM) Microwave Imager (TMI), WindSat, Advanced Microwave Scanning Radiometer Earth observing system (AMSR-E), Global Change Observation Mission (GCOM) AMSR2, Fengyun-3B (FY-3B) Microwave Radiation Imager (MWRI), among others– may have multi-frequency and/or multi-angular capabilities, or can work at dual polarization, new retrieval algorithms have been developed. Consequently, these algorithms can exploit all available measurements to retrieve more than one variable at the same time. The direct evolution of the SCA is the Dual Channel Algorithm (DCA) [20], which uses the brightness temperatures at two polarizations (vertical and horizontal), to retrieve SM and τ at the same time. Although the DCA algorithm allows estimating two variables at the same time, some studies have shown that the SCA outperforms the DCA when retrieving SM [106]. This may be because the horizontally and vertically polarized brightness temperatures are highly correlated and, in noisy conditions, there is not enough information so as to retrieve the two parameters without errors (see the concept of degrees of information in [107] and [21]). The DCA is the current baseline algorithm for the SMAP mission. The Land Parameter Retrieval Model (LPRM) [108] is a variant of the DCA, which exclusively uses the horizontal polarization in the cost function to retrieve SM and τ, combining the information of vertical and horizontal polarizations through the Microwave Polarization Difference Index (MPDI) [85]:

$$MPDI = \frac{T_{B_V} - T_{B_H}}{T_{B_V} + T_{B_H}} \tag{2.49}$$

The L-band Microwave Emission of the Biosphere (L-MEB) is based on the geophysical model $\tau - \omega$, which is parameterized and adjusted to reproduce the Earth's emission at L-band [96]. Within the algorithm, soil roughness and some vegetation parameters (i.e., τ and ω) are considered time independent and their values are computed based on a land cover map (ECOCLIMAP, [109]) [49]. The L-MEB is the core of the official SMOS retrieval algorithm [86], and uses SMOS brightness temperature at multiple incidence angles and at two polarizations.

After having introduced some of the most used methods for retrieving SM, it is relevant to mention that the number of unknown parameters that can be estimated depend on the degrees of freedom provided by the measurements (e.g., data fusion using measurements at several incidence angles, polarizations or frequencies). As stated in [21] by Konings et al., the errors in estimations can be reduced by using additional observations to increase the 'degrees of information' in the data used. This can be achieved by combining measurements from different overpasses, if the time between them is short enough. Under these conditions, the vegetation properties can be considered constant across different overpasses. The Multi-Temporal Dual

Channel Algorithm (MT-DCA) [21] method uses time series of dual-polarized microwave observations to simultaneously estimate τ and SM, alongside a constant ω. Thus, there is no dependence on ancillary information of vegetation from optical sensors.

The following two subsections explain in detail the two SM retrieval algorithms used in this Thesis: the SCA and the LPRM.

A. Land parameter retrieval model

The LPRM retrieval model [22] allows to simultaneously retrieve SM and τ using T_B at both vertical and horizontal polarization. It is based on the $\tau - \omega$ model (Equation (2.45)), which requires e_p, ω, T_s, T_v and γ.

The e_p is calculated following three steps: (i) the dielectric constant of the soil is calculated through the Mironov mixing model (Section 2.2.2C) [57], which requires f, CF and SM; (ii) the Fresnel equations (Equation (2.42)) are applied using the absolute value of the dielectric constant and the incidence angle; and (iii) the emissivity is calculated as described in Equations (2.41) and (2.44). The emissivity requires Q, h_s, ${\Gamma_{s,p}}^*$, n_p and incidence angle.

Finally, the value of γ in the $\tau - \omega$ model is obtained from Equation (2.46). The core of the LPRM is the analytical formula proposed by Meesters et al. [85] (Equation (2.50)), applied together with the MPDI (see Equation (2.49)), and the parameters a and d (see Equations (2.51) and (2.52)), to calculate polarization-independent [110] τ at nadir.

$$\tau = \cos\theta \ln\left(ad + \sqrt{(a \cdot d)^2 + a + 1}\right) \tag{2.50}$$

where

$$a = \frac{1}{2}\left(\frac{e_v + e_h}{MPDI} - e_v - e_h\right) \tag{2.51}$$

$$d = \frac{1}{2}\left(\frac{\omega}{1 - \omega}\right) \tag{2.52}$$

The LPRM model is applied for a range of SM values to estimate T_{B_H}. The obtained brightness temperatures are then compared with those measured by the satellite. Finally, the selected SM is the one that minimizes the difference between the observed and the modelled T_{B_H}. The LPRM has been applied on Scanning Multichannel Microwave Radiometer (SMMR), TRMM-RMI, and AMSR-E for generating long-term global SM dataset since 1978.

B. Single channel algorithm

The SCA is a SM only retrieval technique, also based on the inversion of the $\tau - \omega$ model (Equation (2.45)). It is a straightforward to implement and computationally fast. In order to be able to estimate the SM using one single polarization (vertical or horizontal), in addition to requiring the same input variables as the LPRM (i.e., e_p, ω, T_s, T_v and γ), the SCA also needs an

extra input, τ. In the SCA the T_{B_H} is generally preferred due to its higher sensitivity to SM (Figure 2.8b), but the same algorithm can be applied to T_{B_V}.

The emissivity and the best SM estimate are calculated exactly as for the LPRM (see Section 2.2.5A).

2.3 L-band satellite missions

This section provides a brief introduction to the two operational L-band space missions specifically dedicated to monitoring temporal and spatial variations of the Earth's SM: the ESA's SMOS and the NASA's SMAP missions. The main features of these instruments are summarized in Table 2.1.

2.3.1 The SMOS mission

SMOS is the second Explorer Opportunity mission of the ESA, launched on November 2nd, 2009. This mission belongs to the ESA's Living Planet Program, in collaboration with the Centre National d'Études Spatiales (CNES) in France, and the Centro para el Desarrollo Tecnológico Industrial (CDTI) Earth Observation in Madrid, Spain. The main objectives of the SMOS mission are [111]: (i) to provide global maps of SM estimates over land surfaces with an accuracy of 0.04 m^3/m^3 at a spatial resolution of ~50 km and a temporal sampling of about 3 days; (ii) to monitor global scale surface salinity estimates over the oceans with an accuracy of 0.1 practical salinity scale units [psu] for a 10-30 days average, covering areas of 200 x 200 km^2; and (iii) to provide daily sea ice thickness estimates with spatial resolutions of 10.000 km^2. Later using this information to develop hydrological, climatological, meteorological and oceanographic applications [112].

SMOS operates at L-band (1.413 GHz, 21 cm), which is considered a suitable frequency band to globally estimate SM [10–12]. As introduced throughout this chapter, this band is highly sensitive to soil moisture changes with a high contrast in microwave permittivity, varying from $\varepsilon = 3$ for dry soils, to $\varepsilon = 80$ for water [113]. Moreover, at these frequencies, the atmosphere is considered nearly transparent, and L-band measurements are less affected by soil roughness and vegetation attenuation than at higher frequencies (e.g., X- or C-bands). However, working within this frequency range implies antenna diameters of several meters, in order to meet the SMOS spatial requirements (~50 km), and a large instrument swath to achieve global coverage of the Earth within three days. SMOS carries a two-dimensional interferometric radiometer, inspired in techniques developed in radio-astronomy, with a large effective antenna aperture synthesized through a distributed network of physically small receivers. While imaging with a real aperture radiometer is done by scanning the antenna beam pixel by pixel, MIRAS obtains two-dimensional images at each snap-shot without the need for mechanical scanning (Figure 2.12).

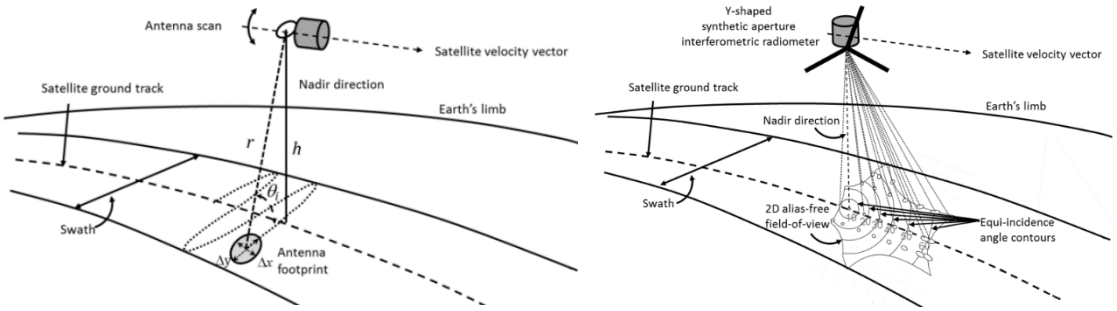

(**a**) (**b**)

Figure 2.12 (a) Real aperture antenna scanning in a cross-track configuration and (b) scanning configuration of a Y-shape two-dimensional synthetic aperture radiometer. From [114].

SMOS has a Sun-synchronous (with a mean inclination = 98.4416°), dawn/dusk (local equator crossing time 6:00 AM on ascending node), and quasi-circular orbit, with a mean altitude of 758 km. SMOS can provide measurements in dual and full polarization, for a range of incidence angles from 0° of 65°, within a swath of approximately 1000 km. Although SMOS was designed as a five-year mission, it has already been operating for more than twelve years.

The MIRAS instrument is composed of a large structure (~8 m of diameter) with three deployable arms which are designed to form 120° angles to each other, giving the SMOS satellite the peculiar Y-shape (Figure 2.13a). Since the arms need to be folded to fit into the launcher and deployed when the satellite reaches orbit, each arm is made up of 3 sections containing 6 L-band radiometers in each section (Figure 2.13b). The 18 radiometers distributed along the arms are complemented by another 12 radiometers on the central hub, for a total of 66 radiometers. Three other Noise Injection Radiometers (NIR) are located within the hub, they are full-polarimetric (capable of measuring the four Stokes elements). These antennas are equally distributed and separated by a distance $d = 0.875\lambda$, which is larger than $d = \lambda/\sqrt{3}$, a requirement to avoid aliasing.

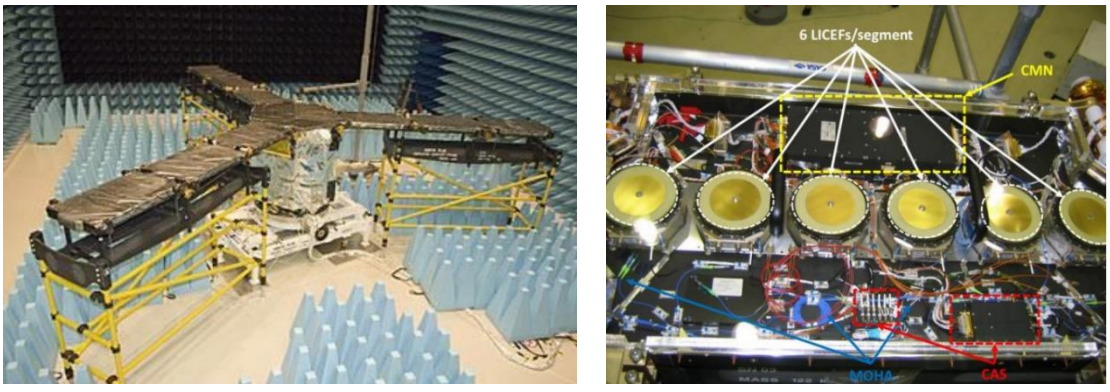

(**a**) (**b**)

Figure 2.13 (a) MIRAS prepared for functional test (credits UPC). (b) MIRAS instrument uses an array of 69 antennas distributed over a hub and the three arms. In the image a section of 6 antennas is shown (credits UPC).

A. SMOS data products

The SMOS data can be classified into different categories according to the level of processing applied to the data [111]:

Level 0 products are the raw data, the unprocessed SMOS data with added Earth Explorer headers.

Level 1 products are divided into three subcategories:

- Level-1A are the calibrated visibilities between the individual antenna receivers. They are provided by ESA in an Earth Explorer File (EEF) format.
- Level-1B (L1B) products are snapshots of radiometrically corrected and calibrated brightness temperatures.
- Level-1C (L1C) product includes the multi-incidence angle brightness temperatures at the top of the atmosphere, geolocated in an equal-area system. The information is available for land and sea, by pixels and by snapshot.

These products are provided by ESA in an EEF format.

Level 2 (L2) over land contains the soil moisture and vegetation optical depth swath-based, and the ancillary data required during processing (the dielectric constant and the brightness temperatures, at the top of the atmosphere and at the land surface; the surface temperature and the soil roughness parameter). Level 2 over ocean includes the retrieved swath-based Sea Surface Salinity (SSS), the SSS anomaly, a corrected version of the SSS that mitigates the impact of the land/sea transition effect, and the brightness temperatures at the top of the atmosphere and at the sea surface level. This product is provided by ESA, and can be found in EEF or Network Common Data Form (NetCDF) format, on a 15-km Icosahedron Snyder Equal Area (ISEA) 4H9 grid.

Levels 3 (L3) and 4 (L4) are provided by the two SMOS Expert centers: the CESBIO and the Barcelona Expert Center (BEC). The BEC was created in 2007, as a joint initiative between the Spanish Research Council (CSIC) and the Polytechnic University of Catalonia (UPC), to provide support to the Spanish SMOS-related activities. The BEC hosts the production and distribution system of the in-house developed remote sensing products, which are freely distributed to the scientific community [115]. This Thesis has been conducted at the BEC facilities and has been focused on BEC L3 and L4 products over land.

The **BEC L3** product over land contains global maps of soil moisture, vegetation optical depth, and dielectric constant for ascending and descending orbits. Data is provided in: (i) a 15-km ISEA 4H9 grid that includes daily maps of the three variables discussed above; and (ii) an Equal-Area Scalable Earth (EASE) grid containing exclusively soil moisture. EASE version 2 (v2) products are provided daily, 3-day, 9-day, monthly and yearly in a 25-km grid. Over the ocean, two different salinity products are available: (i) the nominal product contains global SSS maps for daily (available for ascending and descending orbits), 9-days and monthly (available for combined ascending/descending orbits); and (ii) advanced products containing daily global and local

products allow the SSS retrieval in near-shore areas and at high latitudes. These two products (over land and over sea) are provided by the BEC, in NetCDF format.

The **BEC L4** products are L2 and L3 products enhanced through the use of auxiliary data. Product over land contains daily maps of soil moisture over Europe and the specific region of the Iberian Peninsula, at 1 km of spatial resolution, for ascending and descending orbits. The over-ocean product contains daily maps of SSS at 0.05° x 0.05°. These two products (over land and over sea) are provided by the BEC, in NetCDF format.

2.3.2 The SMAP mission

SMAP mission was developed by NASA's Jet Propulsion Laboratory (JPL), which was commissioned to build the satellite in cooperation with NASA's Goddard Space Flight Center (GSFC). SMAP was launched on January 31st, 2015. It is placed in a Sun-synchronous dawn/dusk orbit (local equator crossing time 6:00 AM on descending node), with an altitude of 685 km. SMAP is composed of a radar and a radiometer, both working in L-band and sharing a 6 m mesh deployable offset-fed reflector antenna (Figure 2.14) that rotates at 14.6 rpm, at a constant incidence angle of 40°, to provide high spatial resolution within a ~1.000-km swath. The SMAP baseline requirements were to provided SM estimates in the top 5 cm of the soil with a target accuracy of 0.04 m^3/m^3, at 10-km spatial resolution (combining active and passive information) with a revisit time of 3-days [89]. The radiometer operates at 1.413 GHz, measuring T_B at two polarizations (horizontal and vertical), and the third and fourth Stoke parameters, obtaining full-polarimetric capabilities. The SMAP radar failed about four months after its launch yet the radiometer continues to operate beyond its 3-year mission design.

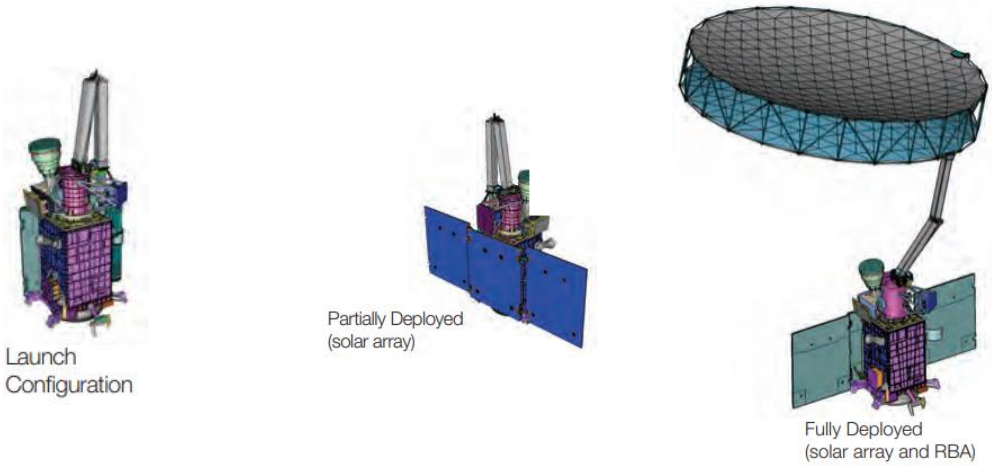

Figure 2.14 SMAP configuration: (a) launch configuration, (b) partially deployed and (c) fully deployed. Adapted from [89].

The original scientific objectives of SMAP can be summarized in five main goals [89]: (i) advance the knowledge of the processes that link terrestrial water, energy, and carbon cycles; (ii) estimate global SM maps of the first 5 cm of the soil; (iii) quantify the net carbon flux in boreal

landscapes; (iv) enhance weather and climate forecast skill; and (v) improve food prediction and drought-monitoring capabilities.

A. SMAP data products

The SMAP mission has generated 24 distributable data products that can be grouped in four levels [116]:

Level 0 consist of the raw instrument data, at the original resolution, time ordered and with communications artifacts filtered.

Level 1 products contain instrument-related data, the information is ordered in granules, based on half-orbits. Level 1 includes three subcategories:

- Level-1A radiometer product, contains all radiometric data downlinked from the spacecraft for one specific half-orbit, at two polarizations, vertical and horizontal.
- Level-1B radiometer product, provides calibrated brightness temperatures, time-ordered, geolocated and radiometrically corrected.
- Level-1C product is a grided version of the SMAP L1B product. Brightness temperatures are resampled to a 36-km EASE v2 grid in three projections: global cylindrical, northern hemisphere, and southern hemisphere.

Level 2 products contain half-orbit soil moisture retrievals provided in a 1/3/9/36-km EASE v2 grid (depending on the subcategory of the selected product). Files also contain all brightness temperatures and ancillary data required to generate the soil moisture maps.

Level 3 products contain daily composites of global soil moisture data provided in a 1/3/9/36-km EASE v2 grid (depending on the subcategory of the selected product).

Level 4 products provide model-derived root-zone soil moisture and carbon net ecosystem exchange.

Table 2.1 Main features of SMOS and SMAP instruments

		SMOS	SMAP
Scientific requirements		SM: 4% in top 5 cm SSS: 0.5-1.5 psu (single observation) or 0.2 psu (monthly average of a 100 x 100-km area)	SM: 4% in top 5 cm for VWC < 5 kg3m^{-2} Capture freeze/Thaw state
Topology	Radiometer	Synthetic aperture	Real aperture
	Radar	-	Synthetic aperture
Frequency	Radiometer	L-Band (1.4-1.427 GHz)	L-Band (1.41 GHz)
	Radar	-	L-Band (tunable from 1.22-1.3 GHz)
Orbit height		758 km	685 km
Local solar time at ascending node		6 A.M.	6 P.M.
Incidence angle		0°-65° (multi-angular)	40° (constant)
Radiometric accuracy		~2-4.5 K	~1.3 K
Spatial resolution	Radiometer	~35-70 km	40 km (radiometer)
	Radar	-	10 Km
Swath coverage		~1000 km	~1000 km
Revisit time		3 days	3 days
Mission duration	Original	Minimum of 3 years	Minimum of 3 years
	Current	More than 12 years	More than 7 years

Chapter 3

Soil moisture spatial enhancement

Within the low-frequency microwave passive remote sensing, L-band has demonstrated [10–12] to be the optimal frequency range to globally estimate SM, although the low spatial resolution (around tens of kilometers) of the resulting SM maps limits their adoption in local and regional scale applications. To overcome this limitation, during the last years, several downscaling techniques have been proposed to disaggregate coarse SM maps to 1 km [27,46,117], hundreds of meters [118], or even tens of meters [119]. Different ways of classifying disaggregation techniques can be proposed, e.g. according to the nature of the linking model or depending on the input of ancillary data, among others [8,25,120]. This chapter provides a comprehensive review of the main disaggregation methods relevant for this Thesis work, grouped as follows: (i) optical-based downscaling techniques, which leverage from the high spatial resolution of the thermal/optical data and their synergies with microwaves; and (ii) active and passive microwave-based downscaling techniques, which include techniques that combine radar and radiometer data, taking advantage of the strengths of both sensors. Model/data-based downscaling techniques overcome the possible limitations of using remote sensing data only, and are based on data assimilation and/or machine learning algorithms. Although model/data-based downscaling techniques are not the focus of this Thesis, a brief review of state-of-the-art has been included. This chapter also contains a description of all the datasets that are used in this Thesis, to develop the proposed disaggregation algorithms, either to calibrate some required parameters, or to validate and compare the results obtained.

3.1 Disaggregation methods

3.1.1 Optical-based downscaling techniques

The relationship between T_S and vegetation parameters to estimate SM was initially suggested by Nemani et al. ([121]), who found a negative slope between these two variables for a wide range of land covers, and suggested a dependence of the slope on the gradient of the SM. This idea was further studied by Gillies et al. [122] and Carlson et al. [123], and evolved into "universal triangle" concept (Figure 3.1), which established an indirect relation between visible (VIS) and infrared (IR) parameters, such as NDVI and T_S, to SM.

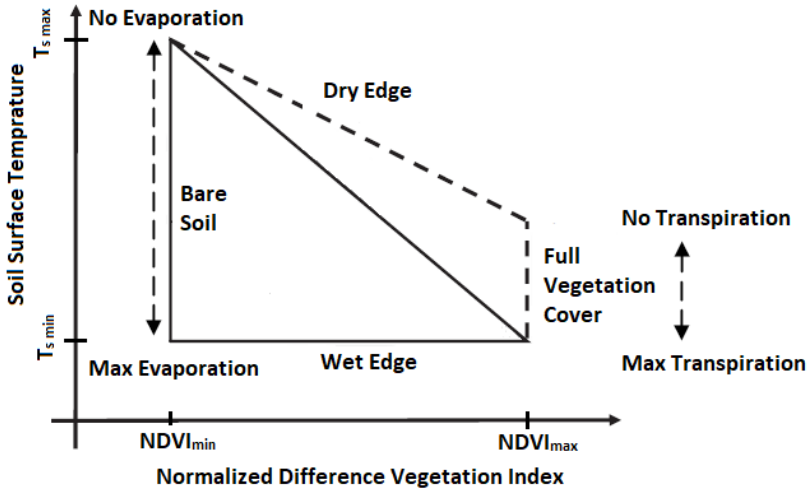

Figure 3.1 Trapezoidal/triangular space of VIS(NDVI)/IR(T_S). Adapted from [25,124].

The sensitivity of T_S to changes in SM depends on the surface conditions (e.g., vegetation density). The relationship of these three variables (T_S, SM, and NDVI) can be represented through a scatter plot that acquires a triangular or trapezoidal shape (in case dry and wet edges cross beyond the maximum NDVI value [25]) [124].

Several studies [27,29,125,126] have used the "universal triangle" concept to improve the spatial resolution of the passive microwave-based SM maps, using T_S and other vegetation parameters in the disaggregation process, obtained from VIS/IR observations which are typically available at high spatial resolution. While microwave radiometers have a high radiometric sensitivity (SM accuracies on the order of 0.04 m^3/m^3) under all-weather conditions, optical and thermal remote sensing provides high-resolution information on the heterogeneity of surface features. Still, VIS/IR observations have a limited applicability due to the attenuation effect exerted by vegetation and the Earth's atmosphere on them.

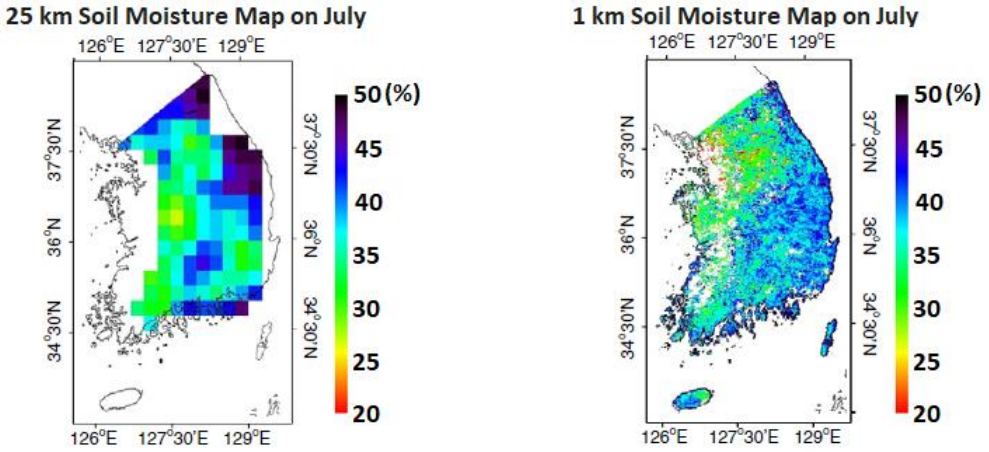

Figure 3.2 SM maps of Korea for July 2007: (a) the radiometer-only SM product, and (b) the 1-km disaggregated SM product. Adapted from [126].

In [127], Chauhan et al. propose a polynomial fitting method to downscale the SM based on a previous model presented by Zhan et al. [128]. This method was applied to data from the Special Sensor Microwave Imager (SSM/I) and the Advanced Very High-Resolution Radiometer (AVHRR). It is a two-step approach, based on the Carlson's concept of "universal triangle" [129]: (i) low-resolution SM estimates are first obtained by inverting dual-polarized T_B; (ii) low-resolution SM is then linked to ω, NDVI and T_s. The high-resolution VIS/IR parameters are first aggregated to the microwave-derived low-resolution SM grid, to build the linking model (Equation (3.1)). The regression relation obtained is then used in conjunction with the high-resolution NDVI, T_s and ω, in Equation (3.1), to retrieve SM at high resolution. Chauhan et al. [127] expressed the relationship between SM and measurable land parameters as:

$$m_v = \sum_{i=0}^{i=2} \sum_{j=0}^{j=2} \sum_{k=0}^{k=2} a_{ijk}\, NDVI^{*(i)}\, {T_s}^{*(j)}\, \omega^{*(k)} \tag{3.1}$$

where ${T_s}^*$, $NDVI^*$, ω^*, are the normalized T_s, NDVI and ω, respectively. This technique was applied by Choi and Hur in [126], to disaggregate the AMSR-E SM from 25 km to 1 km over Korea (Figure 3.2), using auxiliary data from MODIS. The disaggregated 1-km SM reported slightly better error bias, RMSE and R coefficients than the 25-km AMSR-E SM. Zhao and Li [130] used this fitting model to downscale the low-resolution AMSR-E SM (Figure 3.3) using the Meteosat Second Generation (MSG) Spinning Enhanced Visible and Infrared Imager (SEVIRI) data. A simple modification was introduced to Equation (3.1), substituting T_s by the normalized-mid-morning temperature and the normalized maximum temperature. The high-resolution SM (5 km) was estimated through two different methods: the first, using the original model (Equation (3.1)), and the second, modifying T_s as mentioned above. Results were validated over the Soil Moisture Measurements Station Network of the University of Salamanca (REMEDHUS) network (in Zamora, Spain), obtaining poor correlations due to the low spatial representativeness of the *in situ* network at MSG-SEVIRI scale. However, the new methodology showed better performance than Chauhan et al. [127] model.

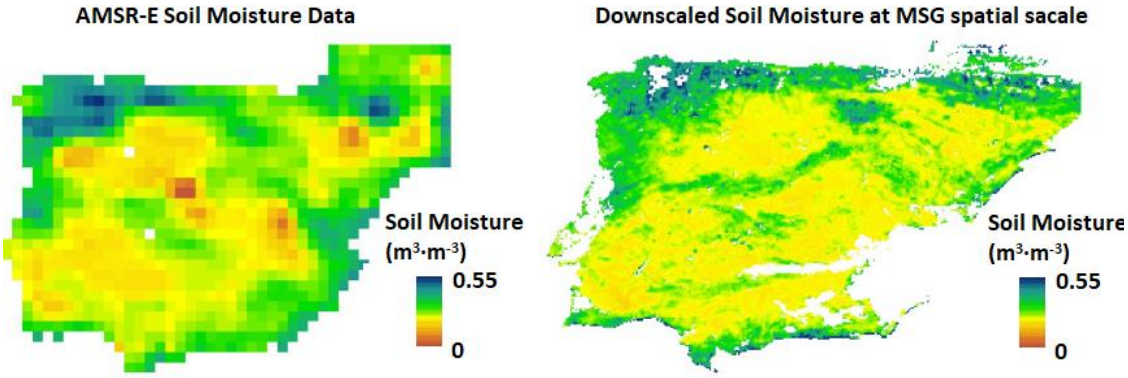

(**a**) (**b**)

Figure 3.3 (a) AMSR-E LPRM SM at 25 km and (b) disaggregated SM with Meteosat MSG-SEVIRI data at 1 km, for July 5th, 2007. Adapted from [130].

Piles et al. [29] improved the polynomial fitting model by replacing ω from Equation (3.1), with the coarse-resolution SMOS T_B, to strengthen the relationship between the land surface parameters and SM (Figure 3.4). Brightness temperature includes the information on all the parameters involved in the land surface emissions (e.g., SM, T_s, h_s, CF, and τ and ω). Thus, Equation (3.1), was modified to:

$$m_v = \sum_{i=0}^{i=2} \sum_{j=0}^{j=2} \sum_{k=0}^{k=2} a_{ijk}\, NDVI^{*(i)}\, {T_s}^{*(j)}\, {T_B}^{*(k)} \tag{3.2}$$

The downscaling algorithm was applied to SMOS T_B, and to NDVI and T_s derived from MODIS, to obtain high-resolution SM at 10 km and 1 km. The resulting SM maps, over the Yanco region in New South Wales, Australia, were able to capture SM variability at both spatial scales, preserving the SM sensitivity at 10 km and being moderately degraded at 1 km, without a significant degradation of RMSE.

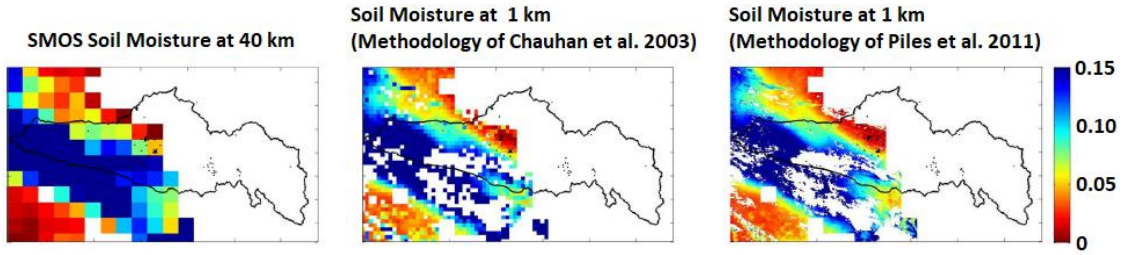

(**a**) (**b**) (**c**)

Figure 3.4 (a) SMOS SM at 40 km , (b) SM disaggregated at 1 km using Chauhan et al. [127] methodology and (c) SM disaggregated at 1 km using Piles et al. methodology [29], over Murrumbidgee catchment, for February 21st, 2010. Adapted from [29].

In [46], Piles et al. modified the algorithm (Equation (3.2)) to make full use of SMOS polarimetric and multi-angular capability:

$$S_m = a_0 + a_1 T_s^* + a_2 NDVI^* + \sum_{i=1}^{3} a_{3i}\, T^*_{B_{H,\theta i}} + \sum_{i=1}^{3} a_{4i}\, T^*_{B_{V,\theta i}} \tag{3.3}$$

where $T^*_{B_{H,\theta i}}$ and $T^*_{B_{V,\theta i}}$ are the normalized horizontal and vertical polarized T_B, respectively, at the incidence angles (θ_i) 32.5°, 42.5° and 52.5°. a_k are the model fitting coefficients. The spatio-temporal correlation of downscaled SM was analyzed by comparing it with the observations provided by the REMEDHUS SM *in situ* network (Figure 3.5). Downscaled maps compared well to the ground-based measurements, with an improved slope of the linear regression line with respect radiometer only SM (Figure 3.5b). The downscaled product showed similar performance across seasons, including winter periods, when other microwave/optical methods based on evaporation efficiency have a limited applicability [47]. This methodology was implemented at BEC facilities (see Figure 3.6) to generate and distribute the center's first high-resolution SM maps, from the year 2012 to 2019. However, the temporal availability and the impact of atmospheric effects on the MODIS data, limit the temporal resolution of the downscaled SM maps. To overcome this drawback, Piles et al. [30] investigated the synergies of SMOS microwave and MSG-SEVIRI observations. The same model as in [46] (Equation (3.3)) was used to provide a temporal average SM product from the instantaneous 3-km downscaled SM, acquired every 15 min, allowing higher coverage in presence of clouds.

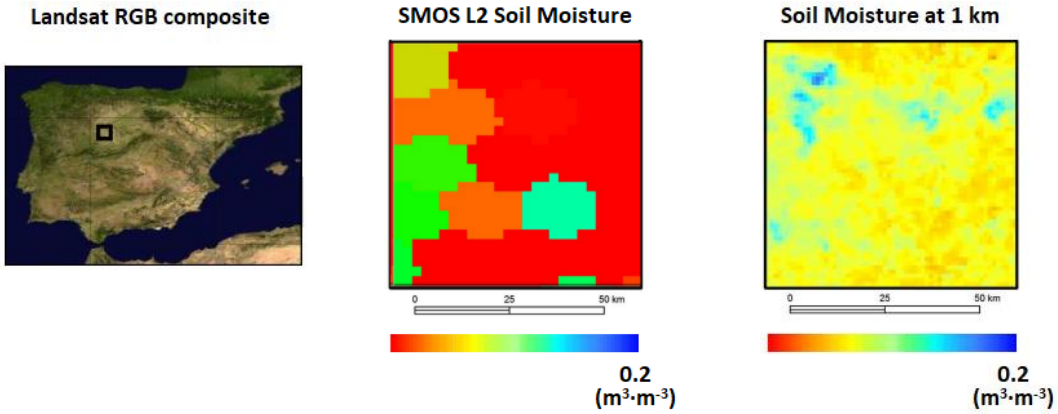

Figure 3.5 (a) Image of Landsat RGB composite over the Iberian Peninsula with the REMEDHUS area selected (black square), (b) SMOS L2 SM and (c) SMOS SM disaggregated at 1 km over REMEDHUS. Adapted from [46].

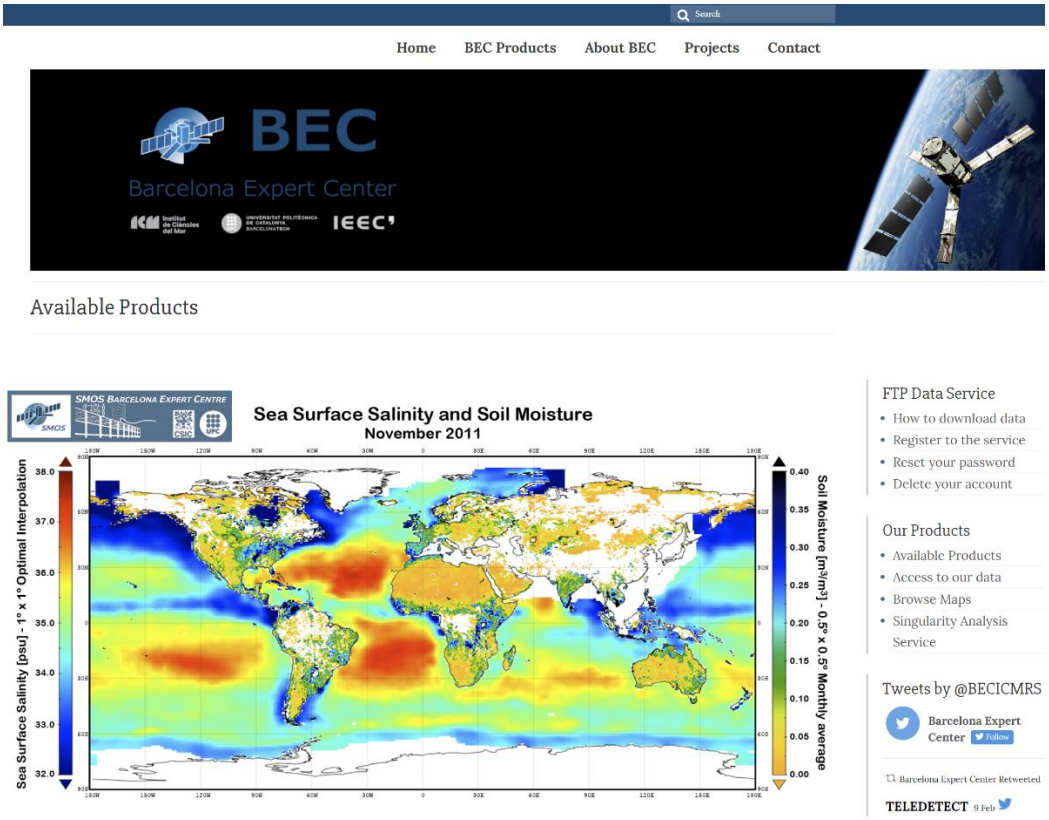

Figure 3.6 Barcelona Expert Center website: http://bec.icm.csic.es. Within the 'Available Products' section of the website it can be find the links to access different land (soil moisture at high and low resolution) and oceanic variables (sea surface salinity, sea ice concentration and singularity exponents).

Sanchez et al. ([131]) investigated the use of other less common vegetation/water indices i.e., ShortWave InfraRed (SWIR) indices, extracted from MODIS products, and applied together with MODIS T_S and SMOS T_B using the linking model in Equation (3.3). These indices were calculated as the normal ratio of the 1240, 1640, and 2130 nm SWIR bands and the 858 nm near infrared band from the 8-days 500 m land surface reflectance MODIS product. From this study, two major conclusions were stated: (i) the dynamic range of the vegetation index does not have a crucial effect in the linking model; and (ii) SM can be estimated at the spatial scale of the vegetation index (e.g., SWIR or NDVI) even if the T_S is at low spatial resolution.

The applicability of the linking model through the Equation (3.3), using airborne data, was also tested. A flight campaign over the area of Gimenells (Lleida) acquired simultaneous observations from the Compact Airborne Spectrographic Imager (CASI), the Thermal Airborne Spectrographic Imager (TASI), and the Airborne RadIomEter at L-band (ARIEL-2). ARIEL-2 T_B, CASI NDVI, and TASI T_S were employed to estimate SM at the spatial resolution of the optical sensors (2 m) by using a simplification of the linking model in Equation (3.3), exclusively using the single look-angle (nadir) T_B at horizontal polarization. Detailed information can be found in [132].

The application of Equation (3.3) was limited to areas with similar climatic conditions, because a single set of fitting parameters a_k was calculated for the entire study area. In [27], Portal et al. proposed a new method, based on an adaptive moving window, to calculate a set

of fitting parameters for each low-resolution pixel. Using SMOS and MODIS observations, the resulting high-resolution SM maps at 1 km (Figure 3.7) did not show degraded accuracy with respect to previous versions [30] and allowed to better capture the landscape heterogeneity features. This method was performed as part of this Thesis, and is explained in detail in Chapter 4. Also, this is the current methodology implemented by the BEC to provide high-resolution SM maps at continental scale (from the year 2019 to present).

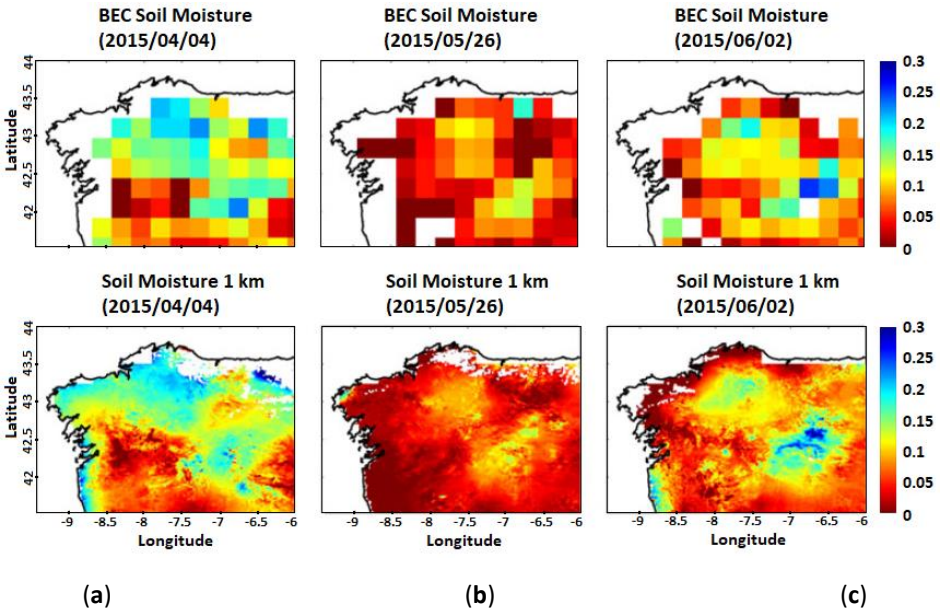

Figure 3.7 SMOS BEC L3 SM in a 25-km grid (first row) and SMOS SM disaggregated at 1 km (second row), for (a) April 4th, (b) May 26th and (c) June 2nd, 2015. Adapted from [27].

Another well-known optical-microwave disaggregation method is the Disaggregation algorithm based on Physical And Theoretical scale Change (DisPATCh) presented by Merlin et al. [47]. It is based on the soil evaporation process from the 0-5 cm soil layer, linking optical and near-surface SM data, and requiring mathematical tools, such as partial derivatives, projection techniques [28,133] and Taylor series expansions [8]. DisPATCh uses Soil Evaporative Efficiency (SEE) as a proxy for surface SM variability within the radiometric pixel. The link between SM and SEE is described by the SEE model [134] and the following downscaling relationship:

$$m_v(HR) = m_v(CR) + \frac{\partial m_{v_{mod}}}{\partial SEE} \cdot (SEE_{obs}(HR) - \langle SEE_{obs}(HR) \rangle) \tag{3.4}$$

where $m_v(HR)$ is the disaggregated SM, $m_v(CR)$ is the radiometric SM, SEE_{obs} is the soil evaporative efficiency at high resolution, and $\langle SEE_{obs} \rangle$ its average within the radiometric pixel. $\partial m_{v_{mod}}/\partial SEE$ is the partial derivative of the radiometric SM with respect to the evaporative efficiency. In [47], DisPATCh was applied to SMOS data using MODIS observations over the Australian Airborne Calibration/validation Experiments for SMOS (AACES) area. It was concluded that the performance of the downscaled products was highly related to season. A R ≈ 0.7 was obtained between disaggregated SM and *in situ* measurements during the summer, while this

correlation was approximately zero during the winter period for the same area. Showing weaker coupling between SM and evaporation in temperate than in semi-arid climate. In [118] a new version of DisPATCh was presented, with two updates [47]: (i) atmospheric effects on the temperature data were removed by using a quality index filter, and (ii) topographic effects were corrected. In that study, the 40-km resolution SMOS SM was disaggregated to 1 and 3 km, using MODIS data (Figure 3.8), and to 100 m using the Advanced Spaceborne Thermal Emission and Reflection radiometer (ASTER) and Landsat-7 data (Figure 3.9). Both the linear and nonlinear behavior of SEE were tested, revealing that while a linear SEE model was adequate at kilometric scale, a linear assumption resulted in a poorer performance at the hundred-meter scale. Further improvements of DisPATCh are discussed in [135], proposing an additional topographic correction for T_S including both illumination and elevation effects.

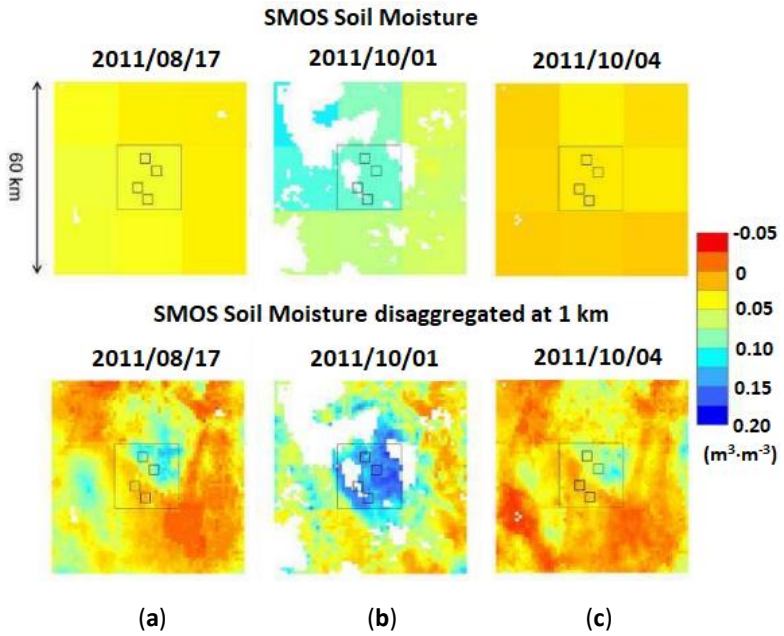

Figure 3.8 SMOS SM at 20 km (first row) and SMOS SM disaggregated at 1 km (second row), for (a) August 17th, (b) October 1st and (c) October 4th, 2015. The 60 x 60-km region corresponds to an area located east of Lleida in Catalunya, Spain. Adapted from [118].

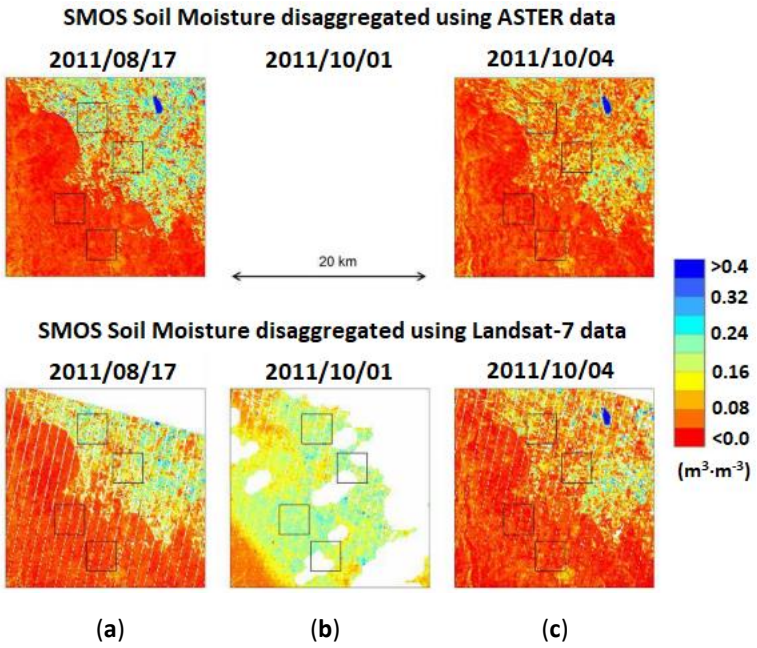

Figure 3.9 SMOS SM disaggregated at 100 m in nonlinear mode using ASTER (first row) and Landsat-7 (second row) data, for (a) August 17th, (b) October 1st and (c) October 4th, 2015. The 20 x 20-km region corresponds to an area located east of Lleida in Catalunya, Spain. Adapted from [118].

Kim and Hogue [136] presented a simple, computationally fast and stand-alone (using remote sensing data exclusively) downscaling algorithm based on previous approaches (the "universal triangle" concept and the DisPATCh technique). The objective of the approach was to merge high-resolution information from MODIS (~1 km) with low-resolution data from AMSR-E (~25 km) to obtain 1-km SM maps. This method, noted as UCLA, uses a linear relationship to relate SM to a Soil Wetness (SW) index:

$$m_v(HR) = m_v(CR)\frac{SW(HR)}{\langle SW(HR)\rangle} \tag{3.5}$$

where $m_v(CR)$ is the AMSR-E SM, $SW(HR)$ is the SW at the MODIS scale, and $\langle SW(HR)\rangle$ is the mean of $SW(HR)$ within the AMSR-E pixel. In that study, the UCLA method was compared to the algorithm proposed by Chauhan et al. [127] and the one proposed by Merlin et al. [137,138] (Figure 3.10), and the polynomial fitting approach was found to perform worse than the other two methods. In [120] Peng et al. modified Equation (3.5) by substituting the soil SW index by the Vegetation Temperature Condition Index (VTCI) calculated from MODIS. In that study, the spatial resolution of the Climate Change Initiative (CCI) SM was improved to 5.6 km using VTCI as the only input, maintaining the accuracy of the original CCI SM products but presenting much more detail on the spatial variations.

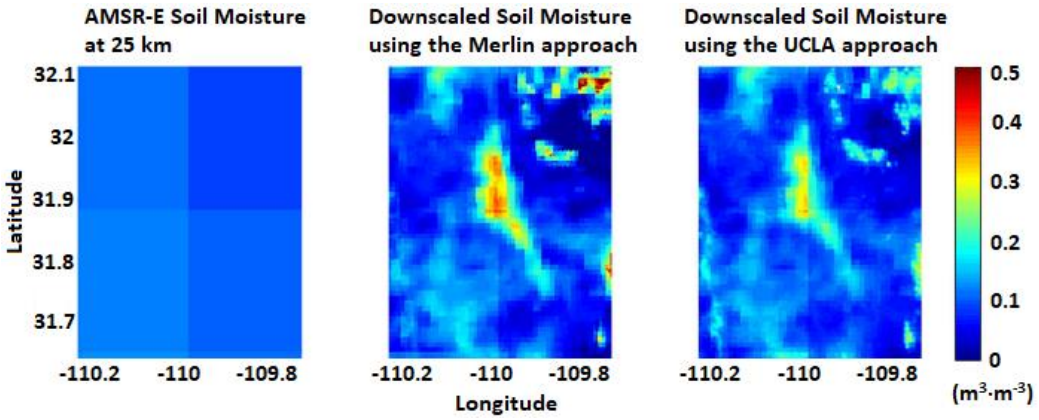

Figure 3.10 (a) AMSR-E SM, (b) AMSR-E SM downscaled using Merlin's approach [137,138], and (c) AMSR-E SM downscaled using the UCLA approach. Adapted from [136].

In [139] Song et al. proposed to first disaggregate the AMSR-E Ku-band T_B from 25 km to 1 km, to later retrieve the SM at high resolution applying the improved SCA (Section 2.2.5B) using the Q_p model [140]. The performance of the algorithm was tested in the northwest of China, through a comparison between retrieved 1-km SM and ground measurements. Resulting in a R>0.71 and a RMSE<0.12 m^3/m^3.

3.1.2 Active/passive microwave-based downscaling techniques

The active/passive microwave data combination aims at obtaining an optimal blend of the high accuracy of passive sensors and the high spatial resolution of active sensors. Microwave radiometers have a high radiometric sensitivity (leading to SM accuracies on the order of 0.04 m^3/m^3) and a high revisit time (3-day), but suffer from coarse spatial resolution, typically 30-40 km from space. Therefore, microwave radars, especially Synthetic Aperture Radars (SARs) step in, since their spatial resolution is significantly higher, in the range of a few meters [141,142]. However, backscatter commonly has a lower temporal resolution (about a week) and may be significantly affected by the soil roughness and the soil-covering vegetation canopy, which reduces the accuracy of the measurements and complicates the active-only SM retrieval.

One of the first investigations that explored the fusion of active/passive data to disaggregate SM maps was proposed by Njoku et al. in [143]. In that study it is proposed a change detection algorithm, investigating the sensitivities of multi-polarization active/passive measurements (1.26 GHz-3.15GHz) to SM changes using the Passive and Active L- and S-bands (PALS) sensor. PALS is a combined polarimetric radiometer (1.413 GHz) and NASA licensed radar (1.26 GHz), sharing a rotating planar array antenna [144]. It is the prototype for the Aquarius [145] and SMAP missions, and has flown for hundreds of hours in support of NASA campaigns. Figure 3.11 shows the T_B (Figure 3.11a) and radar backscatter (Figure 3.11b) maps, with approximately the same spatial resolutions, obtained using L-band data from the PALS sensor, collected during the Southern Great Plains Experiment in 1999 (SGP99). It can be seen that the spatial patterns of T_B

and the radar backscatter maps are quite different. This can be attributed to different sensitivities to vegetation and roughness characteristics.

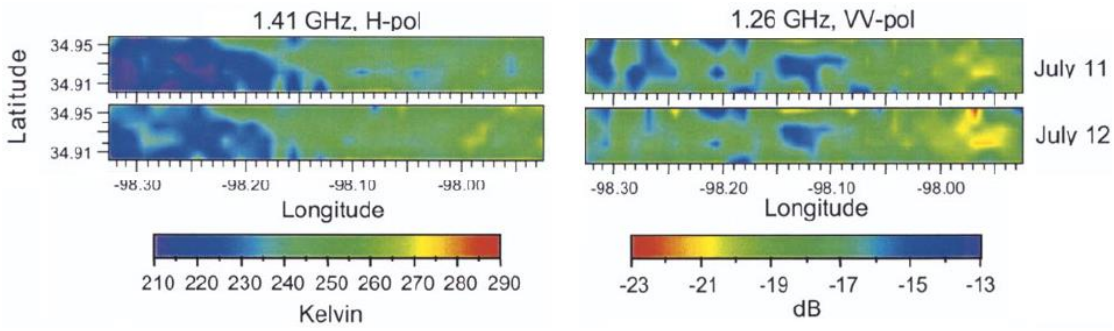

(**a**) (**b**)

Figure 3.11 Effects of soil wetting and drying over PALS data acquired on July 11th and 12th, 1999 on (a) radiometric T_B (at H polarization, 1.41 GHz) and on (b) radar backscatter (at VV polarization, 1.26 GHz). Adapted from [143].

Njoku et al. proposed a linear relation between SM and T_B, and also between SM and the radar backscatter:

$$T_B = A + B\, m_v \tag{3.6}$$

$$\sigma_{0,dB} = C + D\, m_v \tag{3.7}$$

where $\sigma_{o,dB}[dB]$ is the radar backscatter, and A, B, C, D are the regression coefficients which are functions of surface vegetation and roughness. These coefficients can be considered relatively invariant on short time scales; therefore, the time differences can be performed to remove the bias terms:

$$\Delta T_B = B\, \Delta m_v \tag{3.8}$$

$$\Delta \sigma_{0,dB} = D\, \Delta m_v \tag{3.9}$$

Figure 3.12 shows that the spatial patterns of active and passive sensitivities to SM variations (relative changes) are similar, after computing the differences in T_B (Figure 3.12a) and in radar backscatter (Figure 3.12b), for July 11th and 12th, with respect to July 9th, 1999. It can be seen the effect of vegetation and roughness on the sensor are considerably reduced when analyzing difference maps, indicating that SM is separable from the other effects.

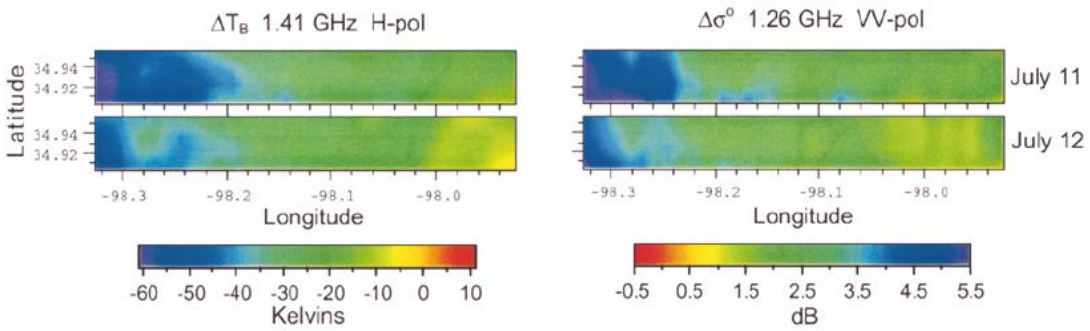

(**a**) (**b**)

Figure 3.12 Changes in (a) T_B and (b) $\sigma_{0,dB}$ (ΔT_B and $\Delta\sigma_{0,dB}$). Calculated as July 11th and 12th, minus July 9th, 1999. Adapted from [143].

In that study Njoku et al. proposed a SM retrieval approach, using active and passive measurements, under the conditions that radar observations should be available over a number of seasonal cycles and associated *in situ* observations of SM must also be available. In that approach, SM was first estimated using radiometer data (m_v in Equations (3.10) and (3.11)). Soil moisture estimates for two different soil conditions, dry (Equation (3.10)) and wet soils (Equation (3.11)), were used as ground truth data together with backscatter to solve a system of equations:

$$\sigma_{0,dB}(dry) = C + D\, m_v(dry) \tag{3.10}$$

$$\sigma_{0,dB}(wet) = C + D\, m_v(wet) \tag{3.11}$$

Figure 3.13a shows the SM distribution, obtained using a single-channel linear retrieval due to the almost linear relationship between the PALS radiometer T_B and *in situ* SM. Figure 3.13b also shows the retrieved SM but obtained using radar data together with the calibration parameters C and D (Equations (3.10) and (3.11)). Radiometer and radar SM are exactly the same for July 11th, since the SM maps of this specific day are used to calibrate the regression parameters. On July 12th, radar-based SM is estimated using the regression parameters, and the resulting SM map is similar in spatial patterns and dynamic range to that obtained using exclusively passive measurements.

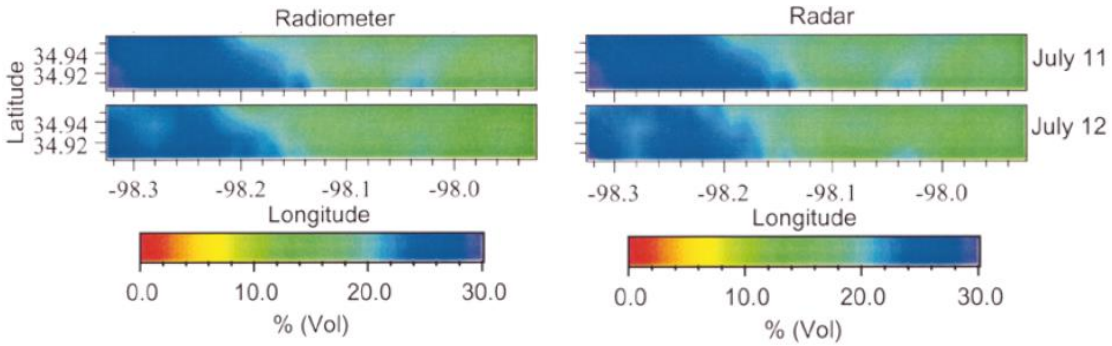

Figure 3.13 Soil moisture distribution retrieved from: (a) the radiometer (at H polarization, 1.41 GHz) algorithm, using coefficients derived from the regression line with *in situ* data; and (b) from radar (VV polarization, 1.26 GHz) algorithm, using coefficients derived from radiometric data. Maps for July 11th and 12th, 1999. Adapted from [143].

This study proved the potential of radar-radiometer change detection approaches for the retrieval of SM at high resolution. In [146], Narayan et al. successfully applied this change detection estimation algorithm to coincident PALS and Airborne Synthetic Aperture Radar (AIRSAR) datasets acquired during the Soil Moisture Experiments held during June-July 2002 (SMEX02) at Iowa. The aim of this study was to estimate the SM change at the spatial resolution of radar by combining radar (100-m spatial resolution) and radiometer (400-m spatial resolution) data. It was assumed that m_v and $\sigma_{o,dB}$ were linearly related. Equations (3.10) and (3.11) can be rewritten as:

$$m_v(HR,t) = \alpha(HR) + \beta(HR) \cdot \sigma_{o,dB}(HR,t) \tag{3.12}$$

where HR refers to high resolution (100 m) at a time t, and $\sigma_{o,dB}(HR,t)$ is the radar backscatter aggregated to 100 m. $\alpha(HR)$ and $\beta(HR)$ are parameters of each pixel in the coincident radar and radiometer images, and they may depend on vegetation and roughness. Considering the vegetation changes much lower than the change in SM when varying $\sigma_{o,dB}$, and being β and $\sigma_{o,dB}$ changes uncorrelated:

$$\langle \Delta m_v(HR,t) \rangle = \langle \beta(HR) \rangle \cdot \langle \Delta \sigma_{o,dB}(HR,t) \rangle \tag{3.13}$$

where $\langle \cdot \rangle$ stands for the spatial average of the HR within the 400-m coarse resolution (CR) pixels. Assuming that variations in vegetation occur at large scales, then $\beta(HR) = \langle \beta(HR) \rangle = \beta(CR)$. So, the change in SM at high resolution can be expressed as:

$$\Delta m_v(HR,t) = \langle \beta(HR) \rangle \cdot \Delta \sigma_{o,dB}(HR,t) \tag{3.14}$$

$\langle \beta(HR) \rangle$ can be calculated as the slope of the regression between the radiometer and the spatially averaged radar data at CR resolution.

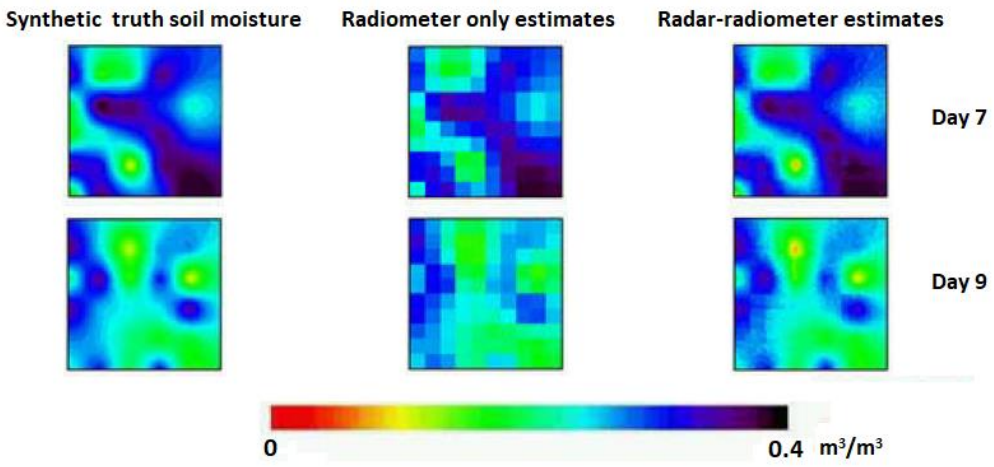

Figure 3.14 Soil moisture maps for two different days. From left to right: synthetic truth SM, SM obtained from a typical radiometer, and the result after applying the change detection algorithm to disaggregate SM. Adapted from [146].

Figure 3.14 shows that the variability captured by the resulting SM, obtained through the active/passive algorithm (third column), is higher than the SM obtained with the radiometer data exclusively (second column). Piles et al. [31] proposed a change detection based approach for SMAP and applied it to four-months Observation System Simulation Experiment (OSSE) data, considering the time differences as:

$$m_v(HR,t) = m_v(CR,t-t_R) + \langle \beta(HR) \rangle \cdot \Delta \log\left[\sigma_o(HR,t)\right] \tag{3.15}$$

where σ_o is the radar backscatter in linear, t_R is the revisit time of the observations, and $m_v(CR,t-t_R)$ is the radiometer-scale SM retrieval. This study consolidated the results obtained by Narayan et al. in [146]; the change detection method allowed obtaining better performance and more spatial details than the radiometer-only method (see Figure 3.15).

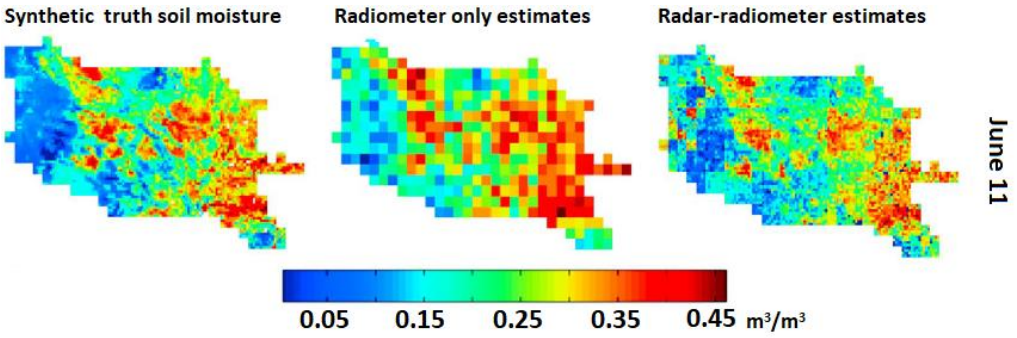

Figure 3.15 Soil moisture maps for June 11th, over the Red Arkansas river basin. From left to right: synthetic ground-truth SM, low-resolution (40 km) SM obtained from a typical radiometer, and high-resolution (10 km) SM obtained through the active/passive method. Adapted from [31].

Das et al. proposed an improved version of the change detection algorithm to robustly merge L-band active/passive observations from the SMAP mission [32]. Three spatial resolutions were defined for this algorithm: (i) a 36-km coarse spatial resolution, (ii) a 3-km high spatial resolution, and (iii) a 9-km medium spatial resolution (MR). As in previous versions of the approach [31,143,146], the formulation begins assuming a linear relationship between m_v and $\sigma_{o,dB}$:

$$m_v(MR_N, t) = \alpha(MR_N) + \beta(MR_N) \cdot \sigma_{o,dB}(MR_N, t) \tag{3.16}$$

where the subscript N refers to the number of pixels of MR spatial resolution within a CR pixel. $\alpha(MR_N)$ and $\beta(MR_N)$ are empirical parameters. Spatially averaging both sides of Equation (3.16), it can be rewritten as:

$$\langle m_v(MR_N, t)\rangle = \langle \alpha(MR_N)\rangle + \langle \beta(MR_N) \cdot \sigma_{o,dB}(MR_N, t)\rangle \tag{3.17}$$

Assuming that significant variations in the parameters $\alpha(MR_N)$ and $\beta(MR_N)$, related to vegetation and soil roughness, are homogeneous within CR, then $\alpha(MR_N) = \langle \alpha(MR_N)\rangle = \alpha(CR)$ and $\beta(MR_N) = \langle \beta(MR_N)\rangle = \beta(CR)$. Subtracting Equation (3.17) from Equation (3.16):

$$m_v(MR_N, t) = m_v(CR, t) + \beta(CR) \cdot \left\{\sigma_{o,dB}(MR_N, t) - \langle \sigma_{o,dB}(MR_N, t)\rangle\right\} \tag{3.18}$$

$\beta(CR)$ is based on time-series regression, $m_v(CR, t)$ is obtained from the radiometer data, $\sigma_{o,dB}(MR_n, t)$ and its spatial average $\langle \sigma_{o,dB}(MR_n, t)\rangle$ are obtained from the radar data. It has also been considered $\langle m_v(MR_N, t)\rangle = m_v(CR, t)$. Using this information, a linear regression is applied to compute $\beta(CR)$. Note this methodology makes it possible to estimate an absolute SM value (see Figure 3.16) rather than a relative change, it uses time-series information and, unlike [31] and [146], it has the advantage of not requiring previous satellite overpass observations.

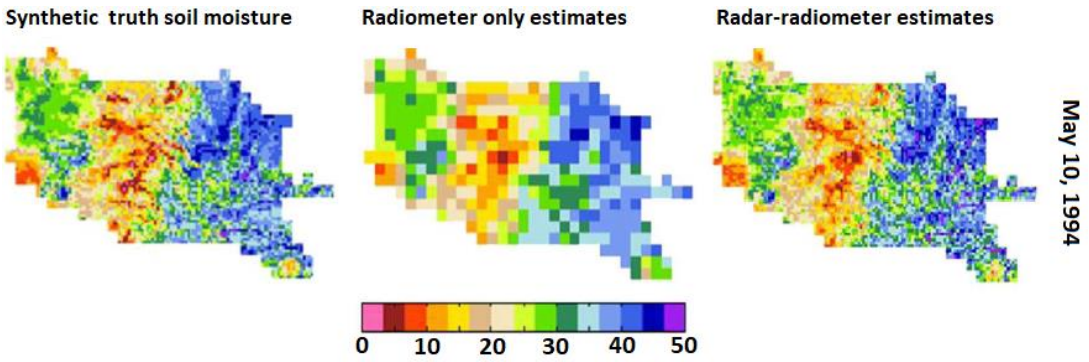

Figure 3.16 Soil moisture maps for May 10th, 1994, over the Red Arkansas river basin. From left to right: synthetic ground-truth SM, low-resolution (40 km) SM obtained from a typical radiometer, and high-resolution (9 km) SM obtained through the active/passive method. Adapted from [32].

In the above approaches, the accuracy of the high-resolution SM depended on the accuracy of the passive retrieved SM, and the retrieval accuracy of active/passive at 9 km was generally inferior to the one obtained by the passive-only coarse-resolution SM [147]. To overcome this limitation, Das et al. [147] proposed to use the backscatter to first downscale the T_B data and then estimate the high-resolution SM using a passive-only retrieval algorithm (see Section 2.2.5). This was the algorithm stablished as the baseline approach for SMAP active/passive products at a 3-km high-resolution scale and a 9-km medium-resolution scale. It is based on the assumption of a linear relationship between T_B and the backscatter:

$$T_{B_V}(CR) = \alpha(CR) + \beta(CR) \cdot \sigma_{0,dB_{VV}}(CR) \tag{3.19}$$

where $\sigma_{0,dB_{VV}}[dB]$ is the backscatter co-polarized at V-V polarization, $\sigma_{0,dB_{VV}}(CR) = 1/nf \cdot \sum_{nf}^{i=1} \sigma_{0,dB_{VV}}(HR_i)$, being nf the number of HR grid cell within CR. $\alpha(CR)$ and $\beta(CR)$ can be statistically estimated using time-series regressions of radiometer $T_{B_V}(CR)$ and spatially averaged radar data $\sigma_{0,dB_{VV}}(CR)$. The active/passive algorithm evaluated at MR:

$$T_{B_V}(MR_j) = \alpha(MR_j) + \beta(MR_j) \cdot \sigma_{0,dB_{VV}}(MR_j) \tag{3.20}$$

where $\sigma_{0,dB_{VV}}(MR_j) = 1/mf \cdot \sum_{mf}^{i=1} \sigma_{0,dB_{VV}}(HR_i)$, being mf the number of HR grid cell within MR. $T_{B_V}(MR_j)$ is the target variable of the algorithm. Subtracting Equation (3.20) from Equation (3.19):

$$\begin{aligned} T_{B_V}(MR_j) = T_{B_V}(CR) &+ \left\{\beta(CR) \cdot \left[\sigma_{0,dB_{VV}}(MR_j) - \sigma_{0,dB_{VV}}(CR)\right]\right\} \\ &+ \left\{\left[\alpha(MR_j) - \alpha(CR)\right] + \left[\beta(MR_j) - \beta(CR)\right] \cdot \sigma_{0,dB_{VV}}(MR_j)\right\} \end{aligned} \tag{3.21}$$

The first term on the right, $T_{B_V}(CR)$, is the T_B measured by the radiometer; the second term, $\left\{\beta(CR) \cdot \left[\sigma_{0,dB_{VV}}(MR_j) - \sigma_{0,dB_{VV}}(CR)\right]\right\}$, can be calculated as indicated above; and the third term, $\left\{\left[\alpha(MR_j) - \alpha(CR)\right] + \left[\beta(MR_j) - \beta(CR)\right] \cdot \sigma_{0,dB_{VV}}(MR_j)\right\}$, represents the subgrid heterogeneity effect and can also be expressed as:

$$\begin{aligned} \beta(CR) \cdot \Gamma \cdot \left[\sigma_{0,dB_{HV}}(CR) - \sigma_{0,dB_{HV}}(MR_j)\right] \\ = \left\{\left[\alpha(MR_j) - \alpha(CR)\right] + \left[\beta(MR_j) - \beta(CR)\right] \cdot \sigma_{0,dB_{VV}}(MR_j)\right\} \end{aligned} \tag{3.22}$$

where $\sigma_{0,dB_{HV}}$ is the backscatter cross-polarized at H-V polarization.

Then Equation (3.21) can be rewritten as:

$$T_{B_v}(MR_j) = T_{B_v}(CR) + \beta(CR)\left\{\left[\sigma_{0,dB_{VV}}(MR_j) - \sigma_{0,dB_{VV}}(CR)\right] + \Gamma \cdot \left[\sigma_{0,dB_{VH}}(CR) - \sigma_{0,dB_{VH}}(MR_j)\right]\right\} \quad (3.23)$$

where $\Gamma = \left[\delta\sigma'_{0,dB_{VV}}(MR_j)/\delta\sigma'_{0,dB_{HH}}(MR_j)\right]_{CR}$ is the sensitivity which is specific to the particular grid *CR*. The retrieved SM after applying the baseline algorithm (Figure 3.17a) shows better performance than the retrieved using the radiometer data only (Figure 3.17b). Also, it was stated that the retrievals using Equation (3.23) are just slightly better than the SM obtained through the active/passive option algorithm presented in [32]. However, the baseline algorithm (Equation (3.23)) provides the added value of high-resolution brightness temperature, which can be used as input to develop other products, e.g., SMAP L4 (surface and root zone soil moisture).

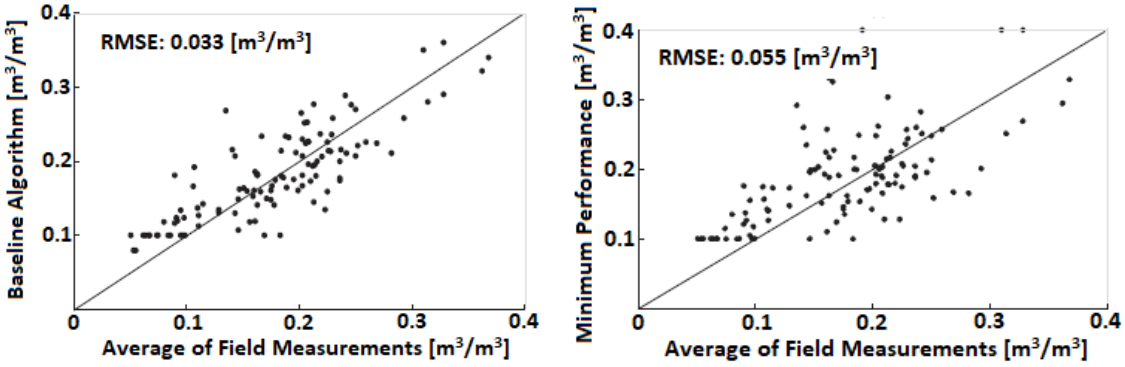

(**a**) (**b**)

Figure 3.17 Comparison of SM retrieved from Soil Moisture Experiment 2002 (SMEX02) PALS data for eight days and field averaged SM using: (a) the baseline algorithm and (b) the passive-only resampled at a higher spatial grid. Adapted from [147].

In [148], Wu et al. performs a robustness analysis of the change detection algorithm, the active/passive option from [32] and the SMAP baseline [147] algorithm, using data collected from the Soil Moisture Active Passive Experiments (SMAPEx) in Australia. It was concluded that the poorest performance corresponded to the change detection algorithm while the active/passive option from [32] performed better both in the representation of the correct SM spatial patterns and in terms of correlation.

In [149], Montzka et al. proposed a linear relationship between radiometer- and radar-only SM estimates to disaggregate SM:

$$m_{v,T_B,\sigma_0}(MR_j) = m_{v,T_B}(CR) + \beta_{m_v}(CR) \cdot (m_{v,\sigma_0}(MR_j) - m_{v,\sigma_0}(CR)) \quad (3.24)$$

where $m_{v,T_B,\sigma_0}(MR_j)$ is the disaggregated SM, $m_{v,T_B}(CR)$ is the radiometer SM product, and m_{v,σ_0} is the radar SM product. β_{m_v} is based on time-series regression using m_{v,T_B} and m_{v,σ_0} products. This study uses data from the passive L-band system Polarimetric L-band Multi-beam Radiometer (PLMR2) and the active L-band system F-SAR. The performance of this method was analyzed against the active/passive option from [32] and the SMAP baseline [147] downscaling algorithm. Montzka et al. concluded that the best performance was obtained by the active/passive option from [32]. However, the new radar-radiometer-only SM technique revealed slightly lower accuracy and similar spatial patterns to those of the baseline retrievals. Figure 3.18 shows the SM estimated applying a single-source retrieval from PLMR2 and F-SAR, as well as the SM estimated by merging two single-source SM products from radar and radiometer. The radar-radiometer-only SM product shows a similar pattern than the PLMR2 SM but at a higher spatial heterogeneity level.

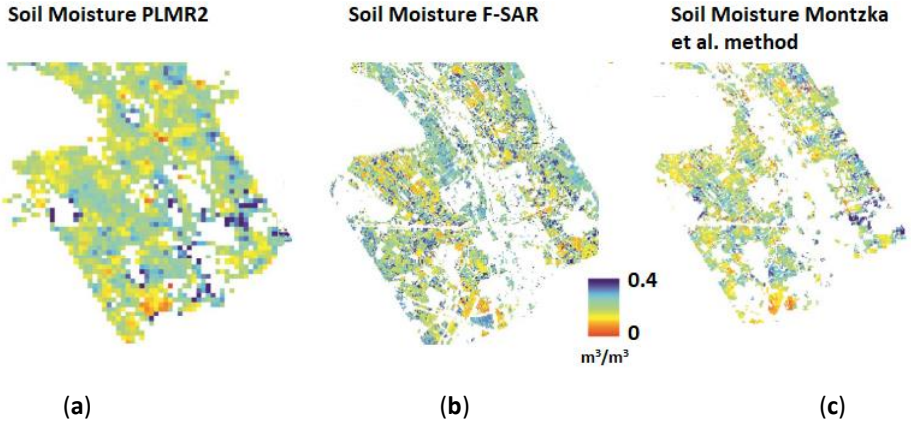

Figure 3.18 Soil moisture estimation results obtained using a single-source retrieval from (a) PLMR2, (b) F-SAR, and (c) using the active/passive L-band microwave fusion method proposed by Montzka et al. in [149]. Results for the Juelich area for April 17th, 2013. Adapted from [149].

A few months after the SMAP launch, on July 2015, its radar stopped transmitting and became inoperable (Section 2.3.2). Consequently, the generation of the high-resolution SM product was compromised. To restart the production of this SM product, it was proposed to substitute the SMAP radar with Sentinel-1A/B SAR data. Sentinel-1 was selected due to its nearly similar orbit configuration, allowing a swath overlap with a minimal time difference. However, three main aspects needed to be taken into consideration to adapt the previous version of the downscaling algorithm (Equation (3.23)) to work with Sentinel-1 data: (i) Sentinel-1 operates in C-band while SMAP operates in L-band; (ii) Sentinel-1 has multiple incidence angles while SMAP operates at a constant 40°; and (iii) Sentinel-1 has a ~250-km swath width, while SMAP's is 1000 km. Equation (3.23) was modified to work in emissivity instead of T_B, and with Sentinel-1 backscatter ($\sigma_{0_{VV}}(MR_j)$, $\sigma_{0_{VV}}(CR)$, $\sigma_{0_{VH}}(CR)$, $\sigma_{0_{VH}}(MR_j)$) in linear scale. The SMAP/Sentinel-1 active/passive algorithm becomes:

$$T_{B_v}(MR_j) = \left\{ \frac{T_{B_v}(CR)}{T_s} + \beta'(CR)\left\{\left[\sigma_{0_{VV}}(MR_j) - \sigma_{0_{VV}}(CR)\right] + \Gamma \cdot \left[\sigma_{0_{VH}}(CR) - \sigma_{0_{VH}}(MR_j)\right]\right\}\right\} \cdot T_s \tag{3.25}$$

where $\Gamma[-]$ is calculated as in Equation (3.23), but in linear scale. Due to the missing synchronization between the SMAP and Sentinel-1 orbits, the statistical estimation of $\beta'(CR)$ could include periods in which the vegetation and roughness conditions do not remain constant. To alleviate this problem, Jagdhuber et al. [150] proposed a snapshot approach to estimate $\beta'(CR)$, from every overlap between the SMAP and Sentinel-1 observations as follows:

$$\beta'(CR) = \frac{\frac{T_{B_V}}{T_s} - (\gamma + (1-\omega)(1-\gamma))}{\sigma_{0_{VV}}(MR_j) - \Gamma \cdot \sigma_{0_{VH}}(MR_j)} \tag{3.26}$$

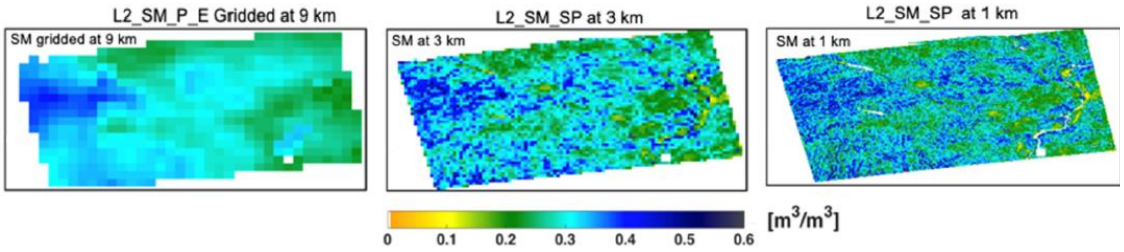

(**a**) (**b**) (**c**)

Figure 3.19 Comparison of retrieved SM in Southern Iowa, May 5th, 2018. From left to right: (a) SM obtained from the SMAP radiometer at 9 km, and SM obtained at a spatial resolution of (b) 3 km and (c) 1 km using the SMAP/Sentinel-1 Active/Passive algorithm. Adapted from [117].

Due to the high spatial resolution of the backscatter provided by Sentinel-1, it is possible to retrieve the SM at 3-km or even 1-km scales (Figure 3.19). In [117] Das et al. presented this new version of the algorithm and its performance was tested by comparing the resulting high-resolution SM maps with the *in situ* SM measurements provided by core validation sites (e.g., REMEDHUS, VAS, Yanco), and including different land covers. It was concluded that the resulting high-resolution SM achieved good accuracy (unbiased Root Mean Square Error (uRMSE) ≤0.05 m^3/m^3) and that this product was capable of capturing sharp and large-contrast features below the radiometer resolution. Still, the SMAP/Sentinel-1 SM product has a slightly degraded accuracy and less frequent revisit than the product obtained with radiometer data only.

3.1.3 Model/data-based downscaling techniques and outlook

Among the model/data-based downscaling techniques, there is currently an explosive growth of algorithms based on the application of machine learning techniques to multi-sensor data (see Figure 3.20). Machine learning allows to relate SM to different meteorological, hydrological and topographic variables from training data, in an empirical and nonlinear way, without requiring prior knowledge of the physical behavior of the land surface processes. Soil moisture disaggregation using machine learning techniques includes a variety of algorithms such as Artificial Neural Network (ANN) [34], Support Vector Machine (SVM) [35], Relevance Vector Machine (RVM) [36,37], Random Forest (RF) [38], boosted regression trees (BRT) [39], and Cubist approaches (CUB). The resulting SM data [151,152] complements the satellite-based and model-derived datasets. Although these approaches have not been the focus of this Thesis, a brief discussion of main contributions to the field are included hereafter as a review of state-of-the-art, for completion. As stated in Section 1.1, this Thesis focuses in techniques based upon physics for exploitation of multi-sensor synergies and process understanding, for which both machine learning and physically based approaches could be ultimately linked [40].

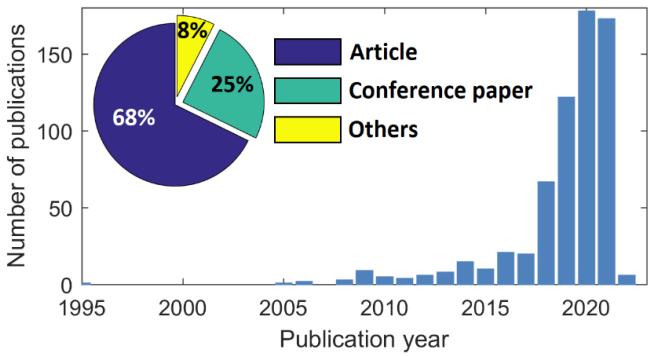

Figure 3.20 Number of publications in the Scopus [153] database for a general search on "machine learning" and "soil moisture". The category 'Others' includes: review, book chapter, data paper and erratum.

Srivastava et al. evaluated the performance of ANN, SVM and RVM machine learning techniques, applied to downscale SMOS SM [154]. Their work concluded that ANN substantially outperformed SVM and RVM, improving the data quality and providing higher spatial resolution compared to the original SMOS data. A similar analysis was conducted by Im et al. [155], where the performance of three machine learning approaches (RF, BRTs and CUB) was evaluated when disaggregating the AMSR-E SM from 25 km to 1 km, using MODIS products. Random forest outperformed the other approaches, obtaining a correlation (R) value ~0.95-0.97 and a RMSE ~0.024-0.027 m^3/m^3, including two study regions (South Korea and Australia).

A recent study presented by Vergopolan et al. [119] introduces the SMAP-HydroBlocks product, which is a high-resolution satellite-based soil moisture dataset at 30-m resolution (2015-2019) across the conterminous United States. It uses a cluster-based scheme to merge high-resolution land surface modeling, radiative transfer modeling, machine learning, SMAP satellite microwave data, and *in situ* observations, to generate a 30-m high-resolution SM

dataset across United States. The resulting dataset was evaluated over 1,192 observational sites showing a median correlation of 0.73±0.13, outperforming SMAP baseline products.

In summary, great progress has been made in the development of SM disaggregation techniques. This allows to downscale SM from the original resolution of the microwave sensor to resolutions of a few kilometers or even tens of meters, which may allow the use of the resulting SM maps for regional scale applications. The results obtained with some of the downscaling techniques presented in this section do not necessarily perform better than the SM retrieved with the radiometer- or radar-only methods, but instead, in most cases, disaggregated maps are able to capture more spatial details.

3.2 Datasets used throughout this Thesis

The following subsections describe the complete datasets, products and variables used throughout this Thesis (see Table 3.1). Coastal areas have been discarded in most of the results to screen out the effect of sea-land contamination (excluding the clay fraction and land cover maps).

3.2.1 SMOS data

Two SMOS L3 T_B products were produced at BEC facilities and used in this Ph.D. Thesis. They were obtained by quality-filtering the operational ESA SMOS L1C T_B product, ensuring that measurements were not affected by any Radio Frequency Interference (RFI), neither center nor tails. Resulting data were corrected by the geometry of the antenna plane, the Faraday rotation due to the ionosphere, and the atmospheric effects. Later, they were linearly interpolated to the selected incidence angles (32.5°, 42.5° and 52.5°) by least squares using all observations in a range of ±5° with respect the desired angle, and gridded into a 25-km and a 12.5-km EASEv2 mesh. In the maps at 12.5 km, pixels with data gaps within the orbit swath were filled with an inverse-distance weighting interpolation of T_B values at a distance lower than 2 pixels. Then, daily maps of surface T_{B_V} and T_{B_H} at three different angles —32.5° (±5°), 42.5° (±5°) and 52.5° (±5°)— were obtained. Figure 3.21 compares the BEC SMOS T_{B_V} at both 12.5 km and 25 km grids.

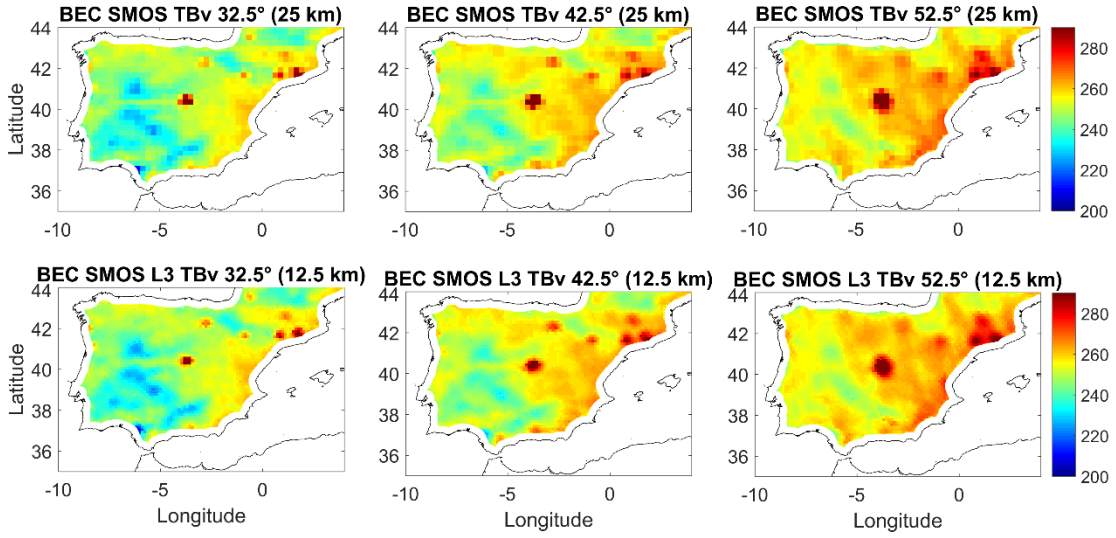

(a) (b) (c)

Figure 3.21 Temporally-averaged maps of daily BEC SMOS T_{B_V} for the Iberian Peninsula for January 2018. Results were obtained at different incidence angles: (a) 32.5°, (b) 42.5°, and (c) 52.5°. Data were gridded into a 25-km (first row) and a 12.5-km (second row) EASEv2 grid.

Two SM products produced and distributed by the BEC have been used in this work:

- The BEC SMOS L3 SM product, version 3. It is obtained by filtering and binning ESA SMOS L2 SM, producing daily SM maps in a 25-km EASE2v2 grid by a weighted average. Filtering consists of discarding grid points with failed retrievals, affected by RFI, without geophysical sense, or with a Data Quality Index (DQX) value greater than 0.07 m^3/m^3. A DQX-weighted average is applied to bin the data from Icosahedral Snyder Equal Area (ISEA) to the 25-km EASEv2 grid [156] (Figure 3.22a).

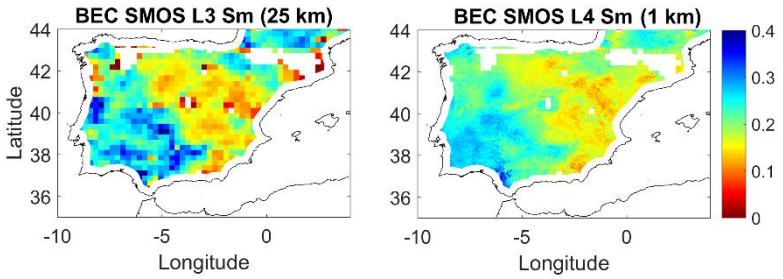

(a) (b)

Figure 3.22 Temporally-averaged maps of daily (a) BEC SMOS L3 SM (25 km) and (b) BEC SMOS L4 SM (1 km), for the Iberian Peninsula for January 2018.

- The BEC SMOS L4 SM, version 5. It is a SMOS-based disaggregated SM with an enhanced spatial resolution [156]. This SM product is generated following the methodology presented in Chapter 4, using the following input parameters: daily BEC SMOS L3 SM at 25-km EASEv2; daily SMOS L1 T_B at 25-km EASEv2; daily skin temperature at 12 h at around 9 km, which is provided by the operational ECMWF model; and 16-day Terra

MODIS NDVI at 1 km. The final SM product is provided in a 1-km EASEv2 grid (Figure 3.22b). Note that this is the high-resolution SM product used in Chapter 5.

Note that the corresponding flags provided for each product have been used to rule out observations that are not of acceptable quality, including pixels affected by RFI, pixels where the SM retrieval algorithm was not successfully applied or pixels where the retrieved geophysical data are outside the extended range [156].

3.2.2 SMAP & Sentinel-1 data

Three SMAP datasets are used in this Thesis (morning passes exclusively):

- The SMAP L2 Radiometer (SMAP L2), version 6 [48]. It is a radiometer-only based SM product derived directly from the SMAP Level-1C T_B (SMAP L1C T_B) product in a 36-km EASEv2 grid. To obtain the SMAP L2 SM from the SMAP L1C T_B, the SCA at vertical polarization (SCA_V) is used. In this Thesis both SMAP L1C T_B and SMAP L2 SM (see an example in Figure 3.23a) have been used.

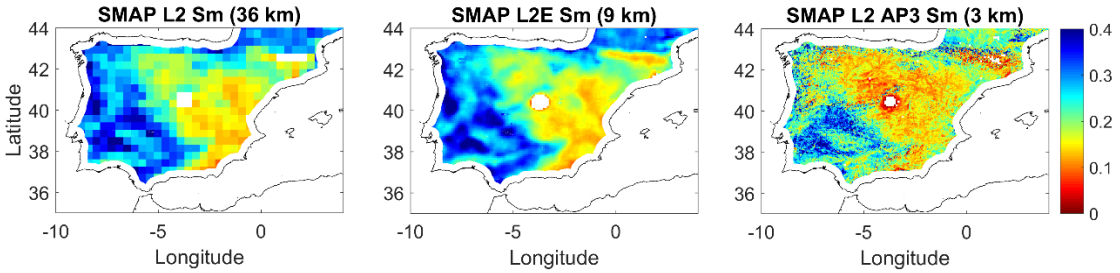

(**a**) (**b**) (**c**)

Figure 3.23 Temporally-averaged maps of daily (a) SMAP L2 SM (36 km), (b) SMAP L2E SM (9 km), and (c) SMAP L2 AP3 SM (3 km), for the Iberian Peninsula for January 2018.

- The SMAP Enhanced L2 Radiometer (SMAP L2E), version 5 [157]. It is the result of extracting the maximum information from the SMAP antenna by taking advantage of the SMAP radiometer oversampling, to generate an enhanced radiometer-based SM product, posted in a 9-km EASEv2 grid. The SMAP L2E dataset contains the SM and all the ancillary data required to estimate this variable from the radiometer measurements —e.g., ω, h_s, τ, VWC and T_s. In this work, the SM (see an example in Figure 3.23b), the τ at nadir and the T_s (see an example in Figure 3.24) provided in a 9-km EASEv2 grid have been used.

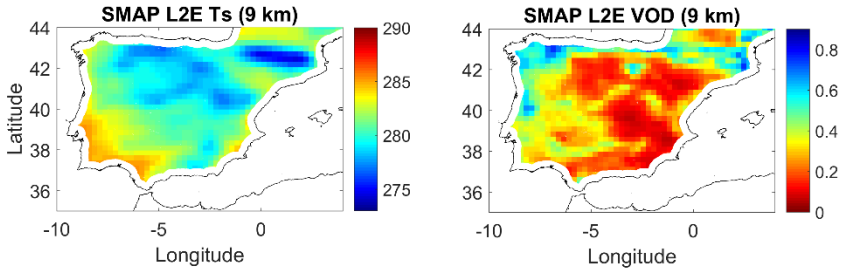

(**a**) (**b**)

Figure 3.24 Temporally-averaged maps of daily (a) SMAP L2E T_s (9 km), and (b) SMAP L2E τ (9 km), for the Iberian Peninsula for January 2018. Note that VOD stands for Vegetation Optical Depth.

- The SMAP/Sentinel-1 L2 Radiometer/Radar (SMAP L2 AP), version 3 [158]. It contains estimates of the land surface conditions obtained by combining passive SMAP ascending and descending half-orbit passes, and active information from the Sentinel-1A and -1B SAR [158]. A part from the resulting T_B and the retrieved SM provided in a 1-km and 3-km EASEv2 grids; this dataset contains the ancillary data required to calculate these two variables. In fact, the Sentinel-1 backscatter (σ_0), the VWC, the τ and the T_s provided in a 1-km EASEv2 grid within the SMAP files, are employed in this Thesis (see examples in Figure 3.25 and Figure 3.26). The Copernicus Project Sentinel-1A and Sentinel-1B data [159] used in this study are specifically the data acquired under the Interferometric Wide Swath (~250-km swath width) mode, which provides C-band co-pol (VV) and cross-pol (VH) backscatter observations, at multiple incidence angles. The reason for using this specific version is that the high-resolution (~25 m) Sentinel-1A/1B observations are conveniently pre-processed by the SMAP team with tailored calibration, noise subtraction, and terrain correction. These data are also filtered, using a hybrid spatial filtering [117] to remove the effect of urban and manmade structures, and aggregated from the ~25-m native resolution to the SMAP 1-km grid.

Note that the SMAP SM used in this Thesis is that retrieved using the SCA, which was the original postlaunch baseline algorithm for the SMAP mission from 2015 to 2021. In the same way as for SMOS, the corresponding flags provided for each product have been used to rule out observations that does not have acceptable quality.

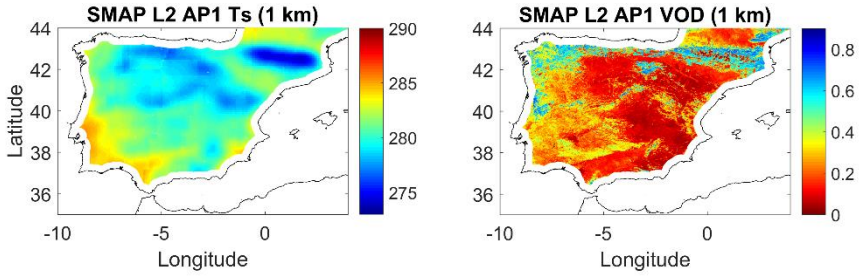

Figure 3.25 Temporally-averaged maps of daily (a) SMAP L2 AP1 T_s (1 km), and (b) SMAP L2 AP1 τ (1 km), for the Iberian Peninsula for January 2018. Note that VOD stands for Vegetation Optical Depth.

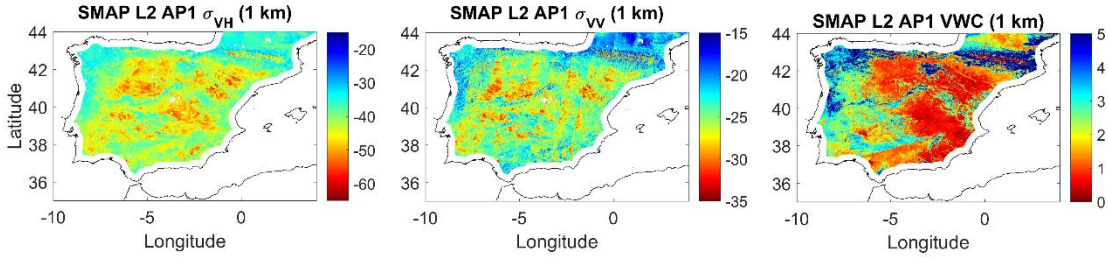

Figure 3.26 Temporally-averaged maps of daily (a) SMAP L2 AP1 $\sigma_{0,dB_{VH}}$ (1 km), (b) SMAP L2 AP1 $\sigma_{0,dB_{VV}}$ (1 km), and (c) SMAP L2 AP1 VWC (1 km), for the Iberian Peninsula for January 2018.

The SMAP clay fraction map, presented in Figure 3.27, has also been used in this Thesis. It is provided by the National Snow and Ice Data Center (NSIDC) in a 9-km EASEv2 grid within the SMAP L4 Global 9-km EASE-Grid Surface and Root Zone Soil Moisture Land Model Constants, Version 5 (SMAP L4 LMC) [160].

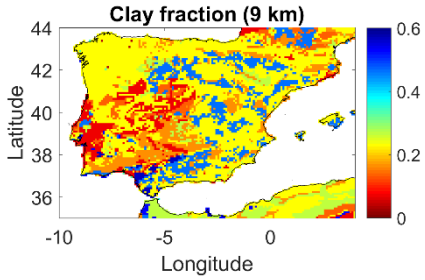

Figure 3.27 Static map of clay fraction for the Iberian Peninsula.

3.2.3 MODIS data

Data measured by the MODIS instrument onboard of the Terra and Aqua spacecrafts are also used in this work: Terra NDVI (MOD13A2 version 5) [161] provides information of the vegetation conditions, while Aqua T_S (MYD11A1 version 5) [162] measures the temperature of the first millimeters of the soil. These maps are generated and distributed with a spatial resolution of 1 km, and a periodicity of 16 days and 1 day, for NDVI and T_S, respectively. A recent study suggested that the daily maximum T_S might provide a better representation of the SM/T_S relationship than the instantaneous T_S [163]. This study uses the day-time Aqua MODIS T_S since it is closer (in time) to the daily maximum T_S than other available MODIS products [164]. These two products (Figure 3.28) are provided by the U.S. Land Processed Distributed Active Archive Center (LPDAAC).

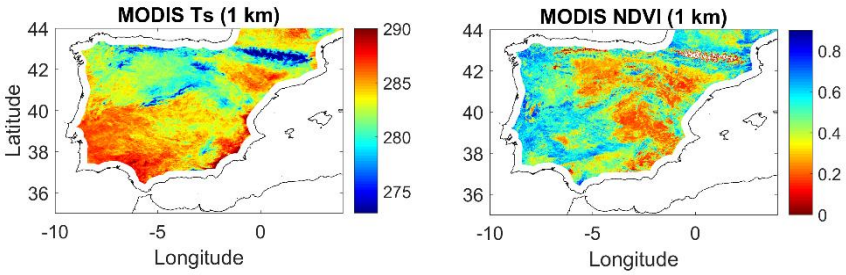

Figure 3.28 Temporally-averaged maps of daily (a) MODIS T_S (1 km) at day-time, and (b) MODIS NDVI (1 km), for the Iberian Peninsula for January 2018.

In addition, LPDAAC distributes the combined Aqua+Terra MODIS land cover product (MCD12Q1 version 6), that provides annual land cover maps with a spatial resolution of 500 m [165] (Figure 3.29a). This work uses the MODIS International Geosphere-Biosphere Programme-Land Cover (IGBP LC). This classification contains 17 classes based on three canopy components: above ground biomass (perennial and annual), leaf longevity (evergreen and deciduous), and leaf type (needleleaf, broadleaf and grasses). These are critical variables for seasonal climate and carbon-balance modeling, carbon cycle and land energy transfer, and for explaining gas exchange characteristics [166].

3.2.4 ESA CCI data

Long-term global data records are being developed as part of ESA's CCI, to support climate studies with observational records across oceans, atmosphere and land. The ESA CCI program includes a variety of biological, physical, and chemical variables known as ECV. The CCI LC provides information on the geographical distribution of global land cover at a resolution of 300 m [167]. This LC map has been used in this research as ancillary data (Figure 3.29b).

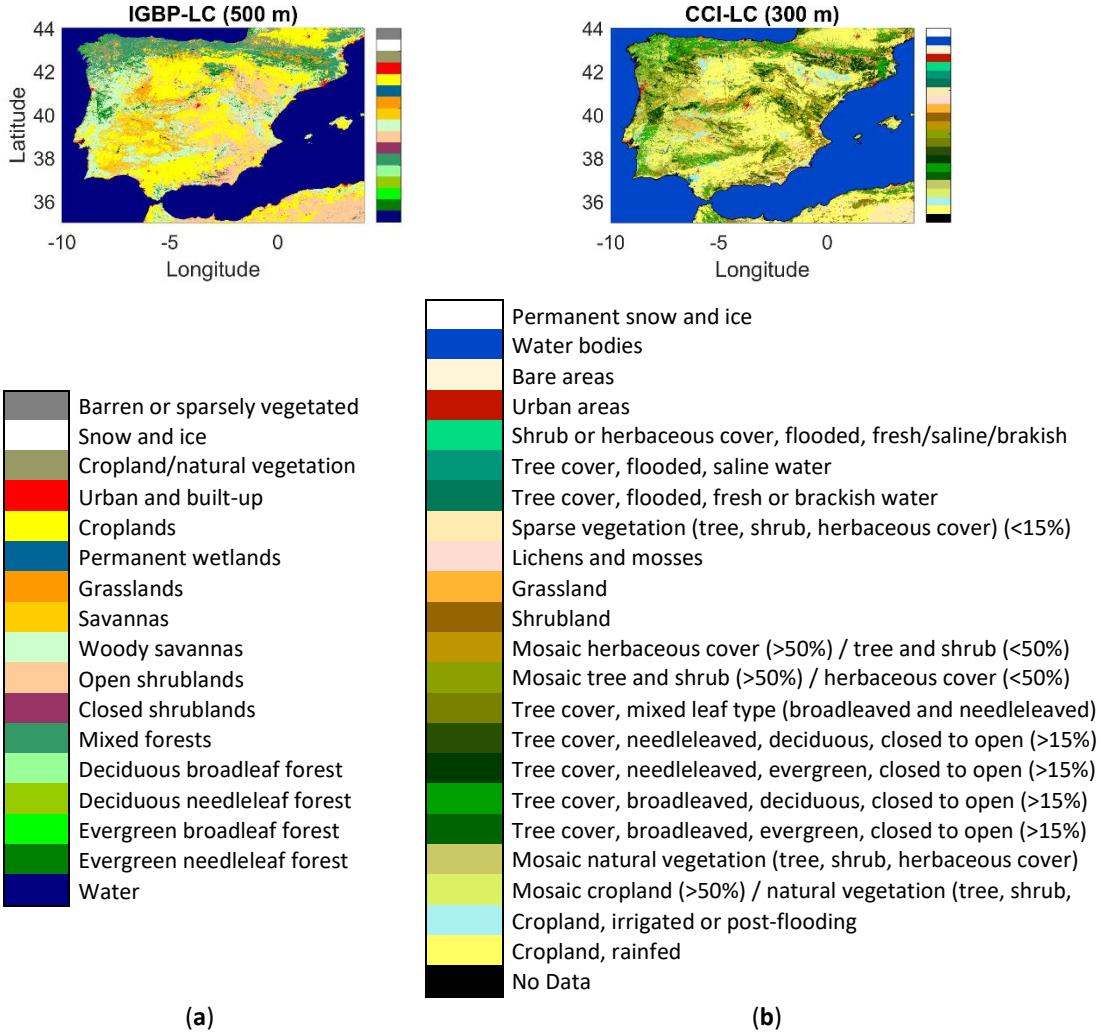

Figure 3.29 Land cover maps for 2018 obtained from: (a) the ESA CCI, and (b) MODIS defined by the IGBP.

3.2.5 ECMWF data

A. ERA5

ERA5 provides hourly estimates of several atmospheric, land and oceanic climate variables, in a 30-km grid, for the period from 1979 to present. ERA5 combines a large number of historical observations [168] into global estimates using advanced modelling and data assimilation systems. The ERA5 T_s L1 at 12 h [169] is used in this work (Figure 3.30a).

B. ERA5-land

ERA5-land is a dataset obtained through global high-resolution numerical integrations of the ECMWF land surface model driven by the downscaled meteorological forcing from the ERA5 climate [170]. ERA5-land describes 53 variables related to the water and energy cycles over land, with global coverage at a spatial resolution of 9 km, providing hourly information for the period

from 1981 to present. In this study, the ERA5-land volumetric soil water content at 06:00 AM (local time) of the soil layer 1 (0-7 cm) is used (Figure 3.30b).

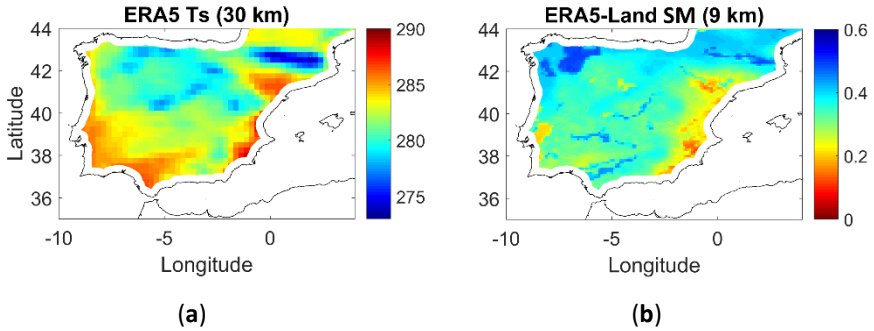

Figure 3.30 Temporally-averaged maps of daily (a) ERA5 T_s (30 km) at 12:00 PM, and (b) ERA5-Land SM (9 km) at 06:00 AM (local time), for the Iberian Peninsula for January 2018.

3.2.6 REMEDHUS SM network

REMEDHUS [77] is a SM *in situ* network located in the central area of the Duero Basin, in Spain (Figure 3.31). This is a nearly flat region, where a continental semi-arid Mediterranean climate predominates. The land is mainly cultivated with rainfed cereals, although patchy areas of forest-pasture, irrigated crops, vineyards and fallow can also be found. The REMEDHUS network is composed of 22 stations equipped with Hydra Probes that provide hourly SM measurements [6] and four automatic weather stations that measure precipitation, air temperature, relative humidity, wind speed, and solar radiation. *In situ* SM measurements are performed at different soil depths, but in this study, it has been exclusively used the topsoil data at 5 cm depth and the daily rainfall data from the weather stations. REMEDHUS SM network has served for several purposes [77]: (i) calibration and validation campaigns [171]; (ii) validation and parametrization of water balance models [172]; (iii) evaluation of SM products obtained through remote sensing [27,46,173,174]; and (iv) perform SM experiments at different scales and methodologies [175]. REMEDHUS is part of the International Soil Moisture Network (ISMN) [6]. Figure 3.32 shows the location of three *in situ* SM stations (Paredinas, Cañizal and Las Vacas) belonging to the REMEDHUS network.

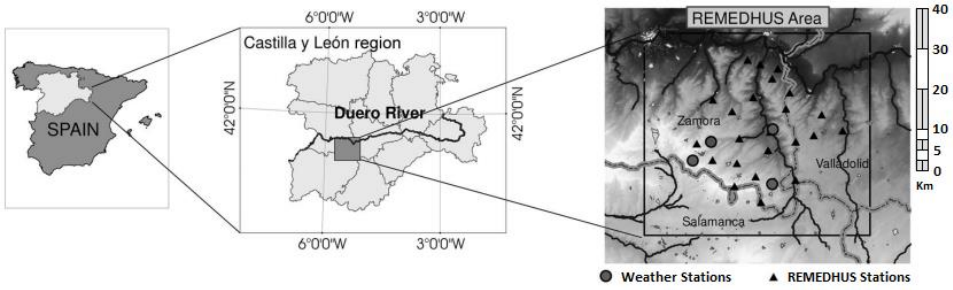

Figure 3.31 Location of the REMEDHUS network in Spain. Adapted from [77].

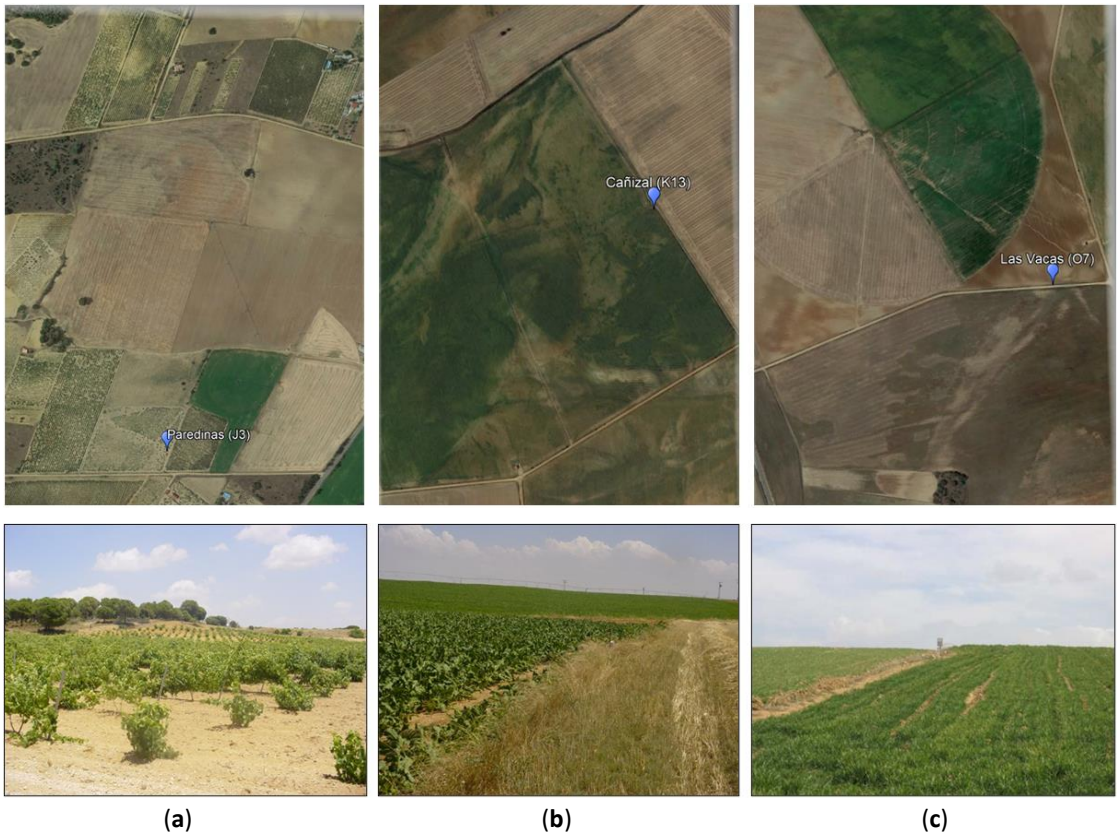

(**a**) (**b**) (**c**)

Figure 3.32 Location of three SM *in situ* station belonging to the REMEDHUS network: (a) Paredinas (vineyard), (b) Cañizal (irrigated), and (c) Las Vacas (rainfed).

3.2.7 OzNet SM network

The OzNet network sits within the 82000-km^2 Murrumbidgee River Catchment in New South Wales, Australia (Figure 3.33). There are seven SM monitoring sites distributed across the northern and eastern fringe of the Murrumbidgee Catchmen, in addition to those associated with the Yanco, Kyeamba Creek, and Adelong Creek sites. In this work, only the 5-cm depth SM information provided by the stations located over Yanco is used. This is a flat 60 × 60-km^2 area that contains much of the Coleambally Irrigation District and has not much woody vegetation. The west of the region contains irrigation fields, mainly rice and barley fields. Elsewhere the land is used as dry land cropping in the north, and native pasture in the south east [176]. There are 37 SM stations around the Yanco region, with two different types of stations. First stations were added in 2006 and the second ones were added in August 2009 as part of the Australian contribution to the SMAP mission for the calibration and validation of the satellite. OzNet SM network has served for several purposes: (i) the validation and development of land surface models [177]; (ii) the assessment and validation of remote sensing data [178–180]; and (iii) other airborne validation and calibration experiments [181]. OzNet is part of the ISMN network [6].

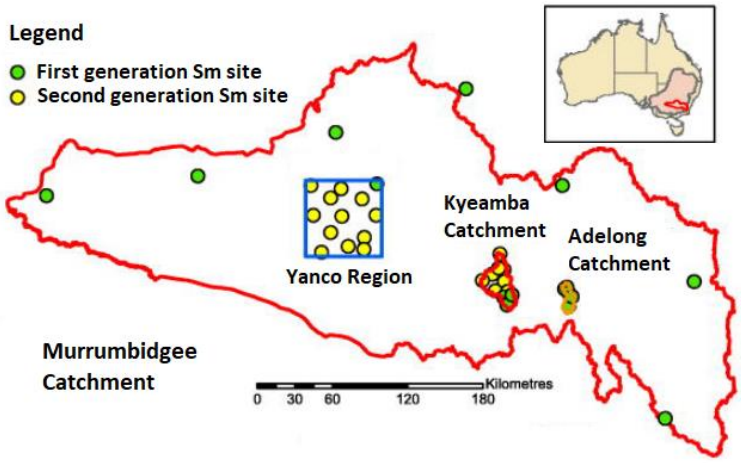

Figure 3.33 Location of the Murrumbidgee SM monitoring network in Australia. First- and second-generation sites are indicated by green and yellow dots, respectively. The three Murrumbidgee sites are displayed: Yanco, Kyeamba and Adelong. Adapted from [176].

Table 3.1 Summary of the data used in this study. * Provided by the Water Resources Research group of the University of Salamanca.

Source	Variable	Product	Spatial Frequency	Temporal Frequency	Reference
SMOS	SM	BEC SMOS L3	25 km	Daily	[156]
		BEC SMOS L4	1 km	Daily	[156]
	T_B	BEC SMOS L3	25/12.5 km	Daily	[156]
SMAP	SM	SMAP L2	36 km	Daily	[48]
		SMAP L2E	9 km	Daily	[157]
		SMAP AP3	3 km	Daily	[158]
		SMAP AP1	1 km	Daily	[158]
	T_B	SMAP L1C	36 km	Daily	[48]
	tau	SMAP L2E	9 km	Daily	[157]
		SMAP L2 AP1	1 km	Daily	[158]
	T_s	SMAP L2E	9 km	Daily	[157]
		SMAP L2 AP1	1 km	Daily	[158]
	VWC	SMAP L2 AP1	1 km	Daily	[158]
	σ_0	SMAP L2 AP1	1 km	Daily	[158]
	CF	SMAP L4 LMC	9 km	Static	[160]
MODIS	T_s	MYD11A1 v5	1 km	Daily	[162]
	NDVI	MOD13A2 v5	1 km	16-Day	[161]
	LC	MCD12Q1 v6	500 m	Annually	[182]
ECMWF	T_s	ERA5	30 km	Hourly	[168,169]
	SM	ERA5-land	9 km	Hourly	[170]
CCI	LC	CCI	300 m	Annually	[183]
REMEDHUS	SM	REMEDHUS	*In situ*	Hourly	[77]
	Precipitation	REMEDHUS	*In situ*	Hourly	*
OzNet	SM	OzNet	*In situ*	Hourly	[176]

Chapter 4

A downscaling approach for SMOS based on an adaptive moving window

In this chapter, a passive microwave/optical downscaling algorithm for SMOS is proposed to obtain high-resolution SM maps (1 km) from the native resolution (~40 km) of the instrument. This algorithm introduces the concept of a shape-adaptive window as an extension of the disaggregation technique presented by Piles et al. [46], enabling its application at continental scale. The approach is based on the "universal triangle" concept, which relates SM with NDVI and T_S. The downscaling technique presented in this chapter uses the T_B from SMOS, the NDVI provided by MODIS and the T_S from two different possible sources, either MODIS or ERA5, resulting in two different version of the algorithm: (i) the "MODIS" version, which takes advantage of the high resolution (1 km) provided by optical-based sensors such as MODIS but being highly affected by cloud coverage; and (ii) the "cloud-free" version, which uses ERA5 T_S obtained through the combination of historical observations into global estimates using advanced modelling and data assimilation systems [184], providing full coverage under all weather conditions but with a 30-km spatial resolution. The proposed methodology: (i) ensures the resulting high-resolution SM maps maintain the dynamic range of the original L3 product; (ii) minimizes the differences between the resulting high-resolution SM maps aggregated to a 25-km EASEv2 grid and the BEC SMOS L3 SM maps; (iii) can be applied to continental areas, even when they integrate different climates; and (iv) is a simple algorithm, easy to implement and fast to run.

The data used in this chapter are presented in Section 4.1. Section 4.2 details the methodology followed to implement the new downscaling technique and to validate the resulting SM maps. Main results are shown in Section 4.3, and conclusions are conveyed in Section 4.4.

4.1 Datasets

Table 4.1 summarizes the data used in the development of the new downscaling algorithm presented in this chapter, including information from SMOS (T_B and SM), MODIS (T_S and NDVI), ECMWF (T_S), and from the REMEDHUS and OzNet *in situ* networks (SM). All these products are described in detail in Section 3.2.

Table 4.1 Summary of the data used in this chapter.

Source	Variable	Product	Spatial Frequency	Temporal Frequency	Reference
SMOS	SM	BEC SMOS L3	25 km	Daily	[156]
	T_B	BEC SMOS L3	25/12.5 km	Daily	[156]
MODIS	T_S	MYD11A1	1 km	Daily	[162]
	NDVI	MOD13A2	1 km	16-Day	[161]
ECMWF	T_S	ERA5	30 km	Hourly	[168,169]
REMEDHUS	SM	REMEDHUS	*In situ*	Hourly	[77]
OzNet	SM	OzNet	*In situ*	Hourly	[176]

4.2 Methodology

4.2.1 Downscaling approach

The downscaling algorithm presented in this chapter is an extension (revision 2) of the algorithm described in [46] by Piles et al. (revision 1). The model links the T_B at horizontal and vertical polarization, T_S, and NDVI, with SM, through the linear Equation (4.1). The flowchart of Figure 4.1 shows that Equation (4.1) is used twice in the algorithm at both low resolution and high resolution.

$$m_v = b_0 + b_1 NDVI^* + b_2 T_s^* + \frac{b_3}{3}\sum_{i=1}^{3} T^*_{B_{V,\theta_i}} + \frac{b_4}{3}\sum_{i=1}^{3} T^*_{B_{H,\theta_i}} \tag{4.1}$$

where b_k are the regression coefficients, T_S* is the normalized surface temperature, NDVI* is the normalized NDVI, and $T^*_{B_{V,\theta_i}}$ and $T^*_{B_{H,\theta_i}}$ are the normalized T_B at vertical and horizontal polarizations, respectively, at the incidence angles 32.5°, 42.5° and 52.5°. The normalization of the variables has been carried out using their maximum and minimum values that depend on the study area and orbit (ascending or descending):

$$X^* = \frac{X - X_{min}}{X_{max} - X_{min}} \tag{4.2}$$

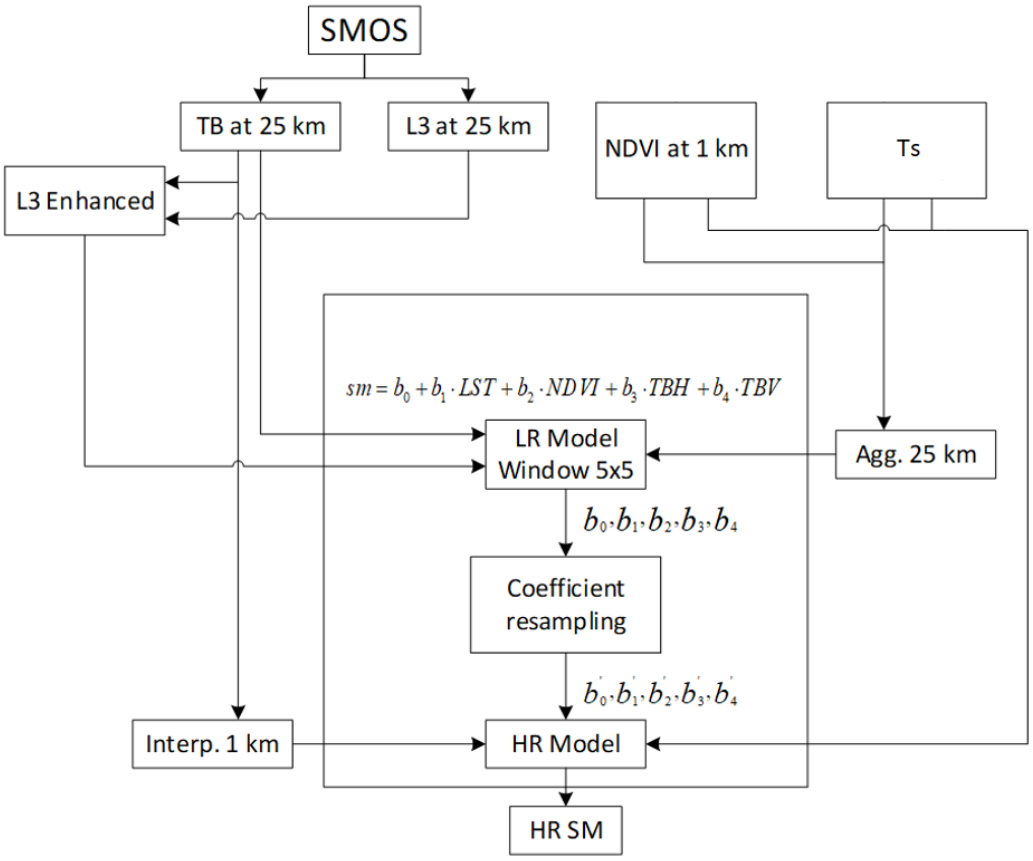

Figure 4.1 SM disaggregation procedure. It is a three-step method, which consist of: (i) generating the enhanced SMOS L3 SM maps, (ii) calculating the linear equation coefficients and (iii) retrieving the high-resolution SM maps.

The flowchart presented in Figure 4.1 shows the steps applied in the new algorithm, which are summarized in the following three points:

1- Generation of the enhanced SMOS L3 SM maps.

In this version of the algorithm, the BEC SMOS L3 SM has been replaced by the enhanced SMOS L3 SM, in which pixels without SM data are estimated using a simple linking model:

$$m_v(LR) = a_0 + \frac{a_2}{3}\sum_{i=1}^{3} T^*_{B_{V,\theta_i}} + \frac{a_3}{3}\sum_{i=1}^{3} T^*_{B_{H,\theta_i}} \quad (4.3)$$

where $m_v(LR)$ is the low-resolution SM (BEC SMOS L3 SM), and a_k are the regression coefficients. First, the model is applied using BEC SMOS L3 T_B and BEC SMOS L3 SM as a reference to obtain the a_k coefficients. Once the regression coefficients have been obtained, they are used in conjunction with T_B for estimating low-resolution SM in areas where the original BEC SMOS L3 SM is not providing information. Figure 4.2 shows an example of this first step.

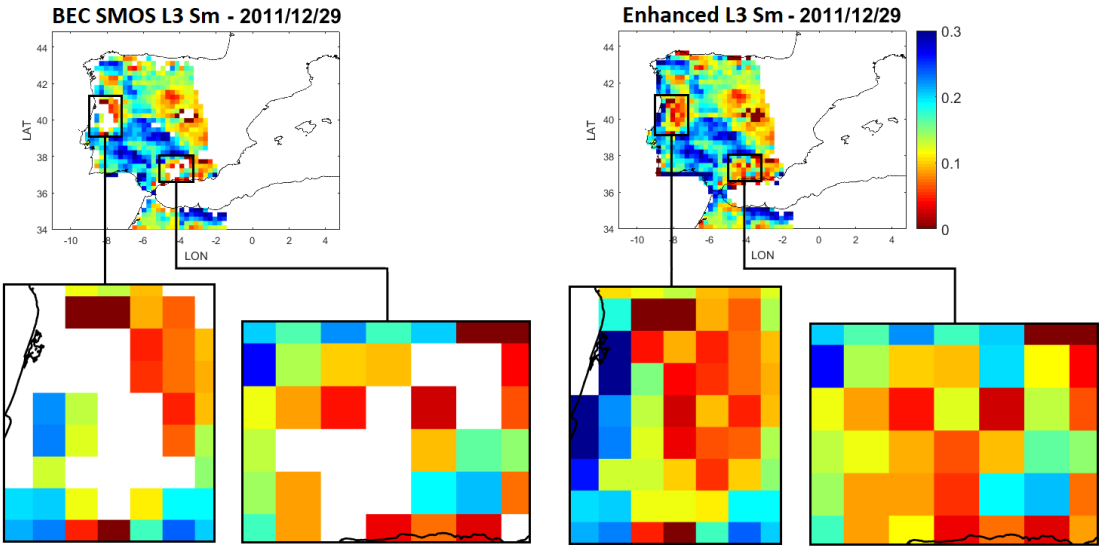

Figure 4.2 (a) Original BEC SMOS L3 SM product and (b) enhanced SMOS L3 SM after applying Equation (4.3) for December 29th, 2011, for the Iberian Peninsula.

2- Calculation of the linear equation coefficients b_i.

Equation (4.1) is first applied at low resolution to obtain the b_i coefficients. Therefore, the MODIS NDVI and the T_S, either from MODIS or ERA5, are resampled to a 25-km EASEv2 grid. MODIS NDVI is aggregated from high resolution to low resolution, that is, from 1 to a 25-km EASEv2 grid. In case of using MODIS T_S, it is also aggregated from 1 to the 25-km EASEv2 grid, and in case of using ERA5 T_S (30 km) these maps are resampled to the 25-km EASEv2 grid. $T^*_{B_{V,\theta_i}}$ and $T^*_{B_{H,\theta_i}}$ are already at low resolution, that is, on a 25-km EASEv2 grid. The enhanced SMOS L3 SM (from the first step) is used as a reference to solve the linear system of equations (Equation (4.1)) and to obtain the b_i coefficients, using a least squares method.

The main innovation of the new algorithm with respect to revision 1, proposed by Piles et al. [46], is the size and shape of the spatial domain of its implementation. In revision 1, only one set of b_i coefficients was employed at a time for the whole study area. In the current version, the linking model is only applied over a local spatiotemporal adaptive moving window. Consequently, in the revision 2 presented in this chapter, a set of b_i coefficients is calculated for each low-resolution pixel. Then, it is used a shape-adaptive window that moves all over the study area [185], trying to keep as constant as possible the number of pixels of this moving window, even along the coast. For this purpose, two windows were defined: one of a fixed size (5 × 5 pixels) and the other shape-adaptive (9 pixels). A detailed explanation of how these two windows are defined and used can be found in Section 4.2.2.

Once a set of b_i coefficients is available for each low-resolution pixel, five maps will be stored, one for each coefficient. In order to avoid a "boxing effect"[1], these coefficient maps are linearly interpolated from the 25-km grid to a 1-km grid (see "Coefficient resampling" box in Figure 4.1).

3- High-resolution SM map retrieval.

The last step is to apply Equation (4.1) at high resolution using the b_i coefficients already stored at 1 km (see second step). In addition, $T^*_{B_{V,\theta_i}}$, $T^*_{B_{H,\theta_i}}$ and T_S (if it is not already in a 1-km grid) need to be linearly interpolated at 1 km, and meanwhile, NDVI is used at its original resolution of 1 km.

4.2.2 Optimal size of the adaptive moving window

The implementation of the downscaling technique presented in this chapter requires the definition of two windows: (i) a fixed square window that moves through the study region and is only used to delimit the area to which the second window can be extended; and (ii) an adaptive window (not necessarily symmetric) composed of a specific number of pixels which are the closest to a central one over which the square window (i) is defined.

The size of the fixed and the adaptive windows used by this new downscaling algorithm are crucial for obtaining accurate high-resolution SM maps (hereinafter referred to as SMOS L4 SM). In order to decide their optimal sizes, different values were tested and compared in terms of accuracy. The use of a very large window causes a loss of the SM dynamic range (Figure 4.3c), but a very small window is not capable of correctly capturing the information surrounding a particular pixel and, consequently, the coefficients obtained are not representative of the SM conditions.

In order to optimize the size of the two windows, the R and uRMSE obtained between the REMEDHUS *in situ* SM and the retrieved SMOS L4 SM maps were calculated for different window sizes, ranging from 5 to 45 pixels in steps of 5 pixels. The results of this first analysis revealed that the optimal number of pixels for the adaptive window, in terms of higher R and lower uRMSE, was around 10. Consequently, a second study was carried out, increasing the window from 5 to 17 pixels in steps of 1 pixel. The results are shown in Figure 4.4, where it can be seen that a window size between 8 and 10 pixels maximizes the R and minimizes the uRMSE. Based on these results, two windows were defined: (i) a 5 x 5-pixel fixed square moving window; and (ii) an adaptive window composed of 9 pixels. An odd number of pixels was chosen for both windows sizes for symmetry reasons.

[1] The boxing effect is defined as the outline of the low-resolution pixels visible in the high-resolution maps.

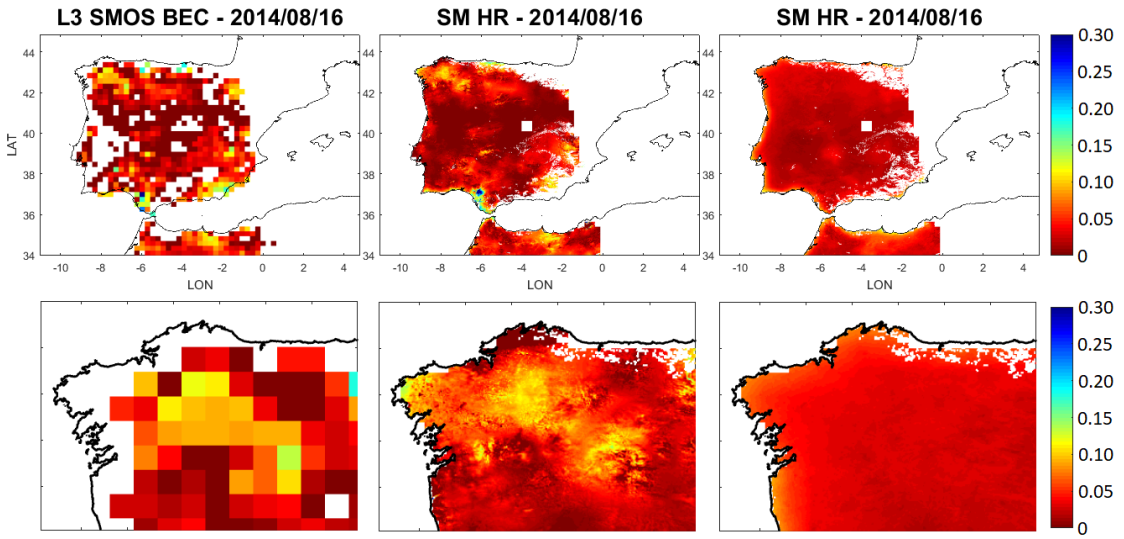

(**a**) (**b**) (**c**)

Figure 4.3 Soil moisture maps obtained for the region on Galicia (northwest of Spain) for August 16th,2014: (a) BEC SMOS L3 SM; (b) SMOS L4 SM map (1 km) after applying the new downscaling algorithm using an adaptive window of 9-pixels within a 5 x 5 coarse cell region; and (c) SMOS L4 SM map (1 km) after applying the new downscaling algorithm using an adaptive window of 534 pixels within 41 × 41 coarse cell region.

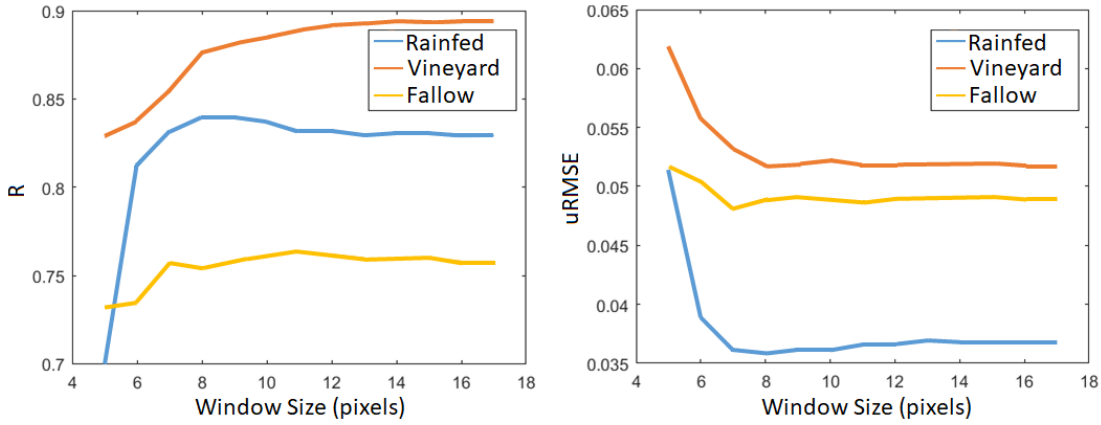

(**a**) (**b**)

Figure 4.4 (a) Correlation and (b) uRMSE for the different sizes of the adaptive window. The window was enlarged in 1-pixel steps, from 5 to 17 pixels. The study has been carried out for fallow (yellow), vineyard (orange) and rainfed (blue).

This method is shape-adaptive because the shape of the window is not constant. This means that when all the pixels are available within the fixed 5 x 5 window, the adaptive window (9 pixels) is symmetric and square (see the gray cells in Figure 4.5a). However, when not all the pixels within the 5 × 5 area are available, for example because some of them are affected by meteorological effects, RFI, or because they are located near the shoreline, the algorithm selects the 9 nearest pixels to a central one, modifying its shape (see the gray cells in Figure 4.5b and Figure 4.5c). Therefore, when possible, the algorithm will always try to use the same number of pixels to solve the system of equations, regardless of whether the window is located on the coast

or elsewhere inland. However, at least 5 available pixels with data are required to robustly solve the linking model.

(a) (b) (c)

Figure 4.5 The two windows used in the algorithm. The 5 × 5-pixel grid represents the constant-size window, the orange color represents land (available pixels), the blue color represents water (unavailable pixels), the dark gray cell is the selected central pixel, and the light gray cells are the additional pixels that compose the adaptive window. Three different cases are represented: (a) all the pixels within a 5 × 5 area are available; and (b and c) the shape of the adaptive window changes to get 9 pixels of information.

4.2.3 Two versions of the downscaling algorithm: the "MODIS" and the "cloud-free" version

The linking model presented in Section 4.2.1 relates $T_{B_{V,\theta_i}}$ and $T_{B_{H,\theta_i}}$, NDVI and T_S with SM to disaggregate the low-resolution SMOS SM maps from the original resolution of SMOS (~40 km) to 1 km. This downscaling technique uses the T_B from SMOS, the NDVI from MODIS, and the T_S from two possible different sources, MODIS or ERA5, resulting in two different version of the algorithm: (i) the "MODIS" version, which takes advantage of the high resolution (1 km) provided by optical-based sensors such as MODIS, but being highly affected by cloud coverage; and (ii) the "cloud-free" version, which uses ERA5 T_S obtained by combining historical observations into global estimates using advanced modelling and data assimilation systems [184], providing full coverage under all weather conditions but with a 30-km spatial resolution.

A. The "MODIS" version

The "MODIS" version was first tested using exactly the same input parameters as in the original version developed by Piles et al. [46]: the BEC SMOS L3 T_B, the BEC SMOS L3 SM, the MODIS NDVI and the MODIS T_S. This section is devoted first to explaining how the resulting SM estimates were validated against measurements provided by the REMEDHUS and OzNet SM networks and, second, to describe how the dynamic range, energy conservation and consistency of the resulting SMOS L4 SM maps were analyzed. The results regarding the "MODIS" version of the downscaling algorithm are presented in Section 4.3.1.

(1) Validation over REMEDHUS and OzNet SM networks

A validation exercise was conducted from 2012 to 2014 over the REMEDHUS site, in Spain (Figure 4.6). It aims to evaluate the agreement between the BEC SMOS L3 SM (25-km grid) and the SMOS L4 SM product (1-km spatial resolution) against *in situ* measurements, and to analyze the effect of the downscaling process on the SM accuracy. To do this, four statistical metrics were studied: R, RMSE, uRMSE , and bias [186]. Since the T_S maps used in the downscaling process can be affected by clouds masking the MODIS information, some pixels have no data and, consequently, SMOS L4 SM maps can have some data gaps. To avoid a possible different number of data samples and consistently compare the statistical results, the same number of samples were used for the BEC SMOS L3 and SMOS L4 SM maps. The results were grouped by land use (rainfed cereal, vineyard, fallow, forest-pasture, and irrigated) and by seasons (see Section 4.3.1A).

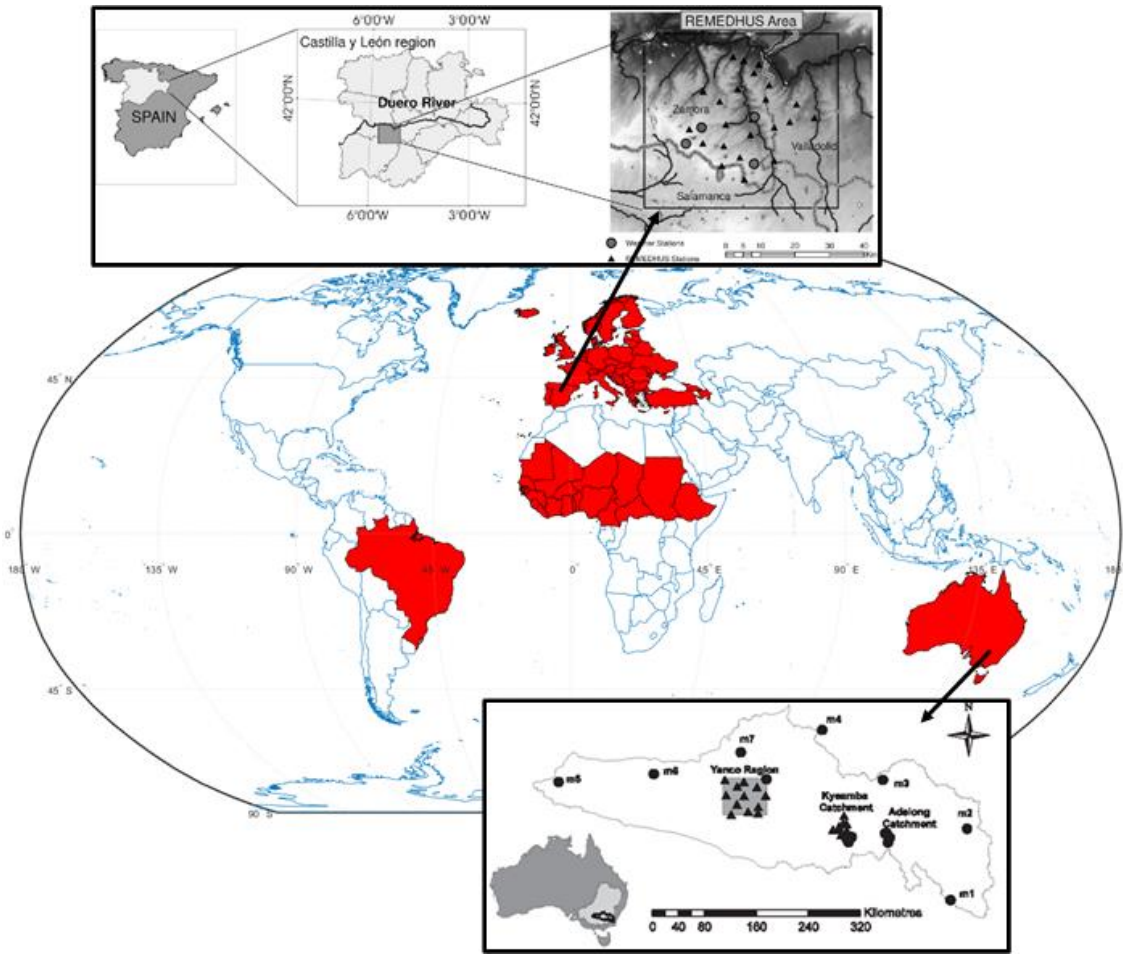

Figure 4.6 World map containing the study regions (in red) where the new downscaling technique was tested. A zoom over the Castilla y León, in Spain, and over New South Wales, in Australia, shows the location of the *in situ* SM networks used in this study.

A similar statistical analysis was carried out over the Yanco region (Australia), where the OzNet SM network is located (see Figure 4.6). Data from 11 different *in situ* stations was used. Registered values by these 11 stations were seasonally averaged for 2015 (see Section 4.3.1A).

(2) Dynamic range, energy conservation and consistency analysis

The dynamic range analysis tests the algorithm's capability to discern specific dry and wet areas while maintaining the SM range of the original BEC SMOS L3 SM product.

To study the energy conservation of the revision 1 of the algorithm presented by Piles et al. [46] and the new methodology proposed in this Thesis (revision 2), the high-resolution SM maps over the Iberian Peninsula (34—45° N, -11—5° W) were aggregated to the original 25-km sampling resolution and daily subtracted from the original (no downscaled) BEC SMOS L3 SM maps. This analysis was carried out for the years 2011, 2012, 2013 and 2014.

Both versions of the algorithm, revision 1 and the new one proposed in this chapter, are based on the "universal triangle" concept. They use a linking model to relate SMOS SM to MODIS NDVI and T_s. It was demonstrated that a unique relationship exists between SM, NDVI, and T_s for a given region under specific climatic conditions and land surface types [129]. Since the first revision by Piles et al. obtained a unique set of b_i coefficients for the whole study region, its application was restricted to areas with similar climate conditions. In this new version, a set of b_i coefficients per pixel is obtained using a shape-adaptive moving window and, therefore, the size of the study area is not a restriction. To evaluate the consistency of the algorithm, it was applied over two regions with different sizes (the largest area containing the smallest): the Iberian Peninsula (country size) and Europe (continental size). For this analysis, a temporal window of 9 days centered on March 20th, 2011, was used, which reduces the number of pixels without data due to the presence of clouds masking the optical data. A map of Europe and another of the Iberian Peninsula were obtained per day, and their values over the Iberian Peninsula were compared. Finally, their differences were averaged.

The dynamic range, energy conservation and consistency for SM maps obtained using the "MODIS" version of the downscaling algorithm are tested in Section 4.3.1B.

B. The "cloud free" version

The "cloud-free" version was developed with the purpose of obtaining high-resolution SM maps independent of meteorological effects. The resulting SMOS L4 SM maps where validated and compared using measurements provided by the REMEDHUS and OzNet SM networks, and the consistency and the energy conservation were tested over different locations around the world. The results regarding the "cloud free" version of the downscaling algorithm are presented in Section 4.3.2.

(1) Validation over REMEDHUS and OzNet SM networks

Regarding the validation within the REMEDHUS area, the results have been grouped for rainfed and vineyard land use, for the period from 2012 to 2014. Whereas 5 OzNet *in situ* stations (Y02, Y05, Y07, Y09 and Y11) were selected to validate the disaggregated SM maps over

the Yanco region, for 2015. For both REMEDHUS and Yanco study areas, a brief comparison between the "MODIS" and the "cloud-free" versions has been included (see Section 4.3.2A).

(2) Spatial coverage, energy conservation and consistency analysis

A brief comparison between the spatial coverage of the high-resolution SM maps of the "MODIS" and "cloud-free" downscaling versions has been added.

The energy conservation was studied for the Australian and European continents, for May 2015 and May 2016, respectively.

The consistency was tested in a North African region (6—21° N, -18—38° W), including the ecoclimatic and biogeographic zone of the Sahel, for January 2015; and in the eastern region of Brazil (-35—3° N, -80—-30° W), for July 2016.

The spatial coverage, energy conservation and consistency for SM maps obtained using the "cloud-free" version of the downscaling algorithm are tested in Section 4.3.2B.

4.3 Results

4.3.1 The "MODIS" version

A. Temporal analysis of SM: validation over REMEDHUS and OzNet SM networks

Table 4.2 summarizes the statistics derived from the temporal intercomparison of low- (BEC SMOS L3 SM) or high-resolution (SMOS L4 SM "MODIS" version) SM products with *in situ* SM measurements from REMEDHUS, using only the concurrent samples. Results are grouped by land use — rainfed cereal (RAI), vineyard (VIN), fallow (FAL), forest-pasture (FOP), and irrigated (IRR) — and by seasons. The worst results are obtained for irrigated and forest-pasture land use. This is because the number of samples obtained under these two land use regions is low (N≤36) for all seasons of the year. Furthermore, this underperformance may probably due to the fact that irrigated and forest-pasture areas are not representative of the land use within the SMOS L4 pixel (1 km). From now on, the results on these two land uses will not be taken into account for the comparison. The correlations for the low- and high-resolution products are very similar, with R ranging from 0.22 to 0.84 for BEC SMOS L3 SM, and from 0.27 to 0.85 for SMOS L4. The correlation values show a seasonal dependence, which is not introduced by the downscaling algorithm, but by the original BEC SMOS L3 SM product, probably due to the fact that, in dry periods (JJA), the SM detected by *in situ* stations is lower than the SMOS sensitivity (0.04 m^3/m^3). In both BEC SMOS L3 SM and SMOS L4 SM products, the uRMSE is approximately 0.04 m^3/m^3, which is the objective accuracy of the SMOS mission. These two products show a dry bias, which is in agreement with several calibration studies on coarse resolution SMOS data at different locations, indicating a general underestimation of SMOS retrievals with respect to 0–5 cm *in situ* SM measurements [30].

Table 4.3 summarizes the statistics derived from the temporal intercomparison of the BEC SMOS L3 SM or the SMOS L4 SM products with in situ SM measurements from OzNet, to validate the new high-resolution SM product over the Yanco region. Concurrent samples (ranging from

44 to 47 per season) are used to compare both products at low and high resolution. The results are grouped by land use (RAI and VIN) and by seasons. As stated in REMEDHUS, the R shows a seasonal dependence, and similar results are obtained at low (values between 0.64 and 0.92) and high resolution (values between 0.63 and 0.92). In both cases the uRMSE ranges between 0.04 and 0.06 m^3/m^3.

Table 4.2 Statistics from the validation of the BEC SMOS L3 SM and SMOS L4 SM ("MODIS" version) products taking the REMEDHUS SM as a reference. The results are obtained by averaging all data by land use: rainfed (RAI), vineyard (VIN), fallow (FAL), forest-pasture (FOP) and irrigated (IRR), for the period from 2012 to 2014. The statistical metrics used are: N [-], R [-], RMSE [m^3/m^3], uRMSE [m^3/m^3] and Bias [m^3/m^3], and are calculated using the same number of samples. The results are shown by seasons.

		BEC SMOS L3 SM - REMEDHUS				**SMOS L4 SM ("MODIS" v.) - REMEDHUS**			
2012-2014	**N**	**R**	**RMSE**	**uRMSE**	**Bias**	**R**	**RMSE**	**uRMSE**	**Bias**
Winter (DJF)									
RAI	47	0.84	0.07	0.04	0.053	0.84	0.07	0.04	0.054
VIN	55	0.84	0.06	0.04	-0.037	0.85	0.06	0.05	-0.043
FAL	47	0.53	0.08	0.06	0.057	0.46	0.09	0.06	0.060
FOP	9	0.78	0.22	0.02	0.221	0.73	0.21	0.03	0.211
IRR	20	0.81	0.11	0.04	0.099	0.83	0.10	0.04	0.092
Spring (MAM)									
RAI	49	0.83	0.07	0.04	0.062	0.84	0.07	0.03	0.065
VIN	54	0.79	0.04	0.04	0.004	0.69	0.04	0.04	0.002
FAL	51	0.79	0.09	0.04	0.078	0.76	0.09	0.04	0.079
FOP	12	0.29	0.14	0.04	0.136	0.32	0.14	0.03	0.141
IRR	27	0.17	0.16	0.08	0.136	0.15	0.16	0.09	0.132
Summer (JJA)									
RAI	70	0.23	0.06	0.03	0.052	0.35	0.06	0.02	0.052
VIN	94	0.22	0.04	0.02	0.027	0.27	0.03	0.02	0.024
FAL	89	0.49	0.09	0.02	0.083	0.56	0.09	0.02	0.082
FOP	7	0.43	0.10	0.01	0.099	0.62	0.10	0.01	0.102
IRR	36	-0.07	0.17	0.05	0.158	-0.22	0.17	0.06	0.158
Autumn (SON)									
RAI	53	0.67	0.06	0.05	0.036	0.73	0.06	0.05	0.039
VIN	56	0.84	0.06	0.05	-0.031	0.85	0.06	0.05	-0.031
FAL	56	0.68	0.07	0.05	0.042	0.67	0.07	0.05	0.042
FOP	4	0.71	0.18	0.06	0.171	0.79	0.17	0.05	0.164
IRR	25	0.17	0.14	0.08	0.115	0.20	0.14	0.08	0.113

Table 4.3 Statistics from the validation of the BEC SMOS L3 SM and SMOS L4 SM ("MODIS" version) products taking the OzNet (Yanco) SM as a reference. Results are obtained by averaging data from the 11 available in situ stations within the Yanco region in 2015. The statistical metrics used are: N [-], R [-], RMSE [m^3/m^3], uRMSE [m^3/m^3] and Bias [m^3/m^3], and are calculated using the same number of samples. The results are shown by seasons.

		BEC SMOS L3 SM - OzNet				SMOS L4 SM ("MODIS" v.) - OzNet			
2015	**N**	**R**	**RMSE**	**uRMSE**	**Bias**	**R**	**RMSE**	**uRMSE**	**Bias**
Summer (DJF)	44	0.64	0.06	0.06	0.007	0.63	0.06	0.06	0.003
Autumn (MAM)	47	0.82	0.04	0.04	-0.003	0.81	0.04	0.04	-0.005
Winter (JJA)	46	0.78	0.08	0.05	-0.057	0.78	0.08	0.06	-0.061
Spring (SON)	46	0.92	0.04	0.04	0.006	0.92	0.04	0.04	0.002

B. Spatial analysis of SM: dynamic range, energy conservation and consistency

(1) Dynamic range analysis

Figure 4.7 and Figure 4.8 show BEC SMOS L3 SM and SMOS L4 SM maps for two different areas within the Iberian Peninsula, Galicia (northwest of Spain) and Andalusia (south of Spain), for four days under different SM conditions. It can be clearly seen how the disaggregation algorithm can discriminate between small dry areas surrounded by humid ones (e.g., Figure 4.7a) and vice versa, small relatively wet regions surrounded by dry areas (e.g., Figure 4.8c). Note that all maps are displayed with the same SM dynamic range and that the SMOS L4 SM maps are consistent with those of BEC SMOS L3 SM.

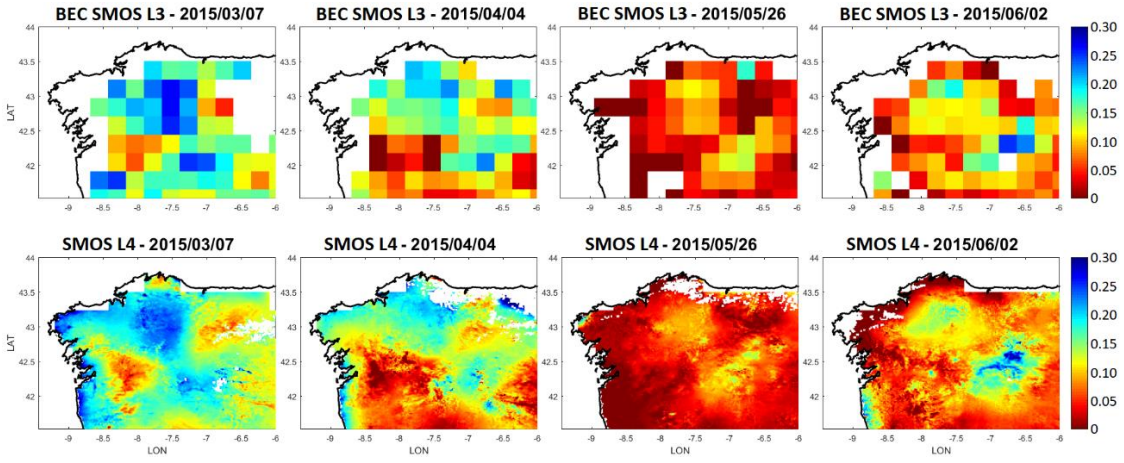

(**a**) (**b**) (**c**) (**d**)

Figure 4.7 BEC SMOS L3 SM maps (first row) and SMOS L4 SM maps (second row), obtained for the region of Galicia (northwest of Spain), for different dates and under different SM conditions.

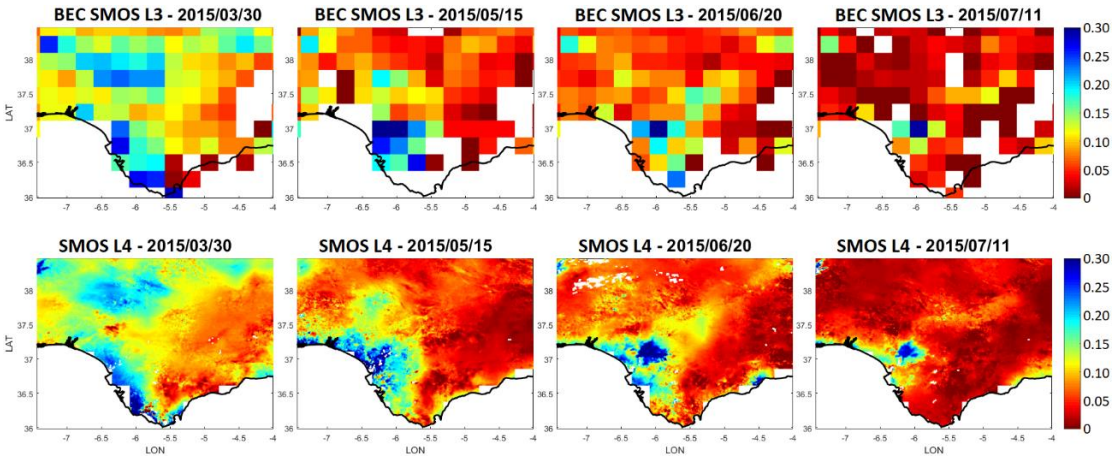

(**a**) (**b**) (**c**) (**d**)

Figure 4.8 BEC L3 SM maps (first row) and SMOS L4 SM maps (second row), obtained for the region of Andalusia (south of Spain), for different dates and under different SM conditions.

(2) Energy conservation analysis

The daily averaged subtraction between the BEC SMOS L3 SM and the SMOS L4 SM maps aggregated to a 25-km EASEv2 grid show a standard deviation (STD) of 0.019, 0.018, 0.02, and 0.02 m^3/m^3 for 2011, 2012, 2013, and 2014, respectively. For the same time period but using the high-resolution SM data obtained from the first revision of the algorithm by Piles et al. [46], these values were 0.048, 0.047, 0.05, and 0.05 m^3/m^3, respectively. The mean is almost 0 in all cases, regardless of the downscaling algorithm version. Figure 4.9 shows an example for October 7th, 2013, over the Iberian Peninsula: the original BEC SMOS L3 SM map (Figure 4.9a), the aggregated SMOS L4 SM map to 25 km (Figure 4.9b), and the difference between them (Figure 4.9c) are presented and demonstrate that the differences are negligible. Furthermore, Figure 4.10 shows the histogram of differences for the whole 2011, between the original BEC SMOS L3 SM and the high-resolution SM map aggregated to 25 km, after using the revision 1 [187] (Figure 4.10a) and revision 2 (Figure 4.10b) of the downscaling algorithm. These results show that the new version of the downscaling algorithm reduces these differences. Therefore, it can be stated that the downscaling technique is not affecting the average SM at low resolution, and also that the new revision of the algorithm represents a substantial improvement compared to the previous one.

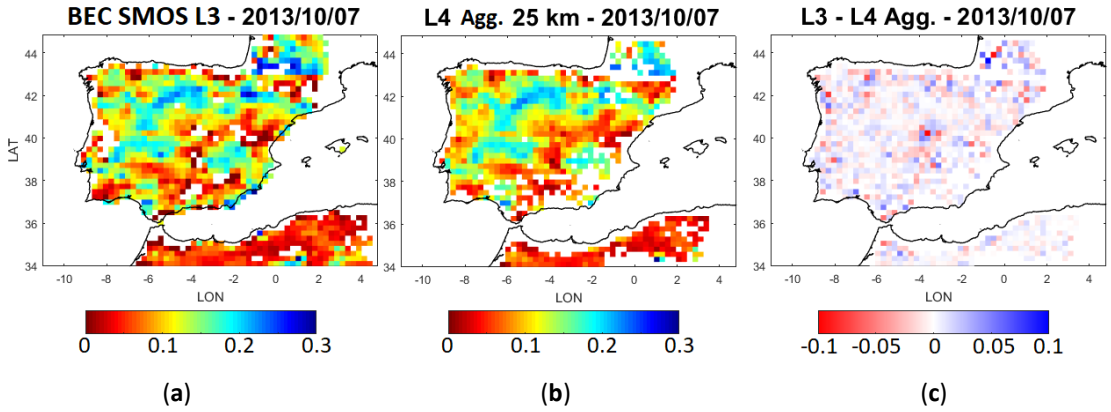

Figure 4.9 Study of energy conservation, when applying the new disaggregation technique over the Iberian Peninsula: (a) original SMOS BEC L3 SM map, (b) SMOS L4 SM product aggregated to a 25-km grid, and (c) energy conservation map calculated as the difference between (a) and (b).

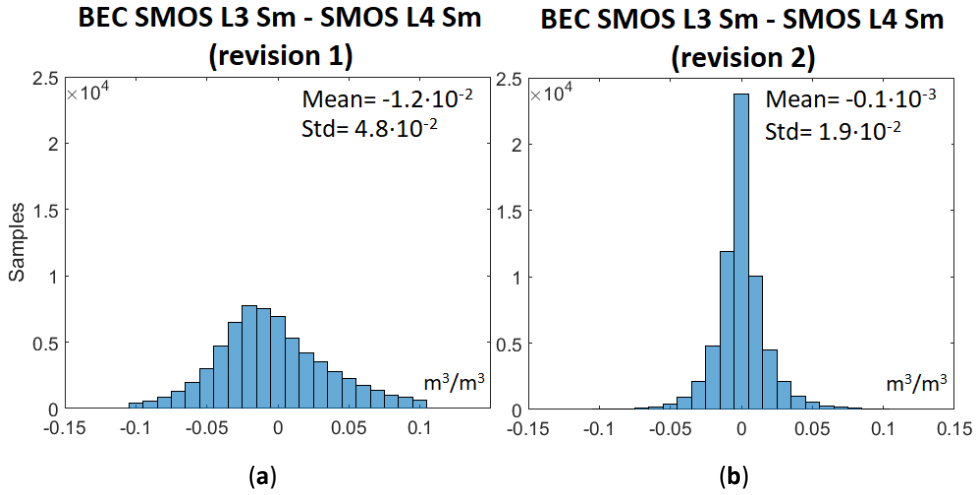

Figure 4.10 Histogram of the difference between the BEC SMOS L3 SM maps (25 km) and the high-resolution SM maps (1 km) aggregated to a 25-km EASEv2 grid. High-resolution SM maps were obtained by applying: (a) revision 1, and (b) revision 2 of the downscaling algorithm.

(3) Consistency analysis

Figure 4.11 shows an example to evaluate the consistency of the algorithm. The downscaling algorithm is applied at two different spatial scales: over Europe (Figure 4.11a) and over the Iberian Peninsula (Figure 4.11b, bottom). In this example, a 9-day temporal window centered on March 20th, 2011 is used to reduce the number of pixels with no data due to the presence of clouds masking the optical information. A map of Europe and another of the Iberian Peninsula were obtained per day, and their values over the Iberian Peninsula were compared. Finally, their differences were averaged (Figure 4.11b, top). This same procedure was applied for the whole year 2011 (not shown). The mean difference between the SMOS L4 SM maps obtained for the Iberian Peninsula area was 0.007 m^3/m^3, and the mean of the standard deviation for the same area was 0.016 m^3/m^3, for 2011. This result confirms that the proposed downscaling technique can be potentially applied to any region, regardless the size of the study area.

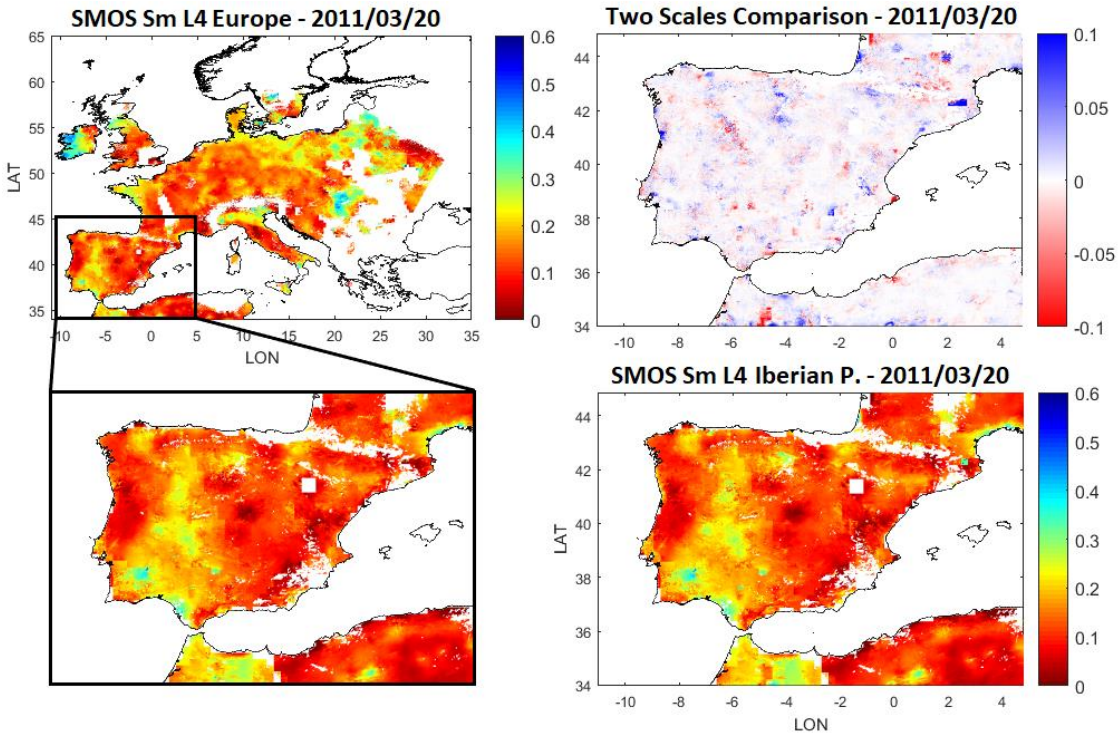

(**a**) (**b**)

Figure 4.11 Result (b, top) obtained by subtracting (a) the SMOS L4 SM map calculated with the coefficients (see Equation (4.1)) derived for all of Europe from (b, bottom) the SMOS L4 SM map computed with the coefficients derived specifically for the Iberian Peninsula.

4.3.2 The "cloud-free" version

A. Temporal analysis of SM: validation over REMEDHUS and OzNet SM networks

Table 4.4 shows the statistical results of the comparison between the SMOS L4 SM product obtained using T_S from MODIS ("MODIS" version) or ERA5 ("cloud-free") in the disaggregation algorithm, with *in situ* data from REMEDHUS, for the period from 2012 to 2014. The same number of samples is used to compare both products. The two products compare well with *in situ* data (R≥0.69 and uRMS≤0.05), excluding the summer season when the R is always ≤0.39. Similar results are obtained for the "cloud free" version, when the statistics are calculated using all available samples (Table 4.5).

The "MODIS" and "cloud-free" versions of the algorithm are also compared between each other over the Yanco region. The results show good performance (R≥0.78 and uRMSE≈0.05) for both versions of the downscaling algorithm, when using the same number of samples (Table 4.6) or all available samples (Table 4.7) for the entire year 2015.

Table 4.4 Statistics from the validation of the SMOS L4 SM product ("MODIS" and "cloud-free" versions) taking the REMEDHUS SM as a reference. The results are obtained by averaging all the data by land use: rainfed (RAI) and vineyard (VIN), for the period from 2012 to 2014. The statistical metrics used are: N [-], R [-], RMSE [m^3/m^3], uRMSE [m^3/m^3] and Bias [m^3/m^3], and are calculated using the same number of samples. The results are shown by seasons.

		SMOS L4 ("MODIS" v.) - REMEDHUS				SMOS L4 ("cloud-free" v.) - REMEDHUS			
2012-2014	**N**	**R**	**RMSE**	**uRMSE**	**Bias**	**R**	**RMSE**	**uRMSE**	**Bias**
Winter (DJF)									
RAI	47	0.84	0.07	0.04	0.054	0.85	0.06	0.04	0.047
VIN	55	0.85	0.06	0.05	-0.043	0.83	0.07	0.05	-0.049
Spring (MAM)									
RAI	49	0.84	0.07	0.03	0.065	0.85	0.07	0.03	0.066
VIN	54	0.69	0.04	0.04	0.002	0.69	0.05	0.05	0.001
Summer (JJA)									
RAI	70	0.35	0.06	0.02	0.052	0.39	0.06	0.02	0.053
VIN	94	0.27	0.03	0.02	0.024	0.33	0.03	0.02	0.024
Autumn (SON)									
RAI	53	0.73	0.06	0.05	0.039	0.74	0.06	0.05	0.037
VIN	56	0.85	0.06	0.05	-0.031	0.85	0.06	0.05	-0.031

Table 4.5 Statistics from the validation of the SMOS L4 SM product ("cloud-free" version) taking the REMEDHUS SM as a reference. The results are obtained by averaging all data by land use: rainfed (RAI) and vineyard (VIN), for the period from 2012 to 2014. The statistical metrics used are: N [-], R [-], RMSE [m^3/m^3], uRMSE [m^3/m^3] and Bias [m^3/m^3], and are calculated using all available samples. The results are shown by seasons.

	SMOS L4 ("cloud-free" v.) - REMEDHUS				
2012-2014	**N**	**R**	**RMSE**	**uRMSE**	**Bias**
Winter (DJF)					
RAI	130	0.84	0.06	0.04	0.041
VIN	131	0.84	0.08	0.05	-0.060
Spring (MAM)					
RAI	138	0.81	0.06	0.04	0.046
VIN	141	0.71	0.06	0.06	-0.021
Summer (JJA)					
RAI	137	0.37	0.06	0.03	0.049
VIN	138	0.37	0.04	0.03	0.021
Autumn (SON)					
RAI	136	0.78	0.06	0.05	0.031
VIN	137	0.78	0.07	0.06	-0.049

Table 4.6 Statistics from the validation of the SMOS L4 SM product ("MODIS" and "cloud-free" versions) taking the OzNet (Yanco) SM as a reference. The results are shown independently for 5 *in situ* stations (Y02, Y05, Y07, Y09 and Y011), for the year 2015. The statistical metrics used are: N [-], R [-], RMSE [m^3/m^3], uRMSE [m^3/m^3] and Bias [m^3/m^3], and are calculated using the same number of samples.

2015		SMOS L4 ("MODIS" v.) - OzNet				SMOS L4 ("cloud-free" v.) - OzNet			
Station	**N**	**R**	**RMSE**	**uRMSE**	**Bias**	**R**	**RMSE**	**uRMSE**	**Bias**
Y02	86	0.82	0.06	0.05	0.038	0.83	0.06	0.05	0.036
Y05	88	0.89	0.05	0.04	-0.034	0.90	0.05	0.04	-0.034
Y07	85	0.89	0.05	0.05	0.022	0.90	0.05	0.04	0.018
Y09	79	0.85	0.07	0.05	0.047	0.84	0.07	0.05	0.045
Y11	74	0.80	0.12	0.06	-0.097	0.81	0.12	0.06	-0.100

Table 4.7 Statistics from the validation of the SMOS L4 SM product ("cloud-free" version) taking the OzNet (Yanco) SM as a reference. The results are shown independently for 5 *in situ* stations (Y02, Y05, Y07, Y09 and Y011), for the year 2015. The statistical metrics used are: N [-], R [-], RMSE [m^3/m^3], uRMSE [m^3/m^3] and Bias [m^3/m^3], and are calculated using all available samples.

2015	SMOS L4 ("cloud-free" v.) - OzNet				
Station	**N**	**R**	**RMSE**	**uRMSE**	**Bias**
Y02	166	0.83	0.06	0.06	0.027
Y05	174	0.90	0.06	0.05	-0.043
Y07	177	0.82	0.06	0.06	0.006
Y09	157	0.82	0.08	0.06	0.042
Y11	143	0.78	0.14	0.07	-0.123

B. Spatial analysis of SM: spatial coverage, energy conservation and consistency analysis

(1) Spatial coverage analysis

Figure 4.12 shows an example of high-resolution SM map obtained after applying the "MODIS" (Figure 4.12, top) and the "cloud-free" version (Figure 4.12, bottom) of the downscaling algorithm, for Australia and for the Iberian Peninsula. Both versions of the algorithm result in similar SM spatial patterns, although the "cloud-free" version has much greater spatial coverage than the "MODIS" version, where clouds are masking a significant part of the information.

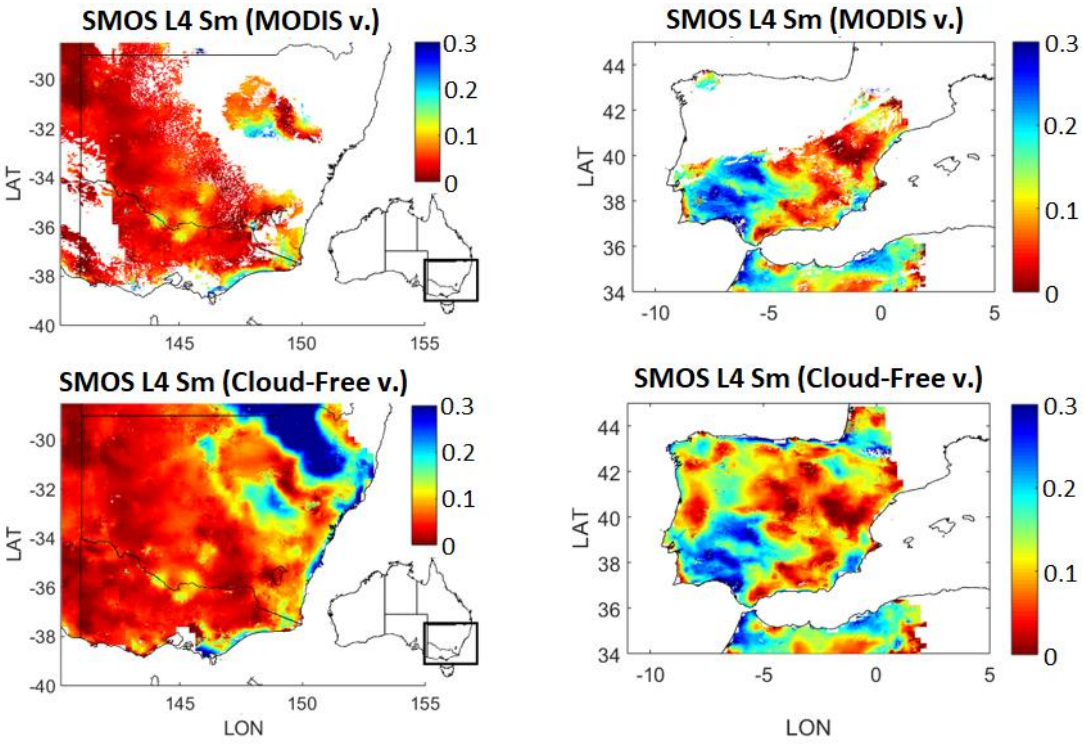

(**a**) (**b**)

Figure 4.12 SMOS L4 SM maps: (first row) "MODIS" and (second row) "cloud-free" versions. The results are obtained for: (a) New South Wales and (b) the Iberian Peninsula, for January 2nd, 2015.

(2) Energy conservation analysis

The consistency of the "cloud-free" version has been tested in a region of Africa (Figure 4.13) and a region of Brazil (Figure 4.14). In both cases, the resulting SMOS L4 SM maps are almost independent of the size of the study area to which the downscaling algorithm is applied. The mean and the STD of the differences between the SM maps obtained for different study areas is almost negligible.

(3) Consistency analysis

Finally, the robustness of the downscaling method is analyzed by applying it to a continental scale. Figure 4.15b and Figure 4.16b show the differences between the aggregated SMOS L4 SM maps at low resolution (25 km) and the respective BEC SMOS L3 SM maps (25 km), for Australia (May 2015) and Europe (May 2016), respectively. The STD of these differences is $0.9 \cdot 10^{-2}$ m^3/m^3 for Australia and $1.2 \cdot 10^{-2}$ m^3/m^3 for Europe, the mean is almost zero in both cases.

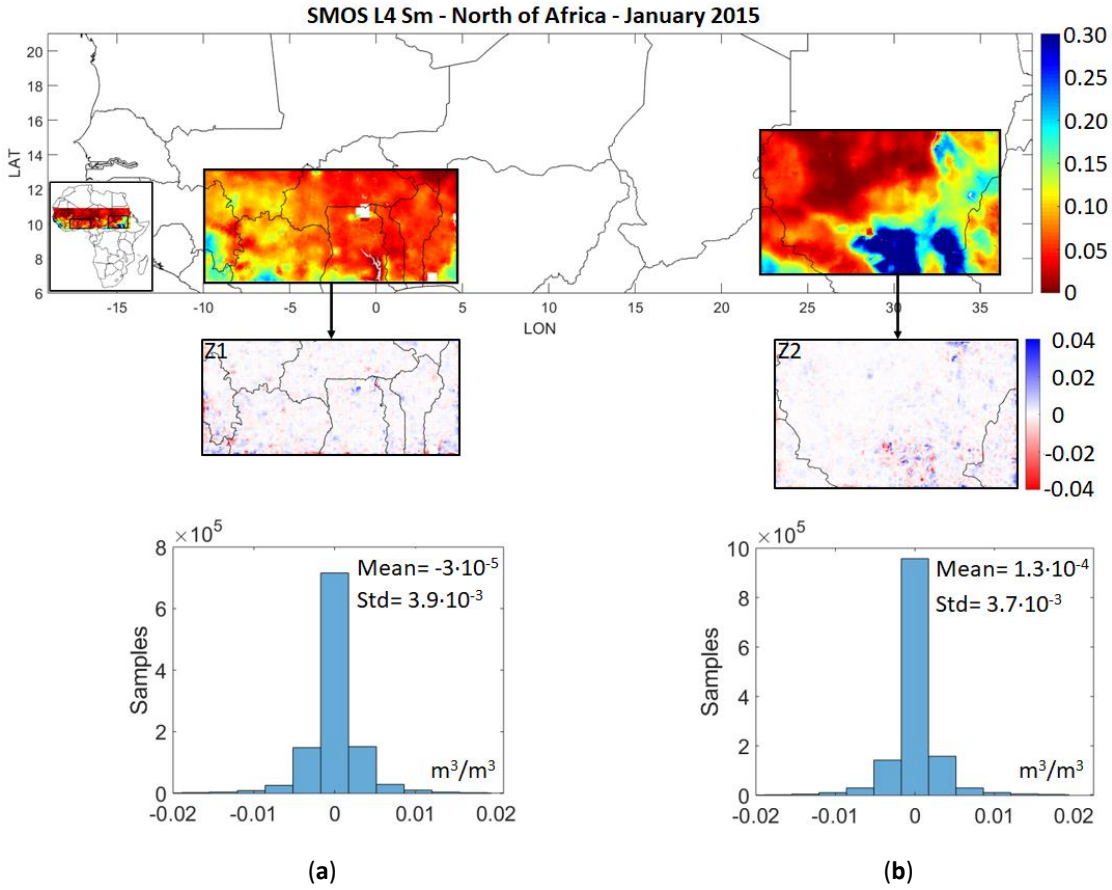

Figure 4.13 Subtraction of the SMOS L4 SM map calculated with the coefficients derived for a huge area in Africa (6—21° N, -18—38° W) from the SMOS L4 SM maps calculated with the coefficients derived specifically over two smaller regions (Z1 and Z2). The histograms of these differences are also included.

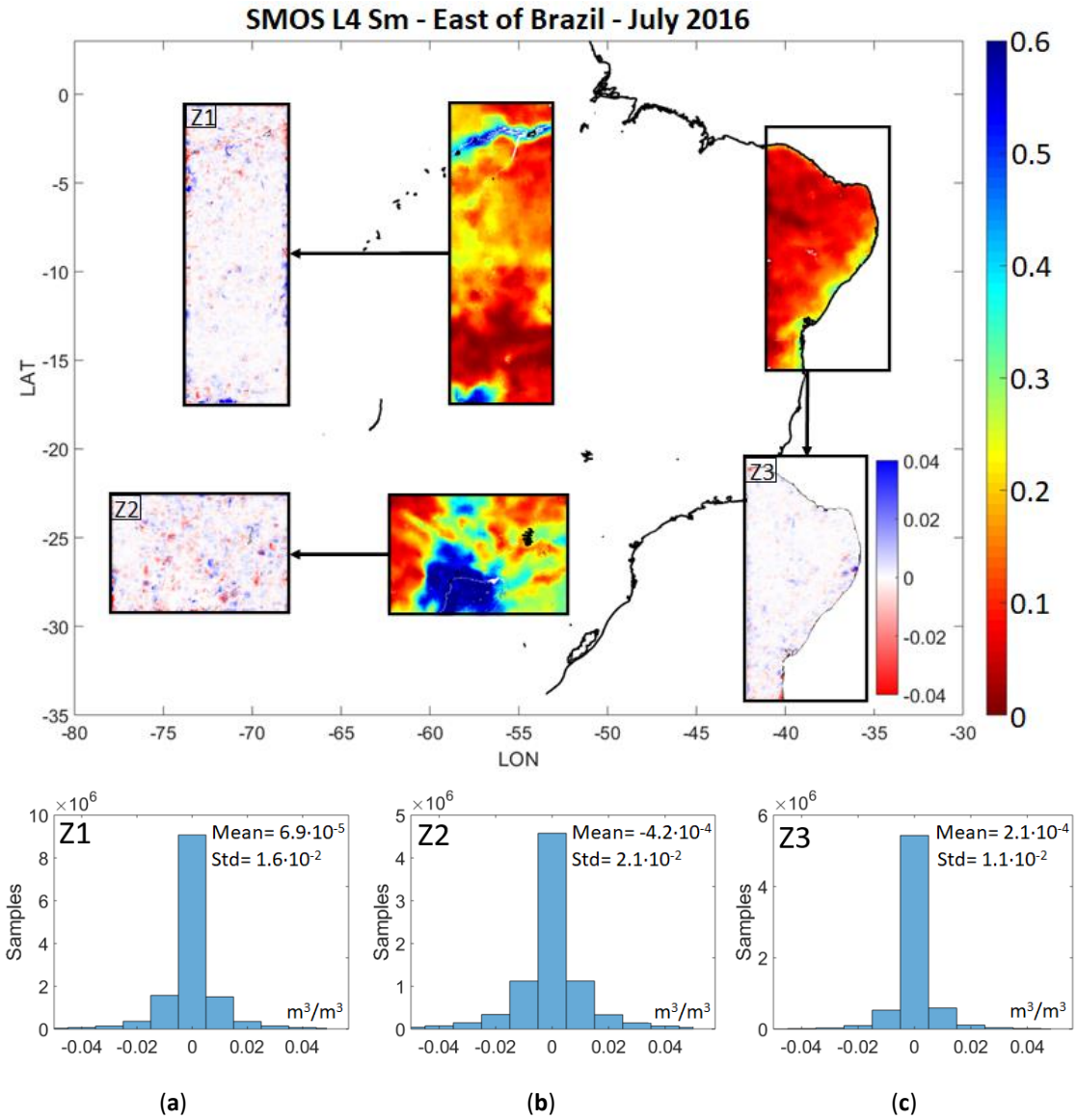

(**a**) (**b**) (**c**)

Figure 4.14 Subtraction of the SMOS L4 SM map computed with the coefficients derived for a huge area in Brazil (-35—3° N, -80—-30° W) from the SMOS L4 SM maps computed with the coefficients derived specifically over three smaller regions (Z1, Z2 and Z3). The histograms of these differences are also included.

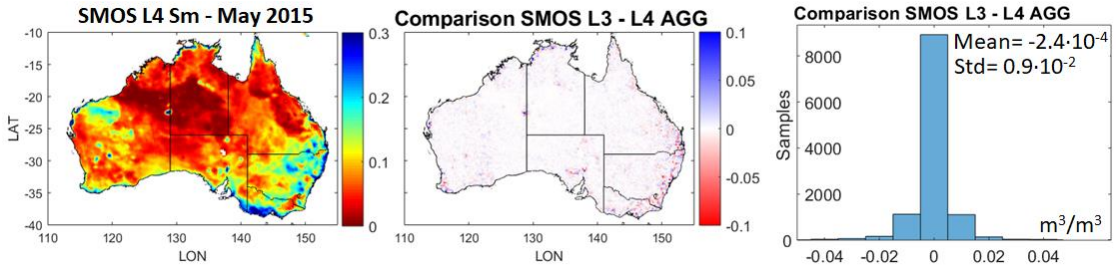

(a) (b) (c)

Figure 4.15 SMOS L4 SM product energy conservation study ("cloud-free" version). (a) SMOS L4 SM map, (b) energy conservation map calculated as the difference between the resulting SMOS L4 SM map aggregated to a 25-km grid and the original BEC SMOS L3 SM, and (c) histogram of these differences.

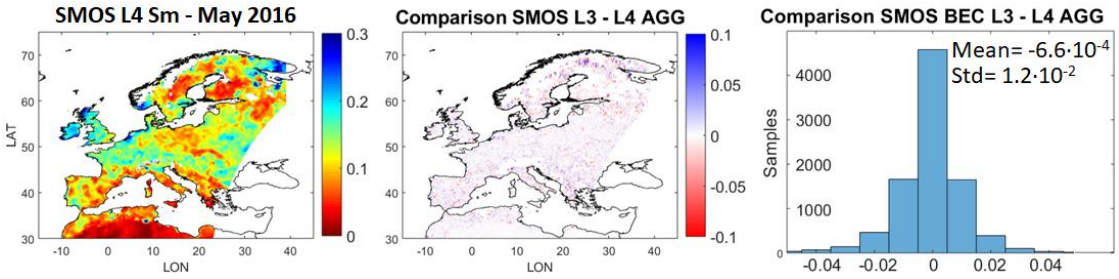

(a) (b) (c)

Figure 4.16 SMOS L4 SM product energy conservation study ("cloud-free" version). (a) SMOS L4 SM map, (b) energy conservation map calculated as the difference between the resulting SMOS L4 SM map aggregated to a 25-km grid and the original BEC SMOS L3 SM, and (c) histogram of these differences.

4.4 Summary and conclusions

This chapter includes the methodology and validation of two versions of a new SM disaggregation technique, which allow obtaining high-resolution SM maps (1 km) from the native resolution (~40 km) of the SMOS satellite. The two versions of the algorithm are: (i) the "MODIS" version, which takes advantage of the high resolution provided by optical-based sensors such as MODIS, but being highly affected by cloud coverage; and (ii) the "cloud-free" version, which uses ERA5 T_S, provides full coverage under all weather conditions but with a 30-km spatial resolution. This algorithm uses a shape-adaptive moving window and a semiempirical downscaling approach based on the "universal triangle" concept. It is an extension of the well-known downscaling technique presented by Piles et al. in [46]. The "MODIS" and the "cloud-free" versions of the algorithm have been tested under different SM conditions, in a variety of climatic conditions around the world (North Africa, East Brazil, Europe and Australia). The validation of the resulting high-resolutions SM maps (SMOS L4 SM) has been carried out using measurements from the REMEDHUS and OzNet *in situ* SM networks.

The statistical analysis revealed that both versions of the algorithm have similar performance when REMEDHUS (Table 4.4) and the OzNet (Table 4.6) SM measurements are used as a reference. Obtaining good statistics for both versions over REMEDHUS — mean R≥0.8 and mean

uRMSE≈0.04 (from Table 4.4, excluding the summer season) — and over OzNet — mean R≥0.85 and mean uRMSE≈0.05 (from Table 4.6). A seasonal dependency was detected not only for both version of the downscaling algorithm, but also for the original BEC SMOS L3 SM product. Hence, it can be stated that this dependency is inherent to the SMOS SM data and it is not introduced by the downscaling technique. The main conclusions about the performances of this new method are given as follows:

i) The use of a small adaptive moving window in the downscaling algorithm allows to maintain the dynamic range of SM when it is disaggregated from 25 km (BEC SMOS L3 SM product) to 1 km (SMOS L4 SM).

ii) When the resulting high-resolution SM maps (SMOS L4 SM) are aggregated from 1 km to 25 km, the energy remains almost the same with respect to the original coarse grid cells.

iii) The downscaling algorithm has been developed so that the generated results are consistent regardless of the size of the study area.

iv) The use of ERA5 T_S instead of MODIS T_S as input parameter in the downscaling algorithm does not lead to a degradation of the statistics (Table 4.4 and Table 4.6), and significantly enhances the spatial coverage (Figure 4.12). However, ERA5 T_S has certain limitations, in particular over agro-ecosystems. Although irrigation parametrizations are becoming more common in land surface models and are growing in sophistication, there is difficulty in assessing the realism of the irrigation implementations, mainly due to limited observations. Future analyzes could be focused on examining the error in the high-resolution SM, estimated using the methodology proposed in this chapter, over irrigated areas.

As a summary, it can be concluded that the main advantage of this new algorithm is that it can potentially be applied at a continental scale i.e., to regions including different climates and biomes. Moreover, the results show that if the high-resolution of the soil vegetation parameter (NDVI) is maintained, having a T_S at a coarser spatial resolution does not substantially affect the resulting high-resolution SM maps. In this study, T_S from two different sources (MODIS and ERA5) was used, but other T_S products could potentially be used, such as the one provided by Sentinel-3 [188], ERA5-land or by the ECMWF operational model. The downscaling algorithm presented in this chapter was implemented at BEC facilities in 2019 to distribute daily high-resolution SM maps over Europe using the following input parameters [115]:

i) Daily BEC SMOS L3 SM at 25-km EASEv2 grid.

ii) Daily BEC SMOS L3 T_B at both horizontal and vertical polarization at 25-km EASEv2 grid, at the Earth surface and at three incidence angles (32.5°, 42.5° and 52.5°).

iii) Daily T_S or skin temperature at 12:00 PM at around 9 km, which is provided by the operational ECMWF model.

iv) 16-Day Terra MODIS NDVI (MOD13A2 v6 or MOD13A4N v6 at 1 km).

Miriam Pablos et al. [156] validated this version of the high-resolution SM product by selecting five SM networks spread across Europe. They were located in areas with different

topographical complexity and with different climates [189]: REMEDHUS network [77], established at the Duero river basin, to the north of the Iberian Peninsula Plateau, where a warm-summer Mediterranean climate prevails; SMOSMANIA (Soil Moisture Observing System-Meteorological Automatic Network Integrated Application) network [190], located in the south of France, along a transect between the Atlantic Ocean and the Mediterranean Sea, with humid oceanic climate in the West and hot-summer Mediterranean climate in the East; HOBE (Hydrological Observatory) network [191], located in the Skjern river catchment, Denmark, where the humid oceanic climate predominates, with mild summers; RSMN (Continous Soil Moisture & Temperature Ground-based Observation Network) network [192], distributed in Romania, in an area characterized by its humid continental climate; and FMI (Finnish Meteorological Institute) network [193], located in the Sodankylä Artic research region, Finland, with a subarctic climate.

Table 4.8 Median value of statistics (N [-], R [-], RMSE [m^3/m^3], uRMSE [m^3/m^3] and Bias [m^3/m^3]) for the period from 2015 to 2016. Adapted from [156].

Network	N	R	RMSE	uRMSE	Bias
REMEDHUS	310	0.7	0.092	0.054	-0.026
SMOSMANIA	295	0.58	0.108	0.064	-0.064
HOBE	266	0.6	0.066	0.057	0.003
RSMN	229	0.52	0.086	0.074	0.034
FMI	294	0.38	0.192	0.066	0.178

Table 4.8 summarizes the statistical scores obtained between the downscaled SM and the *in situ* measurements. REMEDHUS shows the highest correlation (median of 0.7) and the lowest RMSE (median of 0.054 m^3/m^3), while the lowest correlation is obtained for FMI (median of 0.38) and the highest uRMSE for RSMN (median of 0.074 m^3/m^3). There is a positive bias in HOBE, RSMN and FMI, revealing an overestimation of the satellite SM against in situ measurements. A negative bias can be appreciated in SMOSMANIA and REMEDHUS.

This validation document also analyzes the patterns of the resulting high-resolution SM maps over Europe for the years 2015 and 2016. As expected, high-latitude regions (over Sweden, Finland, Netherlands, Ireland, and some parts of United Kingdom, Norway and Denmark) are wetter than those located in southern of Europe (over some parts of Spain, Italy, Croatia, Bosnia and Herzegovina, Montenegro, Albania, Greece, and Macedonia). Likewise, the main mountain ranges (Scandinavian, Pyrenees, Alps, Carpathians, Apennines and Balkan Mountains) show low values of SM, due to the impact of topography on the L2 retrievals, which affects the L3 and, ultimately, the L4 product (see [156] for more detail).

A variety of applications have successfully used this product e.g., for crop yield estimation [194,195] and forest decline modelling [196], which is an indirect validation of the synergistic approach.

The content of this chapter was published in a symposium [197] and in a journal [27].

Chapter 5

Assessment of multiscale SMOS and SMAP soil moisture products

Over the years different approaches have been proposed to spatially disaggregate coarse-resolution SM maps (see Chapter 3 for details). These approaches rely on synergies between multi-sensor observations and are built upon different physical assumptions. In this chapter, temporal and spatial characteristics of six SM products derived from SMOS and SMAP are assessed in order to diagnose their distinct features, and the rationale behind them. The study is focused on the Iberian Peninsula and covers the period from April 2015 to December 2017. A temporal inter-comparison analysis is carried out using *in situ* SM data from REMEDHUS network to evaluate the impact of the spatial scale (1, 3, 9, 25, and 36 km) of different SMOS and SMAP products, and their correspondence in terms of temporal dynamics. A spatial analysis is conducted with emphasis on the added-value that the enhanced resolution products provided based on the microwave/optical (SMOS/MODIS, see Chapter 4) [27] or the active/passive microwave (SMAP/Sentinel-1) [117] sensor fusion. Results show overall agreement among time series of the SMOS and SMAP products regardless of their spatial scale when compared to *in situ* measurements. Still, higher spatial resolution (<1 km) would be needed, for instance to capture local features such as small irrigated areas that are not dominant at the 1-km pixel scale. The degree to which spatial features are resolved by the enhanced resolution products depend on the multi-sensor synergies employed (at T_B or SM level), and on the nature of the fine-scale information used. The largest disparities between these products occur in forested areas, which may be related to the reduced sensitivity of high-resolution active microwave and optical data to soil properties under dense vegetation.

The SMAP and the SMOS-derived SM data products used in this chapter are presented in Section 5.1. Section 5.2 details the methodology followed to conduct the temporal and spatial analyses on the different products. The results of these comparisons are shown in Section 5.3. Section 5.4 discusses the possible reasons for the mismatch found among the different SM products. Finally, Section 5.5 provides the main conclusions and perspectives from this study.

5.1 Datasets

Table 5.1 summarizes the data used in this chapter, including information from SMOS (SM and T_B), SMAP (SM and T_B), CCI (LC) and from the REMEDHUS *in situ* network (SM and precipitation). The BEC SMOS L4 SM product is provided by the BEC following the methodology described in Chapter 4, using the specific input parameters presented in Section 3.2.1. All these products are described in detail in Section 3.2.

Table 5.1 Summary of the data used in this chapter. * Provided by the Water Resources Research group of the University of Salamanca.

Source	Variable	Product	Spatial Frequency	Temporal Frequency	Reference
SMOS	SM	BEC SMOS L3	25 km	Daily	[156]
		BEC SMOS L4	1 km	Daily	[156]
	T_B	BEC SMOS L3	25/12.5 km	Daily	[156]
SMAP	SM	SMAP L2	36 km	Daily	[48]
		SMAP L2E	9 km	Daily	[157]
		SMAP AP3	3 km	Daily	[158]
		SMAP AP1	1 km	Daily	[158]
	T_B	SMAP L1C	36 km	Daily	[48]
CCI	LC	CCI	300 m	Annually	[183]
REMEDHUS	SM	REMEDHUS	*In situ*	Hourly	[77]
	Precipitation	REMEDHUS	*In situ*	Hourly	*

5.2 Methodology

5.2.1 Statistical analysis of SM time series at the network scale

Ground-based SM measurements from REMEDHUS network were selected as a benchmark for a cross-validation of the multi-scale remotely sensed SM products. REMEDHUS stations were placed by the Water Resources Research group of the University of Salamanca (responsible for the maintenance of the network) in areas in which the land use, during the years from 2015 to 2017, were the following: fallow (FAL), rainfed (RAI), forest-pasture (FOP), vineyard (VIN) and irrigated (IRR). A thorough analysis of the 20 operational *in situ* stations available during the study period and their comparison to satellite data was performed. For the sake of clarity and simplicity, this chapter will focus on 11 of these stations (see Table 5.2). They cover the five land uses— and therefore allow studying the impact of land use on the downscaling products— and also provide a good spatial representation when averaged at the network scale.

Table 5.2. Land use of the region where the eleven REMEDHUS *in situ* stations selected for this study were located for the years 2015, 2016 and 2017. The land uses are: fallow (FAL), rainfed (RAI), forest-pasture (FOP), vineyard (VIN), and irrigated (IRR).

	H13	H9	J3	K13	N9	O7	F11	J12	J14	K10	M9
2015	FAL	FOP	VIN	IRR	RAI	RAI	RAI	RAI	RAI	RAI	RAI
2016	FAL	FOP	VIN	IRR	RAI	FAL	FAL	FAL	FAL	FAL	FAL
2017	FAL	FOP	VIN	IRR	RAI	RAI	RAI	RAI	RAI	RAI	RAI

In this first step of the analysis, the data provided by six representative stations (H13, H9, J3, K13, N9 and O7) of the five different land uses available within the REMEDHUS network were used. The SMAP and the SMOS time series of the pixels overlapping these stations were statistically evaluated with *in situ* SM at two spatial levels, at low resolution (from 9 km up to ~40 km) and at high resolution (3 km and 1 km). Performance metrics, such as R, RMSE, uRMSE and bias, together with the number of available samples, were computed for each station-pixel pair. These performance metrics were calculated exactly as described in [186].

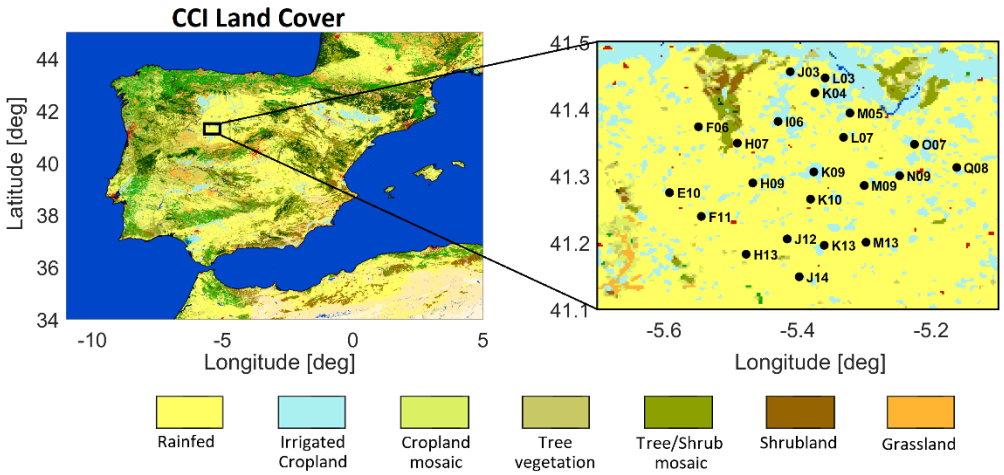

Figure 5.1 CCI land cover map (at 300 m) over the Iberian Peninsula (left) and a close-up of the REMEDHUS area (right). Black dots depict the 22 *in situ* SM stations of the REMEDHUS network that have been available over the years. The distribution of the land cover within the REMEDHUS area is: agriculture, 95.45% (cropland, 75.44%; irrigated, 16.11%; other, 3.90%); forest, 2.70%; grassland, 0.63%; wetland, 0%; settlement, 0.26%; and others, 0.95%.

Since rainfed is the most common land cover type within the REMEDHUS area (Figure 5.1), the second step of the analysis consisted in reproducing the same statistical evaluation, but using only the dataset of the stations located over rainfed/fallow land uses (F11, H13, J12, J14, K10, M9 and O7). The average value of all these rainfed/fallow stations were compared to the average of the respective SMAP and SMOS pixels covering these stations.

Additionally, statistical scores were obtained for all seasons (DJF: December, January, February; MAM: March, April, May; JJA: June, July, August; SON: September, October, November). This analysis is needed to evaluate whether the precision (R), accuracy (bias) and

quadratic errors (RMSE and uRMSE) of the studied products/methodologies have any seasonal dependence.

5.2.2 Analysis of the SM spatial patterns

To consistently analyze the spatial features of the SMAP and SMOS SM maps at 1 km, their maps of daily differences were computed (SMAP L2 AP1 minus BEC SMOS L4) along the entire study period and the histogram of these differences was obtained, together with its mean and STD. In addition, daily SM difference maps were temporally averaged and compared to the spatial distribution of the most common land cover types over the Iberian Peninsula.

Besides, taking into account different ancillary data (e.g. soil roughness, vegetation indices, skin temperature, or single scattering albedo) [48], high-resolution SMAP and SMOS SM maps are derived from their respective T_B, as described in Chapter 3. However, there are noteworthy differences related to T_B polarizations and incidence angles. While the SMAP disaggregation methodology [117] uses one specific polarization (vertical) with a single incidence angle (40°), the SMOS downscaling algorithm [156] employs two polarizations (horizontal and vertical), and the average of three incidence angles (32.5°±5°, 42.5°±5° and 52.5°±5°) over the same target. To analyze the influence of T_B data on the high-resolution SM maps, the vertical SMAP L1C T_B was compared to the vertical BEC SMOS L3 T_B at the Earth's surface, using exclusively the central SMOS angle (42.5°). The BEC SMOS L3 T_B dataset is the result of correcting the ESA SMOS L1C T_B product by the geometry of the antenna, the ionospheric and atmospheric effects, linearly interpolated to the angles range 42.5±5° and binned to a 25-km EASEv2 grid. The SMAP T_B has been interpolated from the initial 36-km EASEv2 grid to the same grid of SMOS, using the nearest neighbor. Then, daily differences (SMAP L1C T_B minus BEC SMOS L3 T_B) have been computed from April 2015 to December 2017. The coastal areas of the Iberian Peninsula were discarded to screen out the effect of sea-land contamination.

A low- versus high-resolution study was performed to assess the variations, in volumetric units, between the original and the downscaled SM maps of the same sensor. In this way, the impact of the different downscaling methods on spatial SM patterns was assessed. To do this, coarse-resolution SMAP and SMOS maps were firstly interpolated to a 1-km grid using the nearest neighbor. The comparison was done by separately calculating the daily differences between the SMAP L2 AP1 SM and the SMAP L2 SM maps, as well as the daily differences between BEC SMOS L4 SM and BEC SMOS L3 SM maps along the entire study period.

5.3 Results

5.3.1 Statistical analysis of SM time series at the network scale

Interestingly, SMAP and SMOS satellite products agree reasonably well among them, capturing the marked wet up and dry down variations along time. Nevertheless, a strong dependence on land use is found in the results obtained when comparing satellite SM products with *in situ* SM data (see Figure 5.2). Both SMAP and SMOS products are overestimating the *in situ* measurements in vineyards (Figure 5.2a). Instead, satellite data underestimate the *in situ*

SM for irrigated crops (Figure 5.2b), while they almost match up with *in situ* observations for fallow/rainfed crops (Figure 5.2c), which are the most common land uses in the REMEDHUS area.

The statistics derived from the temporal inter-comparison of low-resolution SM products (SMAP L2, SMAP L2E and BEC SMOS L3 SM) with *in situ* data using all the concurrent samples available for each dataset are summarized in Table 5.3. Comparing the different instruments, results show that the two SMAP products have the same or a slightly higher correlation ($\Delta R \leq 0.12$) and similar unbiased errors ($\Delta uRMSE \leq 0.01$ m^3/m^3) than the SMOS product in all the study cases. There are no significant differences between the metrics obtained for the SMAP SM (SMAP L2 versus SMAP L2E). Regarding the different land uses, the worst results were obtained for K13, an irrigated station, with a R (and a bias) of 0.46 (and -0.142 m^3/m^3) for SMAP L2E, 0.48 (-0.143 m^3/m^3) for SMAP L2, and 0.46 (-0.183 m^3/m^3) for BEC SMOS L3 SM. Besides, the uRMSE of K13 is twice as high the objective accuracy of both space missions (SMOS and SMAP). This underperformance probably comes from the fact that irrigated land is not the most representative land use within the low-resolution SMAP/SMOS pixels, which is mostly covered by rainfed crops (Table 5.4). On the contrary, the best results are obtained for the stations located over rainfed/fallow land cover (H13 and O07), with a R between 0.79 and 0.83 for both SMAP products (SMAP L2E and SMAP L2), and between 0.70 and 0.80 for SMOS. Their bias is low, between 0.027 and 0.035 m^3/m^3 for SMAP, and between 0.004 and 0.068 m^3/m^3 for SMOS, in absolute values. The uRMSE of these two stations are around 0.04-0.05 m^3/m^3, meeting or almost meeting required accuracy of both missions. In the case of vineyards (J03), intermediate results are obtained. The highest R is obtained for two SMAP products (0.85), but a high R is also obtained for BEC SMOS L3 SM (0.73). The uRMSE is very similar for the three products (from 0.045 to 0.048 m^3/m^3). However, the bias of J03 for the SMAP products is up to two or three times higher (0.106 and 0.103 m^3/m^3) than that aforementioned for rainfed/fallow. At these spatial scales, the number of available samples of SMAP and SMOS with *in situ* samples are of the same order (around 500 days), ensuring a robust statistical analysis.

Table 5.3 Statistics (N [-], R [-], RMSE [m^3/m^3], uRMSE [m^3/m^3] and bias [m^3/m^3]) obtained from the comparison of *in situ* SM with the SM values of the concurrent pixels from the SMOS and SMAP products (radiometer-only): SMAP L2E (left), SMAP L2 (center) and BEC SMOS L3 (right), from April 2015 to December 2017. The *in situ* stations used are: H13, H9, J3, K13, N9 and O7.

	***In situ* vs SMAP L2E**					***In situ* vs SMAP L2**					***In situ* vs BEC SMOS L3**				
	N	**R**	**RMSE**	**uRMSE**	**Bias**	**N**	**R**	**RMSE**	**uRMSE**	**Bias**	**N**	**R**	**RMSE**	**uRMSE**	**Bias**
H13	540	0,83	0,052	0,044	-0,028	492	0,83	0,056	0,044	-0,035	497	0,80	0,086	0,052	-0,068
H09	524	0,64	0,136	0,075	-0,114	506	0,62	0,137	0,077	-0,113	504	0,58	0,167	0,081	-0,146
J03	550	0,85	0,115	0,046	0,106	537	0,85	0,112	0,045	0,103	516	0,73	0,075	0,048	0,057
K13	502	0,46	0,166	0,086	-0,142	483	0,48	0,167	0,086	-0,143	510	0,46	0,201	0,083	-0,183
N09	502	0,67	0,087	0,052	-0,069	536	0,65	0,076	0,055	-0,052	512	0,60	0,117	0,057	-0,102
O07	490	0,79	0,048	0,038	0,030	486	0,79	0,047	0,038	0,027	510	0,70	0,048	0,048	0,004

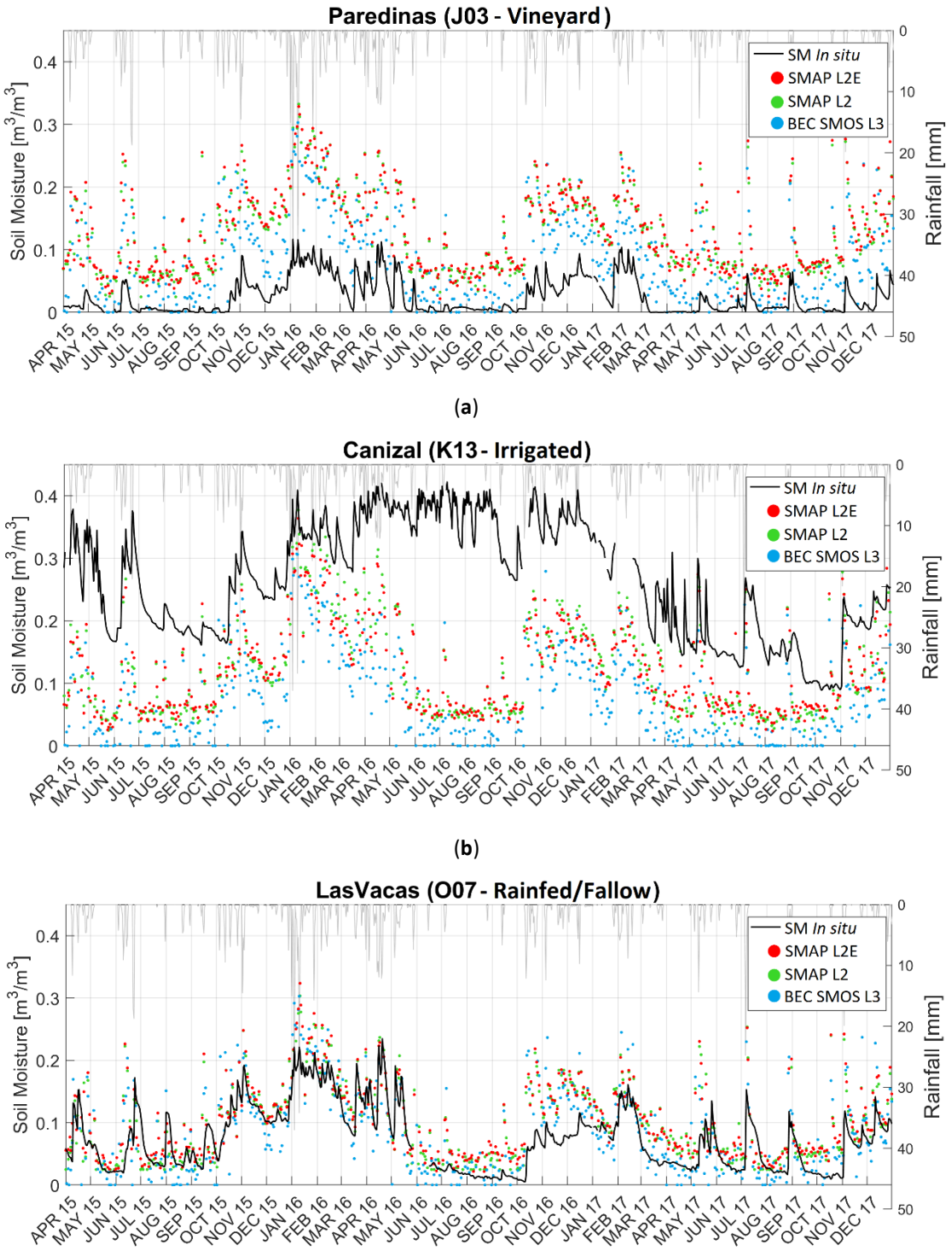

Figure 5.2 Daily evolution of the *in situ* SM (black) and the three low-resolution (radiometer-only) SM (SMAP L2E, red; SMAP L2, green; and BEC SMOS L3, blue) at three REMEDHUS stations: (a) J3 (vineyard), (b) K13 (irrigated) and (c) O7 (rainfed/fallow). Rainfall events and its intensity are plotted in gray.

When analyzing the metrics derived from the validation of SMAP and SMOS at high resolution (Table 5.5), the irrigated station K13 keeps showing the worst results as for the low-resolution

case: a R (and a bias) of 0.45 (-0.142 m^3/m^3) for SMAP L2 AP1, 0.51 (-0.129 m^3/m^3) for SMAP L2 AP3, and 0.42 (-0.186 m^3/m^3) for BEC SMOS L4. This indicates that irrigated areas are not even spatially representative at the scales of 3 km to 1 km, which denotes the small extent of these areas within the satellite footprint (Table 5.4).

Table 5.4 Percentage of rainfed and irrigated croplands (the two most common land covers over the REMEDHUS network according to the CCI LC map) within the SMOS and SMAP pixels (36 km, 25 km, 9 km, 3 km and 1km) enclosing the *in situ* stations J3 (vineyard), K13 (irrigated) and O7 (rainfed/fallow).

	J3 (Vineyard)		K13 (Irrigated)		O7 (Rainfed/Fallow)	
	Rainfed (%)	Irrigated (%)	Rainfed (%)	Irrigated (%)	Rainfed (%)	Irrigated (%)
SMAPL2 (36 km)	67,81	20,83	80,27	17,26	67,97	24,68
SMOSL3 (25 km)	61,06	30,51	92,54	6,47	61,06	30,51
SMAPL2_E (9 km)	39,71	52,16	93,08	6,66	68,69	23,27
SMAP_AP3 (3 km)	43,80	42,98	79,55	20,45	66,94	33,06
SMOSL4 (1 km)	56,25	43,75	68,75	31,25	75,00	25,00

Table 5.5 Statistics (N [-], R [-], RMSE [m^3/m^3], uRMSE [m^3/m^3] and bias [m^3/m^3]) obtained from the comparison of *in situ* SM with the SM values of the concurrent pixels from the SMOS and SMAP products: SMAP L2 AP1 at 1 km (left), SMAP L2 AP3 at 3 km (center) and BEC SMOS L4 at 1 km (right), from April 2015 to December 2017. The *in situ* stations used are: H13, H9, J3, K13, N9 and O7.

	***In Situ* vs SMAP L2 AP1**					***In Situ* vs SMAP L2 AP3**					***In Situ* vs BEC SMOS L4**				
	N	**R**	**RMSE**	**uRMSE**	**Bias**	**N**	**R**	**RMSE**	**uRMSE**	**Bias**	**N**	**R**	**RMSE**	**uRMSE**	**Bias**
H13	100	0,81	0,062	0,040	-0,048	100	0,86	0,046	0,038	-0,025	489	0,80	0,089	0,045	-0,076
H09	96	0,56	0,164	0,086	-0,139	96	0,60	0,155	0,084	-0,131	443	0,59	0,175	0,079	-0,156
J03	98	0,70	0,093	0,046	0,081	98	0,83	0,121	0,043	0,114	513	0,72	0,085	0,054	0,066
K13	97	0,45	0,172	0,097	-0,142	97	0,51	0,156	0,088	-0,129	493	0,42	0,205	0,085	-0,186
N09	101	0,45	0,120	0,071	-0,097	101	0,57	0,101	0,058	-0,082	503	0,63	0,119	0,056	-0,105
O07	98	0,66	0,076	0,063	0,042	99	0,78	0,076	0,050	0,056	501	0,71	0,047	0,047	-0,001

Similarly, the best results are obtained for the stations H13 and O07, with R between 0.66 and 0.86 for SMAP L2 AP1 and AP3, and between 0.71 and 0.80 for BEC SMOS L4. The lowest bias is observed for H13 and O07, ranging between 0.025 and 0.056 m^3/m^3 for SMAP, and from 0.001 to 0.076 m^3/m^3 for SMOS, in absolute values. Again, the reason for that is the predominance of rainfed crops and fallow regions over REMEDHUS (Table 5.4). Therefore, both satellites mostly see the land cover types leading to a cover-characteristic signal at low as well

as at high resolution. As previously observed in Table 5.3, the metrics for vineyard are in a well acceptable range. On the one hand, taking into account both SMAP and SMOS, R varies between 0.70 and 0.83, and the uRMSE is always around 0.04-0.05 m^3/m^3. On the other hand, the bias of J03 is doubled or even tripled (0.081 and 0.114 m^3/m^3) with respect to the stations H13 and O07. All the SMAP and SMOS products are overestimating the *in situ* measurements of J03. One reason could be that grapevines are settled on very fine sand, which causes the water not to be retained and it quickly percolates into deeper layers. Additionally, the vineyard areas of REMEDHUS are not spatially representative at scales of 1 km and beyond.

Due to the missing synchronization of SMAP and Sentinel-1 acquisition orbits, the number of samples of the SM time series generated from the SMAP L2 AP1 and AP3 products (96 to 101 days) is much lower than for the BEC SMOS L4 time series (443 to 513).

Similar statistical scores (see appendix Table App A.1 and Table App A.2) are obtained for the SMOS products when the same number of samples is used at high and low resolution, in line with the results obtained in Chapter 4 (Section 4.3). When the same analysis is conducted for the SMAP products, only slightly worst performances are obtained for the SMAP L2 AP1 product.

Table 5.6 shows the statistics obtained between the average SM values of the stations located over a rainfed/fallow land use (F11, H13, J12, J14, K10, M9 and O7) and the average of the concurrent SMAP and SMOS products at high resolution (Figure 5.3). Lower correlations are obtained during summer season (0.62, 0.64 and 0.65, for SMAP L2 AP1, SMAP L2 AP3 and BEC SMOS L4, respectively). This is consistent with the results of previous studies [27]. Slightly better results are obtained for SMAP in terms of R (and bias) 0.88 (0.014 m^3/m^3), against SMOS, 0.79 (0.04 m^3/m^3) calculated as an average of DJF, MAM and SON.

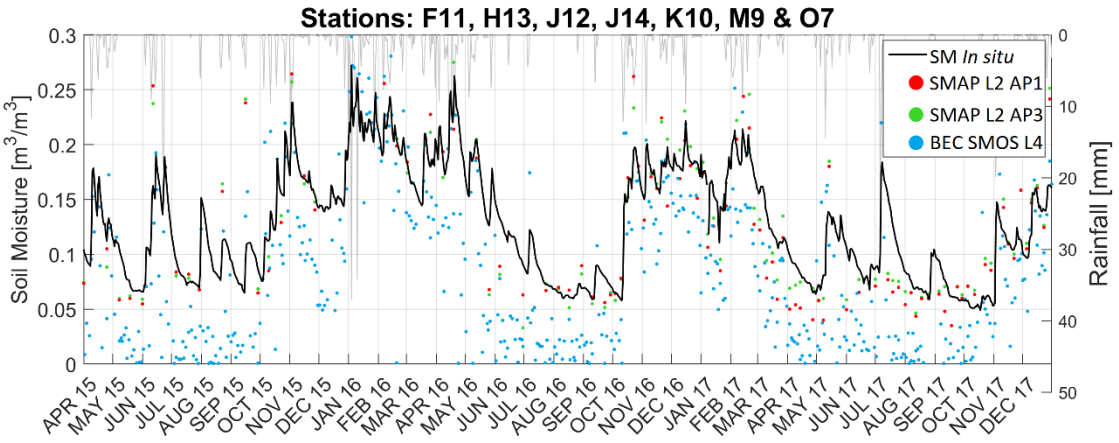

Figure 5.3 Daily evolution of *in situ* SM (black) and the three high-resolution SM products (SMAP L2 AP1 at 1 km, red; SMAP L2 AP3 at 3 km, green; and BEC SMOS L4 at 1 km, blue). The samples are obtained by daily averaging the SM values of all the rainfed/fallow stations (F11, H13, J12, J14, K10, M09 and O07) for the *in situ* data, and by averaging the SM values of concurrent pixel for the remote sensing data. Rainfall events and its intensity are plotted in gray.

Table 5.6 Statistics (N [-], R [-], RMSE [m^3/m^3], uRMSE [m^3/m^3] and bias [m^3/m^3]) obtained from the comparison of *in situ* SM with the SM values of the concurrent pixels from the SMOS and SMAP products: SMAP L2 AP1 at 1 km (left), SMAP L2 AP3 at 3 km (center) and BEC SMOS L4 at 1 km (right), from April 2015 to December 2017, for the different seasons of the year and also for the entire study period (ESP). Statistics are obtained after daily averaging the time series of rainfed/fallow stations (F11, H13, J12, J14, K10, M9 and O7) and the pixels that contain these stations.

	***In situ* vs SMAP L2 AP1**					***In situ* vs SMAP L2 AP3**					***In situ* vs BEC SMOS L4**				
	N	**R**	**RMSE**	**uRMSE**	**Bias**	**N**	**R**	**RMSE**	**uRMSE**	**Bias**	**N**	**R**	**RMSE**	**uRMSE**	**Bias**
DJF	17	0,87	0,056	0,053	0,018	17	0,92	0,060	0,048	0,035	88	0,87	0,056	0,047	-0,031
MAM	22	0,91	0,037	0,033	-0,017	22	0,90	0,027	0,026	-0,008	119	0,72	0,071	0,041	-0,058
JJA	26	0,62	0,037	0,035	-0,012	27	0,64	0,035	0,035	-0,006	128	0,65	0,073	0,030	-0,067
SON	33	0,85	0,034	0,033	0,008	33	0,86	0,034	0,032	0,011	125	0,78	0,052	0,041	-0,032
ESP	98	0.86	0.040	0.040	-0.002	99	0.87	0.039	0.038	0.006	460	0.82	0.064	0.043	-0.048

5.3.2 Analysis of the SM spatial patterns

The study carried out in the previous section shows a general agreement between the temporal dynamics of all the considered SM products regardless of their spatial resolution (low resolution: ~40 km, 9 km; versus high resolution: 3 km, 1 km). However, as it can be seen from the maps shown in Figure 5.4, there are clearly visible differences in the spatial patterns attained by the downscaled SMAP and SMOS high-resolution products. In this section, these differences are examined and specific analyses are conducted to test two hypotheses: (i) that they are due to differences in the multi-sensor synergies they are built upon (optical-microwave or active/passive) and (ii) that they are due to the rationale of the approach (e.g., whether the downscaling is conducted in brightness temperature- or in the soil moisture-space).

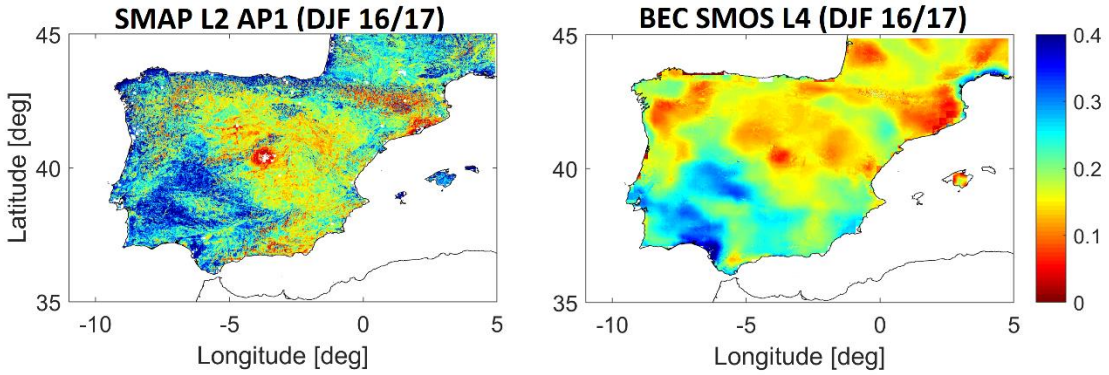

(**a**) (**b**)

Figure 5.4 Temporally-averaged map of daily (a) SMAP and (b) SMOS products at 1 km over the Iberian Peninsula for the period December 2016 to February 2017.

A. Comparison of SM enhanced resolution products

Figure 5.5 shows the daily differences (map and histogram) between the SMAP and SMOS products at 1 km (SMAP L2 AP1 minus BEC SMOS L4) for the whole study period. The mean of these differences is minimal (of 0.03 m^3/m^3), and their STD is also low (of 0.09 m^3/m^3). The same behavior is observed when this study is performed on a year-to-year basis (see appendix Figure App A.1). In addition, the same analysis was conducted per season, and it was found that daily differences ranged between 0.05 and 0.06 m^3/m^3 in mean and from 0.05 to 0.07 m^3/m^3 in STD (see appendix Figure App A.2). These results affirm that the differences cannot be explained by seasonal or yearly differences (e.g., dry or wet year). Yet, the temporally-averaged map of daily SM differences (Figure 5.5a) reveals that there is a geographic spatial pattern that persists over time when comparing the two high-resolution products, with higher differences located in the north, northwest and west of the Iberian Peninsula, in close correspondence to forested areas (Figure 5.6).

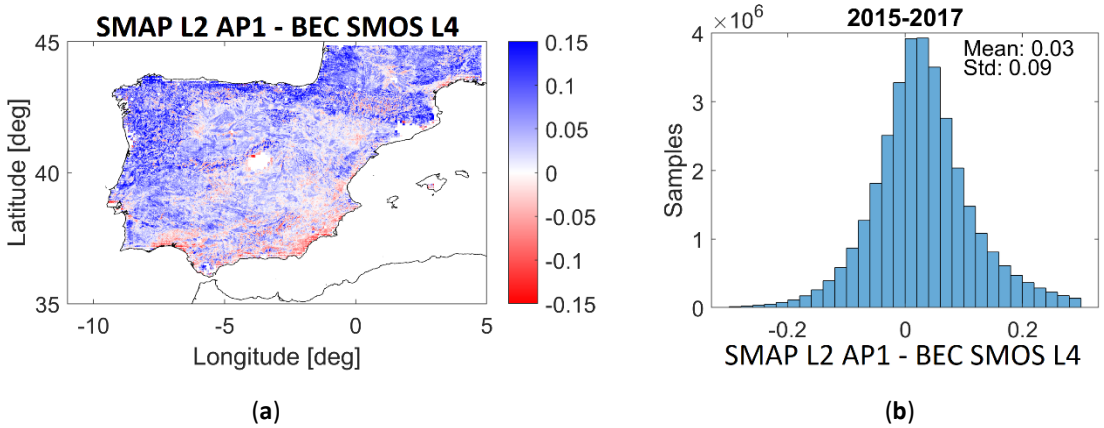

Figure 5.5 (a) Temporally-averaged map of daily SM differences between SMAP and SMOS at 1 km (SMAP L2 AP1 minus BEC SMOS L4) and (b) histogram of daily SM difference maps, for the period April 2015 to December 2017.

The possible dependence of the differences between the two downscaled products on the land cover was further examined. Pixels from the temporally-average map of SM differences (Figure 5.5a) were grouped for the most common land cover classes (agriculture, forest and grassland according to the CCI LC map) and their histograms were analyzed (see Figure 5.6). In general, pixels with SM differences (SMAP minus SMOS) equal or above 0.1 m^3/m^3 are located within forests (66.71% of the pixels) or agriculture (22.47% of the pixels). The largest SM differences are observed for forest land cover, with a mean of 0.04 m^3/m^3 and a STD of 0.11 m^3/m^3.

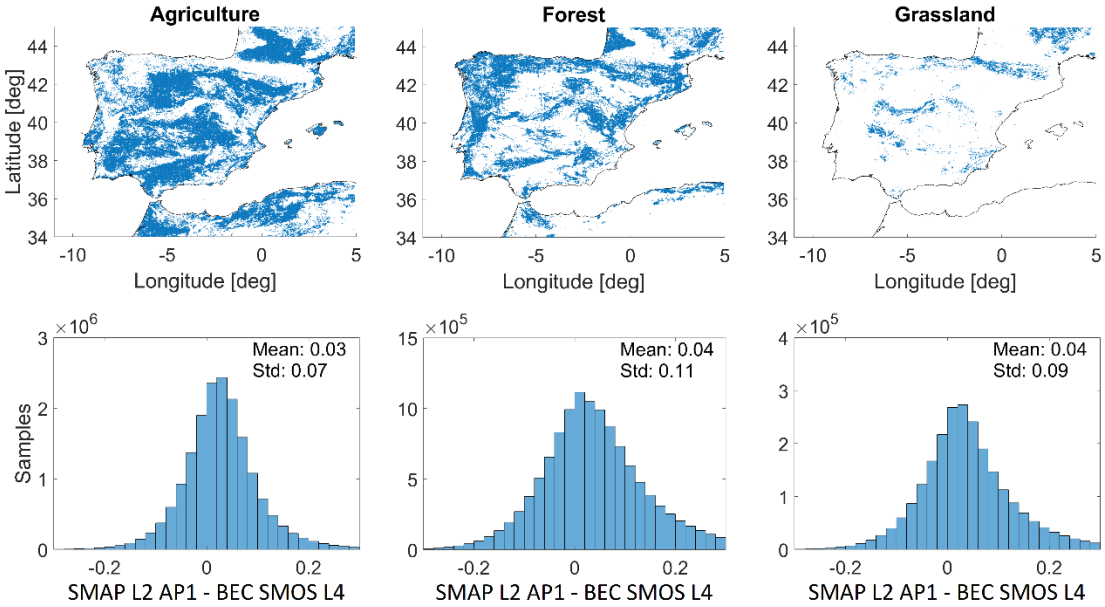

Figure 5.6 (First row) The three most common (according to the CCI LC map) land covers types over the Iberian Peninsula: (a) agriculture, (b) forest, and (c) grassland. (Second row) Histograms of the daily SM differences (SMAP L2 AP1 minus BEC SMOS L4) for the respective land covers.

Land cover only partially explains the SM differences between the SMAP and SMOS products at 1 km. Results show that SM values provided by SMAP over the Iberian Peninsula are systematically higher than the ones provided by SMOS (Figure 5.5), although the absolute difference is minimal (mean difference of 0.03 m^3/m^3). The SM values of SMOS exceed those of SMAP less often and with lower intensity, but this effect is mostly occurring in coastal areas. The same SM difference pattern is found in the temporally-averaged map of daily T_B differences (SMAP minus SMOS T_B) shown in Figure 5.7. Since the spatial pattern is already present at T_B level, it can be concluded that it was not introduced by the SMAP or SMOS downscaling methodologies. Figure 5.7b shows the histogram of the daily T_B differences, with an absolute mean value of 2.92 K. In order to understand to what extent, the 2.92 K cold bias could affect SMAP or SMOS SM retrievals, it was analyzed the study of Davenport et al. [87], who conducted a sensitivity analysis of SM and stated that a bias of around 3° [K] in T_B approximately corresponds to 3-4 [vol.%] error in estimating volumetric soil water content, which would fit to the bias ranges reported in this study.

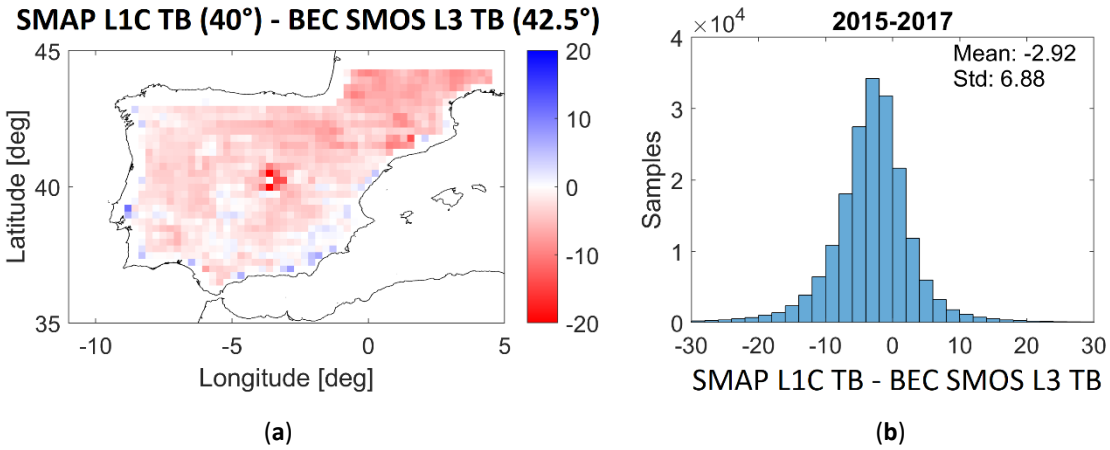

Figure 5.7 (a) Temporally-averaged map of daily T_B differences between SMAP (40° incidence angle) and SMOS (42.5° incidence angle) at 25 km and (b) histogram of daily T_B difference maps, for the period from April 2015 to December 2017.

B. Downscaling impact on SM differences

Figure 5.8 and Figure 5.9 show the maps and histograms of daily SM differences between SMAP L2 AP1 and SMAP L2 (1 km versus 36 km), and between BEC SMOS L4 and BEC SMOS L3 (1 km versus 25 km), respectively. The mean (and STD) obtained after calculating the differences along the complete study period is -0.01 m^3/m^3 (0.07 m^3/m^3) for SMAP, and of ~0 m^3/m^3 (0.03 m^3/m^3) for SMOS. Although mean differences are minimal over the whole domain for both sensors, the resulting average map of the SMAP SM differences reveal some underlying spatial patterns. The highest positive differences obtained for SMAP are concentrated in the forested regions (Figure 5.6) and the highest negative differences appear near the coast and in areas of complex topography. This is possibly due to the reduced sensitivity of the Sentinel-1 signal at C-band to SM in presence of significant vegetation backscattering. According to [150], this leads to a decrease in T_B after downscaling and therefore to an increase in estimated SM. Also, the temporally-averaged map of SMOS SM differences exhibits an underlying boxing effect that can be explained by the use of SMOS SM at low resolution as a reference to obtain the downscaling parameters (see Equation (4.1)), as previously observed in [27,30]. However, this effect is nonetheless negligible and does not have a significant impact in the enhanced resolution product.

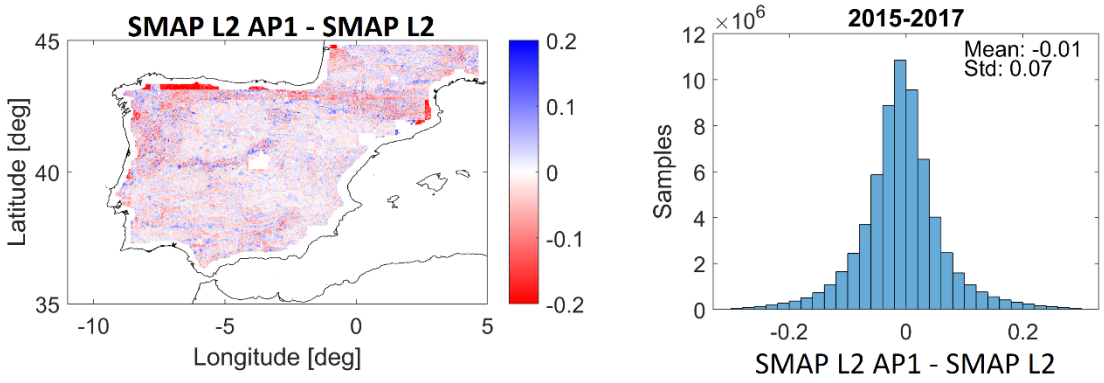

(**a**) (**b**)

Figure 5.8 (a) Temporally-averaged map and (b) histogram of daily SMAP SM differences (SMAP L2 AP1 at 1 km minus SMAP L2 at 36 km), for the period from April 2015 to December 2017.

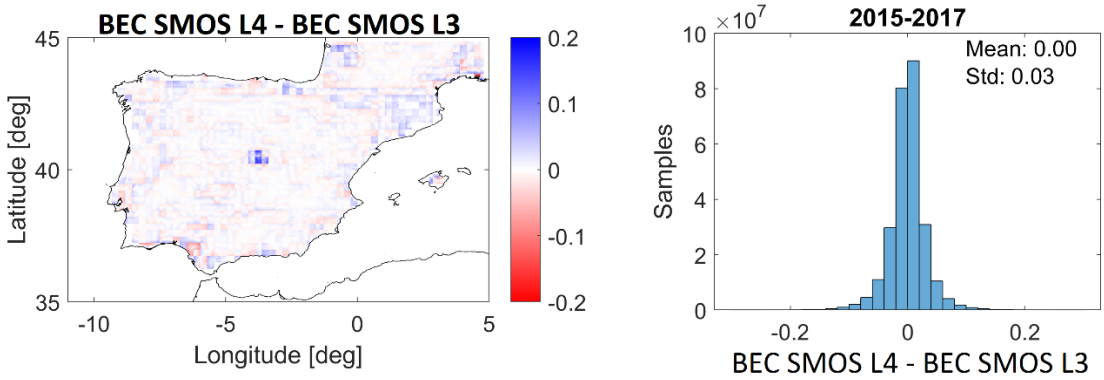

(**a**) (**b**)

Figure 5.9 (a) Temporally-averaged map and (b) histogram of daily SMOS SM differences (BEC SMOS L4 at 1 km minus BEC SMOS L3 at 25 km), for the period from April 2015 to December 2017.

5.4 Discussion

Validation and comparison of SM satellite products using *in situ* networks data is a difficult task. Many factors can intervene and must be taken into account when interpreting the obtained results. Importantly for this work, it is essential to understand that the representativeness of each satellite dataset plays a crucial role when validated. In the case of the SMAP and SMOS products presented in this chapter, the data is stored in maps with spatial grid cells of 36, 25, 9, 3 or 1 km. The information contained in these cells represents an areal-averaged value, while the *in situ* measurements represent an isolated data point. Measurements of the most representative (in terms of land cover within satellite cells) SM *in situ* stations have been averaged (Figure 5.3 and Table 5.6) to validate the large scale SM estimates provided by the satellites [77,198]. It is found that validating satellite-based estimates works best with *in situ* measurements in locations where the dominant land cover of the satellite footprint prevails.

Besides the representativeness error due to the comparison of point-scale versus areal-averaged measurements, the mismatch between satellite observations and *in situ*

measurements can also be originated by the penetration depth of microwave frequencies at L-band, which is of 5 cm on average but also depends on the SM content itself (with greater penetration on drier soils [9]). In contrast, measurements of the REMEDHUS network probes are placed at a depth of 5 cm. This could be one of the reasons explaining the low correlations obtained under water-limited conditions (see Table 5.6 for JJA), when the soil surface dries out and therefore *in situ* sensors might measure slightly wetter values than satellites. Moreover, the surface temperature used in SMAP and SMOS retrievals is derived from models. While the SMAP surface temperature is derived from the NASA GEOS-5 model, the SMOS surface temperature is obtained from the ECMWF model. An underestimation of the surface temperature leads to an overestimation of the soil emissivity and, as a result, to an underestimation of the SM. This could explain the dry bias shown by the SMAP and the SMOS products with respect to the most representative *in situ* stations in REMEDHUS. Our results are in line with previous studies which have also reported this dry bias when comparing the SM SMOS products (at high and low resolution) with the *in situ* data provided by the Valencia Anchor Station (VAS, in Spain), the Soil Moisture Observing System - Meteorological Automatic Network Integrated Application (SMOSMANIA, in France) and OzNet (Australia) network [27,30,199]. In Figure 5.2 SMOS SM estimates with a very low value close to zero can be found, mostly during the summer periods. These values have not been filtered in this study, as the product quality flags do not report they are measurement errors.

Some differences between the SMAP and the SMOS products are intrinsic to the instrument they carry; while SMOS uses an interferometric radiometer with 69 receivers distributed on an Y-shaped antenna array and measurements at different incidence angles are obtained in each snapshot, SMAP uses a large rotating antenna and measurements are performed at a constant incidence angle of 40°. The SM retrieval algorithms have been tailored to the SMAP and SMOS instrument characteristics, and they involve the use of dedicated techniques to reduce or correct disturbing factors (e.g., surface roughness, soil temperature and vegetation canopy). In a global study conducted by Burgin et al. [200] the SMAP SM was compared to the one provided by SMOS, Aquarius, Advanced Scatterometer (ASCAT) and AMSR2. Overall, they found that SMAP and SMOS appeared to be the most similar among the five SM products, in terms of uRMSE and R, excluding forested areas where some discrepancies were found, with SMOS being generally slightly wetter than SMAP. For the particular case of the Iberian Peninsula, which is mostly covered by crops and forested areas (according to the CCI land cover map), it was shown that SMAP is generally wetter than SMOS. Although differences are minor, it was shown that they are already present at the T_B level (Figure 5.7), and are also translated to the SMOS and SMAP derived products at enhanced spatial resolutions (Figure 5.5). Burgin et al. [200], indicate that a highly potential cause of the mismatch between the SMAP and the SMOS products is the use of different ancillary data in the retrieval algorithm. Although both algorithms are based on the $\tau - \omega$ model they use different land cover maps to select the albedo, roughness coefficient and the vegetation opacity; SMAP uses the IGBP LC [201], and SMOS uses the ECOCLIMAP [202]. This could explain the differences observed between the original SMAP and the SMOS products (~40 km), but also between the satellite observations and the *in situ* measurements along the whole study.

Focusing on the enhanced resolution SM products, they allow us to develop applications that will otherwise not be possible using exclusively SMAP and SMOS products at their original resolutions (~40 km). However, it was shown that even the highest resolutions (3 km and 1 km) of SM maps may not be completely suitable for local or regional applications if the study area is small and the land cover is not representative of the SMAP or SMOS pixel to which it belongs (Figure 5.2a and Figure 5.2b). In [203], Merlin et al. proposed a performance metric for SM downscaling methods and it was applied to the 1-km DISPATCH data in central Morocco. They showed that disaggregation applied to irrigated areas surrounded by drylands reduced the negative bias in SMOS observations at 1 km with respect to *in situ* data, but was not yet fully able to solve the sub-pixels variability in SM. The scientific contribution of the downscaled SMAP and SMOS products is undeniable, adding value in a wide range of applications e.g., the prevention management of insect pests [43], the prevention of forest fires [44,45] and the early detection of wild fires [204], but further improvements are needed to reduce the uncertainties when merging information from different sensors.

5.5 Summary and conclusions

In this study, several space-borne SM products (SMAP and SMOS), and their derived products at enhanced spatial resolution (SMAP/Sentinel-1 and SMOS/ERA5/MODIS) have been compared in space, and time.

For the temporal comparison, the *in situ* information of the REMEDHUS network has been used as a benchmark. In order to study the behavior of the remotely sensed data in different scenarios, a variety of *in situ* SM stations located in areas with different land uses (fallow, forest-pasture, vineyard, irrigated and rainfed) were selected. It has been shown that, independently of the spatial resolution, all the SM products were able to capture significant rainfall events (e.g. the rainfall event occurring in January 2016, Figure 5.2), and seasonality patterns (summers with low and winters with high SM values, Figure 5.2 and Figure 5.3). However, even the highest-resolution product used in this study (1 km) is not fine enough to capture local differences that are not dominant within the pixel scale, like the small irrigated areas where station K13 is located (Table 5.3 and Table 5.5). Consequently, when comparing the remotely sensed data with REMEDHUS measurements it is crucial to understand the representativeness of one *in situ* station within the satellite footprint. *In situ* SM measurements are representative at the point scale and are highly sensitive to both the soil characteristics and the effects of precipitation. There are multiple strategies to upscale *in situ* soil moisture measurements for comparison with satellite-based estimates [205,206]. In this study, it was decided to average the SM values of the most representative (in terms of prevailing land cover) *in situ* stations within the satellite footprint. One of the best results when comparing low-resolution as well as high-resolution SMAP/SMOS-based estimates with the *in situ* measurements, are obtained for the stations H13 and O07, which are located in regions with rainfed or fallow land use (the most common land uses in REMEDHUS). On the contrary, the worst results were obtained over stations J3 (vineyard) and K13 (irrigated), which represent only a minor land cover fraction within the footprints (Table 5.4).

Statistically, the differences between the SMAP and SMOS products are considerably low (Table 5.3 and Table 5.5) with a slightly worst performance in terms of correlation (~0.6) during the summer season. In addition, SMOS shows an important bias (-0.067 m^3/m^3) for this period.

Concerning the spatial analysis, the high-resolution (downscaled) SMAP (passive/active) and SMOS (passive/optical) products have been compared across the Iberian Peninsula. Overall, SMAP is slightly wetter than SMOS, especially in the North, North-West and West of the Iberian Peninsula. These differences are more pronounced over forested areas, which may be due to the fact that the microwave (radar) signal at C-band used in the SMAP product is not able to penetrate through dense (forested) vegetation [150,207]. Moreover, differences between the two products can also be seen at the brightness temperature level.

This satellite inter-comparison study has provided and confirmed insights into the SMOS and SMAP multi-scale SM products that are currently being distributed. These products are required in a wide spectrum of application and research studies, generally at the best radiometric accuracy and spatial resolution possible. Over the Iberian Peninsula, it has been shown that all products generally agree in their temporal dynamics, with lowest performances in summer, and SMAP-derived products being wetter than SMOS ones. Yet some differences in spatial patterns are observed in the high-resolution products, linked to the fine-scale information they use and the multi-sensor synergies employed, especially in forested areas. In future studies, the presented analysis can be extended to other regions of the world that have a sufficiently dense SM network to establish reliable estimates at multi-scale resolutions. Also, the proposed spatio-temporal analysis can be widened to global scales with the use of sparse *in situ* networks.

The content of this chapter was published in a journal [208].

Chapter 6

Impact of the incidence angle diversity on soil moisture

Incidence angle diversity of space-borne radiometer and radar systems operating at low microwave frequencies needs to be taken into consideration to accurately estimate SM across spatial scales. In this chapter, the single channel algorithm is first applied to SMOS T_{B_V} to estimate SM at coarse resolution (25 km) and develop a land use-specific and incidence angle (32.5°, 42.5° and 52.5°)-adaptive calibration of radiative transfer parameters ω and h_s. These effective parameters are used together with fine-scale multi-angular Sentinel-1 backscatter in a single-pass active/passive downscaling approach to estimate T_{B_V} at fine scale (1 km) for each SMOS incidence angle. These T_{B_V} are finally inverted to obtain the corresponding high-resolution SM maps. Results over the Iberian Peninsula for the year 2018 show an increasing trend of ω, and a decreasing trend of h_s with SMOS incidence angle, with almost no variability of ω across land cover types. The active/passive covariation parameter is shown to increase with SMOS incidence angle and decrease with Sentinel-1 incidence angle. Coarse and fine T_{B_V} maps from the three SMOS incidence angles show similar distributions (mean differences below 0.38 K). The resulting high-resolution SM maps show maximum mean and standard deviation differences of 0.016 and 0.015 m^3/m^3, respectively, and compare well with *in situ* measurements. The results indicate that current model-based active and passive microwave approach used to estimate SM can be adequately adapted to account for the incidence angle diversity of planned missions such as the Copernicus Microwave Imaging Radiometer (CIMR), the Radar Observing System for Europe in L-band (ROSE-L) and Sentinel-1 next generation.

The data used in this chapter are presented in Section 6.1. Section 6.2 details: (i) the methodology followed to calibrate ω and h_s, (ii) how the downscaling approach is implemented to estimate T_{B_V} at fine scale, and (iii) how the retrieval approach is applied to obtain the high-resolution SM maps. The results are presented and discussed in Section 6.3. Finally, Section 6.4 summarizes the main conclusions and perspectives from this study.

6.1 Datasets

Table 6.1 summarizes the data used in this chapter, including information from SMOS (T_B and SM), SMAP (SM, T_B, τ, T_s, VWC, σ_0, and CF), MODIS (LC), ECMWF (SM) and from the REMEDHUS network (SM and precipitation).

For the purpose of this chapter, the IGBP LC map (Section 3.2.3) was aggregated from the original 500 m to 25 km using the most frequent class, and the 17 classes proposed by the IGBP were aggregated into the four main land cover types (savannas, croplands, grasslands and shrublands) within the Iberian Peninsula. Figure 6.1 shows the resulting land cover map over the Iberian Peninsula.

Table 6.1 Summary of the data used in this chapter. *Provided by the Water Resources Research group of the University of Salamanca.

Source	Variable	Product	Spatial Frequency	Temporal Frequency	Reference
SMOS	SM	BEC SMOS L3	25 km	Daily	[156]
	T_B	BEC SMOS L3	25/12.5 km	Daily	[156]
SMAP	SM	SMAP L2	36 km	Daily	[48]
		SMAP L2E	9 km	Daily	[157]
		SMAP AP3	3 km	Daily	[158]
		SMAP AP1	1 km	Daily	[158]
	T_B	SMAP L1C	36 km	Daily	[48]
	τ	SMAP L2E	9 km	Daily	[157]
		SMAP L2 AP1	1 km	Daily	[158]
	T_s	SMAP L2E	9 km	Daily	[157]
		SMAP L2 AP1	1 km	Daily	[158]
	VWC	SMAP L2 AP1	1 km	Daily	[158]
	σ_0	SMAP L2 AP1	1 km	Daily	[158]
	CF	SMAP L4 LMC	9 km	Static	[160]
MODIS	LC	MCD12Q1 v6	500 m	Annually	[182]
ECMWF	SM	ERA5-land	9 km	Hourly	[170]
REMEDHUS	SM	REMEDHUS	*In situ*	Hourly	[77]
	Precipitation	REMEDHUS	*In situ*	Hourly	*

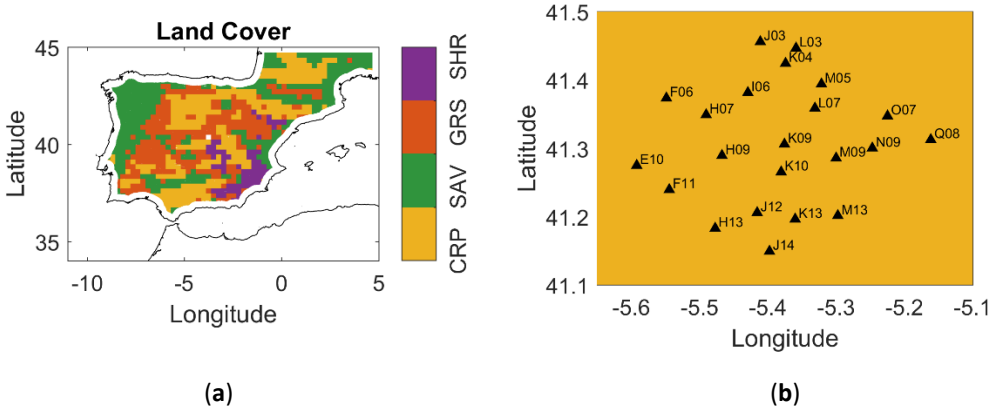

(**a**) (**b**)

Figure 6.1 (a) Classification map of the four most common land cover types over the Iberian Peninsula: croplands (CRP), savannas (SAV), grasslands (GRS) and shrublands (SHR), adapted from MODIS IGBP. (b) Zoom into the region that contains the 22 REMEDHUS validation sites.

6.2 Methodology

This section is intended to: (i) explain how the data are prepared to work with in the following sections; (ii) describe the SCA$_V$ algorithm applied to the SMOS T_{B_V} to calibrate ω and h_s, and explain how this calibration has been carried out and how to validate the resulting optimal parameters ω and h_s; (iii) introduce and explain how the active/passive microwave single-acquisition disaggregation technique is applied, combining SMOS and Sentinel-1 data to obtain a fine-scale (1 km) SMOS T_{B_V}; and (iv) describe how the SCA$_V$ is applied to retrieve the high-resolution SMOS SM maps.

6.2.1 Data preparation

The flowchart in Figure 6.2 shows the steps followed to: (i) calibrate the ω and h_s parameters (top dashed block from Figure 6.2); (ii) downscale the SMOS T_{B_V} to 1 km (middle dashed block from Figure 6.2); and (iii) retrieve the high-resolution SMOS SM (bottom dashed block from Figure 6.2). The flowchart includes the input parameters used in each step and the grid pixel size to which all input data are expressed in order to operate with them. In the ω and h_s calibration step, all data are aggregated to a 25-km EASEv2 grid (see "Aggregation to 25 km" block in Figure 6.2), while for the other two steps, the data are resampled to a 1-km EASEv2 grid (see "Resampling to 1 km" block in Figure 6.2) or aggregated to a 12.5-km EASEv2 grid (see "Aggregation to 12.5 km" block in Figure 6.2). The aggregation is done by averaging the values of all the samples contained within each pixel of the target grid. For the 1-km resampling, nearest neighbor interpolation is used.

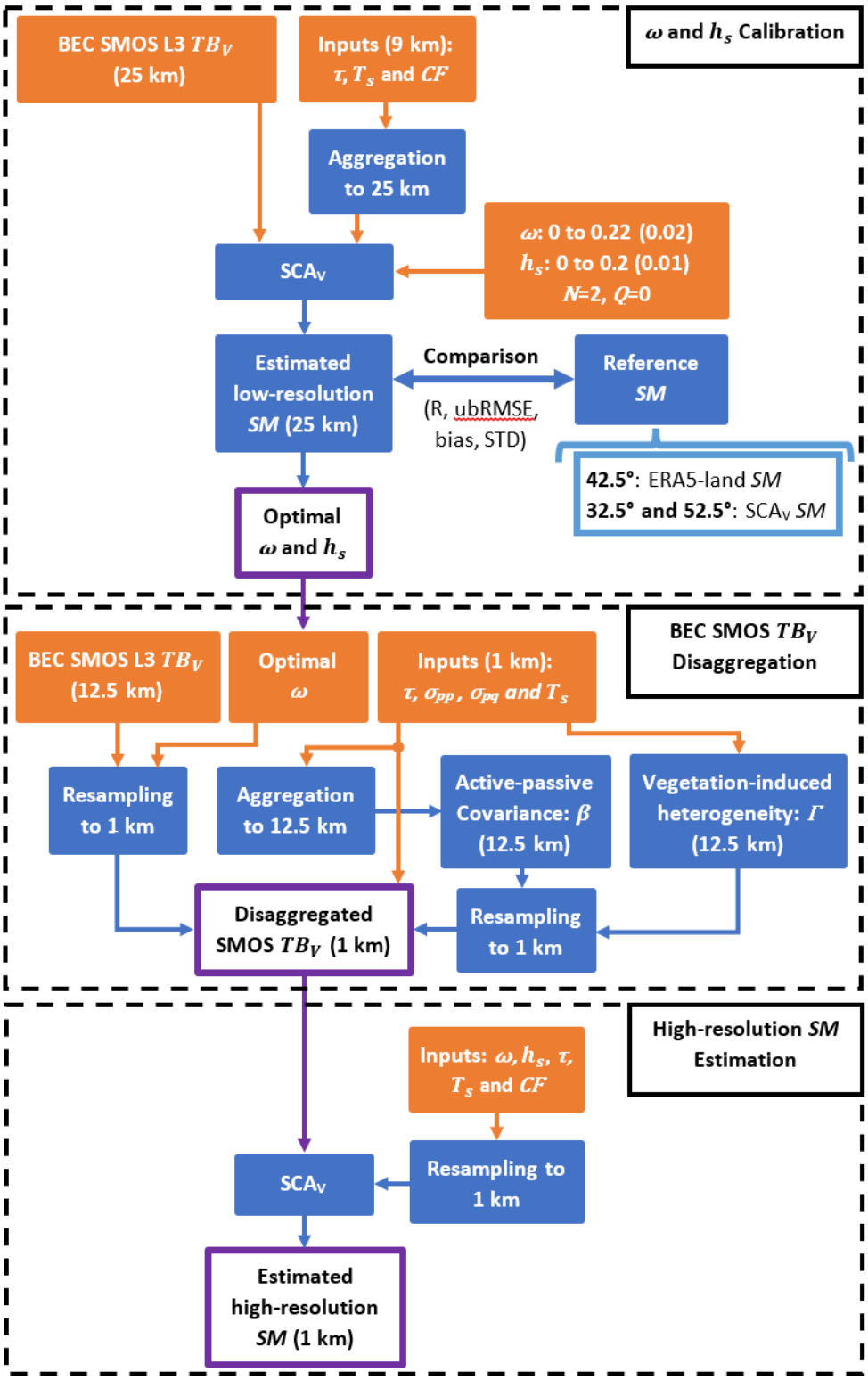

Figure 6.2 Three main steps to obtain the SMOS high-resolution SM maps (dashed black blocks): (i) the calibration of ω and h_s, (ii) the disaggregation of the BEC SMOS T_{B_V}, and (iii) the retrieval of the SMOS high-resolution SM maps. The orange boxes are the required input parameters for each of the three main analyses. The blue boxes are the different operations applied to the input data. The purple boxes are the results obtained at the end of each of the three main steps.

6.2.2 Single channel algorithm applied to SMOS T_B

Over the last years, a variety of SM retrieval approaches using L-band radiometry have been proposed (Section 2.2.5). Among these, those that use both horizontal and vertical polarizations (e.g., DCA, MT-DCA, LPRM or SMOS-IC) can simultaneously retrieve SM and another parameter, usually τ. Furthermore, these techniques can benefit from the high sensitivity to SM due to the high contrast (Figure 6.3) between T_{B_H} and T_{B_V} at highest incidence angles [50,209]. In a previous study [210], we tested the LPRM algorithm (Section 2.2.5A) to calibrate ω and h_s parameters over the Iberian Peninsula for 2016. Very good performance was obtained when comparing the resulting SM maps with the SM observations from the REMEDHUS network (Figure 6.4), with R always higher than 0.81, a bias lower than 0.015 m^3/m^3 and an uRMSE of about 0.04 m^3/m^3 (SMOS target accuracy). Unfortunately, since Sentinel-1 only measures VV+VH polarizations over land, only disaggregated SMOS T_B at vertical polarization can be obtained with the active/passive approach proposed by Das et al. [117], as will be detailed in Section 6.2.3. For this reason, in this chapter, it was decided to use the SCA_V, which only needs T_B at vertical polarization to estimate SM from both coarse (SMOS) and fine scale (SMOS/Sentinel-1).

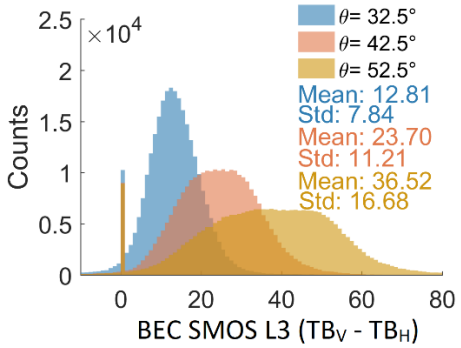

Figure 6.3 Histogram of differences between BEC SMOS L3 T_{B_V} and BEC SMOS L3 T_{B_H}, at 32.5° (blue), 42.5° (red), and 52.5°(yellow).

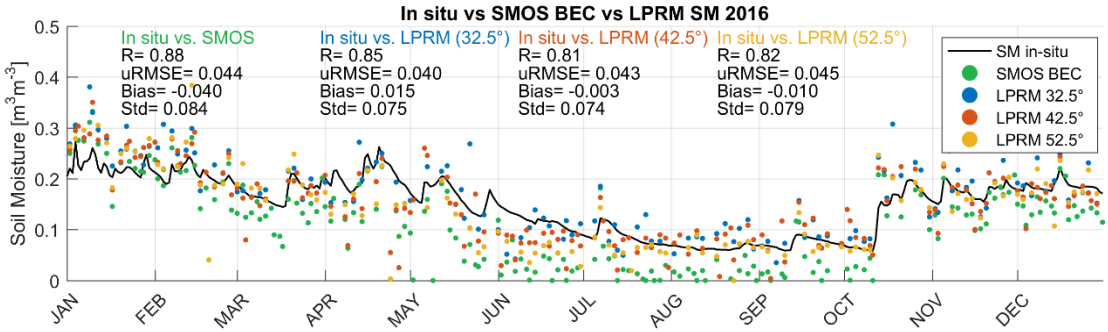

Figure 6.4 Time series of the *in situ* SM measurements (black); the three LPRM-retrieved SM products obtained with the optimal values of ω and h_1 for the incidence angles 32.5° (blue), 42.5° (red) and 52.5° (yellow); and the BEC SMOS L3 SM product (green). The statistical performance metrics of each product are also included. From [210].

The SCA allows to retrieve SM using T_s, T_B at one polarization and the optimal ω [211] and h_s values. It was already introduced in Section 2.2.5B, but for the sake of clarity, the main equations on which it is based are reproduced here. The SCA is based on the $\tau - \omega$ model [212]:

$$TB_p = e_{r,p}T_s\gamma + (1-\omega)T_c(1-\gamma) + (1-e_{r,p})(1-\omega)(1-\gamma)T_c\gamma \quad (6.1)$$

where the subscript p refers to the polarization (vertical in our case), $\gamma = e^{-\tau/\cos\theta}$ is the transmissivity, θ is the SMOS incidence angle (32.5°, 42.5° or 52.5°). T_c stands for the canopy temperature. Thermal equilibrium is assumed ($T_s \approx T_c$) in the SCA, an approximation already used in other microwave-based retrieval algorithms [49,79,117]. The emissivity of a rough surface (e_r) is calculated as follows:

$$e_{r,p(1)} = 1 - \left((1-Q_s)\Gamma^*_{s,p(1)} + Q_s\Gamma^*_{s,p(2)}\right)e^{-h_s cos^{n_{r,p}}(\theta)} \quad (6.2)$$

where the subscripts $p(1)$ and $p(2)$ are the two polarizations (vertical and horizontal), Q_s is the polarization mixing factor, $\Gamma^*_{s,p}$ is the smooth surface reflectivity calculated using the Fresnel equations, h_s stands for the soil roughness and $n_{r,p}$ represents the change in the angular dependence of the reflectivity due to soil roughness. The polarization mixing factor is assumed very small for L-band, here it has been set to Q_s=0 to simplify the model [50,62,96,213]. The Fresnel equations require the dielectric constant that is estimated with the Mironov mixing model [57] (see Section 2.2.2C) and $n_{r,p}$ is set to 2 [213].

A. Multi-angular parametrization

The steps proposed below were followed to obtain the optimized ω and h_s values:

STEP 1) Sensitive ranges were considered for these parameters, with ω varying between 0 and 0.22 (in steps of 0.02), and h_s between 0 to 0.2 (in steps of 0.01). Daily SM was retrieved using the SCA_V for each pair of ω and h_s, and for each low-resolution pixel within the study area. In this step, the BEC SMOS L3 T_B was used at a 25-km grid, rather than a 12.5-km grid, due to the large number of SM estimates required.

STEP 2) The resulting SM time series obtained for each pixel of the study area were compared with the SM used as reference. Four statistical metrics [186] were considered: R, uRMSE, bias and STD. These statistics were averaged by land-cover type (savannas, croplands, grasslands and shrublands), and for each pair of ω and h_s. The optimal ω and h_s values are those that provide the best match, on average, of the resulting SM estimates compared to the reference SM.

The procedure described above was carried out independently for the three proposed incidence angles. At the 42.5° incidence angle, ERA5-land SM was used as reference due to its independence from SM estimates from remote sensing sensors. Observations are not directly used in the production of ERA5-land, but they may have an indirect influence through the atmospheric forcing used. Since a positive bias of ERA-land SM (ERA5-land SM minus *in situ*) was reported [170], optimization of ω and h_s at 42.5° was carried out using R and uRMSE exclusively. Furthermore, the optimal ω and h_s values were selected by comparing them with the results

obtained in previous studies that also use the SCA_V to retrieve SM at a similar incidence angle [213].

However, the procedure discussed above for the 42.5° incidence angle cannot be followed for the other two analyzed incidence angles (32.5° and 52.5°), for which there are no specifically calibrated values of SCA_V reported in literature. The optimization at 32.5° and 52.5° was then carried out using as reference the SM obtained through the SCA_V for the 42.5° incidence angle, instead of using ERA5-land SM. For these last two incidence angles, the R, uRMSE, bias and difference of STD, between the reference (SCA_V SM at 42.5°) and the estimated SM (at 32.5° or 52.5°) were used to find the SM as similar as possible for the three studied incidence angles.

B. Low-resolution SM and validation of retrieval model parametrization

Daily SM maps were obtained through the application of the SCA_V algorithm with the optimal values of ω and h_s to the SMOS T_{B_V} at 25 km. Time series of the three SM data streams (32.5°, 42.5° and 52.5°) over REMEDHUS were obtained and compared to the SM from *in situ* stations. Among all the stations available within the REMEDHUS network, seven were selected (F11, H13, J12, J14, K10, M9 and O7). They are located in a rainfed/fallow land use which is the most representative land use at the SMOS spatial scales, at low (25 km) and high resolution (1 km) [208]. Hourly recorded measurements of these stations were aggregated to a daily average [214] and used as a benchmark to validate the different products.

6.2.3 SMOS T_B disaggregated to 1 km

The active/passive downscaling algorithm [117] proposed by the JPL was originally developed to disaggregate the SMAP T_{B_V} maps. In this study, the SMAP T_{B_V} has been replaced by the BEC SMOS L3 T_{B_V} to adapt the algorithm as follows:

$$TB_{p,\theta,SMOS}(HR) = \left[\frac{TB_{p,\theta,SMOS}(MR)}{T_s} + \beta'(MR) \cdot \left\{\left[\sigma_{pp}(HR) - \sigma_{pp}(MR)\right] + \Gamma' \cdot \left[\sigma_{pq}(MR) - \sigma_{pq}(HR)\right]\right\}\right] \cdot T_s \quad (6.3)$$

where MR accounts for medium resolution (12.5 km) and HR for high resolution (1 km), $TB_{p,\theta,SMOS}(HR)$ is the disaggregated SMOS brightness temperature at 1 km, $TB_{p,\theta,SMOS}(MR)$ corresponds to the satellite observed single-angle SMOS brightness temperature at 12.5 km, $\sigma_{pp}(MR)$ and $\sigma_{pq}(MR)$ denote the Sentinel-1 co- and cross-polar backscatter aggregated at 12.5 km, $\sigma_{pp}(HR)$ and $\sigma_{pq}(HR)$ are the Sentinel-1 co- and cross-polar backscatter aggregated at 1 km, and Γ' and $\beta'(MR)$ are defined in the active/passive downscaling algorithm [117]. The Γ' parameter represents the vegetation-induced heterogeneity within the medium-resolution radiometer (12.5 km) pixel that is detected by the high-resolution (1 km) $\sigma_{pp}(HR)$ and $\sigma_{pp}(HR)$ radar observations [150]. Γ' is estimated as the slope of the linear regression between the high-resolution $\sigma_{pp}(HR)$ and $\sigma_{pq}(HR)$ values contained within a medium-resolution pixel [150,215]:

$$\Gamma' = \left[\frac{\partial \sigma_{pp}(HR)}{\partial \sigma_{pq}(HR)}\right]_{MR} \tag{6.4}$$

The $\beta'(MR)$ parameter represents the covariation between SMOS T_{B_V} and the Sentinel-1 backscatter (VV-VH) at medium resolution:

$$\beta'(MR) = \frac{\frac{TB_{p,\theta,SMOS}(MR)}{T_s} - (\gamma + (1-\omega)(1-\gamma))}{\sigma_{pp}(MR) - \Gamma' \cdot \sigma_{pq}(MR)} \tag{6.5}$$

The active/passive microwave covariation β' parameter of Equation (6.5) was derived in Jagdhuber et al. [150,215] based on electromagnetic modelling. It represents the change in emission for a unit change in backscatter. This study uses the observation-driven approach, where β' values are calculated for each overpass without requiring time series. The variables involved in the computation of β' are: ω, τ, T_s, σ and $TB_{p,\theta,SMOS}$. Optimal ω values at 25 km were obtained through the SCA_V retrieval algorithm for each incidence angle and for each land cover, as explained in Section 6.2.2A. The use of $TB_{p,\theta,SMOS}(MR)$ at each incidence angle, gridded at 12.5 km instead of 25 km, helped to minimize the boxing in the resulting disaggregated T_{B_V} (Equation (6.3)). The rest of these variables (T_s, τ and σ) were provided within the SMAP L2 AP1 product on a 1-km grid. In order to have all the inputs in the same grid and to enable easy data handling, they have been aggregated to a 12.5-km EASEv2 grid. β' has been calculated with the ancillary data described here and its behavior has been analyzed towards the selected three SMOS incidence angles (32.5°, 42.5° and 52.5°), the Sentinel-1 incidence angles, and the VWC.

Finally, Equation (6.3) is applied to obtain three SMOS T_{B_V} datasets with a spatial resolution of 1 km, one for each incidence angle.

6.2.4 High-resolution SM maps

To retrieve the SM at 1 km, from the disaggregated SMOS T_{B_V} (Section 6.2.3), the SCA_V model was applied. The required variables are: T_s, τ, CF, h_s, ω and $TB_{p,\theta,SMOS}(HR)$. T_s and τ are provided within the SMAP L2 AP1 product in a 1-km grid. CF is provided by the NSIDC in a 9-km grid. h_s and ω are obtained through the SCA_V algorithm, as explained in Section 6.2.2A, in a 25-km EASEv2 grid. In order to have all the inputs in the same grid, they have been resampled into a 1-km EASEv2 grid.

6.3 Results and discussion

This section is devoted to: (i) showing the optimal values of ω and h_s at three SMOS incidence angles (32.5°, 42.5° and 52.5°) for four land covers (savannas, croplands, grasslands and shrublands), and validating these parameters through the retrieved SM; (ii) analyzing both the resulting active/passive covariation (β') values and the disaggregated SMOS T_{B_V} maps at the

three analyzed incidence angles ; and (iii) showing preliminary results of high-resolution SM maps obtained from the disaggregated SMOS T_{B_V} at each incidence angle.

6.3.1 Performance of single channel algorithm applied to SMOS T_B

A. Calibration of multi-angular model parametrization

Figure 6.5 shows the mean R and uRMSE obtained through the comparison of the estimated SCA_V SM at the 42.5° incidence angle and ERA5-land SM, which is used as reference to calibrate ω and h_s parameters. Results are obtained independently for savannas, croplands, grasslands and shrublands. As a general trend, it can be seen that R decreases as ω increases for all land covers. For savannas and grasslands, the uRMSE decreases as the ω increases, while for croplands and shrublands it remains almost constant for the entire range of values. The effect of h_s on the results is minimal, both in R and uRMSE. Final calibration of ω and h_s at 42.5° was done according to previous studies in literature, by comparing our obtained results (Figure 6.5) with those obtained with the same SM retrieval algorithm at a similar incidence angle [213]. Table 6.2 shows the selected optimal values of ω and h_s at 42.5° for each land cover, and their respective performance metrics. The optimal value of ω is set to 0.6 for all the land covers, except for shrublands, which have a slightly lower value of 0.4. The optimal h_s fluctuates between 0.08 and 0.15. The highest mean R is obtained for grasslands and croplands (0.82 and 0.81, respectively) and the lowest one is received for shrublands (0.73). The mean uRMSE is about 0.05 m^3/m^3 considering the four land covers.

Table 6.2 Optimal ω and h_s values, and mean R and uRMSE between the retrieved SCA_V SM at the 42.5° incidence angle and the ERA5-land SM [170] obtained for four land covers (savannas, croplands, grasslands and shrublands), using all pixels over the Iberian Peninsula.

			θ=42.5°	
	ω	h_s	R	uRMSE
Savannas	0.06	0.09	0.78	0.053
Croplands	0.06	0.08	0.81	0.051
Grasslands	0.06	0.15	0.82	0.052
Shrublands	0.04	0.10	0.73	0.053

In order to find the optimal ω and h_s values at the other two analyzed SMOS incidence angles (32.5° and 52.5°), four statistics (R, uRMSE, bias and difference of STD) are computed between the retrieved SCA_V SM at 42.5° and the retrieved SCA_V SM at 32.5° and 52.5°, independently for each land cover type. Figure 6.6 shows the performance metrics for the savanna land cover, for the 32.5° (Figure 6.6a), and 52.5° (Figure 6.6b) incidence angles. At 32.5°, the R decreases while the uRMSE and the bias increases as ω increases. Again, the effect of h_s on the results is low, with slightly better statistical performance for higher values. At 52.5°, the optimal ω values are shifted to higher values, while optimal h_s is shifted to lower values. Note that even the highest values of STD differences (~0.015 m^3/m^3) are low enough to neglect this statistic when choosing

the optimal values of ω and h_s. Similar behaviors were displayed for the other land covers (Figure App B.1, Figure App B.2, and Figure App B.3). The optimal ω and h_s values at 32.5° and 52.5°, together with their respective statistics, are summarized in Table 6.3. The optimal values of ω range between 0.02 and 0.04, while h_s is comprised between 0.12 and 0.18, at 32.5°. At 52.5°, the optimal albedo value is set to 0.12 for all four land cover regions, and h_s ranges from 0.01 to 0.05. Both at 32.5° and 52.5°, the mean R is always equal or higher than 0.9. The mean bias reaches a peak of 0.016 m^3/m^3 at 52.5° for shrublands. Analyzing Table 6.2 and Table 6.3, an ascending trend is revealed for ω and a descending trend is found for h_s, as the SMOS incidence angle increases.

Table 6.3 Optimal ω and h_s values, and mean R, bias and STD difference, between the retrieved SCA_V SM at 32.5 / 52.5° incidence angles and the retrieved SCA_V SM at 42.5°, obtained for four land covers (savannas, croplands, grasslands and shrublands), using all pixels over the Iberian Peninsula.

	θ=32.5°						θ=52.5°					
	ω	h_s	R	uRMSE	Bias	Diff. Std.	ω	h_s	R	uRMSE	Bias	Diff. Std.
Savannas	0.04	0.18	0.9	0.058	0.004	0.009	0.12	0.03	0.92	0.056	0.003	0.008
Croplands	0.04	0.12	0.98	0.019	0.003	0.006	0.12	0.05	0.98	0.021	0.008	0.004
Grasslands	0.04	0.16	0.98	0.020	0.000	0.005	0.12	0.02	0.94	0.041	0.005	0.005
Shrublands	0.02	0.15	0.99	0.010	0.005	0.002	0.12	0.01	0.98	0.019	0.016	0.002

The retrieval algorithm used in this research (SCA_V) was the SMAP baseline from 2015 to 2021. In the SMAP algorithm [213], h_s values are slightly higher (0.125-0.156, 0.108, 0.156 and 0.11 for savannas, croplands, grasslands and shrublands, respectively) than those proposed in this study (Table 6.2). As it was already analyzed by Wigneron et al. [61], these h_s values used in SMAP have a narrower range compared to those used in the SMOS baseline algorithm [86], where h_s varies between 0.1 and 0.3. In other global studies, h_s is considered constant, as in Konings et al. [21], where the MT-DCA was applied to Aquarius data to retrieve SM, τ and ω at L-band by assuming a constant h_s of 0.13 in time and space. Regarding the ω, the SMAP algorithm uses a value of 0.05 for croplands, grasslands and shrublands, in line with those proposed in Table 6.2, and a slightly higher value of 0.08 for savannas. Moreover, a global scale study conducted by Van der Schalie et al. [79] applied the LPRM to SMOS observations for optimizing ω. An optimal ω of 0.12 was found, invariant in space and time, and independent of the tested incidence angles (from 42.5° to 57.5°). From Table 6.2 and Table 6.3, it can be seen that the retrieved ω values of this study are almost invariant with the IGBP LC classes. This low sensitivity was also detected by Fernandez-Moran et al. [49], where a global optimal value of ω= 0.10 was selected to estimate SM and τ from SMOS multi-angular data (from 20° to 55°), and by Karthikeyan et al. [216] where a global fixed value of ω=0.06 was assumed to estimate SM, τ and h_s from X-band AMSR-E observations.

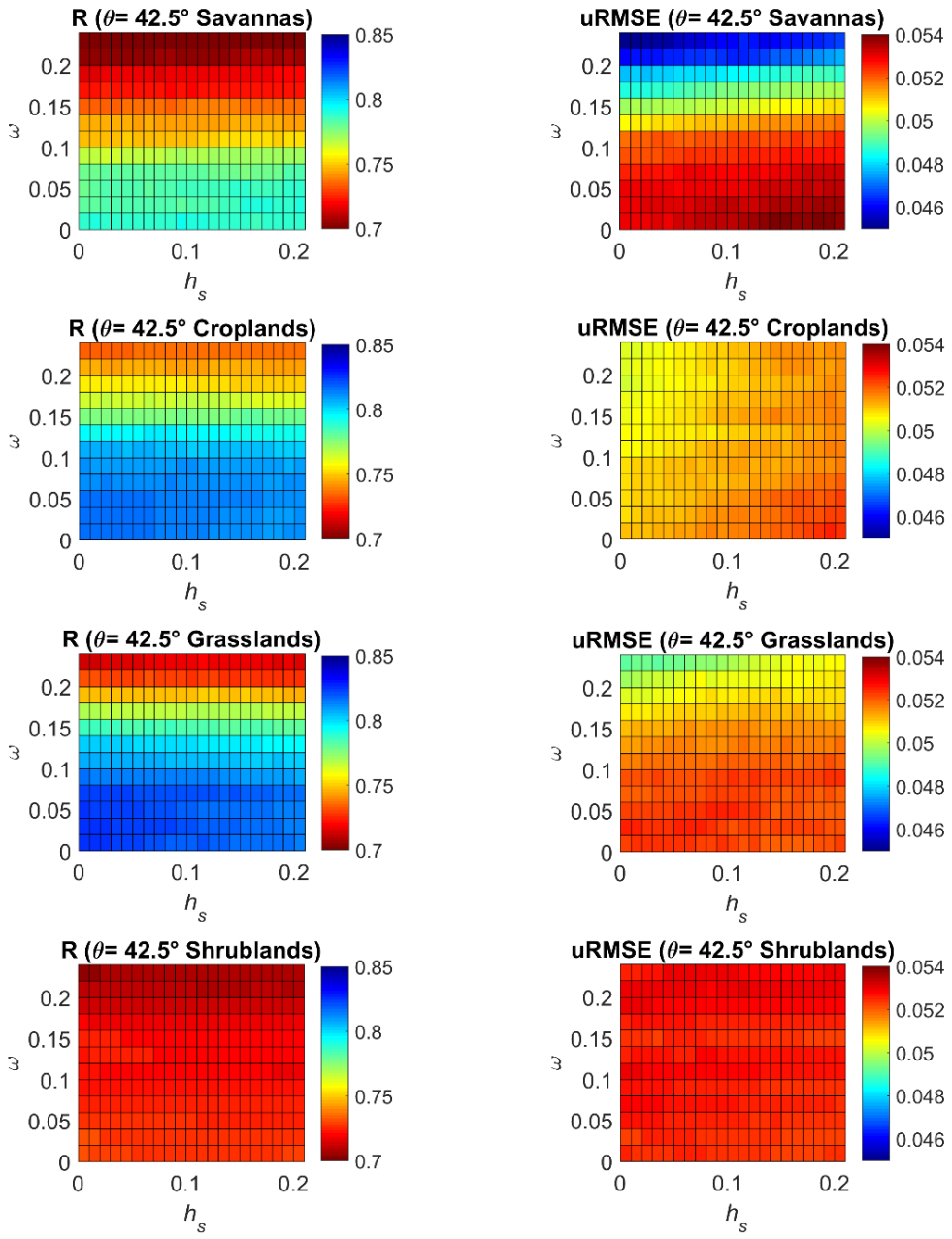

Figure 6.5 (a) Averaged R and (b) RMSE, obtained between SCA_V SM at 42.5° and ERA5-land SM for each pair of ω and h_s (see 6.2.2A STEP2). The results are obtained independently for savannas, croplands, grasslands and shrublands.

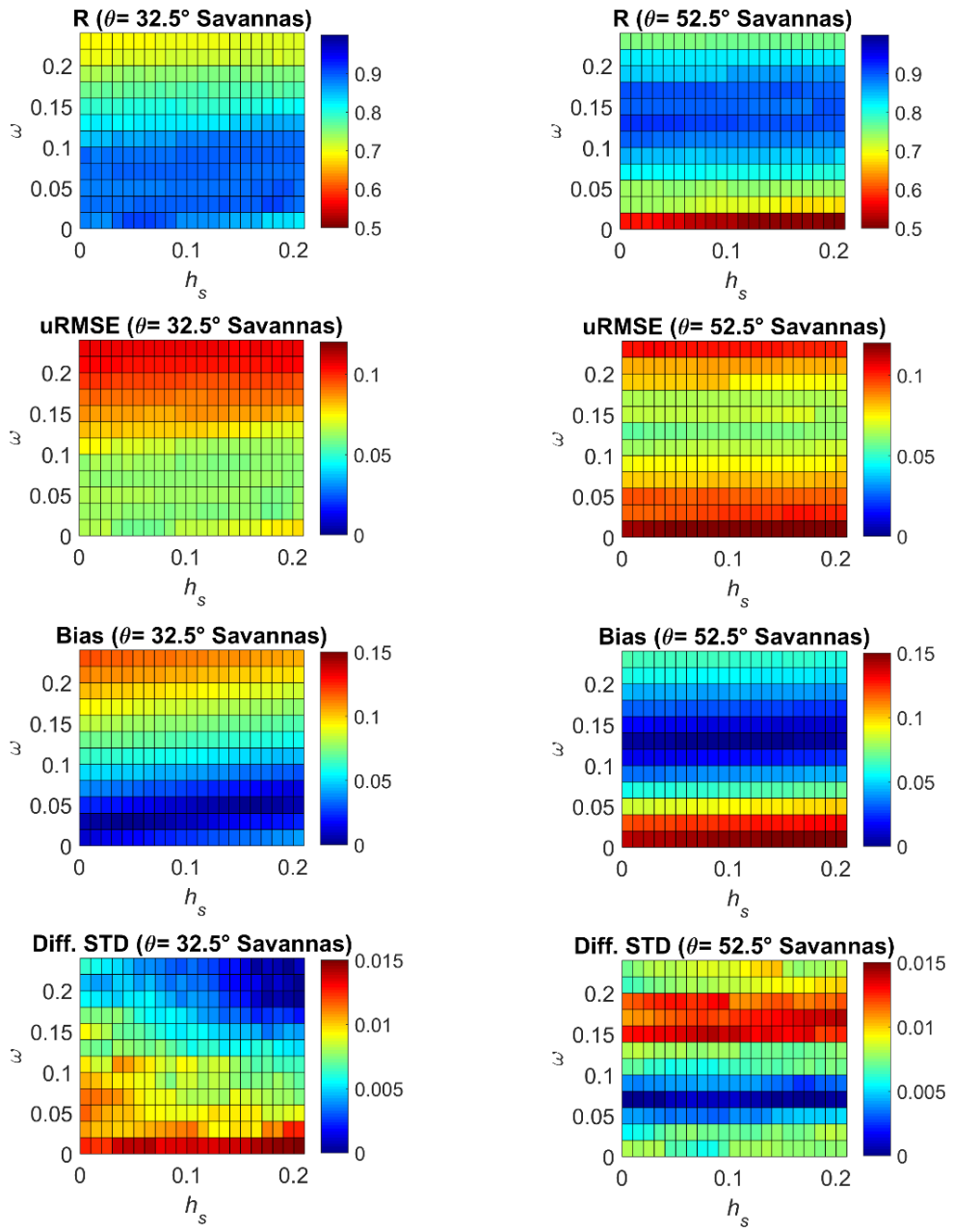

Figure 6.6 Averaged R, uRMSE, bias and difference of STD, obtained between SCA_V SM at 42.5° and SCA_V SM at (a) 32.5° and (b) 52.5°, for each pair of ω and h_s, for the savanna land cover (see Section 6.2.2A STEP2).

B. Validation of retrieved low-resolution SM

Figure 6.7 shows the temporal average of the retrieved daily SM maps and their respective histograms, for the year 2018, at each incidence angle. These results were obtained by applying the SCA_V to the 25-km SMOS T_{B_V} using the optimal ω and h_s parameterizations on Table 6.2 and Table 6.3. These maps show similar spatial patterns, mean and STD. The mean ranges from 0.162 to 0.169 m^3/m^3 and the STD from 0.035 to 0.038 m^3/m^3.

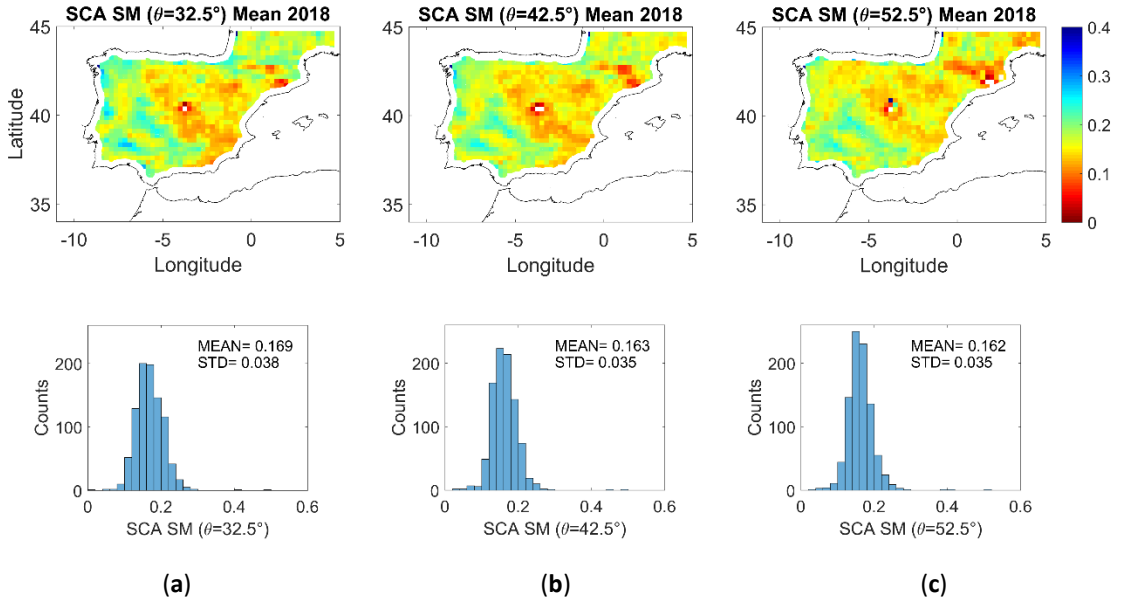

Figure 6.7 Maps of SCA_V SM averaged over time (2018) and their respective histograms, obtained at (a) 32.5°, (b) 42.5° and (c) 52.5° using the optimal values of ω and h_s presented in Table 6.2 and Table 6.3.

Figure 6.8 (top) shows the time series of multi-angular BEC SMOS L3 SM and single-angle retrieved SCA_V SM at 32.5°, 42.5° and 52.5°, which are compared with the *in situ* measurements from REMEDHUS using the R, uRMSE, bias and the STD metrics. Course of daily precipitation acquired over REMEDHUS is also shown in Figure 6.8 (bottom). The SCA_V SM retrieved at the three incidence angles independently agree reasonably well between each other, and show similar temporal patterns when compared to the BEC SMOS L3 SM product. They are able to capture wet up and dry down events. Regarding the performance of the SM retrieval at the three different incidence angles, R oscillates between 0.75 (at 52.5°) and 0.88 (at 32.5°). The uRMSE slightly increases with the increase of the incidence angle, ranging from 0.05 m^3/m^3 to 0.06 m^3/m^3. The three of them have a negative bias with respect to *in situ* SM. This bias remains almost constant along time, but it can turn positive after heavy rain events, as in March 2018. Underestimation of the SMOS SM with respect to *in situ* measurements has already been highlighted in previous studies [27,208], the so-called "dry bias". As reported in [199], this "dry bias" could be the result of underestimating the effective soil temperature. In this study, the soil temperature applied is derived from the National Aeronautics and Space Administration (NASA) Goddard Earth Observing System (GEOS)-5 models. A possible underestimation of the soil temperature would lead to an overestimation of the soil microwave emissivity, resulting in an underestimation of SM. Moreover, there is an inherent scale gap when comparing a point-scale

in situ measurement at REMEDHUS with an area-averaged satellite-based SM estimation, which could also explain this mismatch between *in situ* and satellite observations.

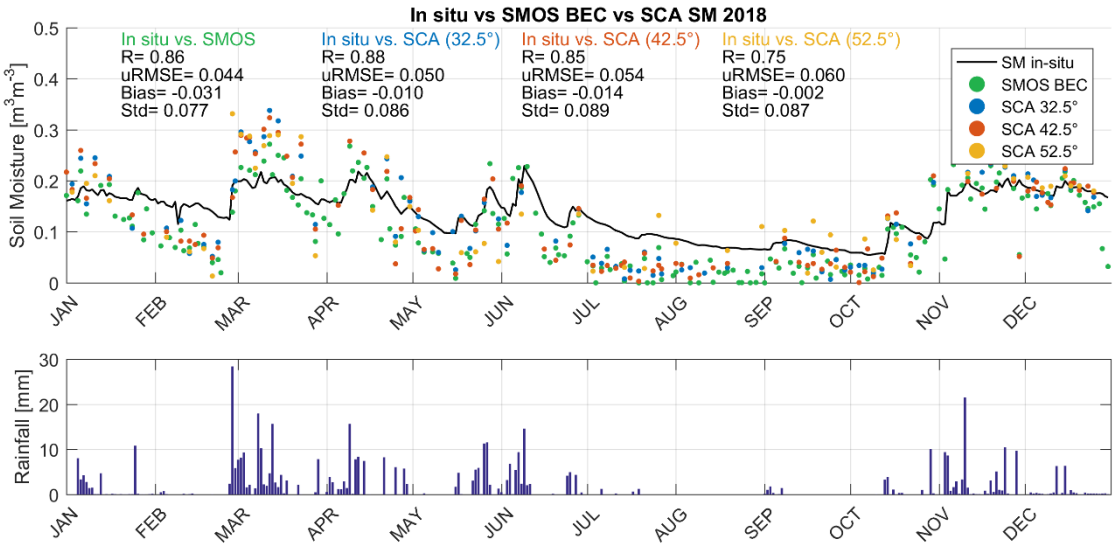

Figure 6.8 *In situ* SM from REMEDHUS (top; black); BEC SMOS L3 SM (top, green); the three retrieved SCA_V SM at 32.5° (top, blue), 42.5° (top, red) and 52.5° (top, yellow); and daily rainfall (bottom).

6.3.2 Analysis of active/passive covariation and disaggregated SMOS T_B

Figure 6.9 shows the active/passive microwave covariation β' between SMOS and Sentinel-1 for different Sentinel-1 incidence angle bins (from 34° to 44°) and for three VWC ranges (0-2, 2-4 and 4-8 kg/m2). The analysis is independently performed for the 32.5°, 42.5° and 52.5° SMOS incidence angles. It can be observed that β' values gradually and gently decrease with increasing Sentinel-1 incidence angle. This effect was also found in a previous study conducted by Jagdhuber et al. [150], where the active/passive covariation between SMAP (θ=40°) and Sentinel-1 was analyzed. Jagdhuber et al. suggested that the dependence of the active/passive covariation on the Sentinel-1 incidence angle was increasingly masked by denser vegetation. The behavior of β' was not provided exclusively as a function of Sentinel-1 angle, but also in relation to different SMOS angles. The largest variation (sensitivity), in magnitude of β', is around 0.7 at the 32.5° SMOS angle (Figure 6.9a). β' dependence with Sentinel-1 angle is less evident for higher SMOS angles, being almost insensitive to Sentinel-1 angle variations. A clear trend of β' with the SMOS incidence angle is also observed; the larger the SMOS angle the closer the values are to zero, which translates into a loss of backscatter sensitivity to changes in emissivity, for the highest SMOS incidence angle (52.5°).

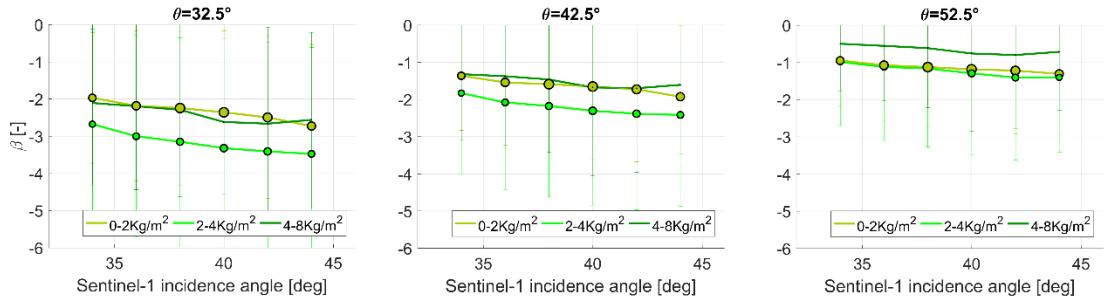

Figure 6.9 Active/passive microwave covariation parameter β' along Sentinel-1 incidence angle for three VWC ranges, obtained independently at (a) 32.5°, (b) 42.5°, and (c) 52.5° SMOS incidence angles. The position of the circles represents the mean values and its size represents the number of samples (the larger the circle, the higher the number of samples, and vice versa). Note that due to the few densely vegetated areas available in the Iberian Peninsula, the number of β' samples for the highest VWC class (4-8 kg/m^2) is very low.

The histograms of the initial SMOS T_{B_V} in a 12.5-km grid and the disaggregated SMOS T_{B_V} at 1 km, obtained from Equation (6.3), are displayed in Figure 6.10. They are obtained using the information of the entire study region along the year 2018. The spread of the distribution is similar for both products with slightly higher differences at 32.5°. The mean difference never exceeds 0.38 K for any of the three SMOS incidence angles, with a STD that is always higher for the disaggregated estimations. Differences between high and low resolution can be partially explained by the fact that the Sentinel-1 signal at C-band, used to disaggregate the SMOS T_{B_V}, cannot penetrate through dense or tall vegetation [150,207]. Figure 6.10 shows that the number of samples is lower for 32.5° and 52.5° compared to 42.5°. This could be explained by the shape of the alias-free field of view of the SMOS instrument, from which the incidence angles, sorted from highest to lowest spatial coverage, are 42.5°, 32.5° and 52.5° [217].

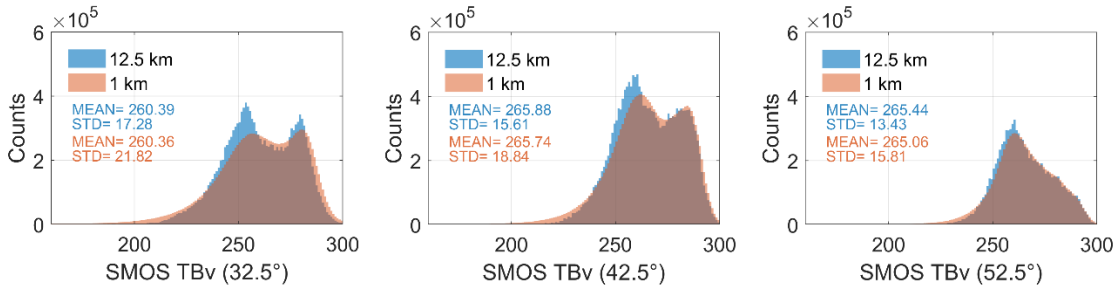

Figure 6.10 SMOS T_{B_V} histograms of data over the Iberian Peninsula for the year 2018, obtained independently at (a) 32.5°, (b) 42.5°, and (c) 52.5°. In blue, the initial SMOS T_{B_V} at 12.5 km, and in red, the disaggregated SMOS T_{B_V} at 1 km.

SMOS T_{B_V} maps at low and high resolution for the incidence angles of 32.5°, 42.5° and 52.5° are presented in Figure 6.11 for January 3rd, 2018. Similarities in the spatial patterns can easily be detected, in agreement with results of Figure 6.10. From Figure 6.11, it can also be understood that the T_{B_V} maps, both at high and low resolution, are highly affected by RFI in

some areas with no information (in the south of the Iberian Peninsula), but this effect is slightly different for each incidence angle, being the steepest angle (52.5°) the most affected. For the particular case of the Iberian Peninsula, this is a common effect, at least during the year 2018, the study period selected for this analysis. An RFI of about 9000 K located in Algeria [218] could explain these data gaps (with a shape of RFI tails) on the Iberian Peninsula. The shape size of the affected area and the steepest angle (52.5°) being the most affected, could indicate that the RFI originates from a directional antenna, pointing towards the horizon.

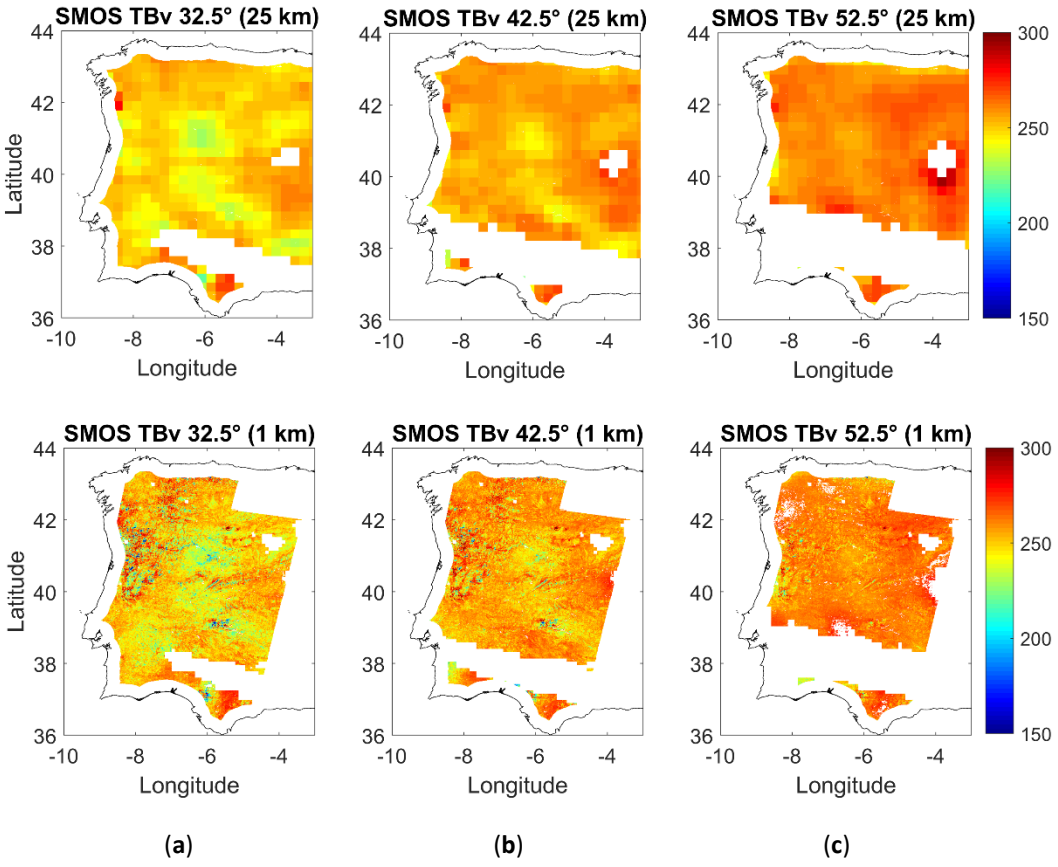

Figure 6.11 SMOS T_{B_V} maps for January 3rd, 2018, obtained independently at (a) 32.5°, (b) 42.5° and (c) 52.5°. At the top, the initial SMOS T_{B_V} in a 12.5-km grid, and at the bottom, the disaggregated SMOS T_{B_V} at 1 km.

6.3.3 Analysis of high-resolution SM maps

Figure 6.12a shows the histograms of the retrieved high-resolution SMOS SM at three incidence angles: 32.5°, 42.5° and 52.5°. Comparing the results for the three angles, it can be seen that the number of samples is lower for 32.5° and 52.5° compared to 42.5° (already discussed on Section 6.3.2). Taking this into consideration, the mean is similar for the three incidence angles, with a maximum value of 0.177 m^3/m^3 at 52.5° and a minimum value of 0.161 m^3/m^3 at 42.5°. The STD ranges from 0.097 m^3/m^3 at 52.5° to 0.112 m^3/m^3 at 32.5°. When the same analysis is carried out using the concurrent samples at the three incidence angles (Figure 6.12b), the STD is 0.109 m^3/m^3, 0.098 m^3/m^3 and 0.09 m^3/m^3 at 32.5°, 42.5° and 52.5°, respectively, and the differences between the means of the high-resolution SMOS SM at these

angles, never exceeds ~0.01 m^3/m^3. Figure 6.13 displays the high-resolution SM time series at the three independent SMOS incidence angles, which are compared with the REMEDHUS measurements. Due to the missing synchronization between Sentinel-1, SMAP and SMOS acquisition orbits, the number of samples is much lower than at low resolution (see Figure 6.8).

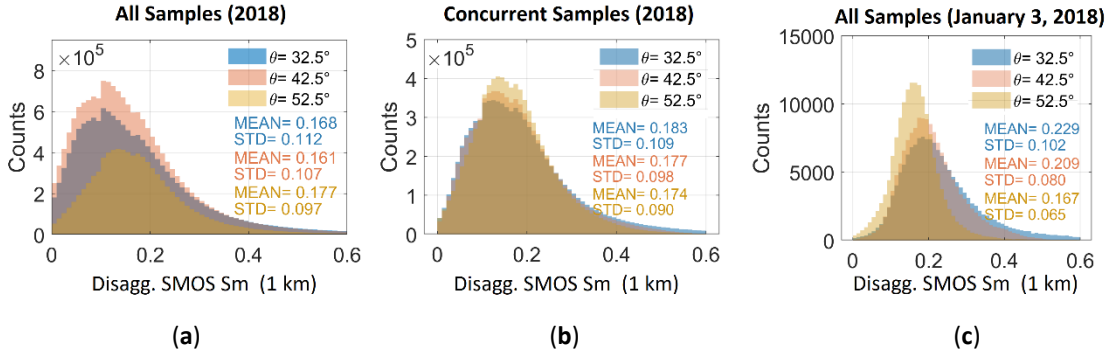

Figure 6.12 Histograms of the high-resolution SMOS SM at 32.5° (blue), 42.5° (red) and 52.5° (yellow), obtained using: (a) all data available for the year 2018; (b) the concurrent samples for the year 2018; and (c) all data available for January 3rd, 2018, over the Iberian Peninsula.

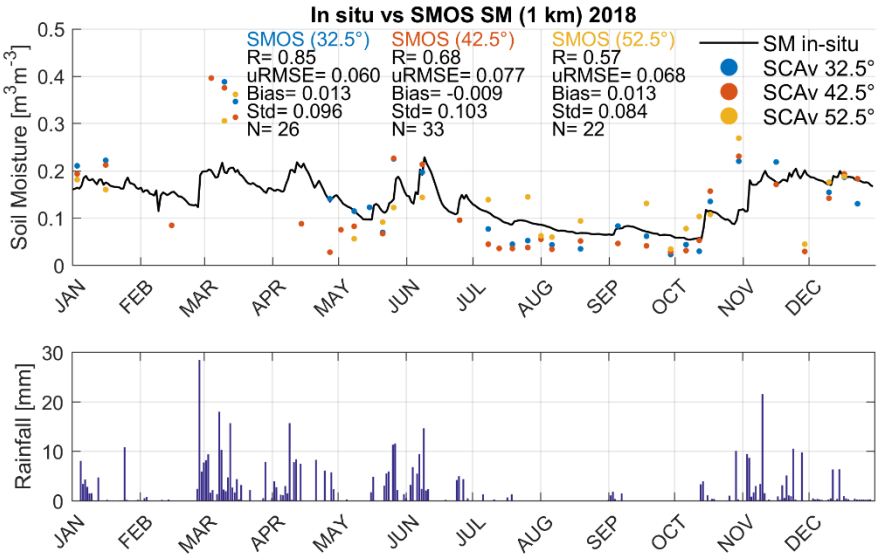

Figure 6.13 Daily evolution of *in situ* SM (black); retrieved high-resolution SCA_V SM at 32.5°, 42.5° and 52.5° (top); and daily rainfall (bottom).

Figure 6.14 shows the low- (top) and high-resolution (bottom) SMOS SM maps for January 3rd, 2018, both retrieved using the SCA_V with the parameters presented in Table 6.2 and Table 6.3. The high-resolution SMOS SM map at 52.5° is dryer than the 32.5° and 42.5° maps. This effect can also be seen at low resolution, which means it is not introduced by the single-acquisition disaggregation technique. Differences in SM maps at individual incidence angles may be due to the fact that one constant set of ω and h_s parameters is obtained for the entire year 2018. The result could potentially be improved by optimizing these parameters for shorter time periods, for example per season, per months or even fortnights.

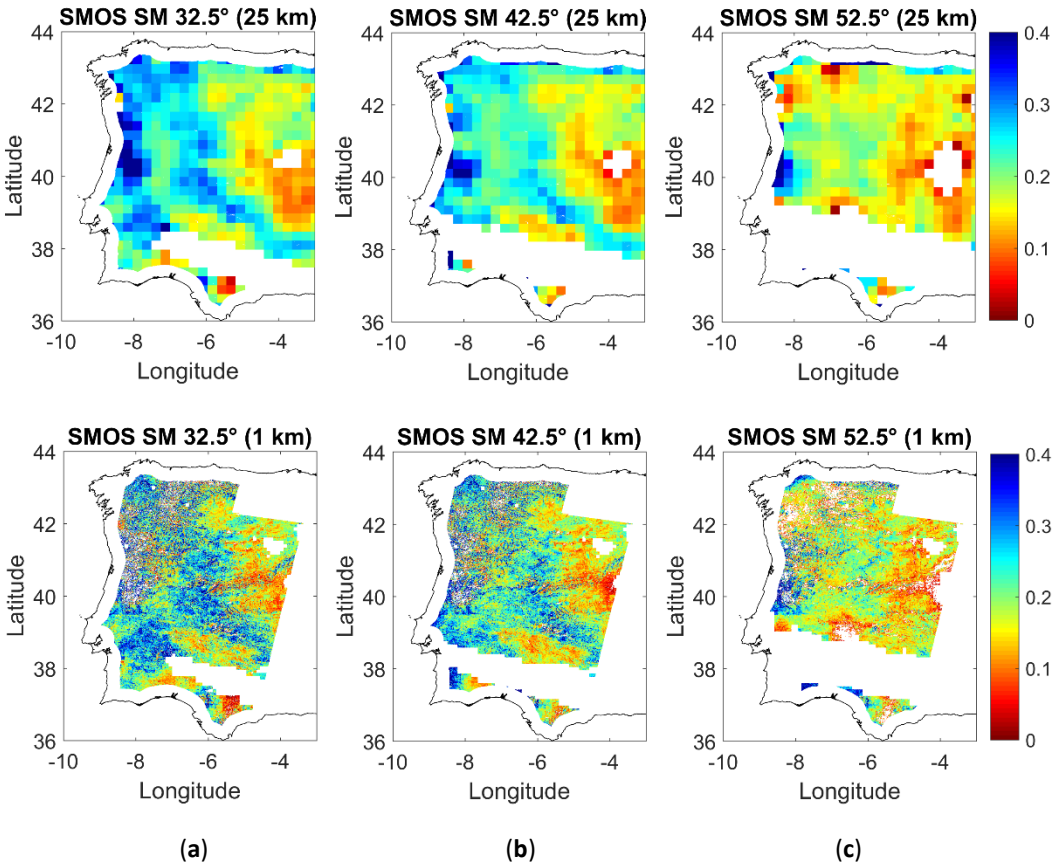

Figure 6.14 Retrieved SMOS SM maps for January 3rd, 2018 at 25 km (top) and 1 km (bottom), obtained independently at (a) 32.5°, (b) 42.5° and (c) 52.5°, using the parameters presented in Table 6.2 and Table 6.3.

6.4 Conclusions and perspectives

In this chapter, the radiative transfer parameters, effective scattering albedo (ω) and soil roughness (h_s), have been calibrated independently for three SMOS incidence angles (32.5±5°, 42.5±5° and 52.5±5°), over the four main land covers (croplands, savannas, grassland and shrublands) within the Iberian Peninsula, for the year 2018. These vegetation and soil parameters have been applied within the SCA_V to low-resolution (25-km grid) SMOS T_B in order to estimate low-resolution SM maps that have been shown to be consistent among them (mean differences below 0.007 m^3/m^3) and show good agreement (R≥0.75 and uRMSE ≤ 0.06 m^3/m^3) with 0-5 cm ground-based measurements from the REMEDHUS network. A single-pass active/passive disaggregation technique (Equation (6.3)) has been applied, using the optimal ω and h_s values, to SMOS and Sentinel-1 data to estimate fine-scale (1 km) T_{B_V} at the three respective incidence angles. Finally, the SCA_V is applied to obtain the high-resolution (1 km) SM maps for the Iberian Peninsula.

Regarding the incidence angle- and land cover-adapted parametrization of ω and h_s, results show (Table 6.2 and Table 6.3) an increasing trend of the estimated ω with increasing SMOS incidence angle, and an opposite trend for h_s. For the three SMOS incidence angles tested, the selection of optimal ω has a significant impact on the results, taking into consideration R,

uRMSE, and bias. Instead, the optimal value of h_s does not affect the final result as much as ω (Figure 6.5 and Figure 6.6). Scattering albedo has shown a very low variability with the land cover type, ranging from a minimum value of 0.02 at 32.5° to a maximum value of 0.12 at 52.5°. Soil roughness ranges from a minimum value of 0.01 at 52.5° to a maximum value of 0.18 at 32.5°, for four land cover types (savannas, croplands, grasslands and shrublands).

The SCA$_V$ algorithm has been applied to retrieve the low-resolution SM maps (25-km grid) using simultaneously the SMOS T_{B_V} with the optimal values of ω and h_s. The resulting SM maps were validated against the REMEDHUS SM *in situ* measurements, using R, uRMSE and bias. Retrieved SM at the different incidence angles have revealed considerable agreement between them, being able to capture wet up and dry down events. The best statistical performance is obtained at 32.5° with a R=0.88 and an uRMSE=0.05 m^3/m^3, while the worst is obtained at 52.5° with a R=0.75 and an uRMSE=0.06 m^3/m^3. A dry bias is present for all three incidence angles. This mismatch between satellite estimations and *in situ* observations at REMEDHUS could be explained by the inherent scale gap when comparing a point-scale *in situ* measurement with an area-averaged satellite-based SM estimation. In addition, the underestimation of SM could be the result of underestimating the soil temperature (derived from the NASA GEOS-5 models), which leads to an overestimation of the soil microwave emissivity and, in turn, in an underestimation of SM.

The active/passive covariation parameter (β') is a crucial variable to disaggregate the SMOS T_{B_V} with the single-acquisition methodology applied in this study. In this way, β' has been retrieved individually for the three SMOS incidence angles. This active/passive covariation has revealed a dependence on the Sentinel-1 incidence angle. The β' values gradually decrease with the increase of the Sentinel-1 incidence angle (Figure 6.9). This effect is less evident for larger SMOS incidence angles (e.g., 52.5°). There is also a dependence of β' with the SMOS incidence angle, the steeper the SMOS angle, the lower the covariation values, in magnitude. This means that it is less sensitive to changes in soil emissivity for higher SMOS incidence angles due to the stronger effect of vegetation during elongated ray path through the canopy. Although it applies to all microwave bands, it should be noted that the impact may be higher at L-band than at C-band, since the cover volume contribution is higher in the former.

The single-acquisition methodology allows us to merge active (Sentinel-1) and passive (SMOS) observations for disaggregating the coarse-resolution SMOS T_{B_V} at θ=32.5±5°, 42.5±5° and 52.5±5°, independently. Disaggregated SMOS T_{B_V} (1 km), obtained using the estimated β', and optimal ω and h_s values (Table 6.2 and Table 6.3), has been compared with the BEC SMOS L3 T_{B_V} (12.5-km grid), across the Iberian Peninsula at 32.5°, 42.5° and 52.5°, independently. Overall, T_{B_V} maps show similar spatial distribution and temporal evolution between high and low resolution (Figure 6.10 and Figure 6.11), for the three incidence angles studied. Slightly higher differences were found at 52.5°, but the mean difference never exceeds 0.38 K.

Finally, the SCA$_V$ algorithm was applied to the disaggregated SMOS T_{B_V}, retrieving high-resolution (1 km) SM maps at 32.5°, 42.5° and 52.5°. A comparison of these high-resolution SM maps, across the Iberian Peninsula for 2018, exhibit similar patterns in their distributions, despite the differences in the number of samples for the different incidence angles. The mean

difference between the three incidence angles was about 0.016 m^3/m^3. When analyzing daily SM maps, some differences can be observed in the retrievals of the same day among three incidence angles (Figure 6.14, bottom). These differences were not introduced by the single-acquisition disaggregation methodology because they were already present at low resolution (Figure 6.14, top). Disparities in retrieved SM maps at different incidence angles may be due to the fact that both ω and h_s parameters were optimized for the entire year of 2018 with a unique value, instead of considering shorter periods (e.g., seasonal or monthly) to derive variable ω and h_s values over time.

Results presented in this study are intended to underline the relevance of developing a land use-specific and incidence angle-adaptive parametrization of radiative transfer models, to accurately estimate SM from space-borne radiometers operating in low-frequency microwaves. In addition, it was implemented SMOS T_B with Sentinel-1 backscatter for any individual incidence angle combination and tested further a single-pass method to downscale (radar and radiometer). This is especially relevant taking into account upcoming missions, such as CIMR, ROSE-L Copernicus high-priority missions and Sentinel-1 next generation, which offer great potential to estimate high-resolution SM through the synergy of active and passive microwave sensors.

Chapter 7

Conclusions and future lines

The crucial relevance of SM for several applications in climatology, hydrology, meteorology and water resource management, and the need of its estimation on a global or planetary scale, have led to the launch of the two first space missions specifically devoted to measure this variable in the last decades: the SMOS, launched in 2009, and the SMAP, launched in 2014. The L-band views of the Earth obtained from these missions along these years have contributed to many applications. The native resolution (~40 km) of the SM maps obtained from SMOS and SMAP while meeting the needs of climate and global scale application, is a limiting factor for regional applications, where spatial resolutions on the order of 1 km or less are required. To help bridge this gap, a variety of disaggregation algorithms have been proposed over the years, allowing an improvement of the spatial resolution of the SM maps to achieve resolutions of 1 km, or even hundreds or tens of meters, by exploiting the synergies of different satellite sensors. This Thesis focuses on the study of the Earth's surface SM, including the implementation of different SM retrieval algorithms, as well as the development, validation and comparison of different downscaling techniques, applied at local, peninsular and continental scale.

This chapter summarizes the main conclusions of this Thesis in Section 7.1, highlights its original contributions in Section 7.2, and discusses suggestions for future work in Section 7.3. Publications arising from this Thesis are compiled in Section 7.4.

7.1 Main conclusions

Chapter 4 presents a novel passive microwave/optical downscaling algorithm to improve the spatial resolution of the SMOS SM maps, as an upgrade of the semi-empirical approach presented by Piles et al. in [46]. The algorithm is built from an extension of the so-called "universal-triangle" concept [122,123] that indirectly relates changes in NDVI and T_S to SM. The novelty of the proposed extension is the introduction of an adaptive moving window [185], which allows obtaining high-resolution SM maps with no limitation in extension or location. Hence, it enables the method to be applied at a continental scale (and potentially at a global scale). The downscaling algorithm uses T_B from SMOS, NDVI provided by MODIS and T_S from two different possible sources, MODIS (1-km spatial resolution) or ERA5 (30-km spatial resolution), resulting in to two different version of the algorithm: the "MODIS" and the "cloud-free" version, using MODIS T_S and ERA5 T_S, respectively. The main conclusions of this chapter are:

- The use of a small (5 x 5 low-resolution pixels) adaptive moving window in the downscaling algorithm allows to maintain the dynamic range of SM when it is disaggregated from 25 km (BEC SMOS L3 SM product) to 1 km (SMOS L4 SM).
- When the resulting high-resolution SM maps (SMOS L4 SM) are aggregated from 1 km to 25 km, the energy remains almost the same with respect to the original coarse grid cells.
- The downscaling algorithm has been developed so that the generated results are consistent regardless of the size of the study area. It has been tested up to a continental (Europe) scale size.
- Both versions of the algorithm show similar performance using REMEDHUS— mean R≥0.8 and mean uRMSE≈0.04 m^3/m^3 (using the information from Table 4.4, excluding the summer season)— and OzNet (Yanco)— mean R≥0.85 and mean uRMSE≈0.05 m^3/m^3 (using the information from Table 4.6)— SM measurements as reference.
- A seasonal dependency is detected not only for both versions of the downscaling algorithm proposed, but also for the original BEC SMOS L3 SM product (25 km). Hence, it can be stated that this dependency is inherent to the SMOS SM data and it is not introduced by the downscaling technique applied.
- The use of ERA5 T_S instead of MODIS T_S as input parameter in the downscaling algorithm does not lead to a degradation of the statistics, but increases the spatial and temporal coverage in a relevant way.

Chapter 5 assesses the temporal and the spatial characteristics of six SM products derived from SMOS (BEC SMOS L3 SM; and BEC SMOS L4 SM) and SMAP (SMAP L2, SMAP L2E, SMAP L2 AP3 and SMAP L2 AP1) in order to diagnose their distinct features and the rationale behind them. The temporal inter-comparison analysis is carried out using *in situ* SM data from REMEDHUS network to evaluate the impact of the spatial scale of different SMOS and SMAP products, and their correspondence in terms of temporal dynamics. The spatial analysis is also conducted for the Iberian Peninsula with emphasis on the added-value that the enhanced resolution products provide based on the microwave/optical (SMOS/MODIS) [27] or the

active/passive microwave (SMAP/Sentinel-1) [117] sensor fusion. The main conclusions of this chapter are:

- Independently of the spatial resolution, all the SM products are able to capture wet up and dry down variations, and seasonality patterns (summers with low and winters with high SM values).
- Not even the highest-resolution (1 km) products used from SMOS (BEC SMOS L4 SM) and SMAP (SMAP L2 AP3 and SMAP L2 AP1) are fine enough to capture local differences that are not dominant within the pixel scale.
- Statistically, the differences between the SMOS and the SMAP products are considerably low e.g., at low resolution (using REMEDHUS data as ground truth) the mean R is 0.7 and the mean uRMSE is about 0.06 m^3/m^3 for SMAP (SMAP L2 and SMAP L2E), while for SMOS (BEC SMOS L3 SM) the mean R is 0.65 and the uRMSE is about 0.06 m^3/m^3 (results from Table 5.5). At high resolution only the information of the most representative REMEDHUS stations is use (F11, H13, J12, J14, K10, M9 and O7) obtaining a R=0.86 and an uRMSE=0.04 m^3/m^3 for SMAP L2 AP1 SM, a R=0.87 and an uRMSE=0.038 m^3/m^3 for SMAP L2 AP3, and a R=0.82 and an uRMSE=0.043 m^3/m^3 for BEC SMOS L4 SM. Both SMOS and SMAP have a slightly worse performance in terms of correlation (~0.6) during the summer season. In addition, SMOS shows an important bias (-0.067 m^3/m^3) during this period.
- Concerning the spatial analysis, overall, SMAP is slightly wetter than SMOS. Some differences in spatial patterns are observed in the high-resolution SM products, linked to the fine-scale information they use and the multi-sensor synergies employed, especially in forested areas. Moreover, some differences between the SMOS and SMAP products can also be seen at the T_B level, and therefore the disparities between the products are not exclusively introduced by the downscaling methodology used.

Chapter 6 analyzes the impact of incidence angle diversity on SM retrievals at coarse and fine scales over the Iberian Peninsula. This chapter is structured in three parts: (i) the SCA_V is applied to the BEC SMOS T_{B_V} to estimate SM at coarse resolution (25 km) and develop a land use-specific and incidence angle (32.5°, 42.5° and 52.5°)-adaptive calibration of ω and h_s parameters; (ii) these effective parameters are used together with the fine-scale multi-angular Sentinel-1 backscatter in a single-pass active/passive downscaling approach, to estimate T_{B_V} at fine scale (1 km) for each SMOS incidence angle; and (iii) the high-resolution T_{B_V} maps are inverted to obtain the corresponding high-resolution SM maps. The main conclusions of this chapter are:

- Regarding the incidence angle- and land cover-adapted parametrization of ω and h_s, results show an increasing trend of the estimated ω with increasing SMOS incidence angle, and an opposite trend for h_s. The selection of the optimal ω has a significant impact on the accuracy of the retrieved SM. Instead, the optimal value of h_s does not affect the final result as much as ω. The scattering albedo has a very low variability with the land cover type, while the soil roughness is slightly more dependent on it.
- The resulting SM maps were validated against the REMEDHUS SM *in situ* measurements, using R, uRMSE and bias. Retrieved SM at different incidence angles (32.5°, 42.5° and 52.5°) has revealed considerable agreement between them, being able to capture wet up and dry down events. The best statistical performance is obtained at 32.5° with a

R=0.88 and an uRMSE=0.05 m^3/m^3, while the worst is obtained at 52.5° with a R=0.75 and an uRMSE=0.06 m^3/m^3.

- The active/passive covariation parameter, crucial to disaggregate the SMOS T_{B_V} with the single-acquisition methodology, which is retrieved individually for the three SMOS incidence angles, has revealed a dependence on the Sentinel-1 incidence angle. The covariation parameter gradually decreases with the increase of the Sentinel-1 incidence angle. This effect is less evident for larger SMOS incidence angles (e.g., 52,5°). There is also a dependence of β' with the SMOS incidence angle, the steeper the SMOS angle, the lower the covariation values, in magnitude. This means that it is less sensitive to changes in soil emissivity for higher SMOS incidence angles due to the stronger effect of vegetation during elongated ray path through the canopy.
- Disaggregated (1 km) SMOS T_{B_V} (at 32.5°, 42.5° and 52.5°, independently), obtained using the estimated β' and the optimal ω and h_s values, has been compared with the BEC SMOS L3 T_{B_V} (12.5-km grid) for the Iberian Peninsula, for each of the three incidence angles. Overall, the histograms of the initial SMOS T_{B_V} in a 12.5-km grid and the disaggregated SMOS T_{B_V} at 1 km show similar distributions, with slightly higher differences at 32.5°.
- The resulting high-resolution SM maps at 32.5°, 42.5° and 52.5° exhibit similar patterns in their distributions, despite the differences in the number of samples for the different incidence angles. When analyzing daily SM maps, some differences can be observed in the retrievals of the same day among the three incidence angles. These differences were not introduced by the single-acquisition disaggregation methodology because they were already present at low resolution. Disparities in retrieved SM maps at different incidence angles may be due to the fact that both ω and h_s parameters were optimized for the entire year of 2018 with a unique value, instead of considering shorter periods (e.g., seasonal or monthly).

7.2 Original contributions

The original contributions of this Thesis are summarized below:

- Improvement of the passive microwave/optical downscaling algorithm initially proposed by Piles et al. [46] by introducing an adaptive moving window. The methodology proposed in Chapter 4 is currently used at BEC facilities (it was introduced in the year 2019) to generate and provide daily high-resolution SM maps over Europe [156]. Before this data, only maps over the Iberian Peninsula were provided. A variety of applications have successfully used this product e.g., for crop yield estimation [194,195] and forest decline modelling [196], which is an indirect validation of the synergistic approach.
- Inter-comparison study to provide insights into main SMOS and SMAP multi-scale SM products that are currently being distributed operationally, and understand their differences, tracing back to the physical assumption and synergies they rely on.

- Calibration of the radiative transfer parameters ω and h_s for several incidence angles and land cover, for passive microwave SM retrieval using two different algorithms: the SCA and the LPRM.
- Implementation and testing of a single-pass method to downscale SMOS T_B with Sentinel-1 backscatter for any individual incidence angle combination. Analysis of the impact of SMOS incidence angle at the T_{B_V} and the SM level, at coarse and fine scales, and analysis of the active/passive covariation parameter, over the Iberian Peninsula.

7.3 Future lines

The future research lines arising from the work presented in this Thesis are:

- Thorough validation of the passive microwave/optical downscaling algorithm (from Chapter 4) on a global scale, focusing on the quality of the resulting SM estimates but also in its computational requirements and execution time.
- Inter-comparison of different SM products, similar to that proposed in Chapter 5, but including also the latest high-resolution SM products obtained through model/data-based downscaling techniques (e.g., machine learning algorithms) [119]. Confront advantages and disadvantages of each method and potentially work towards physics-aware machine learning downscaling approaches.
- Replace the C-band Sentinel-1 backscatter used in Chapter 6 in the single-pass active/passive downscaling approach, with that provided by an L-band SAR mission such as the Satélite Argentino de Observación Con Microondas (SAOCOM) or the upcoming ROSE-L. Analyze the performance of the resulting high-resolution SM maps with focus on vegetated areas.
- Further validate the downscaling algorithms (from Chapter 4 and Chapter 6) over vegetated areas and provide an estimate of their uncertainty. The low number of SM *in situ* stations in these regions complicates the validation yet approaches such as triple collocation could be of help.

7.4 Publications arising from this Thesis

Chapter 4

Portal, G.; Vall-llossera, M.; Piles, M.; Camps, A.; Chaparro, D.; Pablos, M.; Rossato, L. A Spatially Consistent Downscaling Approach for SMOS Using an Adaptive Moving Window. In Proceedings of the 2017 IEEE International Geoscience and Remote Sensing Symposium (IGARSS); July 2017; pp. 4151–4153.

Portal, G.; Vall-llossera, M.; Piles, M.; Camps, A.; Chaparro, D.; Pablos, M.; Rossato, L. A Spatially Consistent Downscaling Approach for SMOS Using an Adaptive Moving Window. *IEEE J. Sel. Top. Appl. Earth Obs. Remote Sens.* **2018**, *11*, 1883–1894, doi:10.1109/JSTARS.2018.2832447.

Chapter 5

Portal, G.; Jagdhuber, T.; Vall-llossera, M.; Camps, A.; Pablos, M.; Entekhabi, D.; Piles, M. Assessment of Multi-Scale SMOS and SMAP Soil Moisture Products across the Iberian Peninsula. *Remote Sens.* **2020**, *12*, 570, doi:10.3390/rs12030570.

Chapter 6

Undergoing review. Portal, G.; Vall-llossera, M.; Piles, M.; Jagdhuber, T.; Camps, A.; Pablos, M.; López-Martínez C.; Das, N.; Entekhabi, D. "Impact of Incidence Angle Diversity on Soil Moisture Retrievals at Coarse (SMOS) and Fine (SMOS & Sentinel-1) Scales". Under Review for IEEE Transactions on Geoscience and Remote Sensing.

Portal, G.; Vall-llossera, M.; Jagdhuber, T.; Camps, A.; Pablos', M.; Piles, M. Incidence Angle Diversity on L-Band Microwave Radiometry and Its Impact on Consistent Soil Moisture Retrievals. In Proceedings of the 2021 IEEE International Geoscience and Remote Sensing Symposium IGARSS; July 2021; pp. 6186–6189.

These publications were supported by the projects: "Productos y Servicios innovadores con sensores de microondas, SMOS y Sentinels para observación de la Tierra" (Ref. to: ESP2015-67549-C3-1-R), "Potential of spaceborne GNSS-R for land Applications" (Ref. to: ITT AO/1-8816/16/NL/AF/eg), "L-Band: Sobre la continuidad de las misiones satelitales de banda L. Nuevos paradigmas en productos y aplicaciones" (Ref. to: ESP2017-89463-C3-2-R) and by the project PID2020-114623RB-C32, funded by MCIN/ AEI /10.13039/501100011033.

Other contributions

M. Piles et al., "Synergistic use of SMOS and Sentinel-3 for retrieving spatiotemporally estimates of surface soil moisture and evaporative fraction," Copernicus Meetings, EGU21-16478, Mar. 2021. doi: 10.5194/egusphere-egu21-16478.

Zhan, Q.; Vall-llossera, M.; Pablos, M.; Camps, A.; **Portal, G**.; Chaparro, D. Improving the Rice Yield Estimation Using SMOS and CYGNSS GNSS-R Data. In Proceedings of the IGARSS 2020 - 2020 IEEE International Geoscience and Remote Sensing Symposium; September 2020; pp. 5254–5257.3.

Spatafora, L.R.; El Khayati, M.; Vall-llossera, M.; Gurgel, H.; Camps, A.; Angelis, C.F.; **Portal, G**.; Chaparro, D. Evaluation of Dengue Disease in Brazil: Multivariable Analysis. In Proceedings of the IGARSS 2019 - 2019 IEEE International Geoscience and Remote Sensing Symposium; July 2019; pp. 7112–7115.

Park, H.; Camps, A.; Castellvi, J.; Vall-llossera, M.; **Portal, G**.; Rossato, L. Sensitivity to Soil Moisture and Observation Geometry of Spaceborne GNSS-R Delay-Doppler Maps. In Proceedings of the IGARSS 2019 - 2019 IEEE International Geoscience and Remote Sensing Symposium; July 2019; pp. 8358–8361.

Pablos, M.; Vall-llossera, M.; Piles, M.; Camps, A.; González-Haro, C.; Turiel, A.; Herbert, C.J.; Chaparro, D.; **Portal, G**. Influence of Quality Filtering Approaches in BEC SMOS L3 Soil Moisture

Products. In Proceedings of the IGARSS 2019 - 2019 IEEE International Geoscience and Remote Sensing Symposium; July 2019; pp. 6941–6944.

Camps, A.; Vall·llossera, M.; Park, H.; **Portal, G**.; Rossato, L. Sensitivity of TDS-1 GNSS-R Reflectivity to Soil Moisture: Global and Regional Differences and Impact of Different Spatial Scales. Remote Sensing 2018, 10, 1856, doi:10.3390/rs10111856.

Pablos, M.; González-Zamora, A.; Sanchez, N.; Martinez-Fernandez, J.; **Portal, G**.; Vall-Llossera, M. Surface Soil Moisture Estimation from Modis Apparent Thermal Inertia: A Comparison With Smos And Smap Soil Moisture Products. In Proceedings of the IGARSS 2018 - 2018 IEEE International Geoscience and Remote Sensing Symposium; July 2018; pp. 80–83.

Camps, A.; Vall-llossera, M.; Park, H.; **Portal, G**.; Rossato, L. Sensitivity to Soil Moisture of SP Aceborne GNSS-R Observables. In Proceedings of the IGARSS 2018 - 2018 IEEE International Geoscience and Remote Sensing Symposium; July 2018; pp. 3161–3164.

Rossato, L.; Vall-Llossera, M.; Camps, A.; **Portal, G**.; Sakuragi, J.; Angelis, C.F.; Zeri, M.; Barbosa, H.; Paredes, F. Validation of Soil Moisture in the Brazilian Semiarid, Using Smos Satellite Product And Simagri Model. In Proceedings of the IGARSS 2018 - 2018 IEEE International Geoscience and Remote Sensing Symposium; July 2018; pp. 84–87.

Sabaghy, S.; Walker, J.; Renzullo, L.; Akbar, R.; Chan, S.; Chaubell, J.; Das, N.; Dunbar, R.S.; Entekhabi, D.; Gevaert, A.; et al. Comparison of Downscaling Techniques for High Resolution Soil Moisture Mapping. In Proceedings of the 2017 IEEE International Geoscience and Remote Sensing Symposium (IGARSS); July 2017; pp. 2523–2526.

Appendix A

Additional results of assessment of multiscale SMOS and SMAP soil moisture products

A.1 Statistical performance over REMEDHUS

Table App A.1 Statistics obtained from the comparison of *in situ* SM with the concurrent low-resolution (radiometer-only) pixels SM time series: of SMAP L2E (left), SMAP L2 (center) and BEC SMOS L3 (right), from April 2015 to December 2017. The *in situ* stations used are: H13, H9, J3, K13, N9 and O7. Statistics were calculated using the same number of samples for all three products.

		***In situ* vs SMAP L2E**				***In situ* vs SMAP L2**				***In situ* vs BEC SMOS L3**			
	N	**R**	**RMSE**	**uRMSE**	**Bias**	**R**	**RMSE**	**uRMSE**	**Bias**	**R**	**RMSE**	**uRMSE**	**Bias**
H13	237	0.82	0.052	0.044	-0.027	0.82	0.056	0.046	-0.032	0.80	0.085	0.052	-0.067
H09	267	0.57	0.136	0.077	-0.113	0.55	0.136	0.078	-0.112	0.55	0.162	0.079	-0.142
J03	260	0.83	0.120	0.047	0.111	0.84	0.117	0.046	0.107	0.80	0.077	0.048	0.060
K13	237	0.42	0.165	0.090	-0.139	0.44	0.165	0.090	-0.138	0.41	0.207	0.090	-0.186
N09	239	0.70	0.084	0.050	-0.067	0.71	0.071	0.050	-0.051	0.67	0.112	0.054	-0.098
O07	230	0.79	0.051	0.037	0.034	0.80	0.048	0.037	0.031	0.76	0.044	0.043	0.009

Table App A.2 Statistics obtained from the comparison of *in situ* SM with the concurrent high-resolution pixels SM time series: of SMAP L2 AP1 (left), SMAP L2 AP3 (center) and BEC SMOS L4 (right), from April 2015 to December 2017. The *in situ* stations used were: H13, H9, J3, K13, N9 and O7. Statistics were calculated using the same number of samples for all three products.

		***In Situ* vs SMAP L2 AP1**				***In Situ* vs SMAP L2 AP3**				***In Situ* vs BEC SMOS L4**			
	N	**R**	**RMSE**	**uRMSE**	**Bias**	**R**	**RMSE**	**uRMSE**	**Bias**	**R**	**RMSE**	**uRMSE**	**Bias**
H13	46	0.68	0.072	0.050	-0.051	0.83	0.048	0.043	-0.022	0.78	0.090	0.043	-0.079
H09	43	0.39	0.161	0.086	-0.137	0.47	0.151	0.081	-0.128	0.60	0.169	0.073	-0.152
J03	47	0.57	0.086	0.044	0.075	0.85	0.124	0.047	0.115	0.70	0.079	0.049	0.062
K13	45	0.39	0.183	0.109	-0.147	0.39	0.171	0.104	-0.135	0.44	0.213	0.082	-0.197
N09	45	0.43	0.125	0.072	-0.103	0.56	0.105	0.060	-0.086	0.56	0.126	0.058	-0.112
O07	43	0.65	0.094	0.079	0.050	0.76	0.081	0.058	0.057	0.65	0.047	0.047	0.001

A.2 SMAP L2 AP1 SM and BEC SMOS L4 SM annual comparison

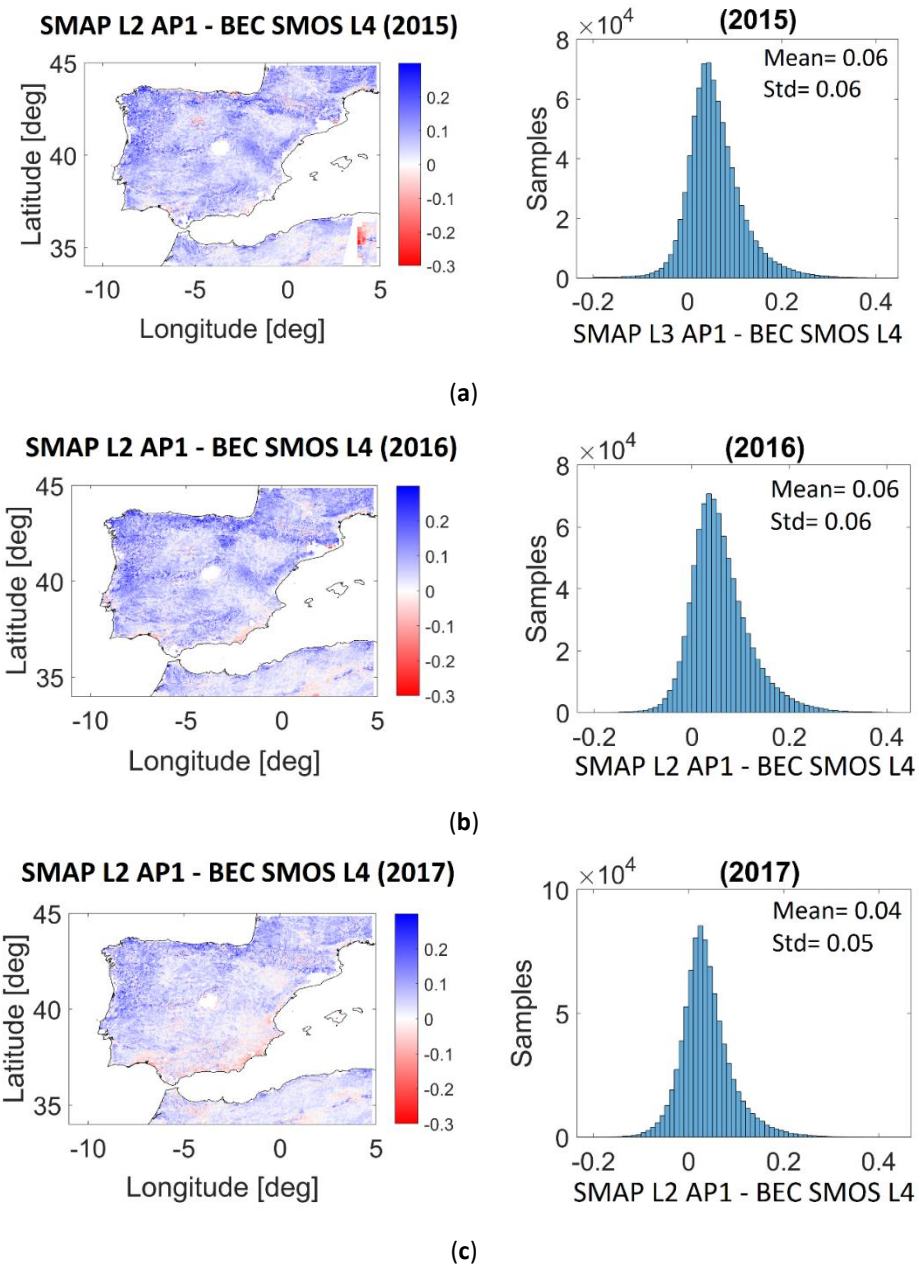

Figure App A.1 (first column) Temporally-averaged map of daily SM differences between SMAP and SMOS at 1 km (SMAP L2 AP1 minus BEC SMOS L4) and (second column) histogram of daily SM differences maps, for (a) 2015, (b) 2016 and (c) 2017.

A.3 SMAP L2 AP1 SM and BEC SMOS L4 SM seasonal comparison

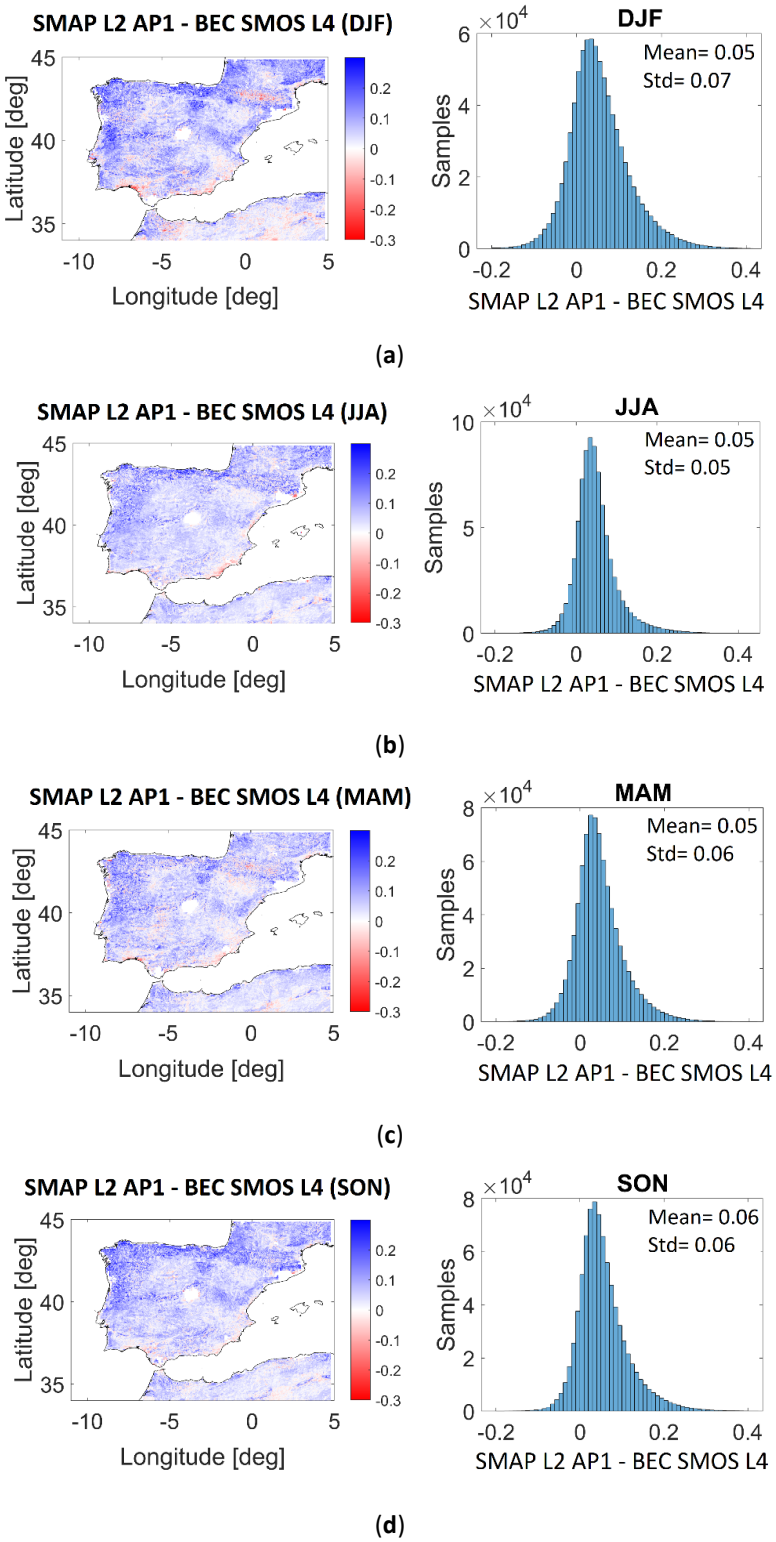

Figure App A.2 (first column) Temporally-averaged map of daily SM differences between SMAP and SMOS at 1 km (SMAP L2 AP1 minus BEC SMOS L4) and (second column) histogram of daily SM differences maps, calculated by seasons: (a) DJF, (b) JJA, (c) MAM and (d) SON, for the period from 2015 to 2017.

Appendix B

Additional results of impact of incidence angle diversity on soil moisture

B.1 Albedo and roughness calibration for the 32.5°, 42.5° and 52.5° incidence angles, for several land covers (croplands, grasslands and shrublands)

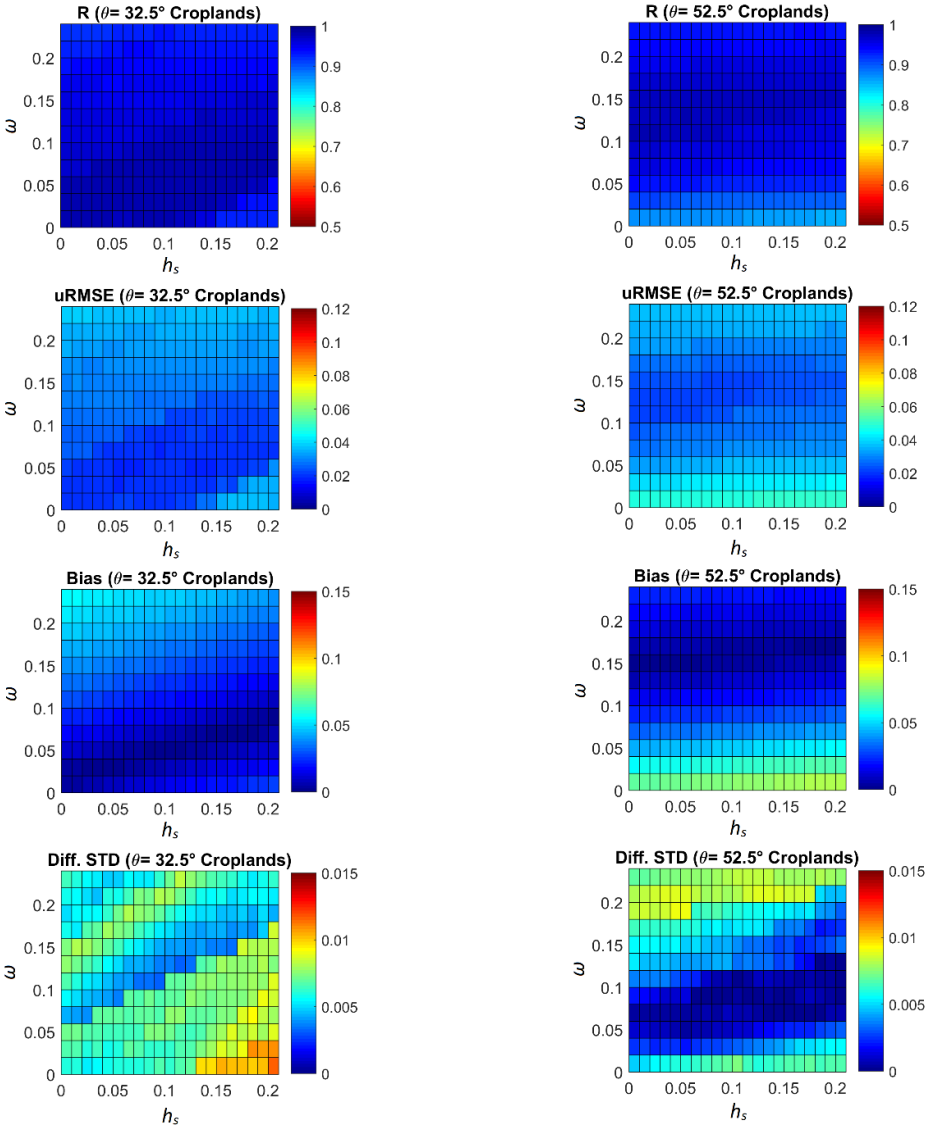

Figure App B.1 Averaged R, uRMSE, bias and difference of STD, obtained between SCA_V SM at 42.5° and SCA_V SM at (a) 32.5° and (b) 52.5°, for each pair of ω and h_s, for croplands (see Section 6.2.2A STEP2).

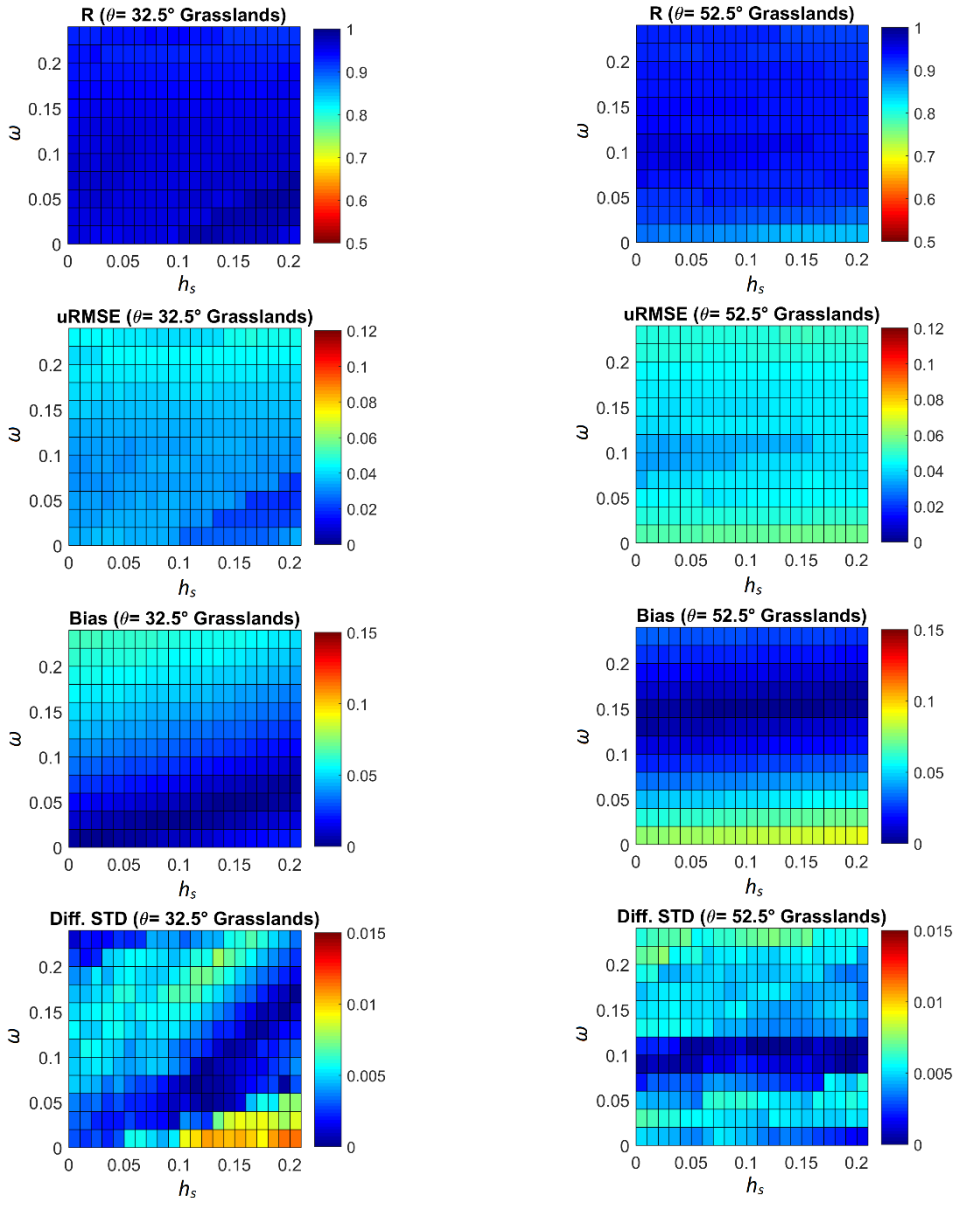

Figure App B.2 Averaged R, uRMSE, bias and difference of STD, obtained between SCA_V SM at 42.5° and SCA_V SM at (a) 32.5° and (b) 52.5°, for each pair of ω and h_s, for grasslands (see Section 6.2.2A STEP2).

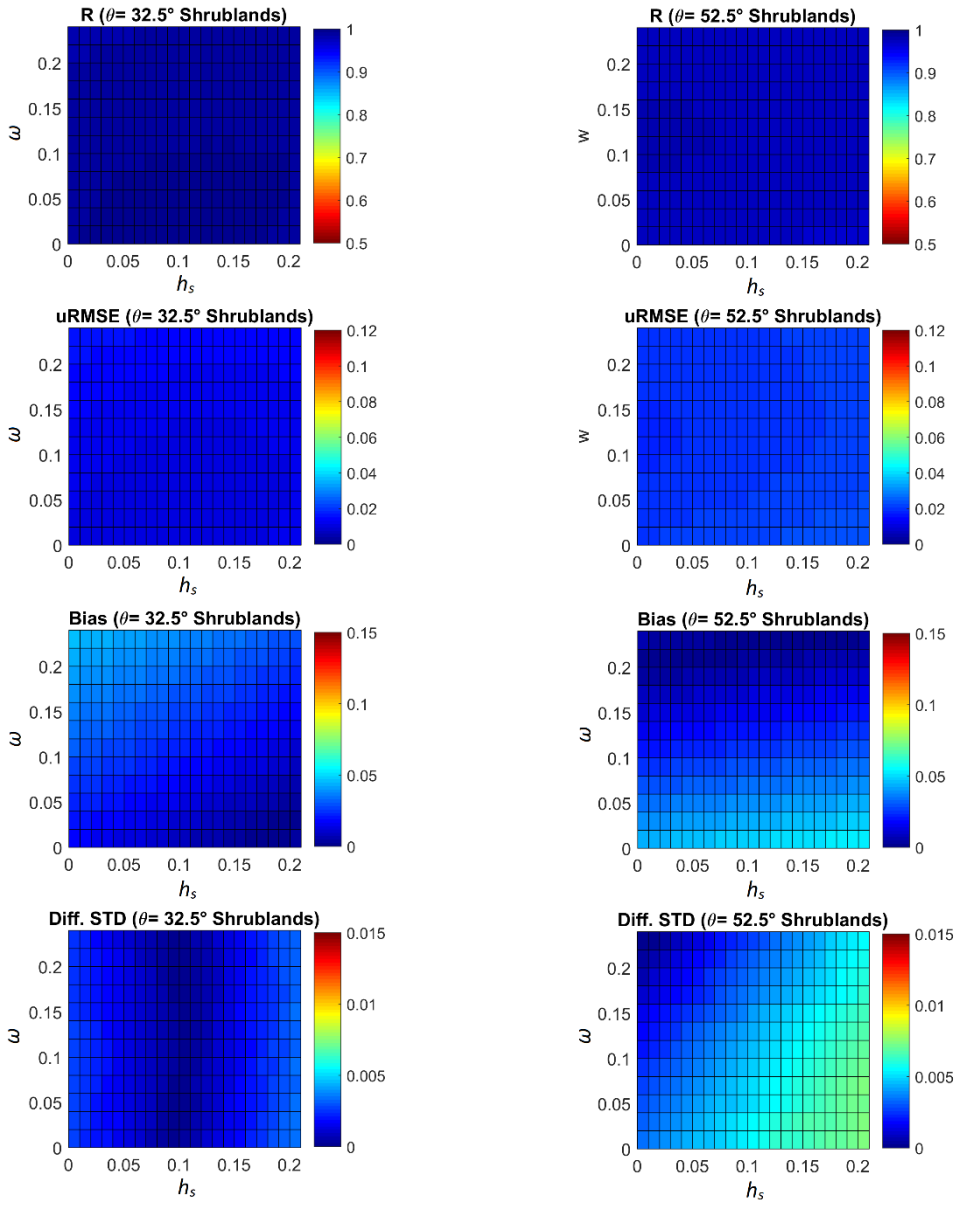

Figure App B.3 Averaged R, uRMSE, bias and difference of STD, obtained between SCA_V SM at 42.5° and SCA_V SM at (a) 32.5° and (b) 52.5°, for each pair of ω and h_s, for shrublands (see Section 6.2.2A STEP2).

Resumen (Abstract in Spanish)

La humedad del suelo es una variable climática esencial que juega un papel crucial en la relación de los ciclos del agua, la energía y el carbono de la Tierra. Es responsable del intercambio de agua entre la superficie de la Tierra y la atmósfera, y proporciona información crucial sobre la evaporación del suelo, la transpiración de las plantas y la distribución de la precipitación en escorrentía, flujo superficial e infiltración. Por lo tanto, es necesaria una estimación precisa de la humedad del suelo para mejorar las predicciones climáticas y meteorológicas, y comprender mejor el ciclo hidrológico y sus extremos (v.g., sequías e inundaciones). Los sensores pasivos y activos en banda L se han usado durante las últimas décadas para estimar la humedad del suelo debido a la relación directa que existe entre esta variable y las propiedades dieléctricas del suelo.

Actualmente, hay dos misiones operativas en banda L específicamente dedicadas a medir la humedad del suelo a escala global: la misión Soil Moisture and Ocean Salinity (SMOS) de la ESA, lanzada en noviembre de 2009; y la misión Soil Moisture Active Passive (SMAP) de la NASA, lanzada en enero de 2015. La resolución espacial de los radiómetros SMOS y SMAP, del orden de unas decenas de kilómetros (~40 km), es adecuada para aplicaciones a escala global. Sin embargo, para satisfacer las necesidades de un número creciente de aplicaciones a escala local o regional, se requiere más detalle espacial (<1 km). Para solventar esta limitación y mejorar la resolución espacial de los mapas de humedad, se han propuesto diferentes técnicas de mejora o desagregación espacial.

Esta Tesis se centra en el estudio de la humedad de la superficie terrestre a partir de datos obtenidos a través de teledetección. Este trabajo incluye la implementación de distintos algoritmos de recuperación de la humedad del suelo y el desarrollo, implementación, validación y comparación de distintas técnicas de desagregación, aplicadas a escala local, regional y continental. Para cumplir estos objetivos, se han explorado sinergias entre diferentes sensores de microondas activos/pasivos (SMOS, SMAP y Sentinel-1) y sensores ópticos/térmicos. Los resultados se presentan de la siguiente manera:

- *Técnica de desagregación espacialmente consistente, basada en una ventana móvil adaptativa, aplicada a los datos SMOS*

Se propone un algoritmo de desagregación del píxel basado en datos obtenidos de medidas radiométricas de microondas en banda L y datos ópticos, para mejorar la resolución espacial de los mapas de humedad del suelo desde la resolución nativa del instrumento (~40 km) hasta resoluciones de 1 km. El algoritmo introduce el concepto de una ventana de contorno adaptativo, como mejora principal sobre la técnica de desagregación presentada en Piles et al. (2014), permitiendo su implementación a escala continental.

- *Análisis multiescalar de productos de humedad del suelo SMAP y SMOS sobre la Península Ibérica*

Se han evaluado las características temporales y espaciales de distintos productos de humedad del suelo SMOS y SMAP, a baja y a alta resolución, para conocer sus características

distintivas y comprender las razones de sus diferencias. Para ello, ha sido necesario rastrear los supuestos físicos en los que se basan.

- *Impacto del ángulo de incidencia en la recuperación de la humedad del suelo a baja y a alta resolución*

Se ha llevado a cabo una calibración adaptada al ángulo de incidencia (32.5°, 42.5° y 52.5°) de los parámetros efectivos, albedo de dispersión simple y rugosidad del suelo, descritos en el modelo de transferencia radiativa $\tau - \omega$, incidiendo en la importancia de esta parametrización para estimar la humedad del suelo de forma precisa a baja resolución. El resultado de las mismas se ha utilizado para estudiar la potencial aplicación de un algoritmo activo/pasivo de desagregación basado en la física para las próximas misiones de microondas, llamadas CIMR, ROSE-L y Sentinel-1 Next Generation. Los mapas de humedad recuperados a los tres ángulos de incidencia, tanto a baja como a alta resolución, se han obtenido para la Península Ibérica y se han comparado entre ellos usando como referencia mediciones de humedad *in situ*.

References

1. Friedl, L.A. Critical Earth Observation Priorities 2012.

   (https://sbageotask.larc.nasa.gov/Final_SBA_Report_US0901a_v2.pdf)

2. Anderson, M.C.; Norman, J.M.; Mecikalski, J.R.; Otkin, J.A.; Kustas, W.P. A Climatological Study of Evapotranspiration and Moisture Stress across the Continental United States Based on Thermal Remote Sensing: 2. Surface Moisture Climatology. *Journal of Geophysical Research: Atmospheres* **2007**, *112*, doi:10.1029/2006JD007507.

3. Robinson, D.A.; Campbell, C.S.; Hopmans, J.W.; Hornbuckle, B.K.; Jones, S.B.; Knight, R.; Ogden, F.; Selker, J.; Wendroth, O. Soil Moisture Measurement for Ecological and Hydrological Watershed-Scale Observatories: A Review. *Vadose Zone Journal* **2008**, *7*, 358–389, doi:10.2136/vzj2007.0143.

4. de Jeu, R.A.M.; Loew, A.; Stacke, T.; Dorigo, W.; Hageman, S. Potential and Limitations of Multidecadal Satellite Soil Moisture Observations for Selected Climate Model Evaluation Studies. *Hydrology and Earth System Sciences* **2013**, *17*, 3523–3542, doi:10.5194/hess-17-3523-2013.

5. Dobriyal, P.; Qureshi, A.; Badola, R.; Hussain, S.A. A Review of the Methods Available for Estimating Soil Moisture and Its Implications for Water Resource Management. *Journal of Hydrology* **2012**, *458–459*, 110–117, doi:10.1016/j.jhydrol.2012.06.021.

6. Dorigo, W.A.; Wagner, W.; Hohensinn, R.; Hahn, S.; Paulik, C.; Xaver, A.; Gruber, A.; Drusch, M.; Mecklenburg, S.; van Oevelen, P.; et al. The International Soil Moisture Network: A Data Hosting Facility for Global in Situ Soil Moisture Measurements. *Hydrology and Earth System Sciences* **2011**, *15*, 1675–1698, doi:10.5194/hess-15-1675-2011.

7. Brocca, L.; Morbidelli, R.; Melone, F.; Moramarco, T. Soil Moisture Spatial Variability in Experimental Areas of Central Italy. *Journal of Hydrology* **2007**, *333*, 356–373, doi:10.1016/j.jhydrol.2006.09.004.

8. Peng, J.; Loew, A.; Merlin, O.; Verhoest, N.E.C. A Review of Spatial Downscaling of Satellite Remotely Sensed Soil Moisture. *Reviews of Geophysics* **2017**, *55*, 341–366, doi:10.1002/2016RG000543.

9. Ulaby, F.T.; Long, D.G.; Blackwell, W. *Microwave Radar and Radiometric Remote Sensing*; University of Michigan Press: Ann Arbor, 2014; ISBN 978-0-472-11935-6.

10. Schmugge, T. Applications of Passive Microwave Observations of Surface Soil Moisture. *Journal of Hydrology* **1998**, *212–213*, 188–197, doi:10.1016/S0022-1694(98)00209-1.

11. Kerr, Y.H.; Waldteufel, P.; Wigneron, J.-P.; Delwart, S.; Cabot, F.; Boutin, J.; Escorihuela, M.-J.; Font, J.; Reul, N.; Gruhier, C.; et al. The SMOS Mission: New Tool for Monitoring Key Elements Ofthe Global Water Cycle. *Proceedings of the IEEE* **2010**, *98*, 666–687, doi:10.1109/JPROC.2010.2043032.

12. Entekhabi, D.; Njoku, E.G.; O'Neill, P.E.; Kellogg, K.H.; Crow, W.T.; Edelstein, W.N.; Entin, J.K.; Goodman, S.D.; Jackson, T.J.; Johnson, J.; et al. The Soil Moisture Active Passive

(SMAP) Mission. *Proceedings of the IEEE* **2010**, *98*, 704–716, doi:10.1109/JPROC.2010.2043918.

13. Fung, A.K.; Li, Z.; Chen, K.S. Backscattering from a Randomly Rough Dielectric Surface. *IEEE Transactions on Geoscience and Remote Sensing* **1992**, *30*, 356–369, doi:10.1109/36.134085.

14. Oh, Y.; Sarabandi, K.; Ulaby, F.T. Semi-Empirical Model of the Ensemble-Averaged Differential Mueller Matrix for Microwave Backscattering from Bare Soil Surfaces. *IEEE Transactions on Geoscience and Remote Sensing* **2002**, *40*, 1348–1355, doi:10.1109/TGRS.2002.800232.

15. Wang, J.R.; Schmugge, T.J. An Empirical Model for the Complex Dielectric Permittivity of Soils as a Function of Water Content. *IEEE Transactions on Geoscience and Remote Sensing* **1980**, *GE-18*, 288–295, doi:10.1109/TGRS.1980.350304.

16. Dubois, P.C.; van Zyl, J.; Engman, T. Measuring Soil Moisture with Imaging Radars. *IEEE Transactions on Geoscience and Remote Sensing* **1995**, *33*, 915–926, doi:10.1109/36.406677.

17. Thoma, D.P.; Moran, M.S.; Bryant, R.; Rahman, M.; Holifield-Collins, C.D.; Skirvin, S.; Sano, E.E.; Slocum, K. Comparison of Four Models to Determine Surface Soil Moisture from C-Band Radar Imagery in a Sparsely Vegetated Semiarid Landscape. *Water Resources Research* **2006**, *42*, doi:10.1029/2004WR003905.

18. Wagner, W.; Scipal, K. Large-Scale Soil Moisture Mapping in Western Africa Using the ERS Scatterometer. *IEEE Transactions on Geoscience and Remote Sensing* **2000**, *38*, 1777–1782, doi:10.1109/36.851761.

19. Jackson, T.J. III. Measuring Surface Soil Moisture Using Passive Microwave Remote Sensing. *Hydrological Processes* **1993**, *7*, 139–152, doi:10.1002/hyp.3360070205.

20. Njoku, E.G.; Li, L. Retrieval of Land Surface Parameters Using Passive Microwave Measurements at 6-18 GHz. *IEEE Transactions on Geoscience and Remote Sensing* **1999**, *37*, 79–93, doi:10.1109/36.739125.

21. Konings, A.G.; Piles, M.; Rötzer, K.; McColl, K.A.; Chan, S.K.; Entekhabi, D. Vegetation Optical Depth and Scattering Albedo Retrieval Using Time Series of Dual-Polarized L-Band Radiometer Observations. *Remote Sensing of Environment* **2016**, *172*, 178–189, doi:10.1016/j.rse.2015.11.009.

22. Owe, M.; de Jeu, R.; Walker, J. A Methodology for Surface Soil Moisture and Vegetation Optical Depth Retrieval Using the Microwave Polarization Difference Index. *IEEE Transactions on Geoscience and Remote Sensing* **2001**, *39*, 1643–1654, doi:10.1109/36.942542.

23. Fernandez-Moran, R.; Al-Yaari, A.; Mialon, A.; Mahmoodi, A.; Al Bitar, A.; De Lannoy, G.; Rodriguez-Fernandez, N.; Lopez-Baeza, E.; Kerr, Y.; Wigneron, J.-P. SMOS-IC: An Alternative SMOS Soil Moisture and Vegetation Optical Depth Product. *Remote Sensing* **2017**, *9*, 457, doi:10.3390/rs9050457.

24. Peng, J.; Albergel, C.; Balenzano, A.; Brocca, L.; Cartus, O.; Cosh, M.H.; Crow, W.T.; Dabrowska-Zielinska, K.; Dadson, S.; Davidson, M.W.J.; et al. A Roadmap for High-Resolution Satellite Soil Moisture Applications – Confronting Product Characteristics with

User Requirements. *Remote Sensing of Environment* **2021**, *252*, 112162, doi:10.1016/j.rse.2020.112162.

25. Sabaghy, S.; Walker, J.P.; Renzullo, L.J.; Jackson, T.J. Spatially Enhanced Passive Microwave Derived Soil Moisture: Capabilities and Opportunities. *Remote Sensing of Environment* **2018**, *209*, 551–580, doi:10.1016/j.rse.2018.02.065.

26. Munoz-Martin, J.F.; Llaveria, D.; Herbert, C.; Pablos, M.; Park, H.; Camps, A. Soil Moisture Estimation Synergy Using GNSS-R and L-Band Microwave Radiometry Data from FSSCat/FMPL-2. *Remote Sensing* **2021**, *13*, 994, doi:10.3390/rs13050994.

27. Portal, G.; Vall-llossera, M.; Piles, M.; Camps, A.; Chaparro, D.; Pablos, M.; Rossato, L. A Spatially Consistent Downscaling Approach for SMOS Using an Adaptive Moving Window. *IEEE Journal of Selected Topics in Applied Earth Observations and Remote Sensing* **2018**, *11*, 1883–1894, doi:10.1109/JSTARS.2018.2832447.

28. Merlin, O.; Chehbouni, A.G.; Kerr, Y.H.; Njoku, E.G.; Entekhabi, D. A Combined Modeling and Multispectral/Multiresolution Remote Sensing Approach for Disaggregation of Surface Soil Moisture: Application to SMOS Configuration. *IEEE Transactions on Geoscience and Remote Sensing* **2005**, *43*, 2036–2050, doi:10.1109/TGRS.2005.853192.

29. Piles, M.; Camps, A.; Vall-llossera, M.; Corbella, I.; Panciera, R.; Rudiger, C.; Kerr, Y.H.; Walker, J. Downscaling SMOS-Derived Soil Moisture Using MODIS Visible/Infrared Data. *IEEE Transactions on Geoscience and Remote Sensing* **2011**, *49*, 3156–3166, doi:10.1109/TGRS.2011.2120615.

30. Piles, M.; Petropoulos, G.P.; Sánchez, N.; González-Zamora, Á.; Ireland, G. Towards Improved Spatio-Temporal Resolution Soil Moisture Retrievals from the Synergy of SMOS and MSG SEVIRI Spaceborne Observations. *Remote Sensing of Environment* **2016**, *180*, 403–417, doi:10.1016/j.rse.2016.02.048.

31. Piles, M.; Entekhabi, D.; Camps, A. A Change Detection Algorithm for Retrieving High-Resolution Soil Moisture From SMAP Radar and Radiometer Observations. *IEEE Transactions on Geoscience and Remote Sensing* **2009**, *47*, 4125–4131, doi:10.1109/TGRS.2009.2022088.

32. Das, N.N.; Entekhabi, D.; Njoku, E.G. An Algorithm for Merging SMAP Radiometer and Radar Data for High-Resolution Soil-Moisture Retrieval. *IEEE Transactions on Geoscience and Remote Sensing* **2011**, *49*, 1504–1512, doi:10.1109/TGRS.2010.2089526.

33. Pellenq, J.; Kalma, J.; Boulet, G.; Saulnier, G.-M.; Wooldridge, S.; Kerr, Y.; Chehbouni, A. A Disaggregation Scheme for Soil Moisture Based on Topography and Soil Depth. *Journal of Hydrology* **2003**, *276*, 112–127, doi:10.1016/S0022-1694(03)00066-0.

34. Anderson, J.A. *An Introduction to Neural Networks*; A Bradford Book: Cambridge, MA, USA, 1995; ISBN 978-0-262-01144-0.

35. Vapnik, V.; Golowich, S.E.; Smola, A. Support Vector Method for Function Approximation, Regression Estimation and Signal Processing. In Proceedings of the Proceedings of the 9th International Conference on Neural Information Processing Systems; MIT Press: Cambridge, MA, USA, December 3 1996; pp. 281–287.

36. Bishop, C.M.; Tipping, M.E. Variational Relevance Vector Machines. In Proceedings of the Proceedings of the Sixteenth conference on Uncertainty in artificial intelligence; Morgan Kaufmann Publishers Inc.: San Francisco, CA, USA, June 30 2000; pp. 46–53.

37. Tipping, M.E. Sparse Bayesian Learning and the Relevance Vector Machine. *J. Mach. Learn. Res.* **2001**, *1*, 211–244, doi:10.1162/15324430152748236.

38. Breiman, L. Random Forests. *Machine Learning* **2001**, *45*, 5–32, doi:10.1023/A:1010933404324.

39. Friedman, J.H. Stochastic Gradient Boosting. *Computational Statistics & Data Analysis* **2002**, *38*, 367–378, doi:10.1016/S0167-9473(01)00065-2.

40. Reichstein, M.; Camps-Valls, G.; Stevens, B.; Jung, M.; Denzler, J.; Carvalhais, N.; Prabhat Deep Learning and Process Understanding for Data-Driven Earth System Science. *Nature* **2019**, *566*, 195–204, doi:10.1038/s41586-019-0912-1.

41. Camps-Valls, G.; Svendsen, D.H.; Cortés-Andrés, J.; Mareno-Martínez, Á.; Pérez-Suay, A.; Adsuara, J.; Martín, I.; Piles, M.; Muñoz-Marí, J.; Martino, L. Physics-Aware Machine Learning for Geosciences and Remote Sensing. In Proceedings of the 2021 IEEE International Geoscience and Remote Sensing Symposium IGARSS; July 2021; pp. 2086–2089.

42. Ochsner, T.E.; Cosh, M.H.; Cuenca, R.H.; Dorigo, W.A.; Draper, C.S.; Hagimoto, Y.; Kerr, Y.H.; Larson, K.M.; Njoku, E.G.; Small, E.E.; et al. State of the Art in Large-Scale Soil Moisture Monitoring. *Soil Science Society of America Journal* **2013**, *77*, 1888–1919, doi:10.2136/sssaj2013.03.0093.

43. Escorihuela, M.J.; Merlin, O.; Stefan, V.; Moyano, G.; Eweys, O.A.; Zribi, M.; Kamara, S.; Benahi, A.S.; Ebbe, M.A.B.; Chihrane, J.; et al. SMOS Based High Resolution Soil Moisture Estimates for Desert Locust Preventive Management. *Remote Sensing Applications: Society and Environment* **2018**, *11*, 140–150, doi:10.1016/j.rsase.2018.06.002.

44. Chaparro, D.; Vall-llossera, M.; Piles, M.; Camps, A.; Rüdiger, C.; Riera-Tatché, R. Predicting the Extent of Wildfires Using Remotely Sensed Soil Moisture and Temperature Trends. *IEEE Journal of Selected Topics in Applied Earth Observations and Remote Sensing* **2016**, *9*, 2818–2829, doi:10.1109/JSTARS.2016.2571838.

45. Chaparro, D.; Piles, M.; Vall-llossera, M.; Camps, A. Surface Moisture and Temperature Trends Anticipate Drought Conditions Linked to Wildfire Activity in the Iberian Peninsula. *European Journal of Remote Sensing* **2016**, *49*, 955–971, doi:10.5721/EuJRS20164950.

46. Piles, M.; Sánchez, N.; Vall-llossera, M.; Camps, A.; Martínez-Fernández, J.; Martínez, J.; González-Gambau, V. A Downscaling Approach for SMOS Land Observations: Evaluation of High-Resolution Soil Moisture Maps Over the Iberian Peninsula. *IEEE Journal of Selected Topics in Applied Earth Observations and Remote Sensing* **2014**, *7*, 3845–3857, doi:10.1109/JSTARS.2014.2325398.

47. Merlin, O.; Rudiger, C.; Al Bitar, A.; Richaume, P.; Walker, J.P.; Kerr, Y.H. Disaggregation of SMOS Soil Moisture in Southeastern Australia. *IEEE Transactions on Geoscience and Remote Sensing* **2012**, *50*, 1556–1571, doi:10.1109/TGRS.2011.2175000.

48. ONeill, Peggy E.; Chan, Steven; Njoku, Eni G.; Jackson, Tom; Bindlish, Rajat; Chaubell, M. Julian SMAP L2 Radiometer Half-Orbit 36 Km EASE-Grid Soil Moisture, Version 6 2019.

49. Fernandez-Moran, R.; Wigneron, J.-P.; De Lannoy, G.; Lopez-Baeza, E.; Parrens, M.; Mialon, A.; Mahmoodi, A.; Al-Yaari, A.; Bircher, S.; Al Bitar, A.; et al. A New Calibration of the Effective Scattering Albedo and Soil Roughness Parameters in the SMOS SM Retrieval Algorithm. *International Journal of Applied Earth Observation and Geoinformation* **2017**, *62*, 27–38, doi:10.1016/j.jag.2017.05.013.

50. van der Schalie, R.; Parinussa, R.M.; Renzullo, L.J.; van Dijk, A.I.J.M.; Su, C.-H.; de Jeu, R.A.M. SMOS Soil Moisture Retrievals Using the Land Parameter Retrieval Model: Evaluation over the Murrumbidgee Catchment, Southeast Australia. *Remote Sensing of Environment* **2015**, *163*, 70–79, doi:10.1016/j.rse.2015.03.006.

51. Ulaby, F.T.; Moore, R.K.; Fung, A.K. *Microwave Remote Sensing Active and Passive*; Artech House: Dedham, Mass, 1986; ISBN 978-0-89006-192-3.

52. Le Vine, D.M.; Abraham, S. The Effect of the Ionosphere on Remote Sensing of Sea Surface Salinity from Space: Absorption and Emission at L Band. *IEEE Transactions on Geoscience and Remote Sensing* **2002**, *40*, 771–782, doi:10.1109/TGRS.2002.1006342.

53. RECOMMENDATION ITU-R P.531-14 - Ionospheric Propagation Data and Prediction Methods Required for the Design of Satellite Networks and Systems. *Technical Report* 25.

54. Randa, J.; Lahtinen, J.; Camps, A.; Gasiewski, A.; Hallikainen, M.; Vine, D.; martin-neira, M.; Piepmeier, J.; Rosenkranz, P.; Ruf, C.; et al. Recommended Terminology for Microwave Radiometry. **2008**.

55. Topp, G.C.; Davis, J.L.; Annan, A.P. Electromagnetic Determination of Soil Water Content: Measurements in Coaxial Transmission Lines. *Water Resources Research* **1980**, *16*, 574–582, doi:10.1029/WR016i003p00574.

56. Dobson, M.C.; Ulaby, F.T.; Hallikainen, M.T.; El-rayes, M.A. Microwave Dielectric Behavior of Wet Soil-Part II: Dielectric Mixing Models. *IEEE Transactions on Geoscience and Remote Sensing* **1985**, *GE-23*, 35–46, doi:10.1109/TGRS.1985.289498.

57. Mironov, V.L.; Kosolapova, L.G.; Fomin, S.V. Physically and Mineralogically Based Spectroscopic Dielectric Model for Moist Soils. *IEEE Transactions on Geoscience and Remote Sensing* **2009**, *47*, 2059–2070, doi:10.1109/TGRS.2008.2011631.

58. Birchak, J.R.; Gardner, C.G.; Hipp, J.E.; Victor, J.M. High Dielectric Constant Microwave Probes for Sensing Soil Moisture. *Proceedings of the IEEE* **1974**, *62*, 93–98, doi:10.1109/PROC.1974.9388.

59. Rodríguez-Iturbe, I.; Porporato, A. *Ecohydrology of Water-Controlled Ecosystems: Soil Moisture and Plant Dynamics*; Cambridge University Press: Cambridge, 2005; ISBN 978-0-521-03674-0.

60. Mialon, A.; Richaume, P.; Leroux, D.; Bircher, S.; Bitar, A.A.; Pellarin, T.; Wigneron, J.-P.; Kerr, Y.H. Comparison of Dobson and Mironov Dielectric Models in the SMOS Soil Moisture Retrieval Algorithm. *IEEE Transactions on Geoscience and Remote Sensing* **2015**, *53*, 3084–3094, doi:10.1109/TGRS.2014.2368585.

61. Wigneron, J.-P.; Jackson, T.J.; O'Neill, P.; De Lannoy, G.; de Rosnay, P.; Walker, J.P.; Ferrazzoli, P.; Mironov, V.; Bircher, S.; Grant, J.P.; et al. Modelling the Passive Microwave Signature from Land Surfaces: A Review of Recent Results and Application to the L-Band

SMOS & SMAP Soil Moisture Retrieval Algorithms. *Remote Sensing of Environment* **2017**, *192*, 238–262, doi:10.1016/j.rse.2017.01.024.

62. Wigneron, J.-P.; Laguerre, L.; Kerr, Y.H. A Simple Parameterization of the L-Band Microwave Emission from Rough Agricultural Soils. *IEEE Transactions on Geoscience and Remote Sensing* **2001**, *39*, 1697–1707, doi:10.1109/36.942548.

63. Choudhury, B.J.; Schmugge, T.J.; Mo, T. A Parameterization of Effective Soil Temperature for Microwave Emission. *Journal of Geophysical Research* **1982**, *87*, 1301–1304, doi:10.1029/JC087iC02p01301.

64. Choudhury, B.J.; Schmugge, T.J.; Chang, A.; Newton, R.W. Effect of Surface Roughness on the Microwave Emission from Soils. *Journal of Geophysical Research: Oceans* **1979**, *84*, 5699–5706, doi:10.1029/JC084iC09p05699.

65. Wang, J.R.; Choudhury, B.J. Remote Sensing of Soil Moisture Content, over Bare Field at 1.4 GHz Frequency. *Journal of Geophysical Research: Oceans* **1981**, *86*, 5277–5282, doi:10.1029/JC086iC06p05277.

66. Wang, J.R.; O'Neill, P.E.; Jackson, T.J.; Engman, E.T. Multifrequency Measurements of the Effects of Soil Moisture, Soil Texture, And Surface Roughness. *IEEE Transactions on Geoscience and Remote Sensing* **1983**, *GE-21*, 44–51, doi:10.1109/TGRS.1983.350529.

67. Shi, J.; Chen, K.S.; Li, Q.; Jackson, T.J.; O'Neill, P.E.; Tsang, L. A Parameterized Surface Reflectivity Model and Estimation of Bare-Surface Soil Moisture with L-Band Radiometer. *IEEE Transactions on Geoscience and Remote Sensing* **2002**, *40*, 2674–2686, doi:10.1109/TGRS.2002.807003.

68. Kerr, Y.H.; Njoku, E.G. A Semiempirical Model for Interpreting Microwave Emission from Semiarid Land Surfaces as Seen from Space. *IEEE Transactions on Geoscience and Remote Sensing* **1990**, *28*, 384–393, doi:10.1109/36.54364.

69. Mo, T.; Schmugge, T.J. A Parameterization of the Effect of Surface Roughness on Microwave Emission. *IEEE Transactions on Geoscience and Remote Sensing* **1987**, *GE-25*, 481–486, doi:10.1109/TGRS.1987.289860.

70. Escorihuela, M.J.; Kerr, Y.H.; de Rosnay, P.; Wigneron, J.-P.; Calvet, J.-C.; Lemaitre, F. A Simple Model of the Bare Soil Microwave Emission at L-Band. *IEEE Transactions on Geoscience and Remote Sensing* **2007**, *45*, 1978–1987, doi:10.1109/TGRS.2007.894935.

71. Schneeberger, K.; Schwank, M.; Stamm, C.; de Rosnay, P.; Mätzler, C.; Flühler, H. Topsoil Structure Influencing Soil Water Retrieval by Microwave Radiometry. *Vadose Zone Journal* **2004**, 1169–1179, doi:10.2136/vzj2004.1169.

72. Njoku, E.G.; Chan, S.K. Vegetation and Surface Roughness Effects on AMSR-E Land Observations. *Remote Sensing of Environment* **2006**, *100*, 190–199, doi:10.1016/j.rse.2005.10.017.

73. Peischl, S.; Walker, J.P.; Ryu, D.; Kerr, Y.H.; Panciera, R.; Rudiger, C. Wheat Canopy Structure and Surface Roughness Effects on Multiangle Observations at L-Band. *IEEE Transactions on Geoscience and Remote Sensing* **2012**, *50*, 1498–1506, doi:10.1109/TGRS.2011.2174644.

74. Schlenz, F.; Fallmann, J.; Marzahn, P.; Loew, A.; Mauser, W. Characterization of Rape Field Microwave Emission and Implications to Surface Soil Moisture Retrievals. *Remote Sensing* **2012**, *4*, 247–270, doi:10.3390/rs4010247.

75. de Rosnay, P.; Calvet, J.-C.; Kerr, Y.; Wigneron, J.-P.; Lemaître, F.; Escorihuela, M.J.; Sabater, J.M.; Saleh, K.; Barrié, J.; Bouhours, G.; et al. SMOSREX: A Long Term Field Campaign Experiment for Soil Moisture and Land Surface Processes Remote Sensing. *Remote Sensing of Environment* **2006**, *102*, 377–389, doi:10.1016/j.rse.2006.02.021.

76. Rossato, L.; Vall-Llossera, M.; Camps, A.; Portal, G.; Sakuragi, J.; Angelis, C.F.; Zeri, M.; Barbosa, H.; Paredes, F. Validation of Soil Moisture in the Brazilian Semiarid, Using Smos Satellite Product And Simagri Model. In Proceedings of the IGARSS 2018 - 2018 IEEE International Geoscience and Remote Sensing Symposium; July 2018; pp. 84–87.

77. Sanchez, N.; Martinez-Fernandez, J.; Scaini, A.; Perez-Gutierrez, C. Validation of the SMOS L2 Soil Moisture Data in the REMEDHUS Network (Spain). *IEEE Transactions on Geoscience and Remote Sensing* **2012**, *50*, 1602–1611, doi:10.1109/TGRS.2012.2186971.

78. Lawrence, H.; Wigneron, J.-P.; Demontoux, F.; Mialon, A.; Kerr, Y.H. Evaluating the Semiempirical H - Q Model Used to Calculate the L-Band Emissivity of a Rough Bare Soil. *IEEE Transactions on Geoscience and Remote Sensing* **2013**, *51*, 4075–4084, doi:10.1109/TGRS.2012.2226995.

79. Schalie, R. van der; Kerr, Y.H.; Wigneron, J.P.; Rodríguez-Fernández, N.J.; Al-Yaari, A.; Jeu, R.A.M. de Global SMOS Soil Moisture Retrievals from The Land Parameter Retrieval Model. *International Journal of Applied Earth Observation and Geoinformation* **2016**, *45*, 125–134, doi:10.1016/j.jag.2015.08.005.

80. Bircher, S.; Balling, J.E.; Skou, N.; Kerr, Y.H. Validation of SMOS Brightness Temperatures During the HOBE Airborne Campaign, Western Denmark. *IEEE Transactions on Geoscience and Remote Sensing* **2012**, *50*, 1468–1482, doi:10.1109/TGRS.2011.2170177.

81. Mo, T.; Choudhury, B.J.; Schmugge, T.J.; Wang, J.R.; Jackson, T.J. A Model for Microwave Emission from Vegetation-Covered Fields. *Journal of Geophysical Research: Oceans* **1982**, *87*, 11229–11237, doi:10.1029/JC087iC13p11229.

82. Ulaby, F.T.; Wilson, E.A. Microwave Attenuation Properties of Vegetation Canopies. *IEEE Transactions on Geoscience and Remote Sensing* **1985**, *GE-23*, 746–753, doi:10.1109/TGRS.1985.289393.

83. Jackson, T.J.; Schmugge, T.J.; Wang, J.R. Passive Microwave Sensing of Soil Moisture under Vegetation Canopies. *Water Resources Research* **1982**, *18*, 1137–1142, doi:10.1029/WR018i004p01137.

84. Wigneron, J.-P.; Chanzy, A.; Calvet, J.-C.; Bruguier, N. A Simple Algorithm to Retrieve Soil Moisture and Vegetation Biomass Using Passive Microwave Measurements over Crop Fields. *Remote Sensing of Environment* **1995**, *51*, 331–341, doi:10.1016/0034-4257(94)00081-W.

85. Meesters, A.G.C.A.; De Jeu, R.A.M.; Owe, M. Analytical Derivation of the Vegetation Optical Depth from the Microwave Polarization Difference Index. *IEEE Geoscience and Remote Sensing Letters* **2005**, *2*, 121–123, doi:10.1109/LGRS.2005.843983.

86. Kerr, Y.H.; Waldteufel, P.; Richaume, P.; Wigneron, J.P.; Ferrazzoli, P.; Mahmoodi, A.; Al Bitar, A.; Cabot, F.; Gruhier, C.; Juglea, S.E.; et al. The SMOS Soil Moisture Retrieval Algorithm. *IEEE Transactions on Geoscience and Remote Sensing* **2012**, *50*, 1384–1403, doi:10.1109/TGRS.2012.2184548.

87. Davenport, I.J.; Fernandez-Galvez, J.; Gurney, R.J. A Sensitivity Analysis of Soil Moisture Retrieval from the Tau-Omega Microwave Emission Model. *IEEE Transactions on Geoscience and Remote Sensing* **2005**, *43*, 1304–1316, doi:10.1109/TGRS.2005.845640.

88. Grant, J.P.; Wigneron, J.-P.; De Jeu, R.A.M.; Lawrence, H.; Mialon, A.; Richaume, P.; Al Bitar, A.; Drusch, M.; van Marle, M.J.E.; Kerr, Y. Comparison of SMOS and AMSR-E Vegetation Optical Depth to Four MODIS-Based Vegetation Indices. *Remote Sensing of Environment* **2016**, *172*, 87–100, doi:10.1016/j.rse.2015.10.021.

89. Entekhabi, D.; Yueh, S.; E. O'Neil, P.; H. Kellogg, K.; Allen, A.; Bindlish, R.; Brown, M.; Chan, S.; Colliander, A.; T. Crow, W.; et al. *SMAP Handbook Soil Moisture Active Passive*; JPL Publications;

90. Jackson, T.J.; Chen, D.; Cosh, M.; Li, F.; Anderson, M.; Walthall, C.; Doriaswamy, P.; Hunt, E.R. Vegetation Water Content Mapping Using Landsat Data Derived Normalized Difference Water Index for Corn and Soybeans. *Remote Sensing of Environment* **2004**, *92*, 475–482, doi:10.1016/j.rse.2003.10.021.

91. Pellarin, T.; Calvet, J.-C.; Wigneron, J.-P. Surface Soil Moisture Retrieval from L-Band Radiometry: A Global Regression Study. *IEEE Transactions on Geoscience and Remote Sensing* **2003**, *41*, 2037–2051, doi:10.1109/TGRS.2003.813492.

92. Saleh, K.; Wigneron, J.-P.; de Rosnay, P.; Calvet, J.-C.; Escorihuela, M.J.; Kerr, Y.; Waldteufel, P. Impact of Rain Interception by Vegetation and Mulch on the L-Band Emission of Natural Grass. *Remote Sensing of Environment* **2006**, *101*, 127–139, doi:10.1016/j.rse.2005.12.004.

93. JUSTICE, C.O.; TOWNSHEND, J.R.G.; CHOUDHURY, B.J. Comparison of AVHRR and SMMR Data for Monitoring Vegetation Phenology on a Continental Scale. *International Journal of Remote Sensing* **2007**, doi:10.1080/01431168908903994.

94. Chen, D.; Huang, J.; Jackson, T.J. Vegetation Water Content Estimation for Corn and Soybeans Using Spectral Indices Derived from MODIS Near- and Short-Wave Infrared Bands. *Remote Sensing of Environment* **2005**, *98*, 225–236, doi:10.1016/j.rse.2005.07.008.

95. Karthikeyan, L.; Pan, M.; Wanders, N.; Kumar, D.N.; Wood, E.F. Four Decades of Microwave Satellite Soil Moisture Observations: Part 1. A Review of Retrieval Algorithms. *Advances in Water Resources* **2017**, *109*, 106–120, doi:10.1016/j.advwatres.2017.09.006.

96. Wigneron, J.-P.; Kerr, Y.; Waldteufel, P.; Saleh, K.; Escorihuela, M.-J.; Richaume, P.; Ferrazzoli, P.; de Rosnay, P.; Gurney, R.; Calvet, J.-C.; et al. L-Band Microwave Emission of the Biosphere (L-MEB) Model: Description and Calibration against Experimental Data Sets over Crop Fields. *Remote Sensing of Environment* **2007**, *107*, 639–655, doi:10.1016/j.rse.2006.10.014.

97. Bindlish, R.; Jackson, T.J.; Wood, E.; Gao, H.; Starks, P.; Bosch, D.; Lakshmi, V. Soil Moisture Estimates from TRMM Microwave Imager Observations over the Southern

United States. *Remote Sensing of Environment* **2003**, *85*, 507–515, doi:10.1016/S0034-4257(03)00052-X.

98. Pan, M.; Sahoo, A.K.; Wood, E.F. Improving Soil Moisture Retrievals from a Physically-Based Radiative Transfer Model. *Remote Sensing of Environment* **2014**, *140*, 130–140, doi:10.1016/j.rse.2013.08.020.

99. Parrens, M.; Wigneron, J.-P.; Richaume, P.; Al Bitar, A.; Mialon, A.; Fernandez-Moran, R.; Al-Yaari, A.; O'Neill, P.; Kerr, Y. Considering Combined or Separated Roughness and Vegetation Effects in Soil Moisture Retrievals. *International Journal of Applied Earth Observation and Geoinformation* **2017**, *55*, 73–86, doi:10.1016/j.jag.2016.11.001.

100. Feldman, A.F.; Akbar, R.; Entekhabi, D. Characterization of Higher-Order Scattering from Vegetation with SMAP Measurements. *Remote Sensing of Environment* **2018**, *219*, 324–338, doi:10.1016/j.rse.2018.10.022.

101. Schwank, M.; Naderpour, R.; Mätzler, C. "Tau-Omega"- and Two-Stream Emission Models Used for Passive L-Band Retrievals: Application to Close-Range Measurements over a Forest. *Remote Sensing* **2018**, *10*, 1868, doi:10.3390/rs10121868.

102. Wiesmann, A.; Mätzler, C. Microwave Emission Model of Layered Snowpacks. *Remote Sensing of Environment* **1999**, *70*, 307–316, doi:10.1016/S0034-4257(99)00046-2.

103. Li, X.; Al-Yaari, A.; Schwank, M.; Fan, L.; Frappart, F.; Swenson, J.; Wigneron, J.-P. Compared Performances of SMOS-IC Soil Moisture and Vegetation Optical Depth Retrievals Based on Tau-Omega and Two-Stream Microwave Emission Models. *Remote Sensing of Environment* **2020**, *236*, 111502, doi:10.1016/j.rse.2019.111502.

104. Guglielmetti, M.; Schwank, M.; Matzler, C.; Oberdorster, C.; Vanderborght, J.; Fluhler, H. FOSMEX: Forest Soil Moisture Experiments With Microwave Radiometry. *IEEE Transactions on Geoscience and Remote Sensing* **2008**, *46*, 727–735, doi:10.1109/TGRS.2007.914797.

105. Drusch, M.; Wood, E.F.; Jackson, T.J. Vegetative and Atmospheric Corrections for the Soil Moisture Retrieval from Passive Microwave Remote Sensing Data: Results from the Southern Great Plains Hydrology Experiment 1997. *Journal of Hydrometeorology* **2001**, *2*, 181–192, doi:10.1175/1525-7541(2001)002<0181:VAACFT>2.0.CO;2.

106. Chan, S.K.; Bindlish, R.; O'Neill, P.; Jackson, T.; Njoku, E.; Dunbar, S.; Chaubell, J.; Piepmeier, J.; Yueh, S.; Entekhabi, D.; et al. Development and Assessment of the SMAP Enhanced Passive Soil Moisture Product. *Remote Sensing of Environment* **2018**, *204*, 931–941, doi:10.1016/j.rse.2017.08.025.

107. Konings, A.G.; McColl, K.A.; Piles, M.; Entekhabi, D. How Many Parameters Can Be Maximally Estimated From a Set of Measurements? *IEEE Geoscience and Remote Sensing Letters* **2015**, *12*, 1081–1085, doi:10.1109/LGRS.2014.2381641.

108. Owe, M.; Jeu, R. de; Holmes, T. Multisensor Historical Climatology of Satellite-Derived Global Land Surface Moisture. *Journal of Geophysical Research: Earth Surface* **2008**, *113*, doi:10.1029/2007JF000769.

109. Masson, V.; Valéry; Champeaux, J.-L.; Jean-Louis; Chauvin; Fabrice, F.; Meriguet; Christelle; Lacaze, R.; Roselyne A Global Database of Land Surface Parameters at 1-Km Resolution in Meteorological and Climate Models. *Journal of Climate* **2003**, *16*, 1261.

110. Lannoy, G.J.M.D.; Reichle, R.H.; Pauwels, V.R.N. Global Calibration of the GEOS-5 L-Band Microwave Radiative Transfer Model over Nonfrozen Land Using SMOS Observations. *Journal of Hydrometeorology* **2013**, *14*, 765–785, doi:10.1175/JHM-D-12-092.1.

111. SMOS Data Products (Issue November 2017).

(https://earth.esa.int/documents/10174/1854456/SMOS-Data-Products-Brochure)

112. Mission Objectives and Scientific Requiremets of the SMOS Mission (2003), MRD, Version 5.

113. Jackson, T.J.; Schmugge, T.J. Passive Microwave Remote Sensing System for Soil Moisture: Some Supporting Research. *IEEE Transactions on Geoscience and Remote Sensing* **1989**, *27*, 225–235, doi:10.1109/36.20301.

114. Emery, B.; Camps, A. *Introduction to Satellite Remote Sensing: Atmosphere, Ocean, Land and Cryosphere Applications*; Elsevier, 2017; ISBN 978-0-12-809259-0.

115. BEC Products – BEC (Barcelona Expert Center) 2021.

(http://bec.icm.csic.es/data/)

116. Data Products | Data Available online: https://smap.jpl.nasa.gov/data (accessed on 6 February 2022).

117. Das, N.N.; Entekhabi, D.; Dunbar, R.S.; Chaubell, M.J.; Colliander, A.; Yueh, S.; Jagdhuber, T.; Chen, F.; Crow, W.; O'Neill, P.E.; et al. The SMAP and Copernicus Sentinel 1A/B Microwave Active-Passive High Resolution Surface Soil Moisture Product. *Remote Sensing of Environment* **2019**, *233*, 111380, doi:10.1016/j.rse.2019.111380.

118. Merlin, O.; Escorihuela, M.J.; Mayoral, M.A.; Hagolle, O.; Al Bitar, A.; Kerr, Y. Self-Calibrated Evaporation-Based Disaggregation of SMOS Soil Moisture: An Evaluation Study at 3km and 100m Resolution in Catalunya, Spain. *Remote Sensing of Environment* **2013**, *130*, 25–38, doi:10.1016/j.rse.2012.11.008.

119. Vergopolan, N.; Chaney, N.W.; Pan, M.; Sheffield, J.; Beck, H.E.; Ferguson, C.R.; Torres-Rojas, L.; Sadri, S.; Wood, E.F. SMAP-HydroBlocks, a 30-m Satellite-Based Soil Moisture Dataset for the Conterminous US. *Sci Data* **2021**, *8*, 264, doi:10.1038/s41597-021-01050-2.

120. Peng, J.; Loew, A.; Zhang, S.; Wang, J.; Niesel, J. Spatial Downscaling of Satellite Soil Moisture Data Using a Vegetation Temperature Condition Index. *IEEE Transactions on Geoscience and Remote Sensing* **2016**, *54*, 558–566, doi:10.1109/TGRS.2015.2462074.

121. Nemani, R.; Pierce, L.; Running, S.; Goward, S. Developing Satellite-Derived Estimates of Surface Moisture Status. *Journal of Applied Meteorology and Climatology* **1993**, *32*, 548–557, doi:10.1175/1520-0450(1993)032<0548:DSDEOS>2.0.CO;2.

122. Gillies, R.R.; Carlson, T.N. Thermal Remote Sensing of Surface Soil Water Content with Partial Vegetation Cover for Incorporation into Climate Models. *Journal of Applied Meteorology and Climatology* **1995**, *34*, 745–756, doi:10.1175/1520-0450(1995)034<0745:TRSOSS>2.0.CO;2.

123. Carlson, T.N.; Gillies, R.R.; Schmugge, T.J. An Interpretation of Methodologies for Indirect Measurement of Soil Water Content. *Agricultural and Forest Meteorology* **1995**, *77*, 191–205, doi:10.1016/0168-1923(95)02261-U.

124. Srivastava, P.; Petropoulos, G.; Kerr, Y. *Satellite Soil Moisture Retrieval*; Elsevier, 2016; ISBN 978-0-12-803388-3.

125. Merlin, O.; Chehbouni, A.; Walker, J.P.; Panciera, R.; Kerr, Y.H. A Simple Method to Disaggregate Passive Microwave-Based Soil Moisture. *IEEE Transactions on Geoscience and Remote Sensing* **2008**, *46*, 786–796, doi:10.1109/TGRS.2007.914807.

126. Choi, M.; Hur, Y. A Microwave-Optical/Infrared Disaggregation for Improving Spatial Representation of Soil Moisture Using AMSR-E and MODIS Products. *Remote Sensing of Environment* **2012**, *124*, 259–269, doi:10.1016/j.rse.2012.05.009.

127. Chauhan, N.S.; Miller, S.; Ardanuy, P. Spaceborne Soil Moisture Estimation at High Resolution: A Microwave-Optical/IR Synergistic Approach. *International Journal of Remote Sensing* **2003**, *24*, 4599–4622, doi:10.1080/0143116031000156837.

128. Zhan, X.; Miller, S.; Chauhan, N.; DI, L.; Ardanuy, P. Soil Moisture Visible/Infrared Radiometer Suite Algorithm Theoretical Basis Document 2002.

129. Carlson, T.N.; Gillies, R.R.; Perry, E.M. A Method to Make Use of Thermal Infrared Temperature and NDVI Measurements to Infer Surface Soil Water Content and Fractional Vegetation Cover. *Remote Sensing Reviews* **1994**, *9*, 161–173, doi:10.1080/02757259409532220.

130. Zhao, W.; Li, A. A Downscaling Method for Improving the Spatial Resolution of AMSR-E Derived Soil Moisture Product Based on MSG-SEVIRI Data. *Remote Sensing* **2013**, *5*, 6790–6811, doi:10.3390/rs5126790.

131. Combining SMOS with Visible and near/Shortwave/Thermal Infrared Satellite Data for High Resolution Soil Moisture Estimates. *Journal of Hydrology* **2014**, *516*, 273–283, doi:10.1016/j.jhydrol.2013.12.047.

132. Piles, M.; Sánchez, N. Chapter 6 - Spatial Downscaling of Passive Microwave Data With Visible-to-Infrared Information for High-Resolution Soil Moisture Mapping. In *Satellite Soil Moisture Retrieval*; Srivastava, P.K., Petropoulos, G.P., Kerr, Y.H., Eds.; Elsevier, 2016; pp. 109–132 ISBN 978-0-12-803388-3.

133. Merlin, O.; Chehbouni, A.; Kerr, Y.H.; Goodrich, D.C. A Downscaling Method for Distributing Surface Soil Moisture within a Microwave Pixel: Application to the Monsoon ’90 Data. *Remote Sensing of Environment* **2006**, *101*, 379–389, doi:10.1016/j.rse.2006.01.004.

134. Noilhan, J.; Planton, S. A Simple Parameterization of Land Surface Processes for Meteorological Models. *Monthly Weather Review* **1989**, *117*, 536–549, doi:10.1175/1520-0493(1989)117<0536:ASPOLS>2.0.CO;2.

135. Malbéteau, Y.; Merlin, O.; Gascoin, S.; Gastellu, J.P.; Mattar, C.; Olivera-Guerra, L.; Khabba, S.; Jarlan, L. Normalizing Land Surface Temperature Data for Elevation and Illumination Effects in Mountainous Areas: A Case Study Using ASTER Data over a Steep-Sided Valley in Morocco. *Remote Sensing of Environment* **2017**, *189*, 25–39, doi:10.1016/j.rse.2016.11.010.

136. Kim, J.; Hogue, T.S. Improving Spatial Soil Moisture Representation Through Integration of AMSR-E and MODIS Products. *IEEE Transactions on Geoscience and Remote Sensing* **2012**, *50*, 446–460, doi:10.1109/TGRS.2011.2161318.

137. Merlin, O.; Walker, J.P.; Chehbouni, A.; Kerr, Y. Towards Deterministic Downscaling of SMOS Soil Moisture Using MODIS Derived Soil Evaporative Efficiency. *Remote Sensing of Environment* **2008**, *112*, 3935–3946, doi:10.1016/j.rse.2008.06.012.

138. Merlin, O.; Al Bitar, A.; Walker, J.P.; Kerr, Y. A Sequential Model for Disaggregating Near-Surface Soil Moisture Observations Using Multi-Resolution Thermal Sensors. *Remote Sensing of Environment* **2009**, *113*, 2275–2284, doi:10.1016/j.rse.2009.06.012.

139. Song, C.; Jia, L.; Menenti, M. Retrieving High-Resolution Surface Soil Moisture by Downscaling AMSR-E Brightness Temperature Using MODIS LST and NDVI Data. *IEEE Journal of Selected Topics in Applied Earth Observations and Remote Sensing* **2014**, *7*, 935–942, doi:10.1109/JSTARS.2013.2272053.

140. Shi, J.; Jiang, L.; Zhang, L.; Chen, K.S.; Wigneron, J.P.; Chanzy, A.; Jackson, T.J. Physically Based Estimation of Bare-Surface Soil Moisture With the Passive Radiometers. *IEEE Transactions on Geoscience and Remote Sensing* **2006**, *44*, 3145–3153, doi:10.1109/TGRS.2006.876706.

141. Wagner, W.; Pathe, C.; Doubkova, M.; Sabel, D.; Bartsch, A.; Hasenauer, S.; Blöschl, G.; Scipal, K.; Martínez-Fernández, J.; Löw, A. Temporal Stability of Soil Moisture and Radar Backscatter Observed by the Advanced Synthetic Aperture Radar (ASAR). *Sensors* **2008**, *8*, 1174–1197, doi:10.3390/s80201174.

142. Loew, A.; Ludwig, R.; Mauser, W. Derivation of Surface Soil Moisture from ENVISAT ASAR Wide Swath and Image Mode Data in Agricultural Areas. *IEEE Transactions on Geoscience and Remote Sensing* **2006**, *44*, 889–899, doi:10.1109/TGRS.2005.863858.

143. Njoku, E.G.; Wilson, W.J.; Yueh, S.H.; Dinardo, S.J.; Li, F.K.; Jackson, T.J.; Lakshmi, V.; Bolten, J. Observations of Soil Moisture Using a Passive and Active Low-Frequency Microwave Airborne Sensor during SGP99. *IEEE Transactions on Geoscience and Remote Sensing* **2002**, *40*, 2659–2673, doi:10.1109/TGRS.2002.807008.

144. Wilson, W.J.; Yueh, S.H.; Dinardo, S.J.; Chazanoff, S.L.; Kitiyakara, A.; Li, F.K.; Rahmat-Samii, Y. Passive Active L- and S-Band (PALS) Microwave Sensor for Ocean Salinity and Soil Moisture Measurements. *IEEE Transactions on Geoscience and Remote Sensing* **2001**, *39*, 1039–1048, doi:10.1109/36.921422.

145. Le Vine, D.M.; Lagerloef, G.S.E.; Colomb, F.R.; Yueh, S.H.; Pellerano, F.A. Aquarius: An Instrument to Monitor Sea Surface Salinity From Space. *IEEE Transactions on Geoscience and Remote Sensing* **2007**, *45*, 2040–2050, doi:10.1109/TGRS.2007.898092.

146. Narayan, U.; Lakshmi, V.; Jackson, T.J. High-Resolution Change Estimation of Soil Moisture Using L-Band Radiometer and Radar Observations Made during the SMEX02 Experiments. *IEEE Transactions on Geoscience and Remote Sensing* **2006**, *44*, 1545–1554, doi:10.1109/TGRS.2006.871199.

147. Das, N.N.; Entekhabi, D.; Njoku, E.G.; Shi, J.J.C.; Johnson, J.T.; Colliander, A. Tests of the SMAP Combined Radar and Radiometer Algorithm Using Airborne Field Campaign Observations and Simulated Data. *IEEE Transactions on Geoscience and Remote Sensing* **2014**, *52*, 2018–2028, doi:10.1109/TGRS.2013.2257605.

148. Wu, X.; Walker, J.P.; Rüdiger, C.; Panciera, R.; Gao, Y. Intercomparison of Alternate Soil Moisture Downscaling Algorithms Using Active–Passive Microwave Observations. *IEEE Geoscience and Remote Sensing Letters* **2017**, *14*, 179–183, doi:10.1109/LGRS.2016.2633521.

149. Montzka, C.; Jagdhuber, T.; Horn, R.; Bogena, H.R.; Hajnsek, I.; Reigber, A.; Vereecken, H. Investigation of SMAP Fusion Algorithms With Airborne Active and Passive L-Band Microwave Remote Sensing. *IEEE Transactions on Geoscience and Remote Sensing* **2016**, *54*, 3878–3889, doi:10.1109/TGRS.2016.2529659.

150. Jagdhuber, T.; Baur, M.; Akbar, R.; Das, N.N.; Link, M.; He, L.; Entekhabi, D. Estimation of Active-Passive Microwave Covariation Using SMAP and Sentinel-1 Data. *Remote Sensing of Environment* **2019**, *225*, 458–468, doi:10.1016/j.rse.2019.03.021.

151. Metadata Record for: Global Soil Moisture Data Derived through Machine Learning Trained with in-Situ Measurements 2021.

152. Metadata Record for: SMAP-HydroBlocks, a 30-m Satellite-Based Soil Moisture Dataset for the Conterminous US 2021.

153. Scopus Preview - Scopus - Welcome to Scopus Available online: https://www.scopus.com/home.uri (accessed on 16 October 2021).

154. Srivastava, P.K.; Han, D.; Ramirez, M.R.; Islam, T. Machine Learning Techniques for Downscaling SMOS Satellite Soil Moisture Using MODIS Land Surface Temperature for Hydrological Application. *Water Resour Manage* **2013**, *27*, 3127–3144, doi:10.1007/s11269-013-0337-9.

155. Im, J.; Park, S.; Rhee, J.; Baik, J.; Choi, M. Downscaling of AMSR-E Soil Moisture with MODIS Products Using Machine Learning Approaches. *Environ Earth Sci* **2016**, *75*, 1120, doi:10.1007/s12665-016-5917-6.

156. Pablos, M.; González-Haro, C.; Piles, M. BEC SMOS Soil Moisture Products Description 2020.

157. ONeill, Peggy E.; Chan, Steven; Njoku, Eni G; Jackson, Tom; Bindlish, Rajat; Chaubell, M. Julian; Colliander, Andreas SMAP Enhanced L2 Radiometer Half-Orbit 9 Km EASE-Grid Soil Moisture, Version 5 2021.

158. Das, Narendra N.; Entekhabi, Dara; Dunbar, R. Scott; Kim, Seung-bum; Yueh, Simon; Colliander, Andreas; O???Neill, Peggy E.; Jackson, Tom; Jagdhuber, Thomas; Chen, Fan; et al. SMAP/Sentinel-1 L2 Radiometer/Radar 30-Second Scene 3 Km EASE-Grid Soil Moisture, Version 3 2020.

159. Torres, R.; Snoeij, P.; Geudtner, D.; Bibby, D.; Davidson, M.; Attema, E.; Potin, P.; Rommen, B.; Floury, N.; Brown, M.; et al. GMES Sentinel-1 Mission. *Remote Sensing of Environment* **2012**, *120*, 9–24, doi:10.1016/j.rse.2011.05.028.

160. Reichle, Rolf; De Lannoy, Gabrielle; Koster, Randal; Crow, Wade; Kimball, John; Liu, Qing SMAP L4 Global 9 Km EASE-Grid Surface and Root Zone Soil Moisture Land Model Constants, Version 5 2020.

161. Didan, Kamel MOD13A2 MODIS/Terra Vegetation Indices 16-Day L3 Global 1km SIN Grid V006 2015.

162. Wan, Zhengming; Hook, Simon; Hulley, Glynn MYD11A1 MODIS/Aqua Land Surface Temperature/Emissivity Daily L3 Global 1km SIN Grid V006 2015.

163. Pablos, M.; Martínez-Fernández, J.; Piles, M.; Sánchez, N.; Vall-llossera, M.; Camps, A. Multi-Temporal Evaluation of Soil Moisture and Land Surface Temperature Dynamics Using in Situ and Satellite Observations. *Remote Sensing* **2016**, *8*, 587, doi:10.3390/rs8070587.

164. Pablos, M.; Piles, M.; Sánchez, N.; Vall-llossera, M.; Martínez-Fernández, J.; Camps, A. Impact of Day/Night Time Land Surface Temperature in Soil Moisture Disaggregation Algorithms. **2016**, doi:10.13039/501100000780.

165. Friedl, Mark; Sulla-Menashe, Damien MCD12Q1 MODIS/Terra+Aqua Land Cover Type Yearly L3 Global 500m SIN Grid V006 2019.

166. The IGBP-DIS Global 1km Land Cover Data Set, DISCover: First Results Available online: https://pubs.er.usgs.gov/publication/70187679 (accessed on 27 July 2021).

167. Defourny, P.; Lamarche, C.; Bontemps, S.; De Maet, T.; Van Bogaert, E.; Moreau, I.; Brockmann, C.; Boettcher, M.; Kirches, G.; Wevers, J.; et al. Land Cover CCI, PRODUCT USER GUIDE, VERSION 2.0.

168. ECMWF | ERA5 Satellite Data Available online: https://confluence.ecmwf.int/display/CKB/ERA5%3A+data+documentation#ERA5:datadocumentation-Observations (accessed on 29 October 2021).

169. ECMWF | Parameter Details | Soil Temperature Level 1 Available online: https://apps.ecmwf.int/codes/grib/param-db?id=139 (accessed on 29 October 2021).

170. Muñoz-Sabater, J.; Dutra, E.; Agustí-Panareda, A.; Albergel, C.; Arduini, G.; Balsamo, G.; Boussetta, S.; Choulga, M.; Harrigan, S.; Hersbach, H.; et al. ERA5-Land: A State-of-the-Art Global Reanalysis Dataset for Land Applications. *Earth System Science Data* **2021**, *13*, 4349–4383, doi:10.5194/essd-13-4349-2021.

171. Acevo-Herrera, R.; Aguasca, A.; Bosch-Lluis, X.; Camps, A.; Martínez-Fernández, J.; Sánchez-Martín, N.; Pérez-Gutiérrez, C. Design and First Results of an UAV-Borne L-Band Radiometer for Multiple Monitoring Purposes. *Remote Sensing* **2010**, *2*, 1662–1679, doi:10.3390/rs2071662.

172. Sánchez, N.; Martínez-Fernández, J.; Calera, A.; Torres, E.; Pérez-Gutiérrez, C. Combining Remote Sensing and in Situ Soil Moisture Data for the Application and Validation of a Distributed Water Balance Model (HIDROMORE). *Agricultural Water Management* **2010**, *98*, 69–78, doi:10.1016/j.agwat.2010.07.014.

173. Wagner, W.; Pathe, C.; Doubkova, M.; Sabel, D.; Bartsch, A.; Hasenauer, S.; Blöschl, G.; Scipal, K.; Martínez-Fernández, J.; Löw, A. Temporal Stability of Soil Moisture and Radar Backscatter Observed by the Advanced Synthetic Aperture Radar (ASAR). *Sensors* **2008**, *8*, 1174–1197, doi:10.3390/s80201174.

174. Ceballos, A.; Scipal, K.; Wagner, W.; Martínez-Fernández, J. Validation of ERS Scatterometer-Derived Soil Moisture Data in the Central Part of the Duero Basin, Spain. *Hydrological Processes* **2005**, *19*, 1549–1566, doi:10.1002/hyp.5585.

175. Rodriguez-Alvarez, N.; Camps, A.; Vall-llossera, M.; Bosch-Lluis, X.; Monerris, A.; Ramos-Perez, I.; Valencia, E.; Marchan-Hernandez, J.F.; Martinez-Fernandez, J.; Baroncini-Turricchia, G.; et al. Land Geophysical Parameters Retrieval Using the Interference Pattern GNSS-R Technique. *IEEE Transactions on Geoscience and Remote Sensing* **2011**, *49*, 71–84, doi:10.1109/TGRS.2010.2049023.

176. Smith, A.B.; Walker, J.P.; Western, A.W.; Young, R.I.; Ellett, K.M.; Pipunic, R.C.; Grayson, R.B.; Siriwardena, L.; Chiew, F.H.S.; Richter, H. The Murrumbidgee Soil Moisture Monitoring Network Data Set: DATA AND ANALYSIS NOTE. *Water Resour. Res.* **2012**, *48*, doi:10.1029/2012WR011976.

177. Richter, H.; Western, A.W.; Chiew, F.H.S. The Effect of Soil and Vegetation Parameters in the ECMWF Land Surface Scheme. *Journal of Hydrometeorology* **2004**, *5*, 1131–1146, doi:10.1175/JHM-362.1.

178. Ellett, K.M.; Walker, J.P.; Western, A.W.; Rodell, M. A Framework for Assessing the Potential of Remote-Sensed Gravity to Provide New Insight on the Hydrology of the Murray-Darling Basin. *Australasian Journal of Water Resources* **2006**, *10*, 125–138, doi:10.1080/13241583.2006.11465286.

179. Draper, C.; Walker, J.; Steinle, P.; de Jeu, R.; Holmes, T. An Evaluation of AMSR-E Derived Soil Moisture over Australia. *Remote Sensing of Environment* **2009**, *113*, 703–710, doi:10.1016/j.rse.2008.11.011.

180. Guerschman, J.P.; Van Dijk, A.I.J.M.; Mattersdorf, G.; Beringer, J.; Hutley, L.B.; Leuning, R.; Pipunic, R.C.; Sherman, B.S. Scaling of Potential Evapotranspiration with MODIS Data Reproduces Flux Observations and Catchment Water Balance Observations across Australia. *Journal of Hydrology* **2009**, *369*, 107–119, doi:10.1016/j.jhydrol.2009.02.013.

181. Peischl, S.; Walker, J.P.; Rüdiger, C.; Ye, N.; Kerr, Y.H.; Kim, E.; Bandara, R.; Allahmoradi, M. The AACES Field Experiments: SMOS Calibration and Validation across the Murrumbidgee River Catchment. *Hydrology and Earth System Sciences* **2012**, *16*, 1697–1708, doi:10.5194/hess-16-1697-2012.

182. Friedl, Mark; Sulla-Menashe, Damien MCD12Q1 MODIS/Terra+Aqua Land Cover Type Yearly L3 Global 500m SIN Grid V006 2019.

183. Defourny, P.; Lamarche, C.; Bontemps, S.; De Maet, T.; Van Bogaert, E.; Moreau, I.; Brockmann, C.; Boettcher, M.; Kirches, G.; Wevers, J.; et al. Land Cover CCI, PRODUCT USER GUIDE, VERSION 2.0.

184. Hersbach, H.; Bell, B.; Berrisford, P.; Hirahara, S.; Horányi, A.; Muñoz-Sabater, J.; Nicolas, J.; Peubey, C.; Radu, R.; Schepers, D.; et al. The ERA5 Global Reanalysis. *Q.J.R. Meteorol. Soc.* **2020**, *146*, 1999–2049, doi:10.1002/qj.3803.

185. Duveiller, G.; Cescatti, A. Spatially Downscaling Sun-Induced Chlorophyll Fluorescence Leads to an Improved Temporal Correlation with Gross Primary Productivity. *Remote Sensing of Environment* **2016**, *182*, 72–89, doi:10.1016/j.rse.2016.04.027.

186. Entekhabi, D.; Reichle, R.H.; Koster, R.D.; Crow, W.T. Performance Metrics for Soil Moisture Retrievals and Application Requirements. *Journal of Hydrometeorology* **2010**, *11*, 832–840, doi:10.1175/2010JHM1223.1.

187. Piles, M.; Sánchez, N.; Vall-llossera, M.; Camps, A.; Martínez-Fernández, J.; Martínez, J.; González-Gambau, V. A Downscaling Approach for SMOS Land Observations: Evaluation of High-Resolution Soil Moisture Maps Over the Iberian Peninsula. *IEEE Journal of Selected Topics in Applied Earth Observations and Remote Sensing* **2014**, *7*, 3845–3857, doi:10.1109/JSTARS.2014.2325398.

188. Piles, M.; Hernandez, M.P.; Vall-llossera, M.; Portal, G.; Sandric, I.; Petropoulos, G.P.; Hristopulos, D. *Synergistic Use of SMOS and Sentinel-3 for Retrieving Spatiotemporally Estimates of Surface Soil Moisture and Evaporative Fraction*; Copernicus Meetings, 2021;

189. Kottek, M.; Grieser, J.; Beck, C.; Rudolf, B.; Rubel, F. World Map of the Köppen-Geiger Climate Classification Updated. *Meteorologische Zeitschrift* **2006**, *15*, 259–263, doi:10.1127/0941-2948/2006/0130.

190. Calvet, J.-C.; Fritz, N.; Froissard, F.; Suquia, D.; Petitpa, A.; Piguet, B. In Situ Soil Moisture Observations for the CAL/VAL of SMOS: The SMOSMANIA Network. In Proceedings of the 2007 IEEE International Geoscience and Remote Sensing Symposium; July 2007; pp. 1196–1199.

191. Bircher, S.; Skou, N.; Jensen, K.H.; Walker, J.P.; Rasmussen, L. A Soil Moisture and Temperature Network for SMOS Validation in Western Denmark. *Hydrology and Earth System Sciences* **2012**, *16*, 1445–1463, doi:10.5194/hess-16-1445-2012.

192. Zeng, J.; Chen, K.-S.; Bi, H.; Chen, Q. A Preliminary Evaluation of the SMAP Radiometer Soil Moisture Product Over United States and Europe Using Ground-Based Measurements. *IEEE Transactions on Geoscience and Remote Sensing* **2016**, *54*, 4929–4940, doi:10.1109/TGRS.2016.2553085.

193. Ikonen, J.; Vehviläinen, J.; Rautiainen, K.; Smolander, T.; Lemmetyinen, J.; Bircher, S.; Pulliainen, J. The Sodankylä in Situ Soil Moisture Observation Network: An Example Application of ESA CCI Soil Moisture Product Evaluation. *Geoscientific Instrumentation, Methods and Data Systems* **2016**, *5*, 95–108, doi:10.5194/gi-5-95-2016.

194. Mateo-Sanchis, A.; Piles, M.; Amorós-López, J.; Muñoz-Marí, J.; Adsuara, J.E.; Moreno-Martínez, Á.; Camps-Valls, G. Learning Main Drivers of Crop Progress and Failure in Europe with Interpretable Machine Learning. *International Journal of Applied Earth Observation and Geoinformation* **2021**, *104*, 102574, doi:10.1016/j.jag.2021.102574.

195. Zhan, Q.; Vall-llossera, M.; Pablos, M.; Camps, A.; Portal, G.; Chaparro, D. Improving the Rice Yield Estimation Using SMOS and CYGNSS GNSS-R Data. In Proceedings of the IGARSS 2020 - 2020 IEEE International Geoscience and Remote Sensing Symposium; September 2020; pp. 5254–5257.

196. Chaparro, D.; Piles, M.; Martínez-Vilalta, J.; Vall-Llossera, M.; Vayreda, J.; Banqué-Casanovas, M.; Camps, A. Modelling Forest Decline Using Smos Soil Moisture and Vegetation Optical Depth. In Proceedings of the IGARSS 2018 - 2018 IEEE International Geoscience and Remote Sensing Symposium; July 2018; pp. 1459–1462.

197. Portal, G.; Vall-llossera, M.; Piles, M.; Camps, A.; Chaparro, D.; Pablos, M.; Rossato, L. A Spatially Consistent Downscaling Approach for SMOS Using an Adaptive Moving Window. In Proceedings of the 2017 IEEE International Geoscience and Remote Sensing Symposium (IGARSS); July 2017; pp. 4151–4153.

198. Cosh, M.H.; Jackson, T.J.; Bindlish, R.; Prueger, J.H. Watershed Scale Temporal and Spatial Stability of Soil Moisture and Its Role in Validating Satellite Estimates. *Remote Sensing of Environment* **2004**, *92*, 427–435, doi:10.1016/j.rse.2004.02.016.

199. Chen, Y.; Yang, K.; Qin, J.; Cui, Q.; Lu, H.; Zhu, la; Han, M.; Tang, W. Evaluation of SMAP, SMOS and AMSR2 Soil Moisture Retrievals against Observations from Two Networks on the Tibetan Plateau. *Journal of Geophysical Research Atmospheres* **2017**, *122*, 5780–5792, doi:10.1002/2016JD026388.

200. Burgin, M.S.; Colliander, A.; Njoku, E.G.; Chan, S.K.; Cabot, F.; Kerr, Y.H.; Bindlish, R.; Jackson, T.J.; Entekhabi, D.; Yueh, S.H. A Comparative Study of the SMAP Passive Soil Moisture Product With Existing Satellite-Based Soil Moisture Products. *IEEE Transactions on Geoscience and Remote Sensing* **2017**, *55*, 2959–2971, doi:10.1109/TGRS.2017.2656859.

201. Kim, S. Soil Moisture Active Passive (SMAP) - Ancillary Data Report (Landcover Classification) 2013.

202. Faroux, S.; Kaptué Tchuenté, A.T.; Roujean, J.-L.; Masson, V.; Martin, E.; Le Moigne, P. ECOCLIMAP-II/Europe: A Twofold Database of Ecosystems and Surface Parameters at 1 Km Resolution Based on Satellite Information for Use in Land Surface, Meteorological and Climate Models. *Geoscientific Model Development* **2013**, *6*, 563–582, doi:10.5194/gmd-6-563-2013.

203. Merlin, O.; Malbeteau, Y.; Notfi, Y.; Bacon, S.; Er-Raki, S.; Khabba, S.; Jarlan, L. Performance Metrics for Soil Moisture Downscaling Methods: Application to DISPATCH Data in Central Morocco. *Remote Sensing* **2015**, *7*, 3783–3807, doi:10.3390/rs70403783.

204. Chaparro, D.; Vayreda, J.; Vall-llossera, M.; Banqué, M.; Piles, M.; Camps, A.; Martínez-Vilalta, J. The Role of Climatic Anomalies and Soil Moisture in the Decline of Drought-Prone Forests. **2017**, doi:10.1109/JSTARS.2016.2585505.

205. Crow, W.T.; Berg, A.A.; Cosh, M.H.; Loew, A.; Mohanty, B.P.; Panciera, R.; de Rosnay, P.; Ryu, D.; Walker, J.P. Upscaling Sparse Ground-Based Soil Moisture Observations for the Validation of Coarse-Resolution Satellite Soil Moisture Products. *Reviews of Geophysics* **2012**, *50*, doi:10.1029/2011RG000372.

206. Qin, J.; Yang, K.; Lu, N.; Chen, Y.; Zhao, L.; Han, M. Spatial Upscaling of In-Situ Soil Moisture Measurements Based on MODIS-Derived Apparent Thermal Inertia. *Remote Sensing of Environment* **2013**, *138*, 1–9, doi:10.1016/j.rse.2013.07.003.

207. Baur, M.; Jagdhuber, T.; Link, M.; Piles, M.; Akbar, R.; Entekhabi, D. Multi-Frequency Estimation of Canopy Penetration Depths from SMAP/AMSR2 Radiometer and Icesat Lidar Data. In Proceedings of the IGARSS 2018 - 2018 IEEE International Geoscience and Remote Sensing Symposium; July 2018; pp. 365–368.

208. Portal, G.; Jagdhuber, T.; Vall-llossera, M.; Camps, A.; Pablos, M.; Entekhabi, D.; Piles, M. Assessment of Multi-Scale SMOS and SMAP Soil Moisture Products across the Iberian Peninsula. *Remote Sensing* **2020**, *12*, 570, doi:10.3390/rs12030570.

209. Piles, M.; Vall-llossera, M.; Camps, A.; Talone, M.; Monerris, A. Analysis of a Least-Squares Soil Moisture Retrieval Algorithm from L-Band Passive Observations. *Remote Sensing* **2010**, *2*, 352–374, doi:10.3390/rs2010352.

210. Portal, G.; Vall-llossera, M.; Jagdhuber, T.; Camps, A.; Pablos', M.; Piles, M. Incidence Angle Diversity on L-Band Microwave Radiometry and Its Impact on Consistent Soil Moisture Retrievals. In Proceedings of the 2021 IEEE International Geoscience and Remote Sensing Symposium IGARSS; July 2021; pp. 6186–6189.

211. Kurum, M. Quantifying Scattering Albedo in Microwave Emission of Vegetated Terrain. *Remote Sensing of Environment* **2013**, *129*, 66–74, doi:10.1016/j.rse.2012.10.021.

212. Mo, T.; Choudhury, B.J.; Schmugge, T.J.; Wang, J.R.; Jackson, T.J. A Model for Microwave Emission from Vegetation-Covered Fields. *Journal of Geophysical Research: Oceans* **1982**, *87*, 11229–11237, doi:10.1029/JC087iC13p11229.

213. O'Neill, P.; Bindlish, R.; Chan, S.; Chaubell, J.; Colliander, A.; Njoku, E.; Jackson, T. Algorithm Theoretical Basis Document Level 2 & 3 Soil Moisture (Passive) Data Products. 111.

214. Pablos, M.; Martínez-Fernández, J.; Piles, M.; Sánchez, N.; Vall-llossera, M.; Camps, A. Multi-Temporal Evaluation of Soil Moisture and Land Surface Temperature Dynamics Using in Situ and Satellite Observations. *Remote Sensing* **2016**, *8*, 587, doi:10.3390/rs8070587.

215. Jagdhuber, T.; Entekhabi, D.; Das, NN.; Link, M.; Baur, M.; Akbar, R.; Montzka, C.; Kim, S.; Yueh, S.; Baris, I. Physics-Based Modeling of Active-Passive Microwave Covariations for Geophysical Retrievals. In Proceedings of the IGARSS 2018 - 2018 IEEE International Geoscience and Remote Sensing Symposium; July 2018; pp. 250–253.

216. Karthikeyan, L.; Pan, M.; Konings, A.G.; Piles, M.; Fernandez-Moran, R.; Nagesh Kumar, D.; Wood, E.F. Simultaneous Retrieval of Global Scale Vegetation Optical Depth, Surface Roughness, and Soil Moisture Using X-Band AMSR-E Observations. *Remote Sensing of Environment* **2019**, *234*, 111473, doi:10.1016/j.rse.2019.111473.

217. Camps, A.; Vall-llossera, M.; Duffo, N.; Torres, F.; Corbella, I. Performance of Sea Surface Salinity and Soil Moisture Retrieval Algorithms with Different Auxiliary Datasets in 2-D L-Band Aperture Synthesis Interferometric Radiometers. *IEEE Transactions on Geoscience and Remote Sensing* **2005**, *43*, 1189–1200, doi:10.1109/TGRS.2004.842096.

218. [Raúl Díez, Personal Communication].

Acknowledgements

Firstly, I would like to thank my Thesis supervisors, Mercè Vall-llossera and Maria Piles, as well as Adriano Camps, who has also been essential for the development of this work. I have no words to thank you for your support, advice, guidance and the time you have dedicated to me throughout these years, for transmitting your passion for research and for sharing with me your vast knowledge in remote sensing.

I also wish to express a very special thanks to Thomas Jagdhuber, who kindly hosted me during my 3-months stay at DLR in Germany, and for the interest he demonstrated in my research, guiding me ever since. His way of working, his patience and his passion for research are also a reference for me. I would also like to thank Anke Fluhrer and Ismail Baris for the time we shared together at the DLR. I warmly thank José Martínez for allowing me to visit the REMEDHUS network and for sharing his knowledge with me. I want to thank him for the dedication, effort and love he puts into maintaining the REMEDHUS network, which has been essential in validating the results of this research Thesis and in many other projects. I would like to express my gratitude to Dara Entekhabi and Narendra Das for their advice and support during the last stage of the Thesis. I also thank Carsten Montzka, Mehrez Zribi and Nuria Duffo for accepting to be reviewers of this Thesis.

Further, I would also like to thank all the members of the “UPC team”: Miriam Pablos, David Chaparro, Christoph Herbert and Carlos López-Martínez, their support, both professional and personal, has been essential for the development of this Thesis. Also, to all the office colleagues with whom I have shared fun moments: Israel, Roselena, Julio, Luciana, Qian and Claudia. I would like to thank all the members of the SMOS Barcelona Expert Center, especially Verónica González for her help and advice. I also want to thank Beni and Aynie for their administrative support.

Finally, I would like to thank my friends and family, especially my mother, Palmira, for her love, infinite patience, and unconditional support.